



Design of functionally graded parts for additive manufacturing: Methods and tools for variable density Triply Periodic Minimal Surfaces

Emilio Adrian Ramirez Salazar

► To cite this version:

Emilio Adrian Ramirez Salazar. Design of functionally graded parts for additive manufacturing: Methods and tools for variable density Triply Periodic Minimal Surfaces. Material chemistry. Université Grenoble Alpes [2020-..], 2022. English. NNT : 2022GRALI077 . tel-04021430

HAL Id: tel-04021430

<https://theses.hal.science/tel-04021430>

Submitted on 9 Mar 2023

HAL is a multi-disciplinary open access archive for the deposit and dissemination of scientific research documents, whether they are published or not. The documents may come from teaching and research institutions in France or abroad, or from public or private research centers.

L'archive ouverte pluridisciplinaire **HAL**, est destinée au dépôt et à la diffusion de documents scientifiques de niveau recherche, publiés ou non, émanant des établissements d'enseignement et de recherche français ou étrangers, des laboratoires publics ou privés.

THÈSE

Pour obtenir le grade de

DOCTEUR DE L'UNIVERSITÉ GRENOBLE ALPES

École doctorale : I-MEP2 - Ingénierie - Matériaux, Mécanique, Environnement, Energétique, Procédés, Production

Spécialité : 2MGE : Matériaux, Mécanique, Génie civil, Electrochimie

Unité de recherche : Laboratoire des Sciences pour la Conception, l'Optimisation et la Production de Grenoble

Conception de pièces à gradient fonctionnel pour la fabrication additive : Méthodes et outils pour des surfaces minimales triplement périodiques à densité variable

Design of functionally graded parts for additive manufacturing: Methods and tools for variable density Triply Periodic Minimal Surfaces

Présentée par :

Emilio Adrian RAMIREZ SALAZAR

Direction de thèse :

François VILLENEUVE

Professeur des Universités, Université Grenoble Alpes

Directeur de thèse

Franck POURROY

Maître de Conférence, Université Grenoble Alpes

Co-encadrant de thèse

Nicolas BERAUD

Maître de Conférence, Université Grenoble Alpes

Co-encadrant de thèse

Rapporteurs :

Nabil ANWER

PROFESSEUR DES UNIVERSITES, Université Paris Saclay

Marco MONTEMURRO

PROFESSEUR DES UNIVERSITES, École Nationale Supérieure d'Arts et Métiers de Bordeaux

Thèse soutenue publiquement le 10 novembre 2022, devant le jury composé de :

Rémy DENDIEVEL

PROFESSEUR DES UNIVERSITES, Grenoble INP

Président

Nabil ANWER

PROFESSEUR DES UNIVERSITES, Université Paris Saclay

Rapporteur

Marco MONTEMURRO

PROFESSEUR DES UNIVERSITES, École Nationale Supérieure d'Arts et Métiers de Bordeaux

Rapporteur

Gianpaolo SAVIO

PROFESSEUR ASSOCIE, University of Padua (Università degli Studi di Padova)

Examineur

Clément GIRARD

INGENIEUR DOCTEUR, Chef de Produit Fabrication Additive, Hexagon

Examineur

Jorge Luis AMAYA RIVAS

PROFESSEUR ASSOCIE, ESPOL Polytechnic University, Escuela Superior Politécnica del Litoral, ESPOL

Examineur

François VILLENEUVE

PROFESSEUR DES UNIVERSITES, Université Grenoble Alpes

Directeur de thèse



Dedicado a mi mamá,

*Gracias por estar siempre a mi lado,
sin importar que tan difícil sea el camino.*

*Y por enseñarme que
lo que se hace con dedicación
siempre va bien.*

Acknowledgements

This research work was supported by the ANR BeShape Project of the French Agence Nationale de la Recherche, Paris, France [grant number ANR-18-CE10-0014-01].

I would like to thank François Villeneuve, Franck Pourroy and Nicolas Béraud, for their continuous support and supervision during the course of this work, and for letting me be a part of the BeShape Project on G-SCOP laboratory at Grenoble, France. I would also like to thank the industrial and academic partners of the BeShape project, for their contributions during the development of the thesis. Particularly, I am grateful for the precise research direction and personal advice from François Villeneuve, which provided me with the required guidance and tools to carry on the diverse activities and tasks during the thesis.

I would also like to thank Rémy Dendievel, Nabil Anwer, Marco Montemurro, Gianpaolo Savio, Clément Girard and Jorge Luis Amaya for accepting the invitation as jury members for my thesis defence. Especially, I would like to thank Marco Montemurro for his insightful comments and suggestions for the improvement of the work presented.

On a personal note, I would like to thank Jorge Luis Amaya from ESPOL Polytechnic University, Ecuador, for his invaluable support and encouragement to pursue a doctoral degree, for his help in my training as a teacher assistant, and for instructing me in scientific research prior to my travel to France. I would like to thank my mother Ivette Salazar and my family, for their constant support during this adventure. I would also like to thank Macha Raynal-Castang, for her daily support and patience, and for letting me dream big.

Lastly, I would like to thank my laboratory colleagues, in particular Frédéric Vignat, Christelle Grandvallet, Matthieu Museau, Mansour Mbow and Supasit Manokruang for the various musical sessions during the Coffi-Coffa band rehearsals, which helped me to bring art into my research activities.

Résumé

La fabrication additive par fil et arc (WAAM) est une nouvelle technologie de manufacture capable de construire des pièces tridimensionnelles en empilant des cordons de soudure de fils métalliques. En général, ces procédés présentent une vitesse de fabrication plus élevée, la possibilité de créer des pièces de grande taille grâce à l'absence de limitation du volume de la chambre et un rendement élevé des matériaux, par rapport aux autres technologies de fabrication additive métallique. En outre, la possibilité d'un dépôt local de matériau permet de produire des pièces légères en contournant les zones de faible contrainte, qui sont rarement éliminées en raison d'une restriction d'accessibilité. L'opportunité de produire des pièces allégées reste cependant peu exploitée aujourd'hui en WAAM.

Les outils classiques de conception pour la fabrication additive, tels que l'Optimisation Topologique (TO), peuvent fournir des informations sur une distribution "optimale" des matériaux par rapport au comportement mécanique requis, mais la géométrie résultante n'est généralement pas manufacturable en raison des fortes contraintes de fabrication associées au WAAM. Par conséquent, l'objectif de cette thèse est de proposer une approche de conception permettant de créer une pièce en combinant des modèles pouvant être fabriqués individuellement, adaptés à une carte de densité discrète obtenue à partir de procédures de TO ou d'analyse par éléments finis (FEA). Le travail de thèse se concentrera sur la démonstration de la faisabilité de cette approche, qui implique : la modélisation de modèles de motifs génériques, consistant en une forme paramétrique à laquelle sont associées les conditions de fabrication ; la définition de paramètres pour la variation de la densité, afin d'adapter la structure des motifs à une valeur de densité prédéfinie ; le développement de structures à gradient de densité, couvrant au mieux une carte de densité initiale résultant de procédures TO ou FEA et l'évaluation des processus de modélisation dans différentes études de cas, afin d'évaluer la performance mécanique requise.

En conséquence, une étude approfondie de l'utilisation de surfaces minimales triples périodiques (TPMS) Primitives et Gyroïdes comme modèles génériques pour les constructions cellulaires est présentée, sur la base d'une identification préalable des conditions de fabrication favorables sur WAAM. L'adaptabilité de la densité des motifs aux paramètres de leur conception est une étape importante pour relier la modélisation de la structure et les valeurs de densité locale requises. Ainsi, des équations pour la densité relative des motifs en fonction de leur épaisseur et de la taille des cellules unitaires sont développées et analysées. La modélisation des matériaux cellulaires à gradient fonctionnel (FGCM) basés sur des motifs TPMS est accomplie par une méthodologie de conception proposée capable de créer une densité variable en construisant trois scénarios : Variation de la densité des motifs TPMS par ajustement local de l'épaisseur, par modification de la taille des cellules unitaires, et par un changement simultané de l'épaisseur et de la taille. Enfin, la méthodologie proposée est testée sur une poutre cantilever remplie d'une structure TPMS à densité graduelle. En outre, un ensemble d'outils pour la conception de FGCM basés sur des modèles TPMS Primitifs et Gyroïdes a également été développé sous la forme

d'un plug-in "BeShape" personnalisé pour l'environnement de programmation visuelle Grasshopper de la suite CAO Rhinoceros 7.

Mots-clés : Fabrication additive, Matériau cellulaire à gradation des fonctions, Surface minimale triplement périodique, Wire and Arc Additive Manufacturing, Méthode de conception.

Ce document est rédigé en anglais. Une version résumée en français est disponible à la fin de ce document.

This document is written in English. A summary version in French is available at the end of this document.

Abstract

Wire and Arc Additive Manufacturing (WAAM) is a novel fabrication technology capable of constructing three-dimensional parts by stacking weld beads of metallic wire. In general, these processes present higher manufacturing speed, the possibility to create large parts due to their no-limitation regarding chamber volume and high material efficiency, compared with other metallic additive manufacturing technologies. In addition, the capability of a local deposition of material allows the production of lightweight parts by overpassing areas of low stress, which are rarely eliminated due to accessibility restriction. The opportunity to produce lightened parts remains, however, little exploited today in WAAM.

Classical design tools for additive manufacturing, such as Topological Optimization (TO), can provide information on an "optimal" material distribution with respect to the required mechanical behaviour, but the resulting geometry is generally not fabricable due to the high manufacturing constraints associated with WAAM. Consequently, the objective of this thesis is to propose a design approach to create a piece as a combination of individually fabricable patterns, adapted to a discrete density map obtained from TO or Finite Element Analysis (FEA) procedures. The thesis work will focus on showing the feasibility of this approach, which involves the: modelling of generic pattern models, consisting of a parametric shape to which are associated the manufacturing conditions; defining parameters for density variation, to adapt the patterns' structure to a predefined density value; developing gradient density structures, covering at best an initial density map resulting from TO or FEA procedures and evaluating the modelling processes in different case studies, to assess the required mechanical performance.

Accordingly, an in-depth study of the use of Primitive and Gyroid Triply Periodic Minimal Surface (TPMS) as generic patterns for cellular constructs is presented, based on a previous identification of favourable manufacturing conditions on WAAM. The adaptability of the patterns' density to their design parameters is an important step to relate the structure's modelling and the required local density values. Thus, equations for the patterns' relative density as a function of their thickness and unit-cell size are developed and analysed. The modelling of Functionally Graded Cellular Materials (FGCM) based on TPMS patterns is accomplished by a proposed design methodology capable of creating a variable density construct three scenarios: TPMS pattern density variation by local thickness adjustment, by unit-cell length modification, and by a simultaneous thickness and length change. Ultimately, the proposed methodology is tested on a cantilever beam filled with a graded density TPMS structure. Furthermore, a set of tools for the design of FGCM based on Primitive and Gyroid TPMS patterns was also developed as a custom-built "BeShape" plug-in for the Grasshopper visual-programming environment of Rhinoceros 7 CAD suite.

Keywords : Additive manufacturing, Functionally Graded Cellular Material, Triply Periodic Minimal Surface, Wire and Arc Additive Manufacturing, Design method.

Contents

Acknowledgements	iii
Résumé	v
Abstract	vii
List of Figures	xiii
List of Tables	xvii
List of Algorithms	xvii
Terminology	xxi
Glossary	xxiii
Nomenclature	xxv
General introduction	xxvii
BeShape Project	xxvii
Research question	xxviii
Research strategy	xxviii
Main contributions and manuscript organization	xxix
1 Literature review	1
1.1 Metallic additive manufacturing	1
1.2 Cellular materials	4
1.2.1 Metamaterial properties: Equivalent Material Analysis	5
1.2.2 Lattice structures	6
1.2.3 Triply Periodic Minimal Surfaces	9
1.3 Modelling of TPMS patterns	15
1.3.1 Fundamental shape generation	15
1.3.2 Model generation by level-set parameter variation	16
1.3.3 Model generation by surface offsetting	18
1.3.4 Model generation by Catmull-Clark subdivision	19
1.3.5 Fundamental shape assessment	19
1.4 Functionally Graded Cellular Materials	21
1.5 Literature review conclusions	22

2	Design parameters effects on relative density	23
2.1	Patterns design parameters' relationship analysis	23
2.1.1	Level-set effects on relative density	23
2.1.2	Thickness and length effects on relative density	26
2.2	Relative density function development	27
2.2.1	Equation as a function of thickness and length	27
2.2.2	Equation as a function of thickness-to-length ratio	31
2.2.3	Relative density equation error comparisons	33
2.3	Design parameter effects conclusions	34
3	Graded density TPMS patterns	35
3.1	Preliminary studies of variable design parameters	36
3.1.1	Variable thickness by TPMS patches offset	37
3.1.2	Variable unit-cell length by density surface	42
3.1.3	Marching Tetrahedra script for unit-cell length variation	44
3.1.4	Marching Tetrahedra script for thickness variation	47
3.1.5	Summary and discussion	49
3.2	General design methodology and custom-built tools	55
3.2.1	Design methodology overview	55
3.2.2	Density Mapping	58
3.2.3	Design Parameters Calculation	61
3.2.4	Fundamental Shape Generation	63
3.2.5	Pattern Surfaces Creation	66
3.2.6	Boundary Boolean Operations	67
3.2.7	Additional developed tools as Grasshopper components	67
3.3	Modelling tests from a three-dimensional density distribution	70
3.3.1	Comparison of example's design parameters	72
3.4	Graded density TPMS patterns conclusions	73
4	Analysis and evaluation of TPMS patterns	75
4.1	TPMS Equivalent Material analysis	75
4.1.1	Finite Element modelling conditions	76
4.1.2	Metamaterial properties for uniaxial compression loads	78
4.1.3	Metamaterial properties under shear loads	81
4.1.4	Equivalent Material analysis conclusions	83
4.2	Correlation of modelling with EM relationships	83
4.2.1	Finite Element Analysis data processing	84
4.2.2	Determination of relative density from FEA results	84
4.2.3	Evaluation of graded density constructs	85
4.3	Case study: functionally graded cantilever beam	89
4.3.1	Design conditions and preliminary FEA	89
4.3.2	Primitive-based cantilever	91
4.3.3	Gyroid-based cantilever	96
4.3.4	Modelling stage results comparison	99
4.3.5	Modelling evaluation	100
4.4	Analysis and evaluation of TPMS patterns conclusions	112
5	General conclusions and future work	113
5.1	Concluding remarks	113
5.2	Work perspectives	116

Bibliography	119
Appendices	133
A BeShape plug-in for Grasshopper	135
A.1 Main methodology components	137
A.1.1 Density Mapping	137
A.1.2 Design Parameter Mapping	138
A.1.3 TPMS Mesh Generator	139
A.1.4 SDF Offset	140
A.1.5 Simplified TPMS	141
A.2 Components for Equivalent Material analysis	143
A.2.1 ANSYS fileReader	143
A.2.2 Equivalent Material Coefficients	144
A.2.3 Relative Density from FEA	145
A.3 Main process utility components	147
A.3.1 Density Finder	147
A.3.2 Design Parameter Calculation	148
A.3.3 DS Box Expand	149
A.4 Process data components	151
A.4.1 Get and Set Qdata	151
A.4.2 Get and Set Modelling conditions	153
A.5 Utility components for visualization	155
A.5.1 Density Visualizer	155
A.5.2 Mesh Color by Density Map	156
A.5.3 Voxel Visualizer	157
A.6 Finite Element processing components	159
A.6.1 Mesh to SHELL FE	159
A.6.2 Variable Thickness ARRAY	159
B Determination of effective elastic properties	161
C C-shaped body case study	165
D Support information	169
D.1 Algorithm for relative density equation factors' optimization	169
D.2 Cantilever Beam case study	171
D.3 C-shaped body case study	179
E Résumé étendu	181
E.1 Etat de l'art	182
E.2 Effets des paramètres de conception	184
E.3 Méthodologie de conception	186
E.4 Analyse et évaluation des structures TPMS	190
E.5 Conclusions et perspectives	191

List of Figures

1.1	Powder-bed process schematic.	2
1.2	Powder-feed process schematic.	3
1.3	Wire-feed process schematic.	3
1.4	Common strut-based lattice structures.	8
1.5	Fundamental shapes of common TPMS.	10
1.6	Primitive and Gyroid TPMS.	16
1.7	Modelling by level set parameter variation.	17
1.8	Examples for skeletal-based patterns modelled by level set parameter variation.	17
1.9	Examples for sheet-based patterns modelled by level set parameter variation.	18
1.10	Fundamental shape offset process illustration.	19
1.11	Catmull-Clark subdivision process illustration.	19
2.1	Relative density <i>vs</i> level-set <i>C</i> for skeletal-based Primitive and Gyroid patterns.	25
2.2	Relative density <i>vs</i> level-set <i>C</i> for sheet-based Primitive and Gyroid patterns.	25
2.3	Example of thickness differences in sheet-based patterns.	26
2.4	Design parameters for constant thickness TPMS patterns.	27
2.5	Thickness and length effects on relative density of Primitive patterns.	28
2.6	Thickness and length effects on relative density of Gyroid patterns.	29
2.7	Relative density <i>RD</i> as a function of design parameters' ratio $\frac{d}{L}$ for Primitive and Gyroid patterns.	32
3.1	Two-dimensional density distribution in <i>x</i> and <i>z</i>	36
3.2	Patches' identification in a unit-cell.	37
3.3	Graded density by variable thickness process.	38
3.4	<i>Variable UC</i> Cluster	38
3.5	<i>Patch Generator</i> Cluster	40
3.6	Example for patch points' offset.	41
3.7	Patch interfaces interconnectivity after <i>4-point-con-X</i> , <i>Y</i> and <i>Z</i> Clusters.	41
3.8	<i>Patch Meshing</i> Cluster	42
3.9	Variable thickness Primitive pattern assembly by patch offset.	42
3.10	Front view examples of errors in surface continuity for length variation from patch construction.	43
3.11	Graded density by variable length in density surface process.	43
3.12	Density distribution surface.	44
3.13	Variable length Primitive pattern assembly by IsoSurface tool.	44
3.14	Marching Tetrahedra algorithm process.	45

3.15	Marching Tetrahedra script flowchart for Graded density by variable length process.	46
3.16	Variable length pattern assemblies by C# script.	46
3.17	Marching Tetrahedra script flowchart for Graded density by variable thickness process.	48
3.18	Variable thickness pattern assemblies by C# script.	48
3.19	Screenshot of the implemented methodology for the 2x2x2 Primitive pattern assembly with thickness variation.	51
3.20	Correction of topology discontinuities by surface transposing.	52
3.21	Methodology flowchart overview.	56
3.22	Detailed design methodology for graded density TPMS constructs.	57
3.23	Sensitivity and tolerance zones representation.	59
3.24	Density Mapping GH component overview.	60
3.25	Ratio vs inverse length for simultaneous thickness and length variation.	61
3.26	Design Parameter Mapping GH component overview.	62
3.27	Geometry for voxel length factor definition.	63
3.28	TPMS shape lateral projection.	64
3.29	TPMS Mesh Generator GH component overview.	64
3.30	Voxel cloud processing.	65
3.31	SDF Offset GH component overview.	66
3.32	Simplified TPMS GH components overview.	69
3.33	Density Finder utility GH components overview.	69
3.34	Density distribution test on (x, y, z)	70
3.35	Variable thickness tests from a (x, y, z) density distribution.	71
3.36	Variable length tests from a (x, y, z) density distribution.	71
3.37	Variable thickness-to-length ratio tests from a (x, y, z) density distribution.	72
4.1	Boundary conditions for Primitive TPMS FE simulation.	77
4.2	Uniaxial compression results.	80
4.3	Shear load results.	82
4.4	ANSYS fileReader GH component overview.	85
4.5	Equivalent Material coefficients GH component overview.	86
4.6	Relative Density from FEA GH component overview.	86
4.7	Mesh to SHELL GH component overview.	87
4.8	Variable Thickness ARRAY GH component overview.	87
4.9	Plate dimensions and load conditions.	88
4.10	Uniaxial compression results.	88
4.11	Cantilever beam dimensions and load conditions.	90
4.12	Cantilever beam preliminary FEA.	90
4.13	Primitive-based cantilever: Density map from preliminary FEA.	92
4.14	Primitive-based cantilever: Variable thickness modelling.	94
4.15	Primitive-based cantilever: Variable length fundamental mesh.	94
4.16	Primitive-based cantilever: Variable thickness-to-length ratio modelling.	95
4.17	Gyroid-based cantilever: Density map from preliminary FEA.	97
4.18	Gyroid-based cantilever: Variable thickness modelling.	97
4.19	Gyroid-based cantilever: Variable thickness-to-length ratio modelling.	98
4.20	Primitive-based cantilever: Constant density evaluation.	101
4.21	Primitive-based cantilever: Variable thickness evaluation.	102
4.22	Primitive-based cantilever: Variable thickness-to-length ratio evaluation.	103
4.23	Gyroid-based cantilever: Constant density evaluation.	105

4.24	Gyroid-based cantilever: Variable thickness evaluation.	106
4.25	Gyroid-based cantilever: Variable thickness-to-length ratio evaluation.	107
4.26	Variable thickness-to-length ratio redesign.	109
4.27	Primitive-based cantilever: Redesign evaluation.	110
4.28	Gyroid-based cantilever: Redesign evaluation.	111
A.1	BeShape GH plug-in components family.	135
A.2	Design Parameter Calculation utility GH component overview.	148
A.3	DS Box Expand utility GH component overview.	149
A.4	Get Qdata GH component overview.	151
A.5	Q to Qdata GH component overview.	151
A.6	Q Distribution to Qdata GH component overview.	151
A.7	Get modelling_conditions GH component overview.	153
A.8	Set modelling_conditions GH component overview.	153
A.9	Density visualizer GH component overview.	155
A.10	Mesh Color by Density Map GH component overview.	156
A.11	Voxel Visualizer GH component overview.	157
C.1	C-shaped body: Dimensions and load conditions.	165
C.2	C-shaped body: Preliminary FEA.	166
C.3	C-shaped body: Density mapping from FEA.	166
C.4	C-shaped body: Modelling.	167
C.5	C-shaped body: Variable thickness-to-length ratio evaluation.	168
E.1	Topologies à épaisseur constante pour les structures TPMS.	185
E.2	Densité relative RD fonction du rapport des paramètres de conception $\frac{d}{L}$ pour les structures Primitif et Gyroïde.	186
E.3	Méthodologie de conception pour les structures TPMS à gradient fonctionnel.	187
E.4	Illustration des étapes de la méthode proposée.	191

List of Tables

1.1	Metallic additive manufacturing systems classification by feedstock.	2
1.2	SLM lattice structures' test data collected from the literature.	8
1.3	TPMS patterns' test data collected from the literature.	12
1.4	Studies for TPMS mechanical behaviour characterization. CONTINUED .	13
1.5	Reported Gibson-Ashby model's coefficients by FE simulation and experi- mental testing.	14
1.6	Fundamental shape surface-to-volume ratio comparison	20
2.1	C parameter effects on Primitive and Gyroid TPMS patterns.	24
2.2	Summary for RD and C relationships.	25
2.3	RSS and absolute percentage error differences before and after Gradient Descent optimization in relative density equation parameters.	31
2.4	Range of applicability for the proposed relative density equations.	33
2.5	Comparison of RSS and maximum percentage error of relative density equa- tions for Primitive and Gyroid patterns.	33
3.1	Summary of preliminary studies for graded density pattern assemblies by variable thickness.	50
3.2	Summary of preliminary studies for graded density pattern assemblies by variable length.	53
3.3	Design parameter values range from different modelling methodologies. . . .	72
4.1	Gibson-Ashby model's coefficients for uniaxial compression testing scenarios.	78
4.2	Gibson-Ashby model's coefficients shear testing scenarios.	81
4.3	Plate FEA analysis results.	88
4.4	Functionally graded cantilever beam modelling summary.	99
4.5	Functionally graded cantilever beam evaluation results summary.	108
A.1	Developed Grasshopper components.	136
B.1	Effective elastic properties results: Primitive UC $\rho^* = 0.094$	163
B.2	Elastic properties bounds.	163
B.3	Relative elastic properties.	164
C.1	Functionally graded C-shaped body evaluation results.	167

List of Algorithms

A.1.1Density Mapping GH component	137
A.1.2Design Parameter Mapping GH component	138
A.1.3TPMS Mesh Generator GH component	139
A.1.4SDF Offset GH component	140
A.1.5Primitive and Gyroid TPMS GH components	141
A.2.1ANSYS fileReader GH component	143
A.2.2Equivalent Material Coefficients GH component	144
A.2.3Relative Density from FEA GH component	145
A.3.1Density Finder utility GH component	147
A.3.2Density Finder Plus utility GH component	147
A.3.3Design Parameter Calculation utility GH component	148
A.3.4DS Box Expand utility GH component	149
A.4.1Get Qdata GH component	152
A.4.2Q to Qdata GH component	152
A.4.3Q Distribution to Qdata GH component	152
A.4.4Get modelling_conditions GH component	153
A.4.5Set modelling_conditions GH component	153
A.5.1Density visualizer GH component	155
A.5.2Mesh Color by Density Map GH component	156
A.5.3Voxel Visualizer GH component	157
A.6.1Mesh to SHELL FE GH component	159
A.6.2Variable Thickness ARRAY GH component	159
D.1.1Gradient Descent for α, β, γ optimization	169

Terminology

Cellular material Arranged network of individual unit-cell structures.

Cluster Grouping of Grasshopper graphical programming tool components of the Rhinoceros CAD suite.

Design space Three-dimensional zone representing the boundary for design and/or optimization.

Lattice Repetitive arrangement of unit-cells, other than minimal surfaces.

Metamaterial Engineered material, commonly related to micro or nano-scale patterns, designed with customized properties.

Minimal surface Mathematical surface with local minimal area and zero mean curvature.

Model Dense or solid representation of a pattern unit-cell or assembly.

Patch $\frac{1}{8}$ part of the minimal surface. Used to construct a unit-cell of a minimal surface by self-rotations and/or translations.

Pattern One minimal surface unit-cell.

Pattern assembly Three-dimensional arrangement of patterns of any type (not necessarily of the same shape, size and density).

Sensitivity Maximum area size representing the distance considered to look for reference values to determine a local density value.

Sheet-based pattern Pattern modelled as a film.

Skeletal-based pattern Pattern modelled with similar construction to truss lattices.

Strut-based pattern Lattice pattern modelled by a set of struts and nodes.

Step Number of divisions in the TPMS function domain.

Tolerance Maximum area representing the distance for an automatic assignment of a local density value.

Triply Periodic Minimal Surface (TPMS) Minimal surface characterized by a translational periodicity in three-dimensions.

Unit-cell Representation of a single pattern or structure.

Weighted Sum Method for determining a value as the sum of input values, each multiplied by a specified weight.

Glossary

AM	Additive Manufacturing
APDL	ANSYS® Parametric Design Language
API	Application Programming Interface
CAD	Computed Aided Design
CAM	Computed Aided Manufacturing
CMT	Cold Metal Transfer
DED	Direct Energy Deposition
DM	Density Map
DMD	Direct Metal Deposition
DMLS	Direct Metal Laser Sintering
DS	Design Space
EBM	Electron Beam Melting
FEA	Finite Element Analysis
FGCM	Functionally Graded Cellular Material
GH	Grasshopper® visual programming tool
GMAW	Gas Metal Arc Welding
GTAW	Gas Tungsten Arc Welding
I/O	Input/Output
LC	Laser Consolidation
LENS	Laser Engineered Net Shaping
LMD	Laser Metal Deposition
MC	Marching Cubes algorithm
MIG	Metal Inert Gas
MT	Marching Tetrahedra algorithm
PBC	Periodic Boundary Conditions
PBF	Powder Bed Fusion
PWD	Plasma Wire Deposition
RSS	Residual Sum of Squares
SD	Standard Deviation
SDF	Signed Distance Field
SLM	Selective Laser Melting
SLS	Selective Laser Sintering
SMD	Shaped Metal Deposition
STL	Standard Tessellation Language
TO	Topological Optimization
TPMS	Triply Periodic Minimal Surface
UI	User Interface
WAAM	Wire and Arc Additive Manufacturing

Nomenclature

A	Pattern cross-sectional area
α, β, γ	Factors for relative density equation definition
C	Level-set parameter
c	Constant of proportionality, Gibson-Ashby model
d	Pattern thickness
D	Diameter of projected TPMS pore
E, E^*	Young Modulus, Relative Young Modulus
ϵ	Approximation error of circular sector
$f_{P,G}$	TPMS shape function
G, G^*	Shear Modulus, Relative Shear Modulus
h, h^*	Voxel length factor
η_k	Gradient step value
θ_k	Optimization vector
L	Unit-cell length
L_i	Pattern assembly length
λ_i	Dilatation factor
n	Power Law exponent constant, Gibson-Ashby model
n_i	Number of unit-cell instances
N	Number of nodes on strut-based constructs
m	Density map node for weighted sum
M	Maxwell number
O	Point for surface generation transposition
P	Applied load
Q	Density distribution
r	Reference value node for weighted sum
R	Effective radius of projected TPMS pore
RD	Relative density from CAD data
ρ^*	Relative density
S	Number of struts on strut-based constructs
$S/V^{2/3}$	Normalized surface-to-volume ratio
s_f	Security Factor
σ_0	Yield Stress
σ_{perm}	Permissible Stress
σ^*	Relative Strength under compression loads
τ^*	Relative Strength under shear loads
u	Displacement along force line of action
ϕ	Level-set equation
ω	Distance to reference node for weighted sum
Ω	Sum of inverse-squared distances

General introduction

BeShape Project

Wire and Arc Additive Manufacturing (WAAM) is a novel fabrication technology which uses an electric arc as a heat source to fuse a metallic wire. Thus, three-dimensional parts are constructed by stacking weld beads of any type of weldable material. These processes have shown great promise for industrial applications, particularly because of its higher manufacturing speed compared to metallic powder-bed technologies and the possibility to create large parts due to having no-limitation regarding chamber volume and high material efficiency [Gisario et al., 2019]. In addition, the capability of a local deposition of material allows the production of lightweight parts by overpassing areas of low stress, which are rarely eliminated in other technologies, such as subtractive manufacturing, due to accessibility restrictions. The opportunity to produce lightened parts remains, however, little exploited today in WAAM.

Nevertheless, the manufacturing constraints associated with WAAM are very high. An immediate consequence is that classical design tools for additive manufacturing, such as topological optimization (TO), are not directly exploitable. Results of TO provide information on an "optimal" material distribution with respect to the required mechanical behaviour, but the resulting geometry is generally not manufacturable.

Accordingly, the BeShape project for *Conception de pièces légères fabriquées par apport de fil et arc électrique* (Design of light parts manufactured by supply of wire and electric arc) proposes to see this optimal topology as an assembly of patterns. The main objective of the project is to propose a design approach allowing to obtain lightweight parts by assembling predefined patterns fabricable by WAAM, in order to take advantage of the freedoms offered by these processes while respecting the constraints of manufacturability and the requirements formulated by the designer. For this, the project aims to validate if it is possible to design a part by a selection and intelligent combination of individually fabricable patterns.

The BeShape project is coordinated by the laboratory G-SCOP (Sciences pour la conception, l'Optimisation et la Production) of the Université Grenoble Alpes, in partnership with the COSMER laboratory (Conception de Systèmes Mécaniques et Robotiques) of the Université de Toulon and the industrial partners DRPI, PRODWAYS and SAFRAN AE. In particular, this manuscript will present the work on mechanical design and evaluation carried at G-SCOP laboratory, while the construction aspects of manufacturing constraints analysis and tool-path generation are a focus for the COSMER laboratory.

Main research question

According to the BeShape project's context, this manuscript will follow up previous work for the integration of lattice structures on the design of parts to be fabricated by AM [Azman, 2017]. The present work details the surface creation, adaptation of the design to a pre-established density map and evaluation of constructs using Triply Periodic Minimal Surface (TPMS) patterns as building blocks for Functionally Graded Cellular Materials (FGCM), due to previous identification of favourable manufacturing conditions carried on by the COSMER laboratory and a literature review on the application and characterization of these structures. The research question to be examined is:

How to design lightweight parts based on Triply Periodic Minimal Surface (TPMS) patterns, manufacturable by Direct Energy Deposition (DED) processes?

Research strategy

The main approach followed for assessing the research question is detailed in the steps below:

1. **Modelling** generic pattern models, that should consist of a parametric shape to which are associated the manufacturing conditions. This step includes the state-of-the-art review for the employment of TPMS in diverse AM technologies, in order to identify the current perspectives of their design, modelling and mechanical characterization.
2. **Defining** parameters for density variation, to adapt the patterns' structure to a predefined density value. The change on TPMS design parameters, i.e. the manipulation of their mathematical definition, is used to determine the systematic methods to vary their density.
3. **Developing** gradient density structures, covering at best an initial density map resulting from TO or FEA procedures. This includes the examination of the identified methods for density variation in diverse approaches to propose a novel methodology for the developing of gradient density structures. Moreover, the methods for correlation between the density mapping and modelling methodologies is also considered in this stage.
4. **Evaluating** the modelling processes in different case studies, to assess the required mechanical performance. Equivalent material or metamaterial analysis is considered in this step, to obtain the relationships between the mechanical responses of TPMS with respect to their relative density.

Main contributions and manuscript organization

Based on a literature review on metallic Additive Manufacturing (AM) and the suitability of TPMS patterns in *Chapter 1*, this manuscript aims to fill the gap in the state-of-the-art methods and tools for modelling graded density TPMS constructs. The following points details the main contributions of this work:

1. Relations of the relative density of TPMS patterns as a function of thickness and length. For this purpose, *Chapter 2* details the mathematical construction of TPMS and the parameters that influence their shape and the development of a proposed relative density equation as a function of the pattern design parameters.
2. Creation of TPMS of variable thickness and/or length by a proposed methodology based on a Marching Tetrahedra (MT) polygonization algorithm for pattern surface's creation, introduced in *Chapter 3*, by a comparison of various strategies for graded density structures generation.
3. Global design method and implementation for the creation of variable density TPMS. *Chapter 3* contains the proposed general design methodology, along with several design tools for pattern's construction which are further detailed in the appendix sections. Furthermore, *Chapter 4* focus on the design validation stages of the proposed modelling processes results. A case study with different strategies of density variation is used to assess the feasibility of the process, while comparing the results to the solid part configuration.
4. Metamaterial mechanical characterization of Primitive and Gyroid TPMS, completing missing information the literature. The study of TPMS mechanical response as a function of their density is first introduced in *Chapter 4*. The results are used to feed the design methodology to generate structures with localized variations of density according to density distributions from TO or Finite Element Analysis (FEA) simulations.

Supplementary contributions as a result of the research work are as follows:

- Implementation of a variable thickness FE shell meshing procedure, based on the assignation of local thickness values to the Standard Tessellation Language (STL) mesh nodes of FGCM models.
- Construction of regular density maps from FEA simulation results.
- Development and compilation of design tools written in C# programming language, able to be included as a plug-in to the Grasshopper[®] visual-programming environment of Rhinoceros[®] 7 CAD suite.

In addition, peer-reviewed publications were presented for a preliminary formal introduction of a design methodology [Ramírez et al., 2022a], the definition of mechanical responses as a function of the pattern density [Ramírez et al., 2022b], and the equations for the relative density as a function of the design parameters [Ramírez et al., 2021b,a].

Lastly, *Chapter 5* presents the overall conclusions and perspectives resulting from the study of adaptable TPMS structures. Even though the thesis is heavily influenced by the BeShape project applications on WAAM, the contributions are treated in a general scenario that can be applied to different AM technologies. Manufacturing constraints related to WAAM are not a focus of this study.

Chapter 1

Literature review

Introduction

Additive manufacturing (AM), also known as rapid prototyping or three-dimensional (3D) printing, is a novel technology, commonly referred to the freeform fabrication of parts in a layer-by-layer material deposition approach [Urhal et al., 2019], that has presented promising advantages over traditional manufacturing processes regarding its ability to directly produce functional parts of increasing complexity and topology [Gao et al., 2015, Gisario et al., 2019, Vayre et al., 2012, Yuan et al., 2019].

Standard AM workflow starts with a part modelling stage in a Computer Aided Design (CAD) environment, which permits the conception, modification and optimization of the design. The modelled part is then converted to a Standard Tessellation Language (STL) file, commonly used in AM applications, which stores the information of the part's surfaces as an arrangement of triangular facets. STL files are then loaded to the Computer Aided Manufacturing (CAM) software which performs the parts' layering for manufacturing [Yuan et al., 2019]. Depending on AM process characteristics and parameters, these technologies are able to manufacture metallic, polymeric, ceramic or composite parts. Accordingly, ISO/ASTM [2021] establishes a general overview of AM process categories depending on the equipments' working principles.

By being under the BeShape project framework, research focus of this thesis is aimed towards the design of complex parametric patterns to be fabricated by Wire and Arc Additive Manufacturing (WAAM). Consequently, a benchmark of different metallic AM technologies is first introduced to highlight the advantages and limitations of wire-feed systems in comparison to metallic powder-bed and powder feed process. Following, a review on cellular materials is presented with a special attention to Triply Periodic Minimal Surfaces (TPMS), given the research focus of the BeShape project's partners on the manufacturability of these type of surfaces.

1.1 Metallic additive manufacturing

Among the different process categories for AM, metallic feedstock is commonly handled by Powder Bed Fusion (PBF) or Direct Energy Deposition (DED) technologies. Accordingly, ISO/ASTM [2021] defines PBF as a "process in which thermal energy selectively fuses regions of a powder bed" and DED as a "process in which focused thermal energy is used to fuse materials by melting as they are being deposited", while establishing that the energy source can be either laser, electron beam or plasma arc, among others.

Table 1.1: Metallic additive manufacturing systems classification by feedstock.

Classification	AM technology	Advantages	Drawbacks
Powder-bed systems	EBM, DMLS, SLM	Small part fabrication ¹ , high resolution features ^{1,2} , maintain dimensional control ¹	Low deposition rates ¹ , large heat-affected area ^{1,3} , part porosities depending on process parameters ⁴
Powder-feed systems	LENS, DMD, LC, LMD	Can be used to refurbish and repair damaged components ^{1,2} , possibility to produce multi-material parts ^{2,5}	Lower surface quality than powder-bed systems ^{1,2} , lower part accuracy ²
Wire-feed systems	SMD, CMT, PWD, WAAM	Large part fabrication ^{1,3} , high deposition rates ^{1,3,6} , fewer material contamination issues ^{1,6}	Less precision in as-built parts ^{3,7,8} , requires extensive machining post-processes ^{1,8} , presence of residual stresses ^{9,10}

¹[Frazier, 2014], ²[Yuan et al., 2019], ³[Gisario et al., 2019], ⁴[Vayre et al., 2012], ⁵[Yakovlev et al., 2005],
⁶[Martina et al., 2012], ⁷[Rodrigues et al., 2019], ⁸[Cunningham et al., 2018], ⁹[Derekar, 2018], ¹⁰[Ding et al., 2015]

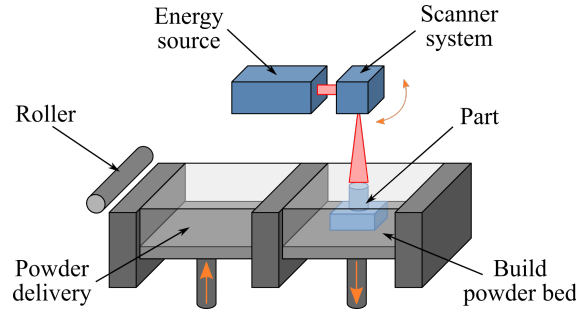


Figure 1.1: Powder-bed process schematic.

An alternative categorization was previously presented by Frazier [2014], broadly dividing metallic AM in terms of the bulk material in: powder bed, powder-feed and wire-feed systems. Based on ISO/ASTM [2021] definitions, both material feed processes fall under DED process category [Dass and Moridi, 2019]. Thus, Table 1.1 summarizes some of the general benefits and drawbacks, as well as the technologies developed for the different systems under this division regarding feedstock, to establish a distinction between powder-feed and wire-feed technologies.

In general, powder-bed or PBF systems such as Electron Beam Melting (EBM), Direct Metal Laser Sintering (DMLS), Selective Laser Melting (SLM), Selective Laser Sintering (SLS), are able to produce parts by solidifying metallic, polymeric or composites powders with the use of a high energy laser or electron beam. The general fabrication process consists in the selective elevation of the powder temperature over the melting point (or the softening point for polymers) to consolidate the particles together [Yuan et al., 2019] by the use of a scanner system. Afterwards, a new layer of particulate material is transferred by a roller from a powder delivery container to the fabrication powder bed, and fused to the previous layers to create a 3D construct [Ngo et al., 2018]. Figure 1.1 presents a schematic of powder-bed systems.

In contrast, the working principle of powder-based DED or powder-feed systems, such as Laser Engineered Net Shaping (LENS), Direct Metal Deposition (DMD), Laser Consol-

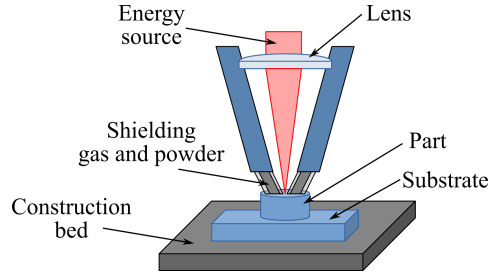


Figure 1.2: Powder-feed process schematic.

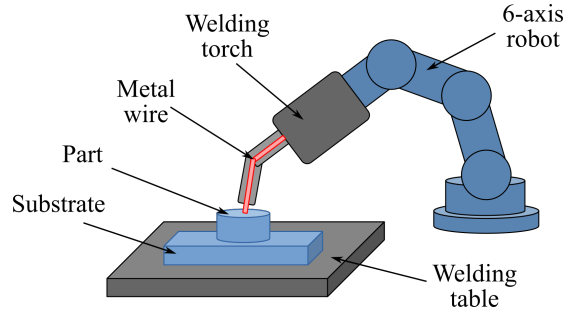


Figure 1.3: Wire-feed process schematic.

idation (LC), Laser Metal Deposition (LMD), relies on the direct deposition and melting of metallic powder by an energy source over a substrate mounted in a construction bed or framework. Usually these processes are oriented to large part fabrication and damaged parts' refurbishing and repair. However, they present a lower part accuracy and surface quality compared with powder bed systems. Figure 1.2 shows a schematic representation of these systems.

Wire-feed systems are a type of DED and, as the name states, utilise metal wire as a supply material for part construction. These types of systems can be further classified in laser-based, arc welding-based and electron beam-based, depending on the energy source [Ding et al., 2015]. The traditional configuration of these systems comprise a welding torch mounted on a 6-axis robot, as depicted by Figure 1.3. The part is commonly built over a substrate structure mounted on a static or rotary welding table. Even though wire-feed processes present higher material usage efficiency and depositions rates when compared with other metallic AM technologies [Ding et al., 2015], the final part quality greatly depends on the control of high level residual stress and heat distortion [Ding et al., 2015, Cunningham et al., 2018, Urhal et al., 2019, Williams et al., 2016].

Previous efforts in process parameters control on Wire and Arc Additive Manufacturing (WAAM) have been presented by Baufeld et al. [2010], utilising inert gas welding (TIG) in Shaped Metal Deposition (SMD) processes to produce tubular components, while defining operational parameters for wire feed speed, travel speed and electrical current. In their study, it is stated that different welding techniques can be selected depending on the required deposition rate, surface quality and environmental (atmosphere) conditions. Cold Metal Transfer (CMT) applications, another type of arc-welding-based process, considers an incorporation of mechanical motion of the wire to the electrical process control [Almeida and Williams, 2010, Pickin et al., 2011], thus lowering the thermal heat input and weld spattering [Almeida and Williams, 2010]. CMT studies have been tested in Ti-6Al-4V deposition by Gas Metal Arc Welding (GMAW) [Almeida and Williams, 2010], and deposition by Metal Inert Gas (MIG) welding of Al-2319 wire [Pickin et al., 2011]. In addition,

Plasma Wire Deposition (PWD) has been tested for plasma arc welding-based of Ti-6Al-4V, providing higher energy density and increased arc stability compared to competing process as Gas Tungsten Arc Welding (GTAW) deposition [Martina et al., 2012]. In this last case, although having higher deposition rates, encountered issues include larger cooling times between layers than the actual deposition times, and layer height inconsistencies [Martina et al., 2012].

Another benefit regarding WAAM is the capability to produce parts without the building space restriction on conventional powder-bed equipment [Gisario et al., 2019, Martina et al., 2012, Nguyen et al., 2018]. While being able to operate with higher degrees of freedom, WAAM requires corrected tool-path trajectories and process planning [Hascoët et al., 2017, Wulle et al., 2017]. For a multi-directional deposition approach, overhangs or bridge-like shapes need to be detected and printed in their own building direction.

Accordingly, previous studies have proposed a method to vary layer thickness and slicing / deposition direction, guided by a centroidal axis location; however, the process had limitations on identifying a geometry change in symmetrical overhang structures [Ruan et al., 2007]. Further studies have also presented a part decomposition-regrouping method, consisting in four processing modules for part simplification, model decomposition, build direction identification and sub-volume slicing [Ding et al., 2016], instead of a multi-direction slicing approach. Algorithm limitations were noted, regarding complex parts with open concave loops or non-sharp edges. A strategy combining the aforementioned approaches has also been studied, i.e. a methodology which decomposed the CAD model and computed the centroidal axis extraction for each subpart, thus, being able to detect symmetrical overhangs and branches in different directions with their own centroidal guide for the slicing and building processes [Nguyen et al., 2018]. However, the opportunity to produce lightweight parts have not been fully exploited for WAAM.

The manufacturing constraints associated with WAAM are very high. For instance, temperature plays an important role on welding bead geometries on CMT process [Robert et al., 2018], and it is strongly related to the manufacturing parameters. Particularly, it has been found that welding bead size highly depends on substrate part's temperature. An increase of temperature improves the wetting angle of aluminium beads, thus, producing a decrease on bead height [Manokruang et al., 2021b]. Recent studies have focused on developing prediction strategies for semicircle-modelled bead geometries as a function of the process parameters [Manokruang et al., 2021a], as well as the use of CMT technologies on metallic coatings [Robert et al., 2019] and the development of smart metal parts with embedded strain sensors [Robert et al., 2021].

1.2 Cellular materials

Cellular materials, which are characterized by a connected network of individual unit-cells, can be configured to create strong load-bearing structures [Ashby, 2006] with a significant change on the physical response when compared to their constituting material [Maconachie et al., 2019]. These low-density architectures are capable of producing a simultaneous weight, stiffness and strength optimization [Ashby and Medalist, 1983, Banhart and Seeliger, 2008] and have been considered attractive for their use as cores for panels and shells [Evans et al., 2001], energy absorption applications [Zhu et al., 2010], and in the development of lightweight structures [Li et al., 2018].

In general, cellular materials can be divided in stochastic (foams) or non-stochastic materials. Metallic foams, a type of stochastic materials, can be fabricated by the addition of gas or foam agents into molten metal, by a relatively low-cost manufacturing process

[Maconachie et al., 2019]. However, the resulting unordered structure can present inconsistent mechanical properties [Smith et al., 2013]. In contrast, non-stochastic materials are characterized by an organized distribution of single unit-cells, providing a reliable control of deformation compared to foam structures [Maskery et al., 2017a]. Thus, following subsections will focus on the analysis and characteristics of non-stochastic materials.

1.2.1 Metamaterial properties: Equivalent Material Analysis

At cellular level, the building blocks or unit-cells can be considered as structures with their own mechanical properties [Maconachie et al., 2019], but behave as homogenised metamaterials in the macro-level or structured arrangement [Amin Yavari et al., 2015]. The term metamaterial is commonly employed to refer to rationally designed materials with mechanical properties directly related to the topology of their micro-architecture [Hedayati et al., 2017]. It has been established that the effects of cellular constructs' topology are more significant than the used material [Hedayati et al., 2018]. Thus, a common, yet limited approach used in the literature is to refer the mechanical responses of a cellular construct as dimensionless parameters under the Gibson-Ashby model [Gibson and Ashby, 1997].

The metamaterial properties can be obtained by an Equivalent Material (EM) Analysis by defining the relative Young modulus E^* , relative Shear modulus G^* and the relative Strength under compression σ^* and shear loads τ^* as a function of the relative density ρ^* of the cellular pattern. Moreover, an EM is defined as a material with a dimension corresponding to the bounding box of the cellular construct, filled with a dense material whose mechanical properties are similar to the properties of the pattern structure [Azman, 2017].

EM analysis considers the relative density as the ratio between the volume of the pattern and the volume of the bounding box, as defined in Equation 1.1. Relative moduli, detailed in Equation 1.2 and Equation 1.3, corresponds to the ratio between the E or G of the pattern and the solid or bulk material E_0 or G_0 moduli, respectively, according to the Gibson-Ashby model. Similarly, relative Strength is defined as the ratio between the strength of the pattern and the theoretical yield stress on the solid material σ_0 , as shown in Equation 1.4 and Equation 1.5 for compression and shear loads, respectively.

$$\rho^* = \frac{\text{pattern volume}}{\text{bounding box volume}} \quad (1.1)$$

$$E^* = \frac{E}{E_0} = c_1 \rho^{*n_1} \quad (1.2) \quad \sigma^* = \frac{\sigma}{\sigma_0} = c_3 \rho^{*n_3} \quad (1.4)$$

$$G^* = \frac{G}{G_0} = c_2 \rho^{*n_2} \quad (1.3) \quad \tau^* = \frac{\tau}{\sigma_0} = c_4 \rho^{*n_4} \quad (1.5)$$

The model's coefficient c is a constant of proportionality, which depends on the type of interconnectivity of the pattern, while the exponent n is related to the mechanical response of the patterns [Sharma and Hiremath, 2021]. For stretch-dominated responses, E^* and σ^* are proportional to ρ^* for n values of $n_1=1$ and $n_3=1$, respectively (Equation 1.6). Likewise, for bending-dominated structures, E^* and σ^* are proportional to ρ^* for n values of $n_1=2$ and $n_3=1.5$, respectively (Equation 1.7) [Ashby, 2006]. In general, structures with stretch-dominated deformation mechanism have a higher modulus and strength, while bending-dominated constructs have better energy absorption characteristics [Deshpande et al., 2001a].

$$\text{Stretch-dominated: } E^* \propto \rho^{*1} \quad \sigma^* \propto \rho^{*1} \quad (1.6)$$

$$\text{Bending-dominated: } E^* \propto \rho^{*2} \quad \sigma^* \propto \rho^{*1.5} \quad (1.7)$$

A FEA of the cellular construct is established to obtain the pattern's E and G moduli, found as the ratio between the applied stress (σ or τ) and the strain defined as u/L between an applied deformation u and the overall pattern size L . Similarly, σ and τ are related to the applied force over the area of the cellular pattern bounding box face related to the applied load. To determine the Gibson-Ashby model's coefficients, the results of the relative parameters are plotted with respect to different values of ρ^* , and the data is approximated by non-linear regression methods to a power curve fit.

The use of Equivalent Material analysis for the determination of a lattice structure with a constant density to replace a solid material was previously presented by Azman [2017]. Depending on the required design conditions of the part, i.e. permissible displacement u_{perm} and permissible stress σ_{perm} , E^* and σ^* can be calculated from the total displacement u and equivalent von Mises stress σ_{eq} results of a FEA of the solid part, by using Equation 1.8 and Equation 1.9, respectively.

$$E^* = \frac{u}{u_{perm}} \quad (1.8)$$

$$\sigma^* = \frac{\sigma_{eq}}{\sigma_{perm}} \quad (1.9)$$

By applying the Gibson-Ashby model equations (i.e. Equation 1.2 and Equation 1.4), two values of ρ^* can be obtained by Equation 1.10 and Equation 1.11. As these values are derived from design constraints, they correspond to the maximum required relative density to replace the solid material by a cellular construct. Consequently, the bigger value will dictate the maximum value for the constant-density scenario. The parameters c and n correspond to case-specific values depending on the cellular material topology. The FEA conditions to establish the model's coefficients are further detailed in section 4.1.

$$\rho_{E^*}^* = \left(\frac{1}{c_1} \frac{u_{max}}{u_{perm}} \right)^{\frac{1}{n_1}} \quad (1.10)$$

$$\rho_{\sigma^*}^* = \left(\frac{1}{c_3} \frac{\sigma_{eq}}{\sigma_{perm}} \right)^{\frac{1}{n_3}} \quad (1.11)$$

The main limitation of the Gibson-Ashby model is their applicability for cellular materials having a macroscopic isotropic behaviour [Refai et al., 2020]. Even though numerical homogenization techniques for the determination of effective elastic properties are out of the scope of this present study, they are discussed on Appendix B.

1.2.2 Lattice structures

Lattice structures are a type of non-stochastic cellular materials characterised by an ordered arrangement of unit-cells [Yan et al., 2014a]. Lattice cell topologies are truss structures formed by a set of struts and nodes that can be analysed as frames using classical mechanics [Maconachie et al., 2019]. These strut-based materials are favoured due to their design simplicity [Xiao et al., 2018] and have been previously used to enhance the material distribution efficiency on structures from topology optimization procedures [Xu et al., 2016].

In general, lattice structures can be characterized by their Maxwell number M (Equation 1.12) depending on the number of struts S and nodes N [Deshpande et al., 2001b]. Positive M values indicate an equilibrium of external loads by axial strut tension or compression, which is characteristic of stretch-dominated structures. In contrast, negative M values indicate the presence of bending stresses due to the non-equilibrated moments at the nodes, resulting in a bending-dominated deformation behaviour.

$$M = S - 3N + 6 \quad (1.12)$$

The most common topologies studied in the literature are body-centred cube (BCC), face-centred cube (FCC), cubic, and their variations with the inclusion of z-struts (BCCZ and FCCZ), octet-truss and diamond lattice structures [Maconachie et al., 2019], which are represented in Figure 1.4. Manufacturing of metallic lattice structures have been extensively explored in the literature, with a predominant use of PBF process such as SLM [Leary et al., 2016]. Table 1.2 presents a summary of previously reported mechanical properties of strut-based lattices fabricated by SLM, adapted from Maconachie et al. [2019].

Given the current project context, the fabrication of lattice structures presents additional challenges for their manufacturing by WAAM. Thus, a possible cellular material alternative is presented in the form of sheet-based unit-cells, characterized by a plate or film-like configuration, than can be manufactured by stacking single weld beads. In general, sheet-based structures have shown better mechanical properties than strut-based cell structures of comparable density [Han et al., 2015, Tancogne-Dejean et al., 2018].

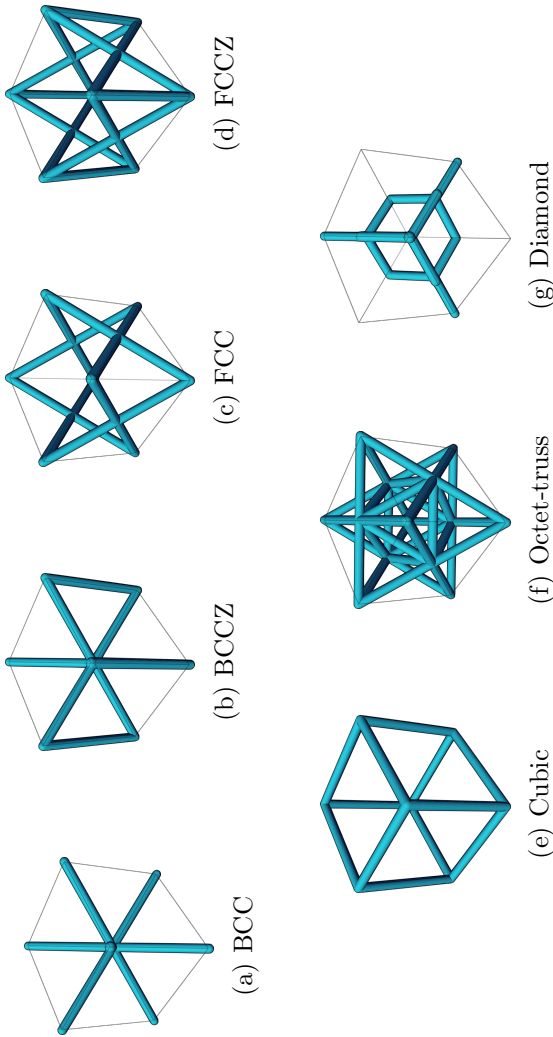


Figure 1.4: Common strut-based lattice structures.

Table 1.2: SLM lattice structures' test data collected from the literature.

Topology	Material	Cell size (mm)	ρ^* (%)	E (MPa)	σ (MPa)	Reference
BCC	316L SS	1.25	(3.15 - 13.8)	(17.89 - 378)	(0.36 - 5.89)	Gümruk and Mines [2013]
BCC, BCCZ	316L SS	(1.5 - 2.5)	(5.3 - 16.6)	(50 - 2700)	(0.92 - 15)	McKown et al. [2008]
BCC, BCCZ, FCC, FCCZ	AlSi10Mg	10	(0.7 - 22.2)	(21.71 - 490.22)	(0.46 - 4.36)	Lei et al. [2019]
BCC, Octet-truss	Inconel 625	(2 - 4)	(2.5 - 13.8)	(22.1 - 1246)	(0.8 - 10.9)	Leary et al. [2016]
Diamond	SS 630 (17-4PH)	-	43	-	(9710 - 13960)	Kang et al. [2019]
Cubic	Ti6Al4V	-	(3.6 - 26.5)	(370 - 4240)	(8.2 - 99.64)	Ahmadi et al. [2014]
	Ti6Al4V	-	(19.4 - 36.2)	(5360 - 8730)	(108 - 170)	Sallica-Leva et al. [2013]

The absence of data is indicated by “-”.

1.2.3 Triply Periodic Minimal Surfaces

Recent studies on layer infill generation have focused on the implementation of Triply Periodic Minimal Surfaces (TPMS) [Feng et al., 2019], as their topological properties permit interlayer support, thus presenting manufacturing advantages over strut-based lattices [Yan et al., 2014b]. In general, a minimal surface is characterized by having a mean curvature of zero at any given point [Carmo, 2016, Mackay, 1985, Al-Ketan and Al-Rub, 2020], thus locally-minimising the area. TPMS are known to periodically extend in three independent directions with no self-intersections [Rajagopalan and Robb, 2006, Karcher et al., 1996].

The most known examples of TPMS that can be found in the literature corresponds to Schwarz’s Primitive or Schwarz-P and Diamond or Schwarz-D [Schwarz, 1972], Schoen’s Gyroid and I-WP [Schoen, 1970], and Neovius [Neovius, 1883] surfaces. These examples are known to have symmetries of a crystallographic group [Karcher et al., 1996], and their representations are shown in Figure 1.5.

One of the benefits of TPMS structures is the possibility to create materials with continuous and interconnected reinforcements, given their capacity to divide space into uninterrupted phases [Abueidda et al., 2019]. To obtain a dense representation of the surface, two methods can be followed. The first one consists on closing one side of the minimal surface, thus obtaining a strut or solid-network-based structure [Sharma and Hiremath, 2021]. The second method consists on using the TPMS as a central surface to be thickened, obtaining a sheet-based construct [Li et al., 2019, Ambu and Morabito, 2018]. It has been determined that strut-based constructs have problems of surface interconnectivity in low-density scenarios [Zhao et al., 2020], while sheet-based structures present an overall better defined curvature [Sharma and Hiremath, 2021]. Further details of TPMS shape modelling are shown in section 1.3.

Moreover, TPMS patterns have been deemed suitable as a lightweight structure alternative due to their overall better mechanical performance compared to traditional lattices obtained by computer-aided design (CAD) [Bobbert et al., 2017]. Particularly, a TPMS approximation of BCC lattices with volume fractions between 10% and 30% have shown an increase of the elastic modulus, yield and compression strength compared to CAD generated alternatives [Zhao et al., 2018]. Regarding uniform density TPMS structures, a comparison between the energy absorption of Primitive, Diamond, Gyroid, and BCC lattices have shown that Diamond patterns have an overall highest mechanical performance, followed by Gyroid, Primitive patterns and BCC lattices [Zhang et al., 2018].

In addition to previous TPMS mechanical response analysis Li et al. [2019] evaluated sheet-based and strut-based Gyroid patterns in uniform and density graded scenarios under compressive loads. By numerical homogenization methods, it was found that sheet-based Gyroid patterns tend to be isotropic. Sheet-based patterns also present a higher elastic modulus and yield strength compared with the strut-based pattern at the same volume fraction. For graded density structures, their energy absorption is better than the uniform structures scenarios, having that larger gradient exhibits better absorption capabilities than those with small gradients.

AM of TPMS patterns have been extensively explored in the literature for SLM [Al-Ketan et al., 2018b, Bobbert et al., 2017, Bonatti and Mohr, 2019a,b, Feng et al., 2019, Yang et al., 2019, 2017, Zhao et al., 2018, Zhang et al., 2018], Selective laser sintering (SLS) [Abueidda et al., 2017, 2019, Jia et al., 2020, Maskery et al., 2017b], Stereolithography (SLA) [Li et al., 2019, 2018, Melchels et al., 2010], ColorJet printing (CJP) [Savio et al., 2019], PolyJet printing (PJP) [Afshar et al., 2016, 2018], and MultiJet printing (MJP) [Yang et al., 2014]. However, there is no information available regarding the manufacturing

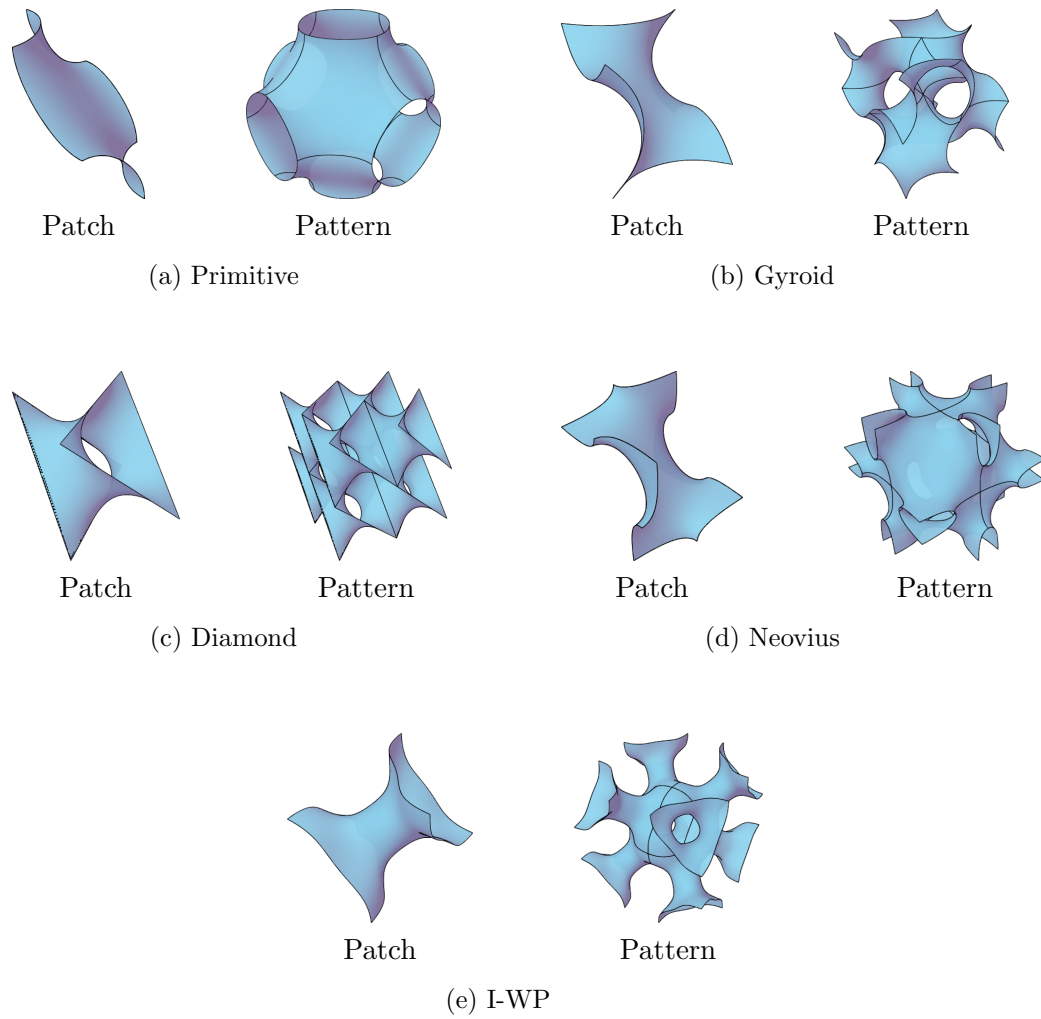


Figure 1.5: Fundamental shapes of common TPMS.

of these types of structures using other alternatives of metallic AM, such as WAAM. A summary of previous studies related to TPMS patterns mechanical characterization is shown in Table 1.3 and Table 1.4, for different AM technologies, unit-cell and pattern assemblies testing dimensions, and relative densities ρ^* ; and their results regarding Young's modulus E and compressive strength σ .

Even though the response of sheet-based TPMS configurations under compressive loads has been extensively studied in the literature, few studies have analysed this type of structures under shear scenarios. Furthermore, there is no information for the determination of the Gibson-Ashby model's coefficients from Finite Element simulations of structures formed by an arrangement of patterns' unit-cell. Table 1.5 summarizes previous results for Gibson-Ashby model's coefficients found in the literature for sheet-based TPMS patterns.

This thesis will focus on the design of Primitive and Gyroid patterns, assuming that these types of TPMS are manufacturable by WAAM. This decision was made based on the relative simplicity of the Primitive and Gyroid patches compared to the other surfaces from the TPMS family. However, manufacturability assessment, surface slicing and the generation of fabrication trajectories, among other topics, are a focus of the academic partners of the BeShape project on the Université de Toulon.

Table 1.3: TPMS patterns' test data collected from the literature.

AM technology	Testing dimensions	Pattern	ρ^*	E (MPa)	σ (MPa)	Reference
SLA Photopolymer resin	6mm unit-cell 6x6x6 pattern assembly	Gyroid strut-based	0.3	39.21	2.92	Li et al. [2019]
			(0.2 - 0.4)	28.25	1.98	
	Gyroid sheet-based		(0.1 - 0.5)	23.96	0.69	
			0.3	62.51	3.89	
			(0.2 - 0.4)	36.67	2.46	
			(0.1 - 0.5)	32.21	0.87	
SLS PA2000	10mm unit-cell 4x4x4 pattern assembly	Gyroid strut-based	0.3	95.00	3.33	Maskery et al. [2018b]
		Diamond strut-based	0.3	93.00	3.85	
		Primitive strut-based	0.3	192.00	4.11	
SLS PA2000	20mm unit-cell 4x4x4 pattern assembly	Gyroid sheet-based	0.14	58.01	2.19	Abueidda et al. [2019]
			0.3	167.33	7.59	
			0.46	303.11	15.23	
SLS PA2000	20mm unit-cell 4x4x4 pattern assembly	Primitive sheet-based	0.126	28.96	1.42	Abueidda et al. [2017]
			0.164	43.20	2.24	
		Neovious sheet-based	0.235	74.58	4.21	
			0.104	58.38	1.54	
			0.152	91.21	2.88	
	I-WP sheet-based		0.237	153.78	5.98	
			0.106	47.17	1.42	
			0.14	73.39	2.40	
			0.256	191.49	7.50	
PJP ABS resin	5mm unit-cell 7x7x7 pattern assembly	Primitive strut-based	0.3	154.5	3.1	Afshar et al. [2016]
			(0.3 - 0.6)	348.7	8	
	Diamond strut-based		0.6	497.7	26.7	
			0.3	79.5	3.6	
			(0.3 - 0.6)	170.0	3.5	
			0.6	336.0	14.6	
SLM Marangin Steel	7mm unit-cell 6x6x6 pattern assembly	Diamond strut-based	0.126	629.08	5.11	Al-Ketan et al. [2018b]
			0.171	1239.17	13.92	
			0.199	1735.14	22.90	
			0.231	2416.01	37.34	
			0.089	267.52	8.03	
	I-WP strut-based		0.135	618.08	19.51	
			0.174	1029.39	33.50	
			0.209	1487.83	49.50	
	Gyroid strut-based		0.123	724.78	21.23	
			0.165	1187.24	38.09	
			0.193	1544.91	52.03	
			0.232	2104.68	75.04	

Table 1.4: Studies for TPMS mechanical behaviour characterization. CONTINUED

AM technology	Testing dimensions	Pattern	ρ^*	E^*	σ^*	Reference
SLM Marangin Steel	7mm unit-cell 6x6x6 pattern assembly	Diamond sheet-based	0.165	2615.78	70.61	Al-Ketan et al. [2018b]
			0.203	2914.66	96.96	
	I-WP sheet-based		0.248	3235.78	131.71	
			0.150	1794.33	46.32	
			0.182	2241.19	67.93	
			0.202	2526.69	83.50	
	Gyroid sheet-based		0.228	2904.17	106.12	
			0.121	1377.20	34.08	
			0.165	2016.87	58.82	
			0.193	2445.72	77.50	
SLM 316L	4mm unit-cell 5x5x5 pattern assembly	Gyroid strut-based	0.232	3067.06	107.15	Yang et al. [2019]
			0.073	635.64	10.39	
	Primitive sheet-based		0.101	972.56	19.51	
			0.137	1449.97	35.25	
			0.171	1938.57	54.19	
			0.206	2474.13	16.02	
	Gyroid sheet-based		0.15	1097.87	26.18	
			$(0.1 - 0.2)^1$	898.05	15.82	
	Primitive sheet-based ³		$(0.1 - 0.2)^2$	1165.49	27.83	
			0.119	7115.74	12.26	
SLM 316L	4mm unit-cell 5x5x5 pattern assembly	Primitive sheet-based ³	0.180	7694.64	30.85	Zhang et al. [2018]
			0.241	8130.98	59.14	
	Diamond sheet-based ²		0.195	8018.10	54.79	
			0.293	14294.67	112.19	
			0.391	21533.42	186.43	
			0.106	47.17	1.42	
	Gyroid sheet-based ²		0.14	73.39	2.40	
			0.256	191.49	7.50	

¹ Graded along building direction² Graded perpendicularly to building direction³ Yield strength and Energy absorption data obtained from derived equations.

Table 1.5: Reported Gibson-Ashby model's coefficients by FE simulation and experimental testing.

Test conditions	ρ^*	E^*			G^*			σ^*			τ^*			Reference
		c_1	n_1	c_2	n_2	c_3	n_3	c_4	n_4					
FE simulation														
Primitive patterns														
Unit-cell	(0.02 – 0.20)	0.562	1.519	0.16	0.974	-	-	-	-	-	-	-	-	Abueidda et al. [2016]
	(0.10 – 0.24)	0.61	1.57	0.16	0.97	0.794	1.36	0.256	0.98	-	-	-	-	Lee et al. [2017]
Gyroid patterns														
Unit-cell	(0.02 – 0.20)	0.555	1.406	0.305	1.531	-	-	-	-	-	-	-	-	Abueidda et al. [2016]
	(0.10 – 0.25)	0.51	1.38	-	-	0.44	1.24	-	-	-	-	-	-	Al-Ketan et al. [2018a]
Experimental testing														
Primitive patterns														
Cyl. Mtx. (Ti6Al4V)	(0.23 – 0.50)	0.107	1.12	-	-	0.967	1.77	-	-	-	-	-	-	Bobbert et al. [2017]
	(0.048 – 0.235)	0.395	1.518	-	-	1.104	1.749	-	-	-	-	-	-	Abueidda et al. [2017]
	(0.073 – 0.206)	0.109	1.31	-	-	1.419	1.77	-	-	-	-	-	-	Al-Ketan et al. [2018b]
	(0.104 – 0.182)	0.56	1.89	-	-	2.67	2.23	-	-	-	-	-	-	Zhang et al. [2018]
Gyroid patterns														
Cyl. Mtx. (Ti6Al4V)	(0.31 – 0.49)	0.112	1.10	-	-	1.235	2.09	-	-	-	-	-	-	Bobbert et al. [2017]
	(0.07 – 0.46)	0.525	1.39	-	-	1.125	1.63	-	-	-	-	-	-	Abueidda et al. [2019]
	(0.121 – 0.232)	0.103	1.23	-	-	0.885	1.43	-	-	-	-	-	-	Al-Ketan et al. [2018b]
	(0.141 – 0.244)	1.14	2.23	-	-	2.74	2.10	-	-	-	-	-	-	Zhang et al. [2018]

The absence of data is indicated by “-”.

Test specimens as a cylindrical arrangement are denoted as “Cyl. Mtx.”.

Matrix assemblies are denoted by the arrangement of unit-cells.

1.3 Modelling of TPMS patterns

This section details the mathematical definitions for Primitive and Gyroid patterns, as well as the general TPMS shape generation by the Marching Cubes algorithm. Two main approaches for solid model generation are detailed: by level-set parameter in skeletal and sheet-based Primitive and Gyroid patterns, and by surface offset for sheet-based Primitive and Gyroid patterns of constant thickness. In addition, a second alternative for fundamental shape generation combined with surface offsetting strategies is detailed. The section finalizes with a comparison between the modelling alternatives.

1.3.1 Fundamental shape generation

TPMS shape is described by pattern-specific implicit functions derived from first-order approximation of nodal equations [Yoo, 2011, von Schnering and Nesper, 1991, Wohlgemuth et al., 2001]. For the purpose of this study, the functions f_P for Primitive and f_G for Gyroid surfaces are detailed in Equation 1.13 and Equation 1.14, respectively, obtained from general algorithms and equations for TPMS geometries by von Schnering and Nesper [1991] and from previous efforts presented in the available literature [Feng et al., 2019, Li et al., 2019, 2018, Zhang et al., 2018, Zhao et al., 2018, Wohlgemuth et al., 2001, Yoo, 2011].

$$f_P(x, y, z) = \cos(\lambda_x x) + \cos(\lambda_y y) + \cos(\lambda_z z) \quad (1.13)$$

$$f_G(x, y, z) = \cos(\lambda_x x) \sin(\lambda_y y) + \cos(\lambda_y y) \sin(\lambda_z z) + \cos(\lambda_z z) \sin(\lambda_x x) \quad (1.14)$$

From the equations, the pattern periodicity is controlled by the dilatation factor λ_i , as a function of the number n_i of unit-cell instances in a three-dimensional pattern assembly and the size L_i of these instances in the x , y and z directions, as shown in Equation 1.15.

$$\lambda_i = 2\pi \frac{n_i}{L_i}, \quad i = x, y, z \quad (1.15)$$

For the surface construction, TPMS modelling commonly uses the level-set approximation approach [Al-Ketan and Al-Rub, 2020], in which a level-set equation $\phi(x, y, z)$ is run through a Marching Cubes algorithm [Lorensen and Cline, 1987], which is a common effective procedure to extract iso-surfaces in 3D-data fields [Feng et al., 2019]. The algorithm generates the surface in a cubic voxelization manner by evaluating the implicit function presented in Equation 1.16 in a predefined regular 3D grid. From the equation, the level-set parameter C controls the position of the boundary surface between void and solid material [Zhao et al., 2018].

$$\phi(x, y, z) = f_{P,G}(x, y, z) - C \quad (1.16)$$

Each grid cell or voxel is defined to be contained by or outside of the surface, hence, regions where $\phi(x, y, z) < 0$ are defined to be inside the surface, while regions where $\phi(x, y, z) > 0$ are defined as voids. By analysing the vertices values of each voxel, the regions are associated with 16 variations of planar facets representations, depending if the vertices have values above or below the iso-surface. Each of these variations contains a different triangular mesh distribution, which is then used for final shape polygonisation. Further details of this process can be consulted on [Lorensen and Cline, 1987, Bourke, 1994]. From Equation 1.16, for a level-set value of $C = 0$, the generated surface by the

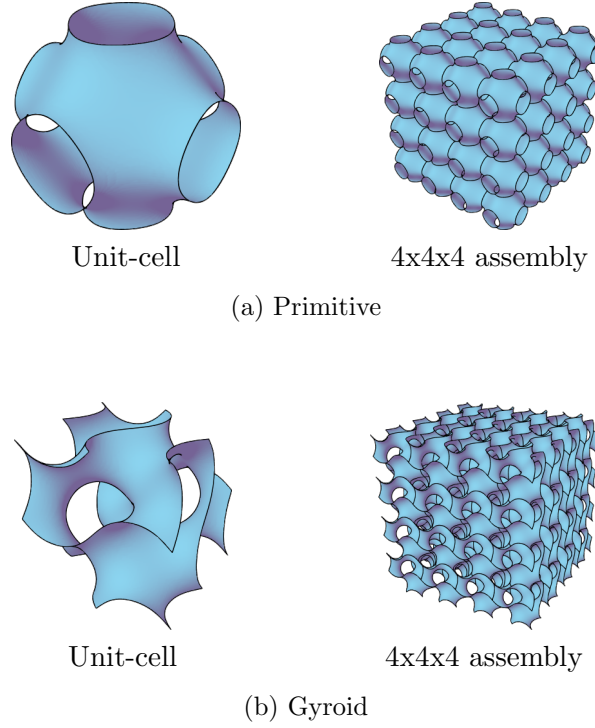


Figure 1.6: Primitive and Gyroid TPMS.

Marching Cubes algorithm divides a 3D bounding box in two equal sections, thus forming the TPMS fundamental shape. Figure 1.6 shows examples for Primitive and Gyroid unit-cells and patterns assemblies based on their fundamental shape.

1.3.2 Model generation by level-set parameter variation

The first strategy considered is the modelling by a variation of the level-set parameter C to determine the volume fractions pertaining to the regions separated by the central surface, as described by Li et al. [2019]. An overview of the methodology for this particular approach is shown in Figure 1.7. The general process starts with the input's definition, namely the pattern length L_i and the number of instances n_i required in the matrix assembly. Subsequently, the TPMS function evaluation initially considers both L_i and n_i to define the pattern periodicity λ_i and the function domain to construct the mathematical identity of the desired pattern. The function evaluation results, as well as the desired level-set C parameter are introduced to an Iso-surface tool component, which executes the Marching Cubes methodology for the surface generation. Final mesh operations consider the trimming and joining of the unit-cell boundary faces to define a closed structure.

As stated before, the level set parameter acts as a threshold for the pattern shape location. By closing one of the surface sides, a solid skeletal-based pattern is obtained, as depicted in Figure 1.8a and Figure 1.8b for Primitive and Gyroid patterns, respectively, for different values of C .

In order to obtain a double-level or sheet-based surface, a modified $v(x, y, z)$ function is needed for the Marching Cubes methodology [Li et al., 2019, Scherer, 2013], as defined in Equation 1.17. In this case, the positive and negative roots of C , in the identity presented in Equation 1.18, act as an inner and outer boundary. Examples for sheet-based Primitive and Gyroid patterns are shown in Figure 1.9a and Figure 1.9b, respectively.

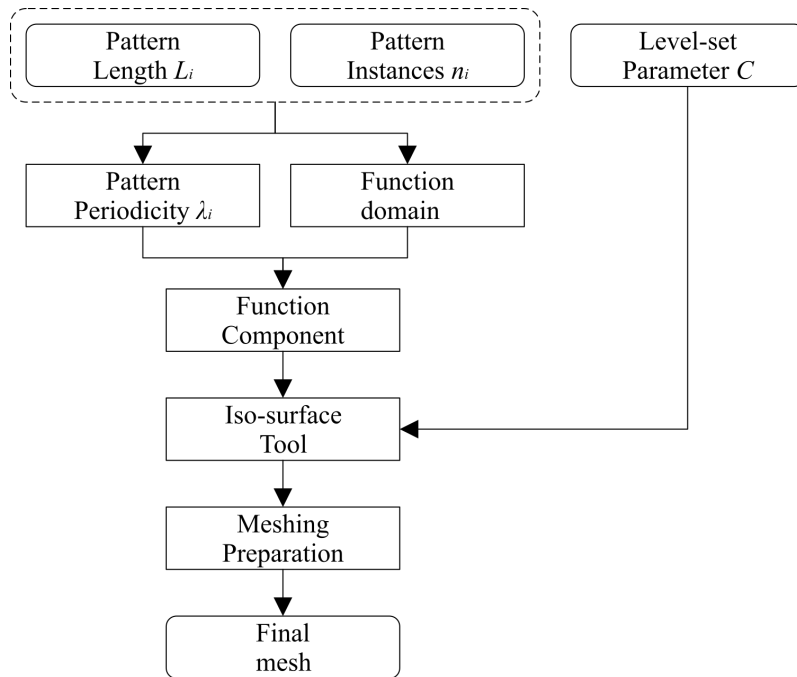


Figure 1.7: Modelling by level set parameter variation.

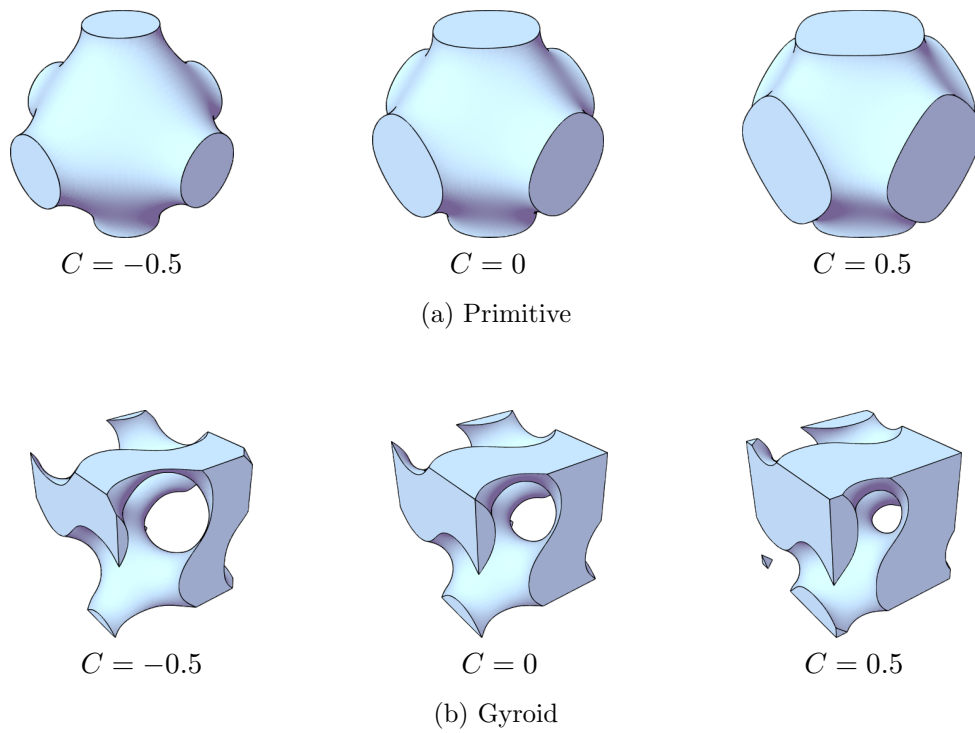


Figure 1.8: Examples for skeletal-based patterns modelled by level set parameter variation.

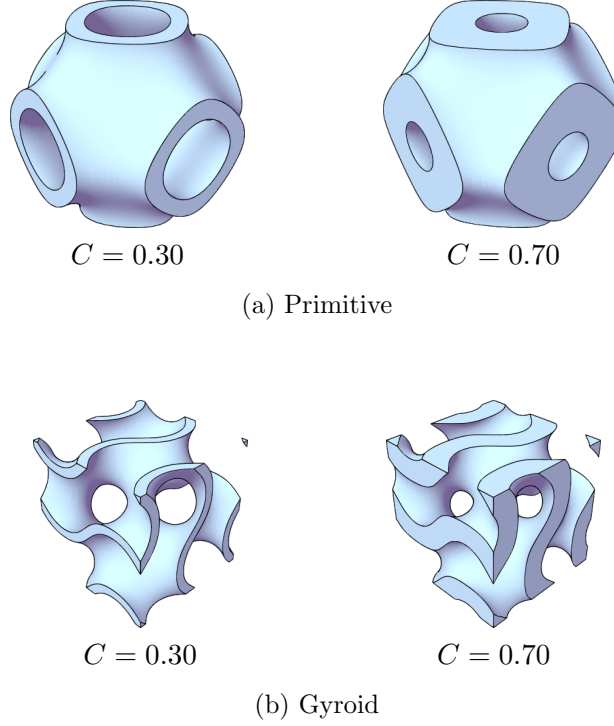


Figure 1.9: Examples for sheet-based patterns modelled by level set parameter variation.

$$v(x, y, z) = [f_{P,G}(x, y, z)]^2 - C^2 \quad (1.17)$$

$$[f_{P,G}(x, y, z)]^2 = C^2 \quad (1.18)$$

In their study, Li et al. [2019] reported equations for the relative density of skeletal-based and sheet-based Gyroid TPMS as a function of the level-set parameter, as shown in Equation 1.19 and Equation 1.20, respectively. However, there is no information in the literature regarding the effects of this parameter on Primitive patterns. The derivation of equations of density as a function of C for Primitive TPMS and the verification of Li et al. [2019] results for Gyroid patterns are detailed in section 2.1.

$$\rho_{G-skeletal}^* = 0.333 C + 0.501, \quad -1.5 < C < 1.5 \quad (1.19)$$

$$\rho_{G-sheet}^* = 0.675 C + 0.012, \quad 0.018 < C < 1.5 \quad (1.20)$$

1.3.3 Model generation by surface offsetting

This second modelling approach consists in offsetting the TPMS fundamental shape to obtain constant-thickness models. For this scenario, some modifications for the methodology shown in Figure 1.7 are needed. For instance, the level set parameter C is set to 0 and the resulting shape is used as a central surface from which the inner and outer boundaries of the final model are obtained by offsetting half the desired pattern thickness d along and contrary to the surface's normals. The process finishes with the surfaces trimming and the addition of boundary faces. An illustration of this process is shown in Figure 1.10 for a Gyroid pattern.

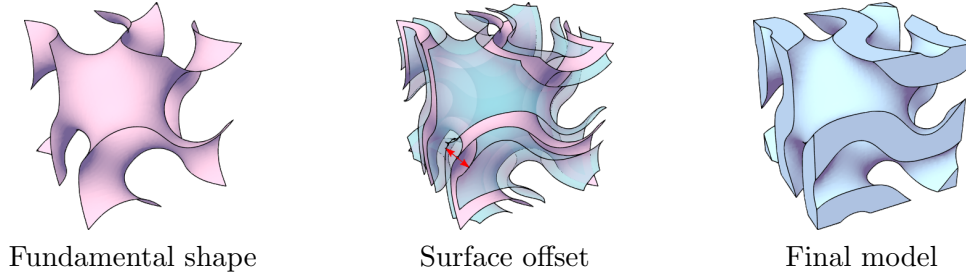


Figure 1.10: Fundamental shape offset process illustration.

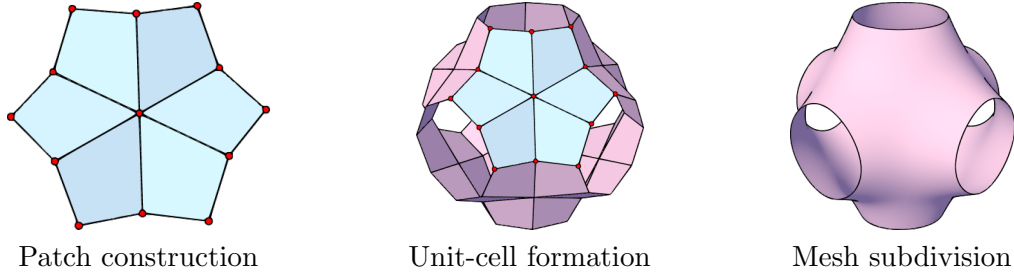


Figure 1.11: Catmull-Clark subdivision process illustration.

Previous studies have used a similar modelling approach for TPMS mechanical characterization tests [Abueidda et al., 2019, Bobbert et al., 2017, Zhang et al., 2018]. However, there is no information available for the effects of thickness and length values in the relative density of the patterns.

1.3.4 Model generation by Catmull-Clark subdivision

The last modelling approach considered, as proposed by Savio et al. [2019], is an alternative method to obtain the TPMS fundamental shape by a recursive mesh subdivision procedure, combined with a surface offset. The procedure, depicted in Figure 1.11 for a Primitive pattern, starts with a patch construction using a set of predefined control points. The patch, which is the minimal repeated piece to construct the pattern, is rotated and translated, and the obtained unit-cell then passes through a Catmull-Clark mesh subdivision algorithm [Catmull and Clark, 1978] to increase the faces count and soften the surface. The process ends with thickening tools to obtain a solid model.

The resulting surface in the subdivision process is smoother and presents a better performance regarding computer-processing, compared with the Marching Cubes modelling approach. However, further testing is needed regarding the definition of control points and mesh joining prior to subdivision procedures in patterns assemblies. A non-exhaustive comparison between models obtained by this methodology and by using the Marching Cubes algorithm was made in the early stages of the research work, yielding similar face count on the obtained meshes, but with an overall better triangular distribution for the Catmull-Clark surfaces. However, these results are not reported in the present document.

1.3.5 Fundamental shape assessment

The last aspect considered is the verification of the fundamental shape generation quality. For this, we used the normalized surface-to-volume ratio $S/V^{2/3}$ as a mean of comparison

Table 1.6: Fundamental shape surface-to-volume ratio comparison

TPMS	Process	$S/V^{2/3}$	Time	Reference	
Primitive	Literature	2.3401	-	Schoen [1970]	
		2.3453	-	Mackay [1985]	
	TPMS Software				
	MSLattice (30 steps)	2.3556	-	Al-Ketan and Al-Rub [2020]	
	MSLattice (100 steps)	2.3528	-		
	GH implementations				
	Catmull-Clark	2.3756	10ms		
		Millipede (30 steps)	2.3532	20sec	
		Millipede (100 steps)	2.3526	14min	
		MT Script (100 steps)	2.3528	368ms	
Gyroid	Literature	2.4533	-	Schoen [1970]	
	TPMS Software				
	MSLattice (30 steps)	3.0995	-	Al-Ketan and Al-Rub [2020]	
	MSLattice (100 steps)	3.0923	-		
	GH implementations				
	Catmull-Clark	3.0592	10ms		
		Millipede (30 steps)	3.0935	40sec	
		Millipede (100 steps)	3.0918	17min	
		MT Script (100 steps)	3.0923	498ms	

The absence of data is indicated by “-”.

between the proposed modelling approaches. Theoretical surface-to-volume ratio values found in the literature represents a quantification of how minimal is the surface area with respect to the volume of the unit-cell [Schoen, 1970].

Table 1.6 summarizes the values of surface area per unit cube for Primitive and Gyroid patterns found in the literature, and their comparison regarding the models resulting from MSLattice (a free software for lattice generation [Al-Ketan and Al-Rub, 2020]), the Catmull-Clark modelling approach proposed by Savio et al. [2019], the Millipede plug-in for Marching Cubes algorithm, and the results from a set of scripts written in C# language running a Marching Tetrahedra (MT) algorithm (similar to Marching Cubes). These scripts were developed during the study of graded TPMS generation and will be detailed in section 3.1. The Catmull-Clark, Millipede and MT Script procedures were implemented in the Grasshopper[®] (GH) visual programming environment, from Rhinoceros[®] 6 CAD suite.

For Primitive patterns, there is a good agreement between the results of $S/V^{2/3}$ from the Millipede and MT script with the available literature. In contrast, Catmull-Clark procedures, although faster, presented bigger ratios, which can be mainly attributed to the approximation nature of the subdivision process. On the other hand, Gyroid results presented variations with respect to the available literature in all modelling alternatives. Mackay [1985] previously associated this issue to the definition used in surface area calculation by complex integrals from Schoen [1970], but for other type of TPMS shapes. Further analysis of the mathematical determination of the surface area are out of the scope of this thesis.

Given the discrete sampling nature of the Marching Cubes (and Marching Tetrahedra) process, the surface area can be influenced by the number of steps (domain divisions) used for generation. This is evidenced by the decrease in the $S/V^{2/3}$ values when increasing

steps from 30 to 100 divisions. Ambu and Morabito [2019] previously determined that the surfaces are well approximated by a grid of 100 steps. However, this is also related to the computing time required to mesh the surface. As shown by the Millipede process results (Marching Cubes), there is a great increase in the time needed to generate the fundamental shape, but this issue was resolved by using the alternative method proposed in the MT script.

In regards to further implementation, the methodology adopted in posterior sections of this document is based on the application of polygonization algorithms, in particular the Marching Tetrahedra procedure. The selection of this approach was based on a practical point of view, as the proposed methodology (to be detailed in section 3.2) has better outcomes when considering the TPMS surface generation by working directly with their mathematical definition, instead of performing adjustments from the modification of the mesh's vertices position.

1.4 Functionally Graded Cellular Materials

The last introductory aspect refers to the development of Functionally Graded Cellular Materials (FGCM), which are characterized by a gradual change in properties along their conformation [Radman et al., 2013]. Design of FGCM can refer to the alteration of the material composition or microstructure by a mix of feedstock [Ansari et al., 2021], or to an optimized distribution of the unit-cells' relative density within a design space [Yang et al., 2019].

Particularly, variable density FGCM have presented greater material efficiency [Maskery et al., 2017b] and energy absorption capabilities [Choy et al., 2017, Li et al., 2019] compared with their uniform counterparts. The design of these type of constructs is commonly related to the application of a density map from Topology Optimization (TO) procedures [Li et al., 2018, Panesar et al., 2018].

TO strategies are of great interest for lightweight part design, as these methods solve a material distribution problem to generate an optimal topology [Brckett et al., 2011]. As stated by Evans et al. [2001], topological design mindset aims to configure the structural part to carry loads at lowest part weight, while permitting the intervening space to spatially distribute plastic deformations in energy absorption scenarios, among other functionalities.

Two of the most known approaches for topological optimization are the element-based Solid Isotropic Material with Penalization (SIMP) that allow a variation in density, and the void-solid discrete approach of the Bi-directional Evolutionary Structural Optimization (BESO). Element-based methods discretise the problem domain in finite elements, thus becoming an extension of FEA. In contrast, discrete approaches are more related to the use of discrete variables in basic topological optimization; however, the mathematical solution tends to have sensitivity analysis issues regarding non-linear constraint functions [Tyflopoulos et al., 2018]. As an extension to the SIMP algorithm, Brckett et al. [2011] identified the use of variable density unit-cells as an opportunity to further improve this approach of topological optimization, and, especially, for the development of inhomogeneous FGCM.

Previous works on FGCM mostly focus on strut-based unit-cells [Yang et al., 2017, Maskery et al., 2016, Al-Saedi et al., 2018, Limmahakhun et al., 2017], but these types of geometries are known to lower the manufacturability [Mazur et al., 2016], and present severe stress concentrations near the joint of struts [Smith et al., 2013]. To overcome this issues, the use of FGCM based on TPMS structures are a topic of ongoing research [Panesar et al., 2018, Yang et al., 2019, Li et al., 2019].

1.5 Literature review conclusions

As evidenced by the consulted literature, the use of TPMS unit-cells is an attractive alternative for the development of lightweight cellular structures due to their significant benefits over traditional lattice structures regarding manufacturability, mechanical behaviour and their capability of self-support between deposited layers as a result of to their unique surface characteristics. Even though manufacturing of metallic TPMS patterns have been extensively tested under PBF processes, their fabrication by WAAM technologies remains as a unexplored research area. Given the context of the BeShape project, the application of TPMS on WAAM technologies is based on research on mechanical design and evaluation of patterns adapted to a density map, and the analysis of manufacturing constraints and tool-path generation. Accordingly, the work presented in the following chapters will focus on TPMS design, in particular Primitive and Gyroid patterns, due to their potential manufacturability advantages over other minimal surface structures, as determined by the initial project evaluation.

Being mathematically defined surfaces, modelling of the fundamental shape of TPMS patterns is heavily influenced by the effects of the selected values on their design variables, namely the level-set parameter C on skeletal-based constructs, or the thickness d and length L of the unit-cells on sheet-based topologies. Even though previous efforts have studied the effects of C on the unit-cells' relative density, (only for Gyroid patterns [Li et al., 2019]), there is still a gap on the influence of other design parameters. Therefore, chapter 2 will present the effects of d and L on Primitive and Gyroid TPMS, as well as the effects of C on Primitive patterns, which has not been previously contemplated in the literature. The outcomes of the analysis of the design parameters' effects is to determine how the relative density of the patterns responds to their variation.

The relation between the patterns' density and their design parameters is an important step towards the creation of FGCM. Even though previous approaches in the literature have developed FGCM with variable density from a density map obtained by TO [Li et al., 2018, Panesar et al., 2018], a formal modelling procedure has not been established. Therefore, a proposed methodology for the design of FGCM based on variable density TPMS is presented in chapter 3.

Lastly, even though previous assessments of the advantages of these graded constructs over constant density scenarios have been presented in the literature, they usually involve linear density distributions [Maconachie et al., 2019]. Thus, one of the objectives of this thesis is to analyse FGCM developed from a three-dimensional density map. Particularly, a process to correlate FEA results of a solid material to a specific density distribution will be introduced, as an alternative to a density mapping from TO procedures. These process will be introduced in chapter 4.

Chapter 2

TPMS Design parameters effects on relative density

Introduction

The adaptability of patterns' density to their design parameters is an important step to relate the structure's modelling and the required local density map resulting from FEA or TO procedures on the development of FGCM. This chapter presents the analysis of Primitive and Gyroid TPMS design and the proposed equations to control their relative density by modifying the patterns' design parameters. Based on the review of strategies for TPMS pattern modelling, two approaches of design parameter variation, i.e. the TPMS function level-set and the pattern's thickness and length, are used to explore the density responses of the patterns.

Initially, for the level-set effects, a study is carried out to extend the analysis by Li et al. [2019] to Primitive patterns. Intervals for pattern design are also detailed and contrasted with previous studies. The chapter concludes with the development and analysis of the main proposed equation for relative density as a function of the pattern thickness and unit-cell length or size.

2.1 Patterns design parameters' relationship analysis

Following the modelling procedures introduced in previous sections, several models with diverse level-sets, lengths and thicknesses were generated for Primitive and Gyroid patterns. The next subsections present in detail the model's dimensions used for each evaluation and the graphical representation of the obtained data.

All CAD data correspond to single pattern models (one unit-cell), as they presented negligible density variance from pattern's matrix assemblies (differences below 0.07%) and better computing performance. In addition, these models were developed to be contained in a cubic bounding box of size L , which complies with the condition of $\lambda_x = \lambda_y = \lambda_z$.

2.1.1 Level-set effects on relative density

Using the methodology shown in Figure 1.7, several skeletal and sheet-based Primitive and Gyroid patterns were generated to explore the effects and to identify the limits of C values for correct surface generation.

Depending on the values of C , TPMS can present irregularities in the surface generation process, especially in skeletal-based models. Regarding sheet-based models, previous

Table 2.1: C parameter effects on Primitive and Gyroid TPMS patterns.

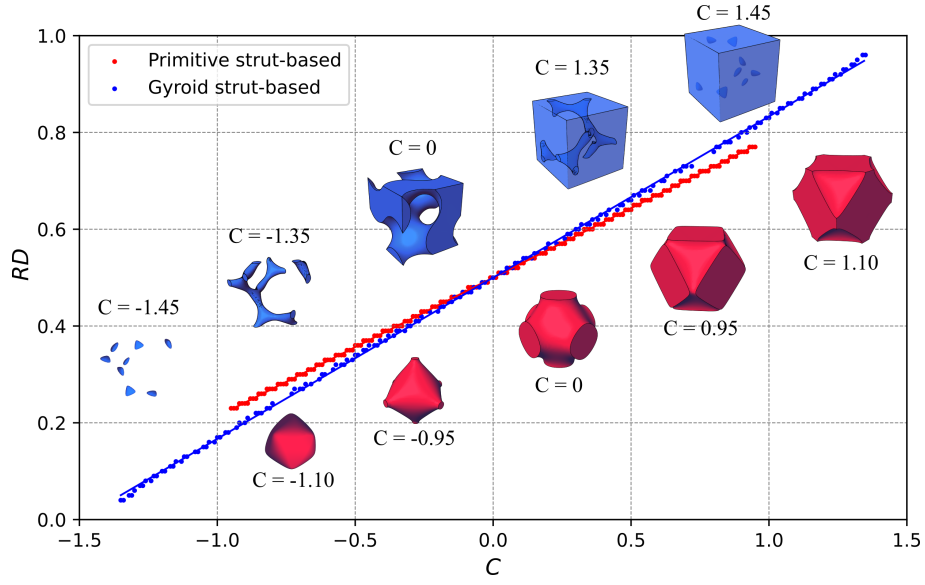
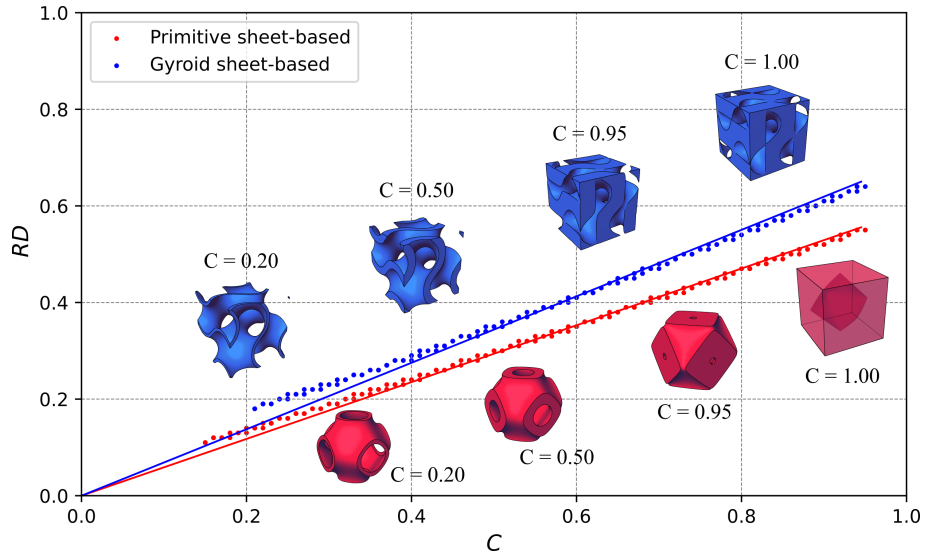
Pattern		C value effects
Primitive	Strut:	Sheet:
	<ul style="list-style-type: none"> • $C < -0.95$: non-connected surfaces • $C = -0.95$: Lower limit for surface generation • $C = 0$: Pattern of $RD = 0.5$ • $C = 0.95$: Upper limit for surface generation • $C > 0.95$: Surfaces are connected, but they lose the initial "Primitive" appearance 	<ul style="list-style-type: none"> • $C = 0$: Lower limit, produces the fundamental shape • $C = 0.862$: Pattern of $RD = 0.5$ • $C = 0.95$: Upper limit for surface generation • $C > 0.95$: Pattern with internal voids or small connections
Gyroid	Strut:	Sheet:
	<ul style="list-style-type: none"> • $C < -1.35$: poorly connected or non-connected surfaces • $C = -1.35$: Lower limit for surface generation • $C = 0$: Pattern of $RD = 0.5$ • $C = 1.35$: Upper limit for surface generation • $C > 1.35$: Pattern with internal voids or small connections 	<ul style="list-style-type: none"> • $C = 0$: Lower limit, produces the fundamental shape • $C = 0.735$: Pattern of $RD = 0.5$ • $C = 0.95$: Upper limit for surface generation • $C > 0.95$: Pattern begins to present self intersections, loses the sense of "sheet"

studies on Gyroid surfaces fixes a lower C limit [Li et al., 2019]. However, this value is strongly related to the number of points used for the polygonization algorithm, and can be avoided by generating the inner and outer surfaces independently. A summary of the effects of C is presented in Table 2.1. It is worth noticing that these restrictions correspond to software modelling limitations, and does not relate to manufacturing constraints.

Using the C value ranges defined in Table 2.1, sets of 200 models were constructed for each pattern skeletal and sheet-based scenarios. For each model, the relative density RD from the CAD data was calculated as the ratio between the pattern volume and a cubic bounding box, according to Equation 1.1. RD was adopted in this stage to represent the relative density, to differentiate between values obtained from CAD data and the relative density ρ^* obtained from the derived equations in subsection 2.2.1 and subsection 2.2.2. Data points and examples of selected models are presented in Figure 2.1 and Figure 2.2, for skeletal and sheet-based patterns, respectively.

Equations for RD as a function of C where determined by using linear regression methods from the obtained data. Table 2.2 presents a summary of these equations, as well as C and RD value ranges. Similarly noted in previous studies [Li et al., 2019, 2016, 2018, Scherer, 2013, Yang et al., 2019, Zhao et al., 2018], there is a linear relationship between C and the RD of the unit-cell. Furthermore, the resulting equations found for the skeletal and sheet-based Gyroid patterns are similar to previous studies [Li et al., 2019, 2016]; currently there is no information available in the literature for Primitive cases.

As a result of the linear relationship between RD and C , the previous methodology can be modified to account for a level-set parameter function $C(x, y, z)$ to develop density

Figure 2.1: Relative density *vs* level-set C for skeletal-based Primitive and Gyroid patterns.Figure 2.2: Relative density *vs* level-set C for sheet-based Primitive and Gyroid patterns.Table 2.2: Summary for RD and C relationships.

Pattern	RD function	C range	RD range
Primitive-skeletal	$0.287C + 0.5$; $R^2 = 1$	$-0.95 < C < 0.95$	$0.23 < RD < 0.77$
Gyroid-skeletal	$0.333C + 0.5$; $R^2 = 1$	$-1.35 < C < 1.35$	$0.05 < RD < 0.95$
Primitive-sheet	$0.588C$; $R^2 = 0.995$	$ C < 0.95$	$RD < 0.56$
Gyroid-sheet	$0.688C$; $R^2 = 0.987$	$ C < 0.95$	$RD < 0.65$

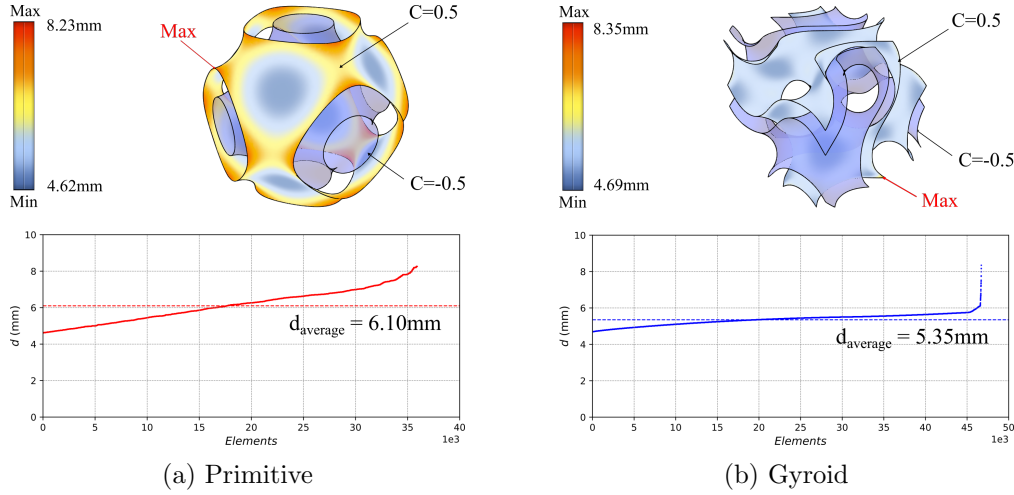


Figure 2.3: Example of thickness differences in sheet-based patterns.

variable structures [Li et al., 2018]. However, further analysis of uniform-density models obtained by C variation show that the pattern thickness in sheet-based models is not constant within unit-cell boundaries, as depicted in Figure 2.3. From the figure, the thickness d is defined as the distance between the mesh vertices of both sides. The sorted thicknesses are located on the *Elements* abscissa to illustrate the deviations from their average value.

Particularly, for a value of $C = 0.5$ in 50mm unit-cells, deviations between 4.62mm to 8.23mm (standard deviation $SD=0.88\text{mm}$) and 4.69mm to 8.35mm ($SD=0.29\text{mm}$) were found for Primitive and Gyroid patterns, respectively. Figure 2.3a clearly shows that bigger values of thickness differences are in the extremes of the unit-cell patches for Primitive patterns. In contrast, Gyroid patterns tends to have a more uniform thickness distribution, evidenced in Figure 2.3b. The local maximum in these cases tends to be compensated when there is a presence of neighbouring unit-cells, but their analysis was out of the scope of this research.

For this reason, the method of adjusting RD by C variation, although simple regarding its implementation, was replaced by a direct manipulation of the length and thickness of the patterns, which is discussed next. Further analysis of skeletal-based patterns was out of the scope of this study.

2.1.2 Thickness and length effects on relative density

This subsection explores the relative density of constant thickness models. The considered TPMS design parameters, i.e. the pattern thickness d and length L , are depicted in Figure 2.4. Diverse sets of models were developed using the previous methodology shown in Figure 1.10, as introduced in subsection 1.3.3.

For Primitive patterns, models with lengths between 30 and 250mm, and thicknesses between 2 and 10mm were created. The dependency of the relative density with the pattern thickness d was initially explored by plotting the diverse RD values obtained for each model. As shown in Figure 2.5a, there is a linear relationship between the relative density and d , and the slope tends to decay for larger values of L .

Afterwards, a relative density *vs* L graph, shown in Figure 2.5b, was used to explore the effects of L variation, which exhibits a non-linear decreasing dependence. From Figure 2.5b, the curves correspond to the different values of d , with 1mm increments. Only

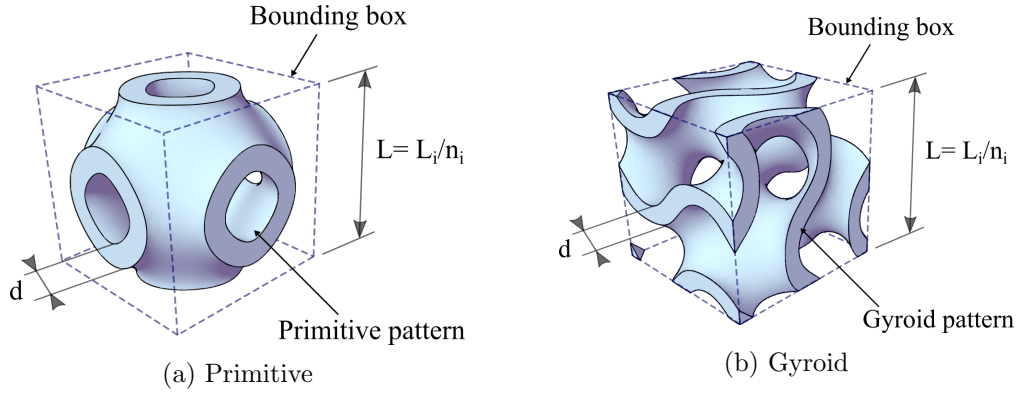


Figure 2.4: Design parameters for constant thickness TPMS patterns.

labels for 2 and 10mm were added due to visualization restrictions.

The same detailed procedure was used to generate Gyroid patterns models with lengths between 50 and 250mm, and thicknesses between 2 and 15mm. As evidenced in Figure 2.6a and Figure 2.6b, Gyroid patterns present the same behaviour as in Primitive patterns regarding the relationships of RD with d and L , respectively. Similarly, Figure 2.6b only presents labels for 2.5 and 11.5mm due to visualization restrictions. Each curve represents an increment of 1mm in thickness.

Even though Gyroid models generated for thicknesses between 2 and 15mm were considered to the initial dependency verification regarding d , the study of the relationships with respect to L and the subsequent analysis for function development considers the models between 2.5 and 11.5mm, for a more uniform data point distribution. The following section further analyses the curves presented in Figure 2.5 and Figure 2.6 for the development of a relative density equation.

2.2 Relative density function development

This section first recalls the work regarding the definition of a relative density function in terms of patterns' thickness and length, which was published in both the 31st CIRP Design Conference (The Netherlands) [Ramírez et al., 2021b] and the 17ème Colloque national S-mart (France) [Ramírez et al., 2021a]. Secondly, new equation definitions, with better data correlation, for the relative density as a function of the thickness-to-length ratio are introduced and contrasted with the previous definitions. The section ends with a discussion on the last proposal equation results.

2.2.1 Equation as a function of thickness and length

In an effort to develop a general equation for relative density as a function of both pattern's thickness d and length L , Equation 2.1 shows a first model which combines the linear relationship with d and a non-linear decreasing relationship regarding L ; α and β are considered as constants.

$$\rho^*(d, L) = \alpha d L^{-\beta} \quad (2.1)$$

Initially, non-linear regression process was employed to estimate the curve's exponents β from the data plotted in the RD vs L graphs (Figure 2.5b and Figure 2.6b). Even though the proposed model considers d and L to be independent, a slight linear correlation was

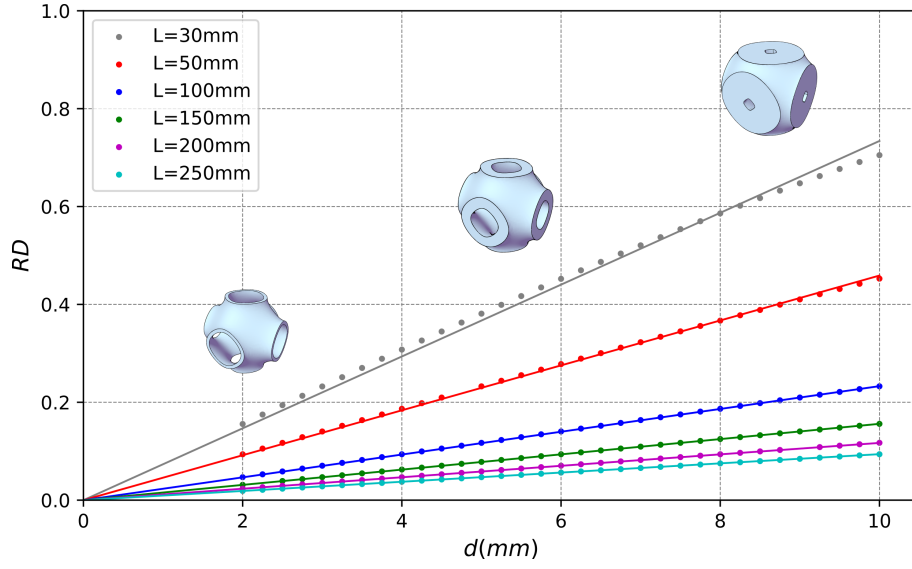
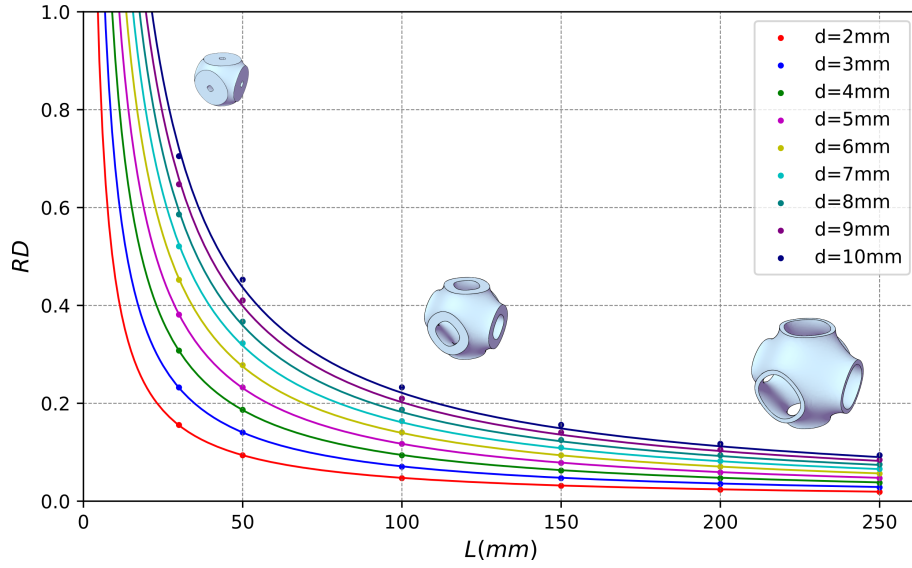
(a) RD as a function of d (b) RD as a function of L

Figure 2.5: Thickness and length effects on relative density of Primitive patterns.

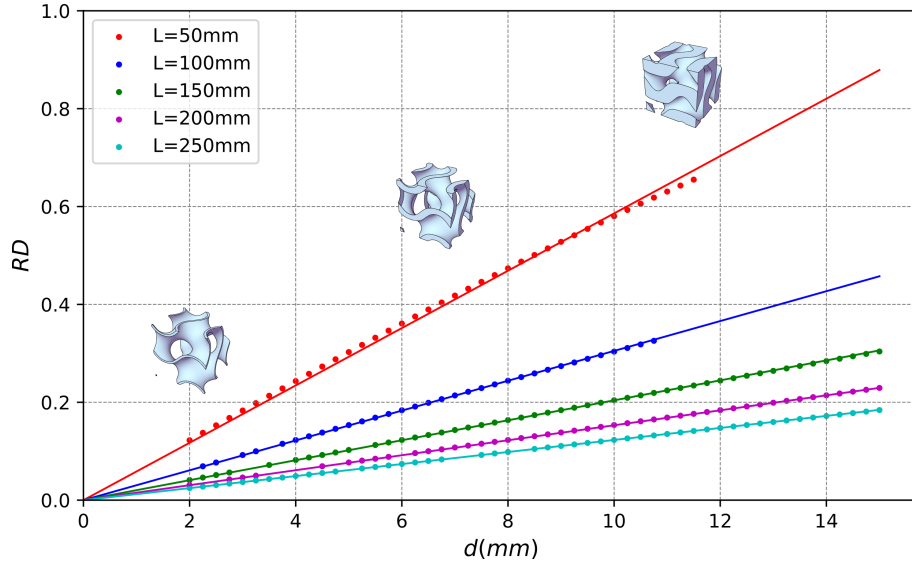
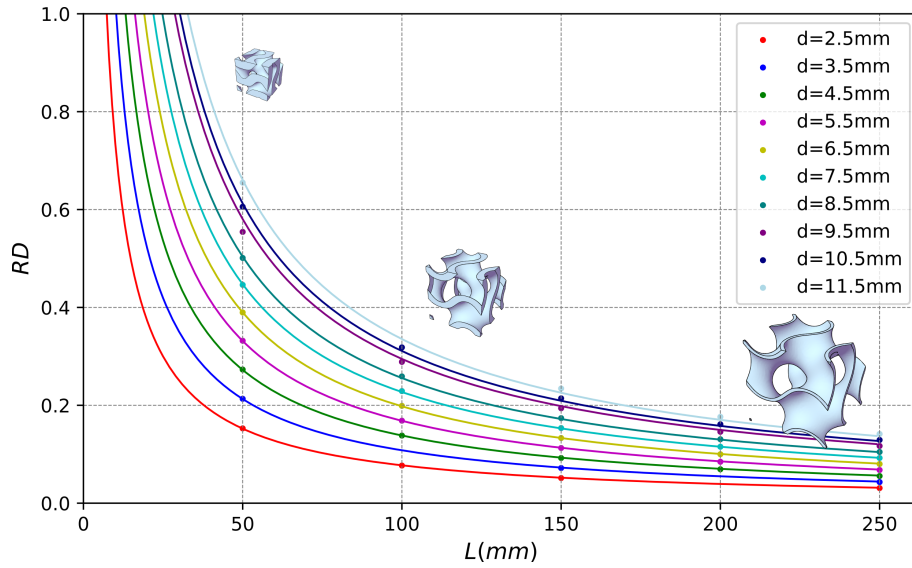
(a) RD as a function of d (b) RD as a function of L

Figure 2.6: Thickness and length effects on relative density of Gyroid patterns.

found between β and d . Nevertheless, this exponent was treated as a constant equal to the mean value of the obtained exponents from all the different d curves. Accordingly, the resulting constant factors for power dependency obtained were $\beta_P = 0.981$ and $\beta_G = 0.978$ for Primitive and Gyroid patterns, respectively.

This assumption of constant β factor was further verified by fitting the data points to a curve of the form $\rho_P^*(d, L) = \alpha_P d L^{-0.981}$ for Primitive patterns, and $\rho_G^*(d, L) = \alpha_G d L^{-0.981}$ for Gyroid patterns, and evidenced by a resulting R^2 value between 0.99 and 1 from the data points. Subsequently, with this curve fits, the constant factors for lineal dependency $\alpha_P = 2.081$ and $\alpha_G = 2.607$ were determined for Primitive and Gyroid patterns, respectively.

With the initial values obtained for α and β , the relative density of the models was calculated and compared to the CAD RD data, resulting in an overall absolute percentual error between 0.97% and 4.51% in Primitive patterns, and between 0.22% and 7.72% for Gyroid patterns. To correct these deviations, a Gradient Descent optimization algorithm was employed to optimize the α and β factors and reduce the Residual Sum of Squares, defined in Equation 2.2, where j corresponds to the different sets of (d, L) .

$$RSS(\alpha, \beta) = \sum_j \left(\rho^*(d, L)_j - RD_j \right)^2 \quad (2.2)$$

The Gradient Descent optimization procedure is detailed in the Appendix D.1. In this process, the CAD data is initially stored in a RD variable. Later, the RSS function is constructed and the values found for α and β are considered as an initial guess $\theta_0 (\alpha_0, \beta_0)$ and stored in a separate variable θ_k to be used in the iterative process. In each iteration, a new value θ_{k+1} is calculated as a decrease of $\eta_k \nabla RSS(\theta_k)$ from an initial θ_k , where η_k is the step value and $\nabla RSS(\theta_k)$ is the gradient of RSS evaluated at θ_k . The algorithm ends once the variation of $\eta_{k+1} - \eta_k$ falls below a precision value, which was fixed at 1E-06.

For Primitive patterns, with the initial guess of $(\alpha_0, \beta_0) = (2.081, 0.981)$, a Python script running the detailed algorithm was developed to obtain the optimized parameters $(\alpha_0, \beta_0) = (2.141, 0.982)$ after 20 iterations, using an initial step value $\eta_0 = 0.001$. The corrected equation $\rho_P^*(d, L)$ for Primitive patterns is shown in Equation 2.3. Although model data for lengths of 30mm were used to develop the initial guess, their corresponding RD data were not used to calculate the optimized parameters, as they introduced errors due to their non-linear behaviour in larger relative density values. A different scenario of initial guess estimation considering these data was also tested, resulting in the same optimized parameters after a longer iterative process.

$$\rho_P^*(d, L) = 2.141 \, d \, L^{-0.982} \quad (2.3)$$

Similarly, for Gyroid patterns, with an initial guess of $(\alpha_0, \beta_0) = (2.607, 0.978)$, the optimized parameters $(\alpha_0, \beta_0) = (2.568, 0.966)$ were obtained after 10 iterations using the same initial step value. The corrected equation $\rho_G^*(d, L)$ for Gyroid patterns is shown in Equation 2.4.

$$\rho_G^*(d, L) = 2.568 \, d \, L^{-0.966} \quad (2.4)$$

Table 2.3 summarizes the RSS and the absolute percentual error results before and after the Gradient Descent optimization in Primitive and Gyroid patterns. In general, there is a one order of magnitude reduction of the obtained RSS . For Primitive patterns the maximum overall absolute percentual error dropped from 4.51% to 1.98%, while Gyroid models presented a reduction from 7.72% to 4.34%.

Table 2.3: *RSS* and absolute percentage error differences before and after Gradient Descent optimization in relative density equation parameters.

Pattern	$L[\text{mm}]$	RSS	Initial Max. error (%)	After Gradient Descent RSS	Max. error (%)
Primitive	Overall	2.57E-03	4.51	2.85E-04	1.98
	$L=50$	1.76E-03	4.51	2.59E-04	1.98
	$L=100$	5.51E-04	3.30	1.36E-05	0.87
	$L=150$	1.72E-04	2.56	4.34E-07	0.20
	$L=200$	6.09E-05	2.01	3.62E-06	0.53
	$L=250$	2.68E-05	1.59	7.69E-06	0.84
Gyroid	Overall	2.16E-02	7.72	3.28E-03	4.34
	$L=50$	9.72E-03	7.72	2.83E-03	4.34
	$L=100$	4.45E-03	6.60	3.50E-04	2.40
	$L=150$	4.17E-03	5.79	4.14E-05	1.13
	$L=200$	2.10E-03	5.17	1.25E-05	0.57
	$L=250$	1.19E-03	4.72	4.53E-05	0.99

Percentual error and *RSS* data are also presented for each tested length. Equation errors tends to decrease as the length increases. As illustrated by the graphical data, the models considered for larger lengths correspond to lower relative density scenarios, which are better adjusted to the linear tendency regarding d . Accordingly, from Figure 2.5a, this linear dependency tends to decay for relative densities of above 0.6, mainly evidenced in the data for $L=30\text{mm}$. In addition, Gyroid patterns tends to present a bigger relative density than Primitive models for a set value of thickness and/or length, hence the increase in the reported *RSS* and maximum errors.

2.2.2 Equation as a function of thickness-to-length ratio

As established in Equation 2.1, the effect of both parameters was considered as independent, but further analysis showed a slight dependency between d and L . In order to explore this relationship, the *RD* data was plotted in a new graph with respect to the thickness-to-length $\frac{d}{L}$ ratio, as show in Figure 2.7. The data presented were obtained from the same set of models used to derive the previous equations.

Therefore, an alternative function model was suggested based on some similarity between the TPMS patches to sections of hollow spheres. After further literature review, it was found that this approach of modelling is feasible based on the mathematical formation of TPMS. Currently, surface equations for TPMS are derived from Weierstrass formulae, which are a set of elliptical integrals [von Schnering and Nesper, 1991] and their parametrization can be found as the inverse of the Gauss map of the surface patches in a unit sphere [Mickel et al., 2012].

Thus, the new proposal for ρ^* assumes than the inner and outer surfaces of the dense models, obtained from offsetting the main TPMS shape, can also be adjusted to a unit sphere. For this, the TPMS surface is supposed to behave like a hollow sphere contained in a unit-cell, which volume is defined in Equation 2.5 with r_1 and r_2 as outer and inner radii, respectively. Based on this formulation, the thickness corresponds to the difference between the inner and outer radii $d = r_1 - r_2$. The bounding box is defined as a cube with an edge $L = 2r_1$ and its volume is shown in Equation 2.6. Furthermore, the thickness-to-length ratio can be expressed as Equation 2.7.

$$pattern\ volume = \frac{4}{3}\pi (r_1^3 - r_2^3) \quad (2.5)$$

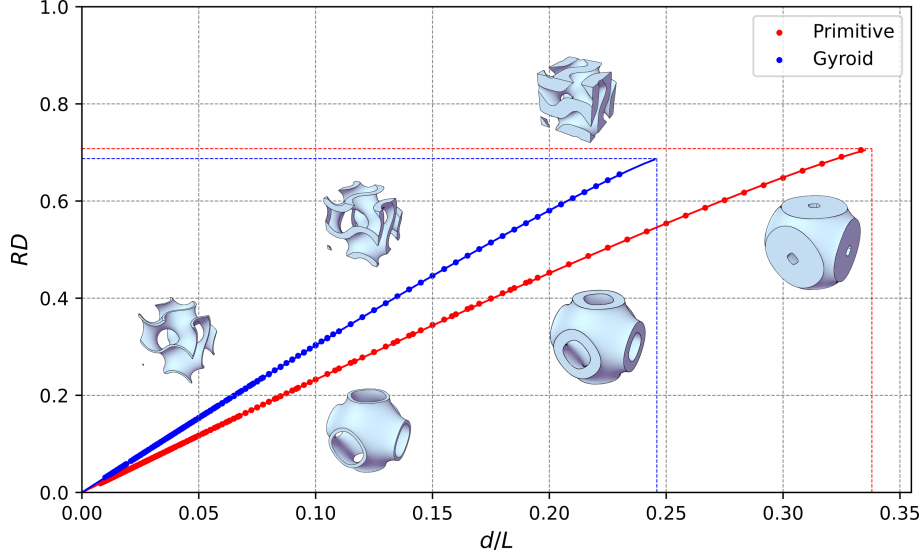


Figure 2.7: Relative density RD as a function of design parameters' ratio $\frac{d}{L}$ for Primitive and Gyroid patterns.

$$\text{bounding box volume} = (2r_1)^3 \quad (2.6)$$

$$\frac{d}{L} = \frac{1}{2} \left(1 - \frac{r_2}{r_1} \right) \quad (2.7)$$

By replacing Equation 2.5, Equation 2.6 and Equation 2.7 on Equation 1.1, ρ^* can be determined by Equation 2.8.

$$\begin{aligned} \rho^* &= \frac{\frac{4}{3}\pi (r_1^3 - r_2^3)}{(2r_1)^3} \\ &= \frac{\pi}{6} \left(1 - \frac{r_2^3}{r_1^3} \right) \\ &= \frac{\pi}{6} \left(1 - \left(1 - 2\frac{d}{L} \right)^3 \right) \\ \therefore \rho^* \left(\frac{d}{L} \right) &= \frac{\pi}{6} - \frac{\pi}{6} \left(1 - 2\frac{d}{L} \right)^3 \end{aligned} \quad (2.8)$$

As Equation 2.8 is derived considering the TPMS surface as a unit-sphere, the adjusted relative density can be determined by Equation 2.9 as a function of the thickness-to-length ratio, where the factors α' , β' and γ' are considered as constants, depending on the analysed TPMS.

$$\rho^* \left(\frac{d}{L} \right) = \beta' - \beta' \left(1 - \alpha' \frac{d}{L} \right)^{\gamma'} \quad (2.9)$$

For the determination of the constant factors, non-linear regression and a Gradient descent optimization procedure was used using the previous CAD data. The final equations for Primitive and Gyroid patterns are detailed in Equation 2.10 and Equation 2.11, respectively.

Table 2.4: Range of applicability for the proposed relative density equations.

Pattern	Lower limit	Upper limit
Primitive	0.095	0.711
Gyroid	0.123	0.688

Table 2.5: Comparison of RSS and maximum percentage error of relative density equations for Primitive and Gyroid patterns.

Pattern		$\rho^* (d, L)$	$\rho^* \left(\frac{d}{L}\right)$
Primitive	RSS	2.85E-04	5.38E-05
	Max. error (%)	1.98%	1.02%
Gyroid	RSS	3.28E-03	1.79E-05
	Max. error (%)	4.34%	0.65%

$$\rho_P^* \left(\frac{d}{L}\right) = 0.711 - 0.711 \left(1 - 2.946 \frac{d}{L}\right)^{1.135} \quad (2.10)$$

$$\rho_G^* \left(\frac{d}{L}\right) = 0.688 - 0.688 \left(1 - 4.057 \frac{d}{L}\right)^{1.114} \quad (2.11)$$

Further analysis of Equation 2.9 maxima shows that the factor β' is analogous to the maximum relative density, and the factor α' to the maximum length-to-thickness $\frac{L}{d}$ ratio that can be modelled. The equation is not mathematically defined for values outside these limits. Table 2.4 presents the lower and upper density limits for the proposed equations. Lower limits were set to the calculated values when considering a pattern thickness $d=2\text{mm}$ for a unit-cell of $L=50\text{mm}$, following WAAM experts' knowledge assessment from the BeShape project partners.

2.2.3 Relative density equation error comparisons

To verify the new proposal improvements, Table 2.5 shows the results for the RSS and the maximum error percentage between the CAD and calculated relative density values, for the ρ^* equations as a function of thickness and length, and thickness-to-length ratio.

As highlighted by these results, there is a better suitability for the prediction of relative density values using the equation proposal with the thickness-to-length ratio. Particularly, the new function greatly reduces the RSS and maximum percentage error values on Gyroid patterns. It is noteworthy that a preliminary equation suggestion from peer-review processes, shown in Equation 2.12 with adjustment coefficients A and B , had a better correspondence to the CAD data, but their implementation was not suitable for the modelling of graded structures (detailed in the next sections) given the interrelation between dependant/independent variables.

$$\rho^* \left(\frac{d}{L}\right)_{peer-review} = A \left(\frac{d}{L}\right) + B \left(\frac{d}{L}\right)^3 \quad (2.12)$$

2.3 Design parameter effects conclusions

Two modelling methodologies for TPMS generation were used to develop different sets of Primitive and Gyroid patterns, to study the effects on relative density of the pattern's design parameters. Regarding the variation of the level-set C , previous studies have developed equations for Gyroid patterns only, but there is no information of its effect on the relative density of Primitive TPMS. For thickness d and unit-cell length L , as stated before, no information was found in the available literature regarding the combined effect of thickness and length on the relative density of Primitive and Gyroid patterns. The present study fills these gaps in geometric modelling analysis and ultimately proposes tools for the calculation of relative density.

From the first modelling by level-set parameter variation, results showed that the pattern thickness, in sheet-based models, is not constant within unit-cell boundaries. This lack of control in the models' properties is considered disadvantageous due to the complexity of correlating the relative density to traditional design parameters of lattice structures, i.e. the thicknesses and unit-cell length. To overcome this issue, a second approach of modelling by fundamental shape offsetting is proposed to develop constant thickness models.

Preliminary observations in constant thickness models showed that the relative density presents a linear relationship with respect to d and a decreasing non-linear relationship regarding L . Specifically, this linear dependency is particularly beneficial for the implementation of density-graded structures. Gyroid patterns tends to present bigger relative density than Primitive models for a set value of thickness and/or length. Even though percentage error results for Gyroid were greater than the values found in Primitive models, they come from the bigger relative density scenarios studied, as it was found that for these cases the linear dependency with respect to the thickness starts to decay. The main applicability of the studied TPMS is considered for lightweight structures, thus this non-linearity is acknowledged but not further corrected.

To better correlate the CAD relative density data to the calculations, a second equation was proposed for relative density ρ^* as a function of the patterns' thickness-to-length ratio $\frac{d}{L}$, being able to significantly reduce the percentage errors, mainly on Gyroid structures. In addition, this equation can be further improved by the inclusion of manufacturing constraints for the redefinition of α' and/or β' factors. In this context, these constraints can be used to define a new initial guess θ_0 to be used in a Gradient Descent algorithm to find the optimized values of the other unknown factors.

Chapter 3

Design of graded density TPMS patterns assemblies

Introduction

Commercial software for TPMS shape generation, such as *MSLattice* by Al-Ketan and Al-Rub [2020] and *TPMS Designer* by Jones et al. [2021] can generate TPMS topologies by applying a variation in the level-set approximation to create dense patterns. However, as stated in subsection 2.1.1, this approach lacks control of the design parameters of the TPMS unit-cell. Particularly, when creating a constant-density pattern by assigning a constant level-set value, there is a non-controlled variation on the thickness. Consequently, the approach of creating a dense pattern by an offset of the TPMS fundamental shape, as introduced in subsection 1.3.3, is the chosen alternative to maintain a control of the pattern thickness. On the other hand, the unit-cell size or length of TPMS is normally controlled by their mathematical definition.

The modelling of Functionally Graded Cellular Materials (FGCM) based on TPMS patterns is a topic of ongoing research. For instance, TPMS software alternatives can develop a TPMS structures with linear density gradients [Al-Ketan and Al-Rub, 2020], but there is no process available to handle a three-dimensional density distribution. Therefore, this chapter details diverse processes to obtain TPMS patterns assemblies with variable density, by controlling the pattern thickness and length with the use of relative density equations defined in subsection 2.2.2, under three-dimensional density distributions.

The chapter starts with the development and comparison of preliminary methods for design parameter variation, which are detailed in section 3.1 before detailing a proposed general design methodology for graded density constructs by independent and simultaneous thickness and length variation in section 3.2. This section also details a set of design tools developed as a custom-built *BeShape* plug-in for Grasshopper[®], by using the RhinoCommon Application Programming Interface (API) for Rhinoceros[®] 7 CAD suite.

The design methodology was tested over an arbitrary three-dimensional density distribution over three scenarios: TPMS pattern density variation by local thickness adjustment, by unit-cell length modification, and by a simultaneous thickness and length change, as presented in section 3.3. The chapter concludes with a summary of the developed design tools characteristics and limitations in section 3.4.

3.1 Preliminary studies of variable design parameters under two-dimensional density distributions

This section presents initial approaches for modelling graded density patterns assemblies by a (non-simultaneous) variation in thickness and length, while using the previously defined relative density (ρ^*) equations (Equation 2.10 and Equation 2.11) to calculate the required design parameters values from a two-dimensional (2D) density map test-bench. This 2D distribution considers a discrete ρ^* value located in the centre of the unit-cell, from which the density would increase or decrease towards the edges depending on the values in neighbour cells. These discrete values are represented by the coloured cells in a x and z plane, as depicted in Figure 3.1.

Following subsections detail the application of this density map on the generation of pattern assemblies of eight 50mm unit-cells in a 2x2x2 arrangement for variable thickness scenarios, or to obtain the modified unit-cell sizes on variable length scenarios with a constant thickness of 2mm. It is noteworthy that even though the structures are three-dimensional, the applied density map does not apply a variation of the design parameters on the y direction.

The preliminary modelling tests detailed in this section are presented chronologically, therefore some of them corrects or adapts previous stages depending on the specific modelling results. Accordingly, the first two preliminary studies of thickness variation by patch offset and length variation by density surface were implemented in Rhinoceros[®] 6 CAD suite, using the Grasshopper[®] (GH) visual programming environment and the Millipede plug-in extension for the Marching Cubes algorithm for STL mesh construction. During the course of the thesis, support service for the Millipede extension was lost (and discontinued), thus having no reliable option for upgrading it to the new version of the CAD software.

As a consequence, the last two explored methods for length and thickness variation were developed as custom scripts written in C# language, inside the GH environment of Rhinoceros[®] 7. This implementation solved the compatibility issues of the Millipede plug-in by implementing an alternative polygonization algorithm (i.e. Marching Tetrahedra), while having a better computing performance. The section finishes with a summary and general discussion of these processes.

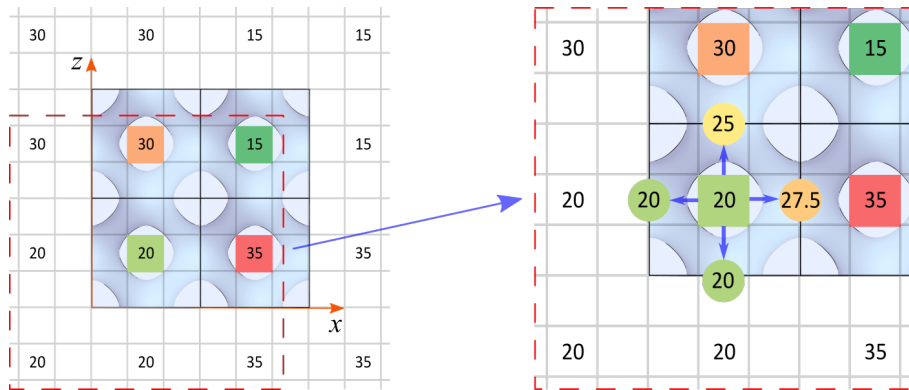


Figure 3.1: Two-dimensional density distribution in x and z .

3.1.1 Variable thickness by TPMS patches offset

The thickness variation scenario was the first methodology explored due to the identification of the (almost) linear effects of d on the relative density. The big interrogation in this stage was how to relate the values from an uniformly distributed density map to the construction of the TPMS pattern. For this, a potential approach is to generate the models based in the formation of the TPMS shape by their patches, having 8 patches per unit-cell, as depicted in Figure 3.2 for a Primitive pattern.

The method assumes that the density map would assign a discrete density to each unit cell, and then use it to calculate the boundary density values to adapt the thickness of the pattern by a displacement of the mesh vertices in each individual patch. The boundary conditions (values outside of the design space) of the pattern assembly were assumed as the same discrete central density values of the immediate neighbour cell, as shown in Figure 3.1. The required density in the unit-cell interfaces was calculated using a double interpolation method.

Accordingly, a modelling process was implemented in GH for Primitive patterns, given their less complex face connections between neighbouring cells compared to Gyroid TPMS. Several clusters were defined to simplify the overall graphical interface and connections between operations. An overview of the methodology is shown in Figure 3.3.

The main component is the *Variable UC* Cluster (Figure 3.4). It receives the unit-cell position, needed for the correct reference of the location of individual patches, the unit-cell size (length) and the density distribution Q , represented by a list of values starting from the bottom row of a 2D matrix. Equation 3.1 shows an example of the Q distribution for the bottom left corner unit-cell of Figure 3.1 (from now on referred as UC_1). For an arbitrary unit-cell, ρ_5 is the central density of the cell to be generated, while other values corresponds to the neighbour and outer boundary densities.

$$Q = \begin{pmatrix} \rho_7 & \rho_8 & \rho_9 \\ \rho_4 & \rho_5 & \rho_6 \\ \rho_1 & \rho_2 & \rho_3 \end{pmatrix} = \begin{pmatrix} 30 & 30 & 15 \\ 20 & 20 & 35 \\ 20 & 20 & 35 \end{pmatrix}_{UC_1} \quad (3.1)$$

Inside *Variable UC* the three inputs are used to construct subsets of density boundaries, each one related to a different patch, used for the interpolation of interface densities. Equation 3.2 details the density subsets from the previous example for Q distribution of UC_1 .

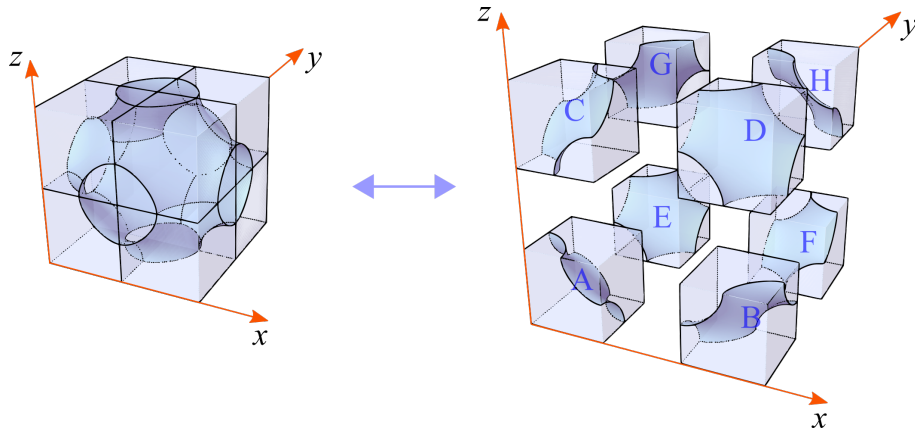


Figure 3.2: Patches' identification in a unit-cell.

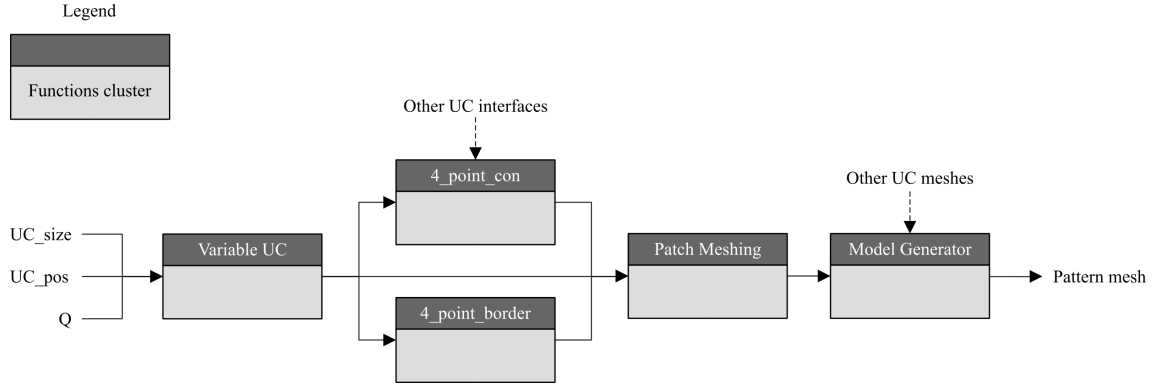


Figure 3.3: Graded density by variable thickness process.

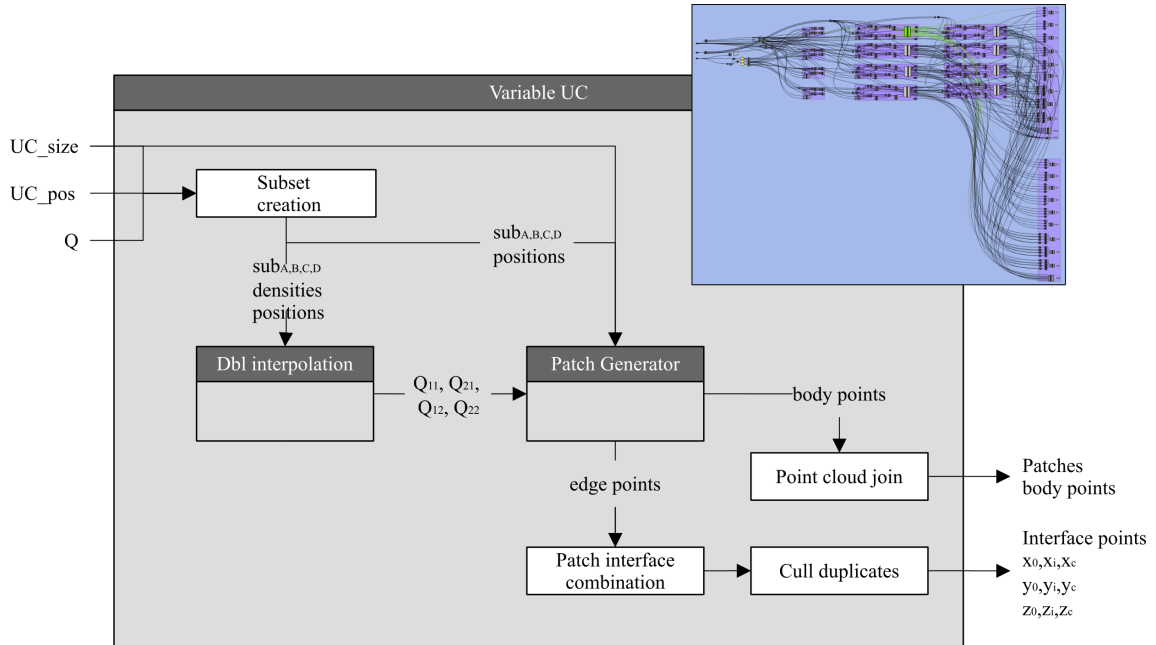


Figure 3.4: Variable UC Cluster

$$\begin{aligned}
Q \rightarrow \begin{pmatrix} sub_C & sub_D \\ sub_A & sub_B \end{pmatrix} &= \begin{pmatrix} \begin{pmatrix} \rho_7 & \rho_8 \\ \rho_4 & \rho_5 \end{pmatrix}_C & \begin{pmatrix} \rho_8 & \rho_9 \\ \rho_5 & \rho_6 \end{pmatrix}_D \\ \begin{pmatrix} \rho_4 & \rho_5 \\ \rho_1 & \rho_2 \end{pmatrix}_A & \begin{pmatrix} \rho_5 & \rho_6 \\ \rho_2 & \rho_3 \end{pmatrix}_B \end{pmatrix} \\
&= \begin{pmatrix} \begin{pmatrix} 30 & 30 \\ 20 & 20 \end{pmatrix}_C & \begin{pmatrix} 30 & 15 \\ 20 & 35 \end{pmatrix}_D \\ \begin{pmatrix} 20 & 20 \\ 20 & 20 \end{pmatrix}_A & \begin{pmatrix} 20 & 35 \\ 20 & 35 \end{pmatrix}_B \end{pmatrix}_{UC_1}
\end{aligned} \tag{3.2}$$

The nomenclature adopted is detailed in Equation 3.3 and Equation 3.4 for density values and patch positions, respectively. Taking the subset sub_D as an example, the patch's interface density values Q_{11} , Q_{12} , Q_{21} , Q_{22} are obtained by double interpolation from the values of ρ_5 , ρ_6 , ρ_8 and ρ_9 using a *Dbl Interpolation Cluster*.

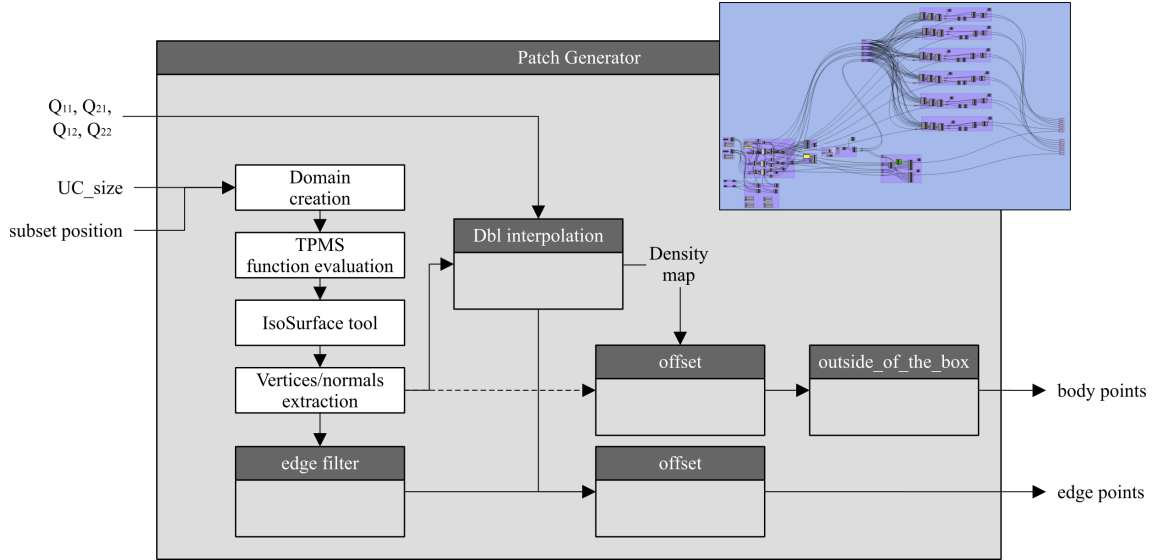
$$sub_D \rightarrow \begin{pmatrix} \rho_8 & \rho_9 \\ \rho_5 & \rho_6 \end{pmatrix}_{densities} = \begin{pmatrix} \rho_8 & & \rho_9 \\ Q_{12} & Q_{22} & \\ Q_{11} & Q_{21} & \rho_6 \end{pmatrix} = \begin{pmatrix} 30 & & 15 \\ 25 & 25 & \\ 20 & 27.5 & 35 \end{pmatrix}_{UC_1} \tag{3.3}$$

Each density value is related to a different location, and the values of x_0 , x_c , x_b , z_0 , z_c , z_b from Equation 3.4 depends on the patch's position. Taking the subset sub_D as an example, (x_0, z_0) corresponds to the unit-cell central position, while (x_b, z_b) is the position of the centre of the ρ_9 neighbour unit-cell. Other positions are determined by sequentially adding half the unit-cell's length.

$$\begin{aligned}
sub_D \rightarrow \begin{pmatrix} \rho_8 & & \rho_9 \\ Q_{12} & Q_{22} & \\ Q_{11} & Q_{21} & \rho_6 \end{pmatrix}_{positions} &= \begin{pmatrix} (x_0, z_b) & (x_c, z_b) & (x_b, z_b) \\ (x_0, z_c) & (x_c, z_c) & (x_b, z_c) \\ (x_0, z_0) & (x_c, z_0) & (x_b, z_0) \end{pmatrix} \\
&= \begin{pmatrix} (\frac{L}{2}, L + \frac{L}{2}) & & (L + \frac{L}{2}, L + \frac{L}{2}) \\ (\frac{L}{2}, L) & (L, L) & \\ (\frac{L}{2}, \frac{L}{2}) & (L, \frac{L}{2}) & (L + \frac{L}{2}, \frac{L}{2}) \end{pmatrix}_{UC_1}
\end{aligned} \tag{3.4}$$

All these information is then fed to a *Patch Generator Cluster* (Figure 3.5), which receives the unit-cell size, patch's position, and Q_{11} , Q_{12} , Q_{21} , Q_{22} values. This cluster first performs the creation of the function domain for the TPMS equation evaluation to be used for the Marching Cubes (MC) algorithm run by Millipede's IsoSurface Tool. The generated mesh vertices location and normals are then extracted and separated in two groups: edge and body vertices.

For body vertices, their positions are run through an *Offset Cluster*, which receives the vertices position, normals, density map, and unit-cell size. The vertices displacements are calculated as half the thickness found by the previously established relative density formulae. The density map values are obtained by double interpolation of the required density in each position, based on the Q_{11} , Q_{12} , Q_{21} , Q_{22} values and positions. The cluster outputs the corrected position of vertices in the inner and outer surfaces. All these values are then run through an *outside-of-the-box* filter Cluster to separate the points corresponding to the body of the patch, and filter the offset projections that are positioned out of the patch boundaries.

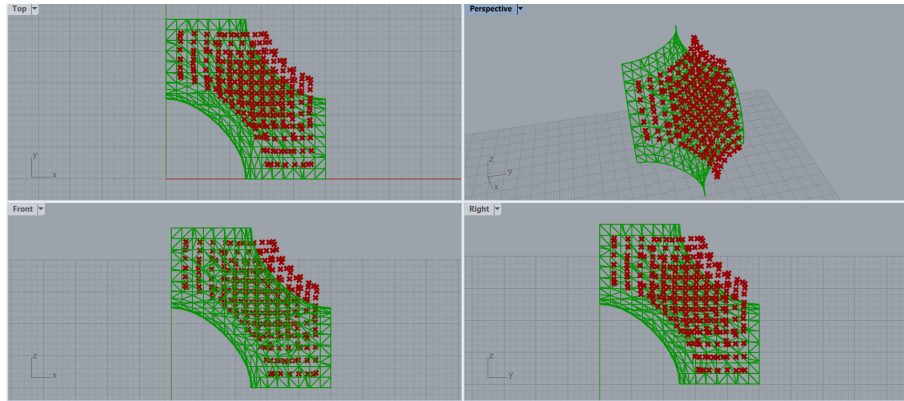
Figure 3.5: *Patch Generator* Cluster

Edges vertices are separated in six groups, each one corresponding to a different interface connection, by a series of filters clusters (not depicted). These filters receive the vertices positions and normal vectors lists, the required boundary location, steps and sensitivity values to control the detection of the edge's vertices. A value of 15 for steps (equal to the discrete domain divisions) and 4 for sensitivity, are set based on a non-exhaustive testing. The edge vertices are then moved along the interfaces, preventing a projection outside of the patch's boundaries. *Patch Generator* cluster finishes returning the displaced points of the body (Figure 3.6a) and the patches' edge in the interfaces (Figure 3.6b) for the inner and outer surfaces.

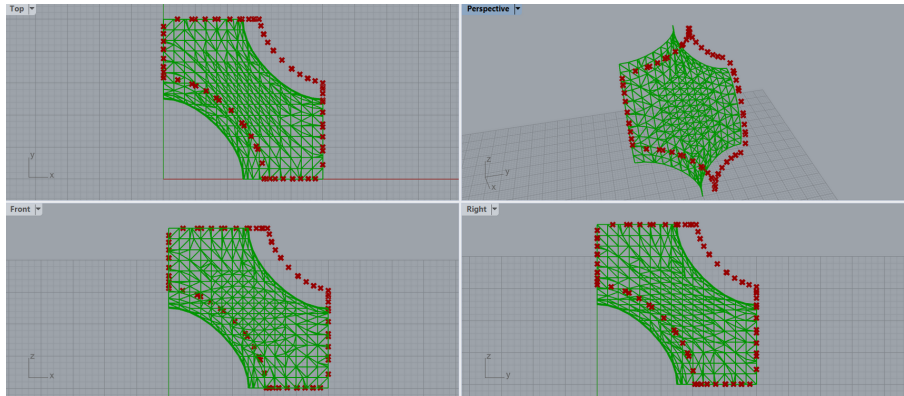
Returning to the parent cluster (*Variable UC*), each patch receives an identification to ease with the creation of boundary connections inside the unit-cell (as shown in Figure 3.2). As an example, to get the boundary cell connection in the $x = 0$ plane, the edges in the x_0 position from the patches A, B, E and F are grouped together. Inner connections are also considered with a similar approach. The connections at the centre of the unit-cell are obtained by combining the patches edge pairs (A,B), (C,D), (E,F) and (G,H). A *Cull* or values filtering operation is also used to eliminate duplicated points within a tolerance of 0.1, before combining the edges for the required output. *Variable UC* finalizes by returning the combined interface points of the patches and the body points.

Before performing the unit-cell mesh reconstruction, clusters named *4_point_con_X*, *Y* and *Z* are run to eliminate duplicated vertices between the connections of neighbouring unit-cell and to add the 4 corner points of the Primitive circular interfaces that are lost during the edge filtering operations. The output of these clusters is a set of vertices that will be used for the reconstruction of the interfaces, thus ensuring pattern mesh's interconnectivity, as shown in Figure 3.7. Variants for outer borders (edges with no connections to other unit-cells) are run by the *4_point_border_X*, *Y*, *Z* Clusters.

With the corrected interfaces and the previous defined body points, a *Patch Meshing* Cluster (Figure 3.8) in which each patch is formed individually before combining them in the final unit-cell model. *Patch Meshing* is run with an additional tolerance input set at 0.6 (for performing a final *Cull* in the individual patch generation). All the points of the patch (body and corrected interfaces) are grouped and run through a *Delaunay* meshing tool, followed by a *Clean* Cluster that removes undesired faces generated by the automated

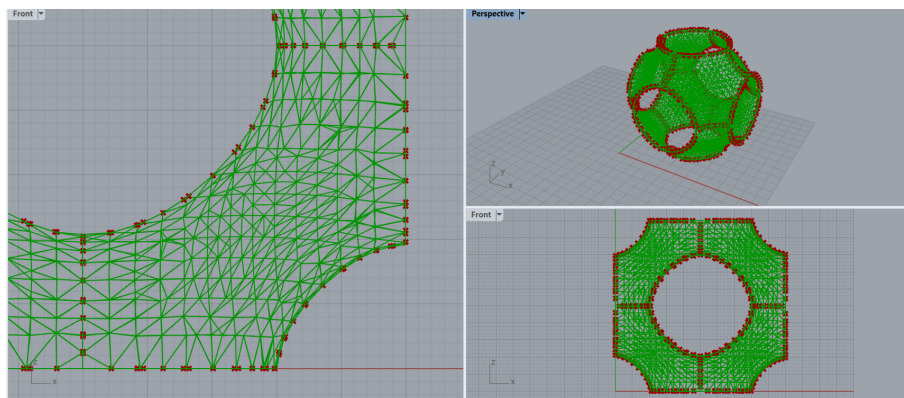


(a) Body points



(b) Edges points

Figure 3.6: Example for patch points' offset.

Figure 3.7: Patch interfaces interconnectivity after $4_point_con_X$, Y and Z Clusters.

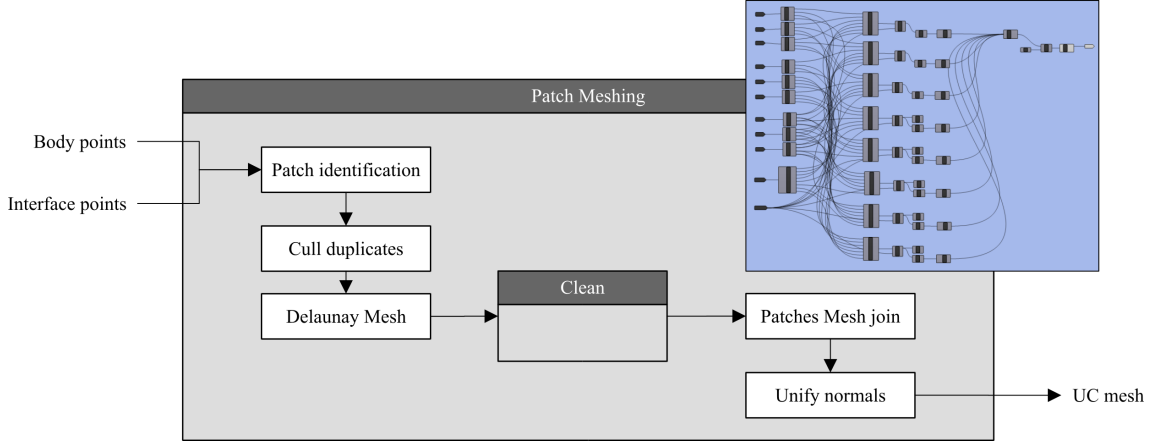
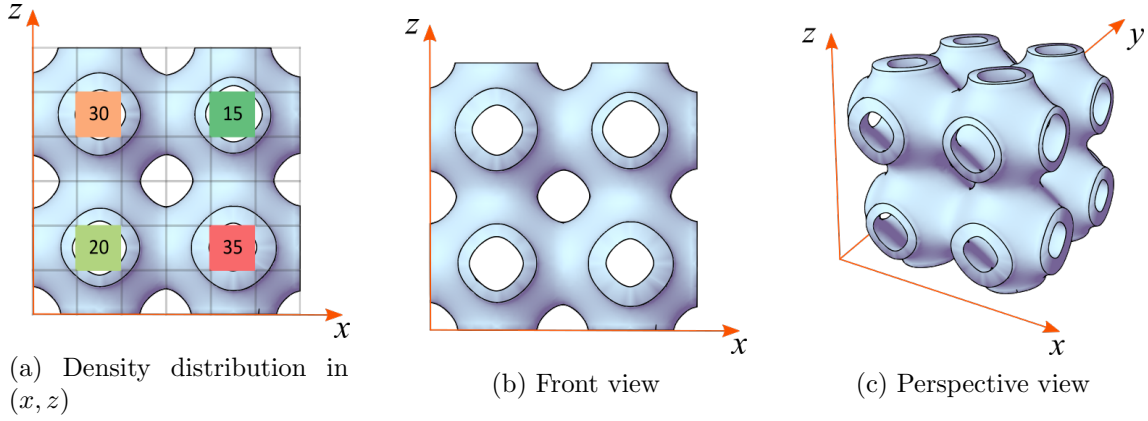
Figure 3.8: *Patch Meshing Cluster*

Figure 3.9: Variable thickness Primitive pattern assembly by patch offset.

mesh generation. The patches of each individual unit-cell are then joined and returned as an output. This cluster is run for both inner and outer surfaces.

Finally, all the external and internal surfaces of the unit-cells in the pattern assembly are fed to a *Model Generator Cluster*, which performs the mesh join between unit-cell instances and adds the surface boundary faces to get the final closed mesh. The relative density of the whole unit-cell assembly is also calculated and returned in this component. Figure 3.9 shows an example of this implementation for a 2x2x2 Primitive pattern assembly, using the density distribution detailed on Figure 3.1, for a unit-cell size of 50mm.

3.1.2 Variable unit-cell length by density surface

The cases of length variation cannot be treated with the previously defined process of unit-cell patch's modifications, as the boundaries of a unit-cell (and patches) will be deformed as the length varies, thus presenting surface continuity issues. Figure 3.10 shows these mesh construction problems for a length variation scenario in a 100x100x100mm design space and a constant thickness of 2mm, while using the previous patch subdivision method. It is important to note that, even though the surface is not smooth, the vertices between sections are still connected.

To correct these errors, the adopted strategy was to feed the length variation L_{var} in the dilatation factor λ , as shown in Equation 3.5, and perform the surface generation using the

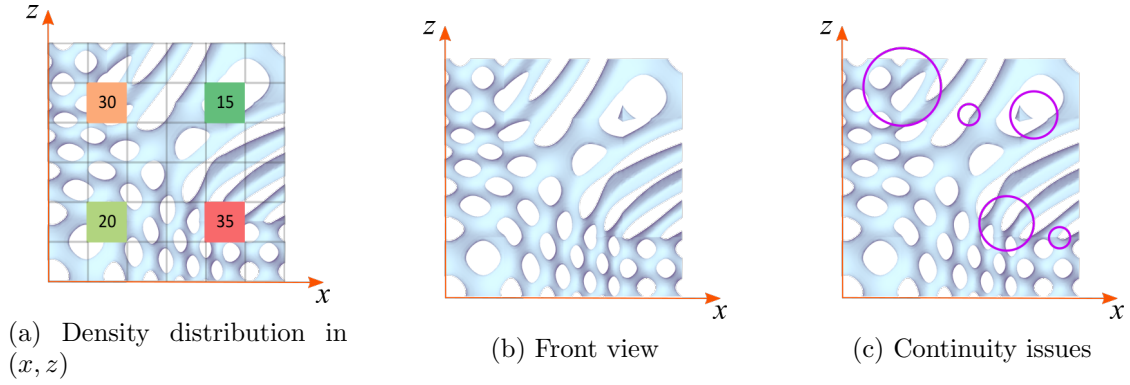


Figure 3.10: Front view examples of errors in surface continuity for length variation from patch construction.

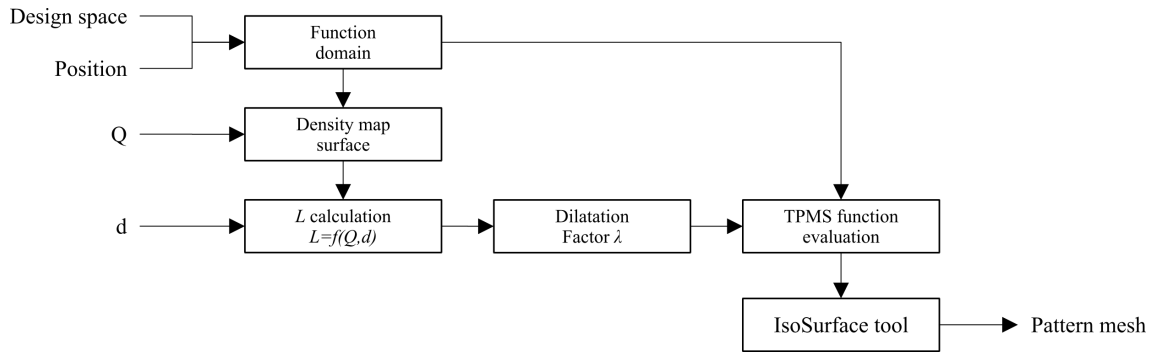


Figure 3.11: Graded density by variable length in density surface process.

whole design space domain without considering the pattern instances n_i . Consequently, λ stays the same for the x , y and z axis, differing from past definitions, in order to maintain the concept of (cubic) voxel generation.

$$\lambda_x = \lambda_y = \lambda_z = \lambda = \frac{2\pi}{L_{var}} \quad (3.5)$$

The process used in this section is illustrated in Figure 3.11. The design space size and position is used first to create the TPMS function domain, which will then serve to create the density map. The required lengths map is then calculated from the densities and a predefined thickness d . As stated before, these length values are used to define the λ variations to be used in the TPMS function evaluation. The obtained results are then fed to the IsoSurface tool to obtain the variable length pattern mesh. Finally, this mesh can be run through a constant thickness offset procedure to generate the solid model.

For this implementation, an example using a density map in x and z was used to define a density distribution surface. The control points for the surface definition were defined using the (x, z) positions of the density map and the density values in the y coordinate, as shown in Figure 3.12. The required discrete density values for the TPMS generation are then encountered as the distance of the projections of the function domain points in $y = 0$ to this density surface, as in Figure 3.12b.

Figure 3.13 illustrates the central surface for the obtained graded density assembly of Primitive patterns in a 100x100x100mm design space for a set thickness of 2mm. It is important to note that, even though the y direction is used to generate the density distribution surface, there is no variation of density in y . As shown, the surface discontinuities

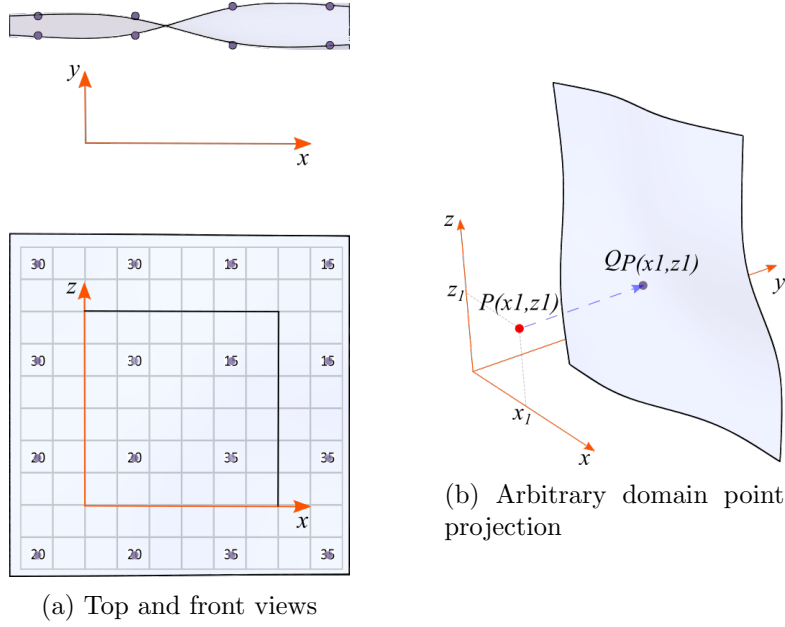


Figure 3.12: Density distribution surface.

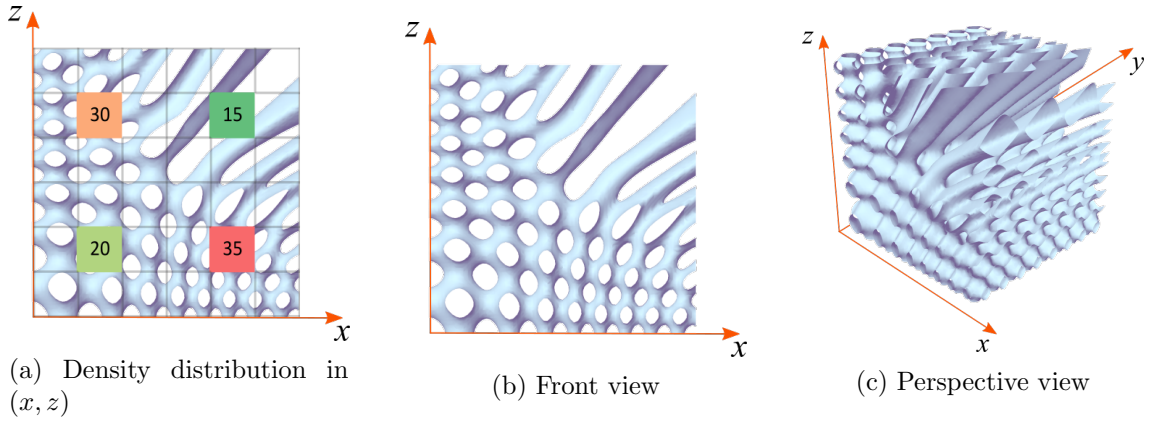


Figure 3.13: Variable length Primitive pattern assembly by IsoSurface tool.

highlighted in Figure 3.10 are no longer present using this construction methodology. In addition, although a thickness value was used for the calculation of ρ^* , the offset of this central surface was not implemented at this stage.

3.1.3 Marching Tetrahedra script for unit-cell length variation

To overcome the increasing complexity and computing times of the previous method, a second approach for length variation modelling was implemented in GH as a custom script written in C# language. This script was developed using previous work by Piker [2021], who based his implementation on a C# translation developed by Delrieu [2020] from a study of polygonization for scalar fields presented by Bourke [1994, 1997]. The scalar field polygonization is one type of implicit surface modelling method. Similarly to the MC algorithm process, scalar field points with a negative value are defined to be contained by the surface, while points with positive values represents zones outside of the surface.

Specifically, Bourke [1997] work details an implementation of a Marching Tetrahedra

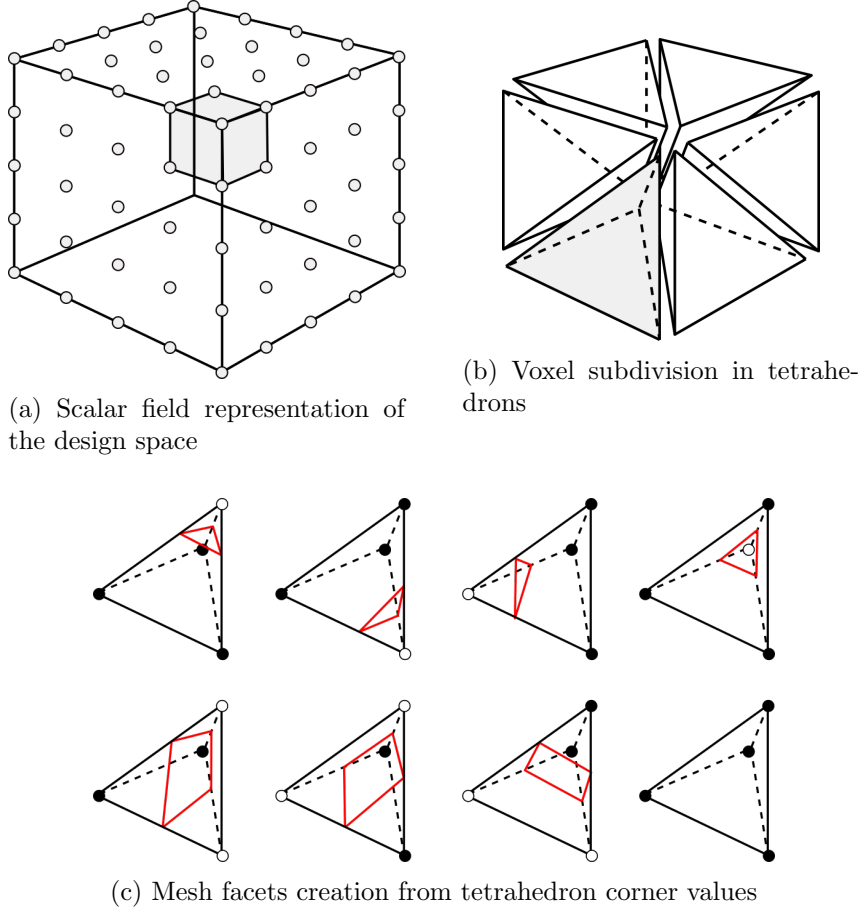


Figure 3.14: Marching Tetrahedra algorithm process.

(MT) algorithm [Doi and Koide, 1991]. This algorithm analyses the field in a discrete manner by grouping adjacent points representing a voxel, which are then subdivided as six tetrahedrons, as shown in Figure 3.14. The triangular facets of the mesh are formed depending if the tetrahedron corners are located above or below the TPMS surface, following 8 cases of scalar values distribution. As depicted in Figure 3.14c, corners in opposite sides are represented by a change of circle's colour. When the tetrahedra corners are located in opposite sides, the location of a point corresponding to the surface mesh is found by interpolating the corner locations depending on their values. When all corners are located in the same side, no facets are created. The main benefit of this method is that it solves ambiguities present in the MC procedure [Bourke, 1997], while being significantly simpler to implement.

The custom modifications added to the script by Piker [2021] includes the process to receive a three-dimensional density distribution map and use their values to calculate discrete lengths to be used in the surface voxelization of the TPMS equations. To this purpose, two functions were added. The first function, **Expand**, receives a three-dimensional density map and remaps it according to the required point resolution and size of the design space for the generation of the TPMS surface. This remapping procedure is executed by triple-interpolating the unknown values based on the initial map by an **Interpolation** function. The **Expand** function also contains the ρ^* equations defined in subsection 2.2.1 to calculate the required lengths.

The mapped values of L are then feed to a **Evaluate** function with the required

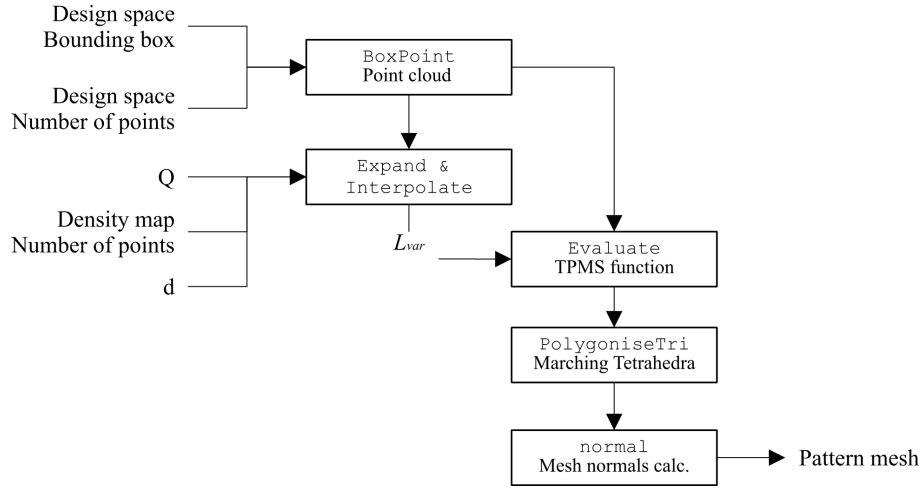


Figure 3.15: Marching Tetrahedra script flowchart for Graded density by variable length process.

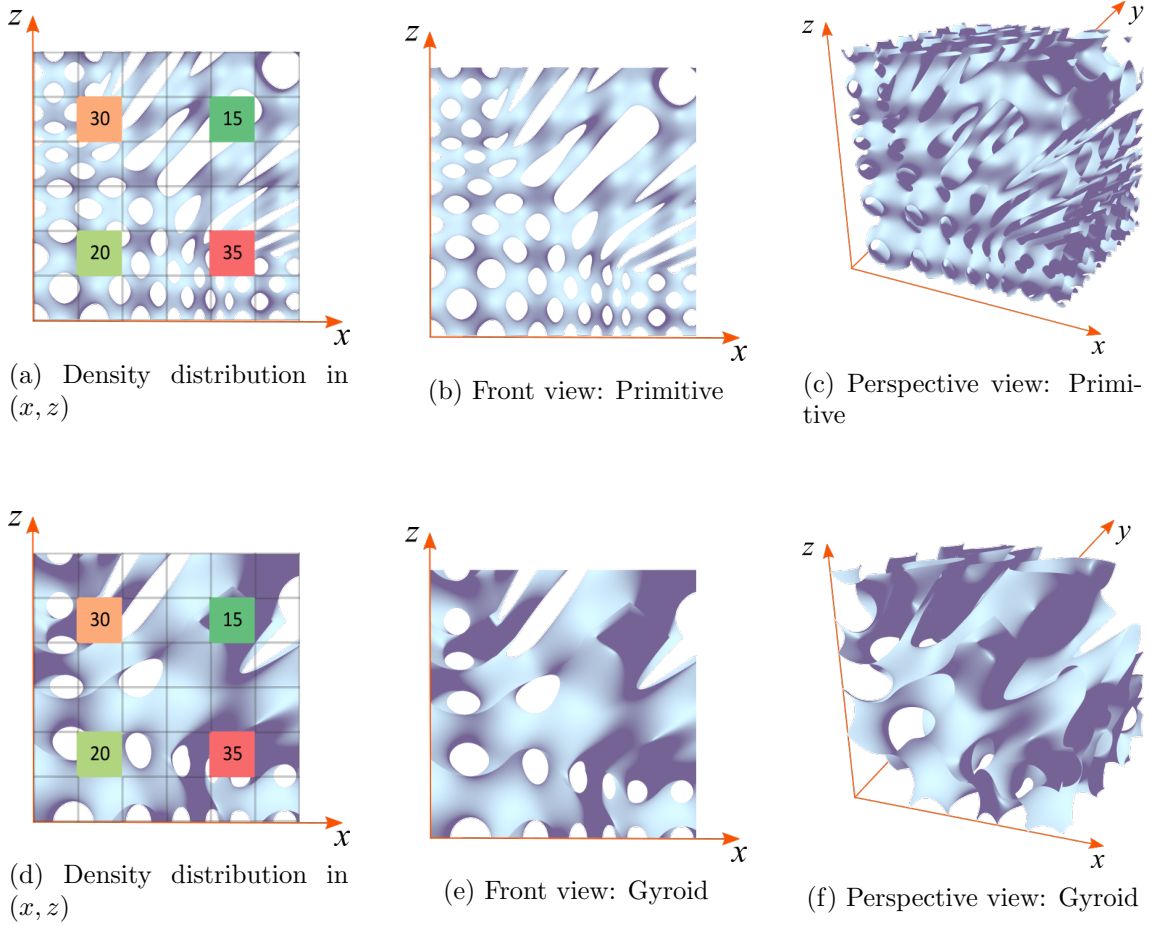


Figure 3.16: Variable length pattern assemblies by C# script.

TPMS shape equation, before creating the mesh sections by a function containing the MT algorithm, named `PolygoniseTri`. To conclude, the mesh slices are joined and the faces normals are calculated by the `normal` function. These processes are illustrated in Figure 3.15.

The arbitrary density map test-bench in x and z was used to evaluate the procedure, and the obtained central surface for Primitive and Gyroid patterns assemblies are shown in Figure 3.16. As before, only the central surface is displayed, as the addition of thickness in the model was not implemented in this stage.

3.1.4 Marching Tetrahedra script for thickness variation

Due to the increased computer performance of the C# script method, an alternative for thickness variation was implemented. The process, depicted in Figure 3.17, utilizes the same functions described in the previous subsection, with the difference that the density map will be used to interpolate the required thickness in each vertex of the generated fundamental shape by `PolygoniseTri`. The interpolated values are then used to offset the mesh vertices to create the final pattern mesh.

Figure 3.18 shows the results of these process in the (x, z) density distribution test. Even though the process is able to generate both Primitive and Gyroid patterns, the image displays only the results for a 2x2x2 Gyroid pattern assembly of unit-cells of 50mm, which was not possible to be easily generated by the previous patch offset procedure.

All the functions involved in the Marching Tetrahedra script (`Expand`, `Evaluate`, among others) contain legacy source code that was updated or replaced during the development of a custom-built Grasshopper[®] plug-in containing a set of tools (components) to assist the generation of variable density TPMS constructs, according to a general design methodology that will be detailed in section 3.2. This legacy source code is not presented in this document.

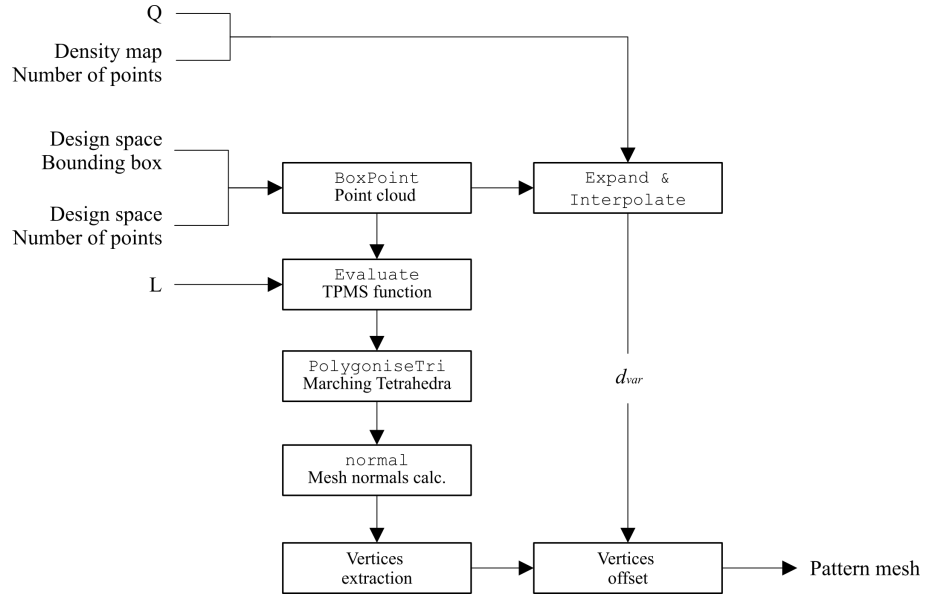


Figure 3.17: Marching Tetrahedra script flowchart for Graded density by variable thickness process.

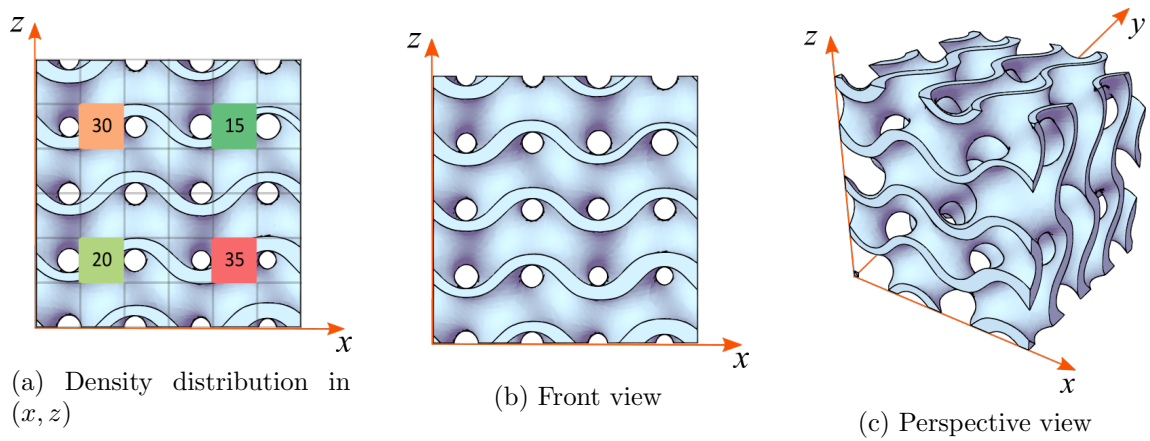


Figure 3.18: Variable thickness pattern assemblies by C# script.

3.1.5 Summary and discussion

Table 3.1 and Table 3.2 summarise the modelling conditions, procedures and drawbacks for the preliminary tests on graded density structures by a variation in thickness or length, respectively.

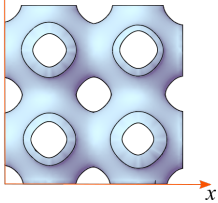
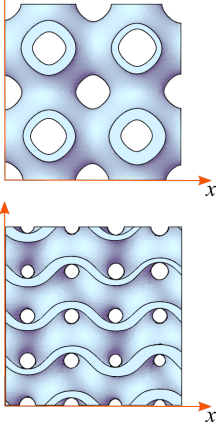
It is noteworthy that both thickness and length variation models presents an additional characterization challenge, as their mechanical behaviour is not related to a homogenized material in the macro-scale. A continuous change in thickness and the unit-cell deformation introduced on length variation modelling methods cannot be directly applied to classical homogenization theories, as these structures does not satisfy the underlying concepts of periodicity of representative volumes. Homogenization methods for heterogeneous materials is a topic of ongoing research [Letov and Zhao, 2022] and were out of the scope of the current work.

Discussion on thickness variation methods

The first method for thickness variation by patch offset was successfully implemented for a 2x2x2 Primitive pattern assembly. Even though the process can potentially be applied for the displacement of inner points on Gyroid patterns, their surface boundaries' complexity produced issues in the function Clusters that performs the connection between patches. In addition, the process is rather tedious to implement, as each different Cluster has to be connected manually. This is highlighted by the GH screen capture presented in Figure 3.19 for the 2x2x2 pattern assembly of Figure 3.9. Each grey component corresponds to a different Cluster instance, the majority of interconnections have been hidden for visualization purposes.

These issues were corrected by the application of the Marching Tetrahedra script that handles the surface creation and the vertices displacement directly, greatly simplifying the graphical interface and optimizing the required computation times. In addition, this process can work with any type of TPMS, with just the inclusion of their required function inside the program. However, the downside of this method is that it can produce self intersections in the offset meshes, as some vertices can potentially have conflicting normals depending on the adjacent faces. This particular problem was solved by using a Signed Distance Field (SDF) offset process, which is detailed in the next section.

Table 3.1: Summary of preliminary studies for graded density pattern assemblies by variable thickness.

Process	Process description		
<p>By TPMS patches offset</p> 	<p>Conditions:</p> <ul style="list-style-type: none"> • Primitive patterns • Two dimensional Density map in (x, z) • Double interpolation of unknown densities • 2x2x2 pattern arrangement on a 100x100x100mm design space 	<p>Procedure:</p> <ul style="list-style-type: none"> • Unit-cell division in patches • Patch mesh generation by IsoSurface tool • Mesh vertices displacement by $d = f(\rho^*, L)$ • Patch's interface vertices correlation • Patch's remeshing and joining 	<p>Drawbacks:</p> <ul style="list-style-type: none"> • Tedious implementation • Procedure is too complex for Gyroid patterns • IsorfaceTool discontinued during the study
<p>By Marching Tetrahedra script</p> 	<p>Conditions:</p> <ul style="list-style-type: none"> • Primitive and Gyroid patterns • Three-dimensional density map in (x, y, z) • Triple interpolation of unknown densities • 2x2x2 pattern arrangement on a 100x100x100mm design space 	<p>Procedure:</p> <ul style="list-style-type: none"> • Density map remapping to design space • Thickness calculation by $d = f(\rho^*, d)$ • Triple interpolation of values on unknown positions • Fundamental shape by Marching Tetrahedra, constant L • Mesh sections normals' calculation • Mesh vertices displacement 	<p>Drawbacks:</p> <ul style="list-style-type: none"> • Discrete density map values need to be equally distanced • Vertices offset can produce self intersections in the resulting mesh

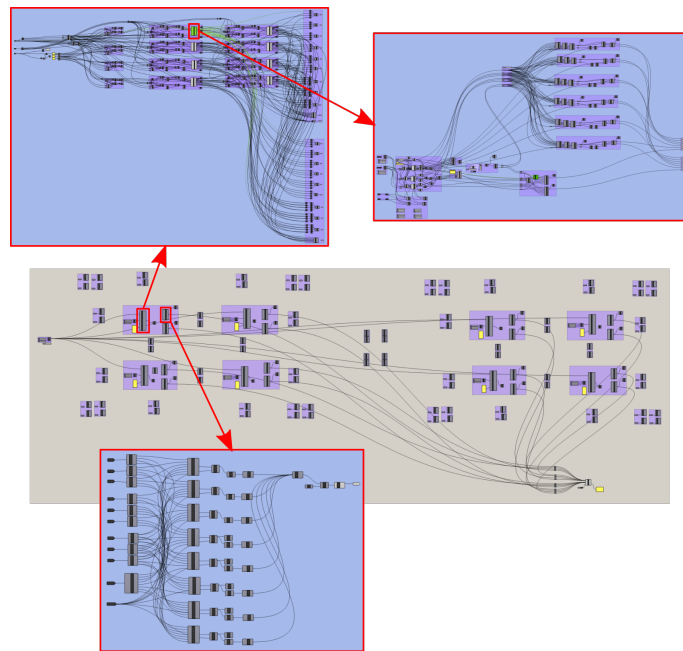


Figure 3.19: Screenshot of the implemented methodology for the 2x2x2 Primitive pattern assembly with thickness variation.

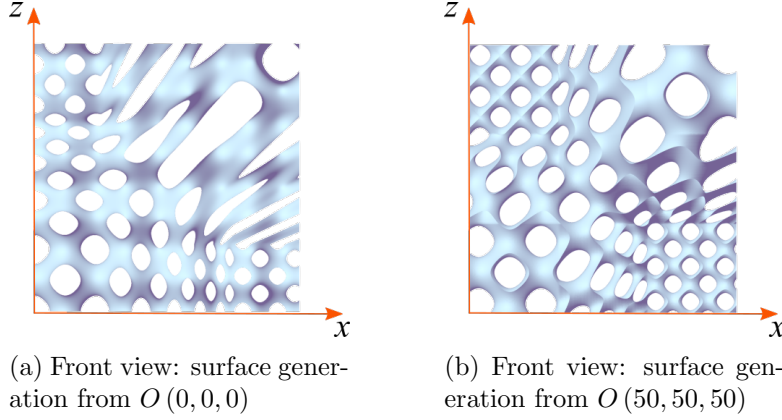


Figure 3.20: Correction of topology discontinuities by surface transposing.

Discussion on length variation methods

The problem with the first implementation of length variation was the high computing times needed for the calculation of the density map surface and their subsequent utilization in the IsoSurface tool. For the example shown in Figure 3.13, the total processing time was approximately 10min, with a relatively low resolution. Bigger densities maps can be developed, but the increased point cloud yielded the implementation and evaluation unpractical. Although this process can potentially handle Gyroid surfaces, their generation was not tested in this stage. In addition, the density surface can only be defined from a two-dimensional density distribution, making this process not applicable for three-dimensional maps from topological optimization or finite element methods.

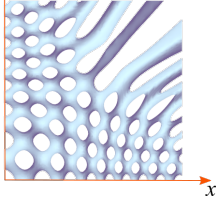
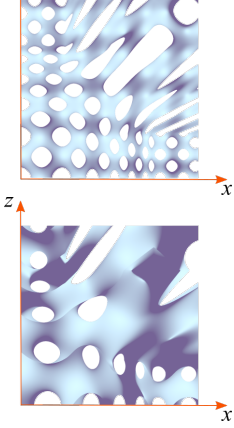
In contrast, the processes of length variation by the Marching Tetrahedra script is able to develop these topologies in seconds, with a much higher point resolution than previous methodologies, showing a great improvement in computation times. However, as shown in Figure 3.16b, the surfaces present similar continuity errors as the ones depicted in Figure 3.10 for Primitive patterns. This can be mainly attributed to the interpolation of unknown values, and due to the utilization of coarse arbitrary density maps with no clear direction for their distribution. Due to their topology, Gyroid patterns tends to handle better these discontinuities.

As length variation cases are directly controlled by the TPMS equations, one potential solution is to move the surface generation from the origin of the coordinate system to a point $O(x, y, z)$ by performing a simple function displacement, as shown on the modified Equation 3.6 and Equation 3.7 for Primitive and Gyroid patterns, respectively. Figure 3.20 presents the differences in surface generation by performing this transposition.

$$f_P(x, y, z) = \cos(\lambda_x(x - O_x)) + \cos(\lambda_y(y - O_y)) + \cos(\lambda_z(z - O_z)) \quad (3.6)$$

$$\begin{aligned} f_G(x, y, z) = & \cos(\lambda_x(x - O_x)) \sin(\lambda_y(y - O_y)) + \\ & \cos(\lambda_y(y - O_y)) \sin(\lambda_z(z - O_z)) + \\ & \cos(\lambda_z(z - O_z)) \sin(\lambda_x(x - O_x)) \end{aligned} \quad (3.7)$$

Table 3.2: Summary of preliminary studies for graded density pattern assemblies by variable length.

Process	Process description		
By density surface 	Conditions: <ul style="list-style-type: none"> • Primitive patterns (Gyroid not tested) • Two-dimensional density map in (x, z) • 100x100x100mm design space 	Procedure: <ul style="list-style-type: none"> • Density map used as control points to create a density surface • Unknown densities on design space found by the projection of their position on density surface • Length calculation by $L = f(\rho^*, d)$ • IsoSurface with L variation in the whole design space 	Disadvantages: <ul style="list-style-type: none"> • High computing times • Relatively low resolution (compared to previous unit-cell models) • Restricted to two-dimensional density distributions • IsoSurfaceTool discontinued during the study
By Marching Tetrahedra script 	Conditions: <ul style="list-style-type: none"> • Primitive and Gyroid patterns • Three-dimensional density map in (x, y, z) • Triple interpolation of unknown densities • 100x100x100mm design space 	Procedure: <ul style="list-style-type: none"> • Density map remapping to design space • Triple interpolation of values on unknown positions • Length calculation by $L = f(\rho^*, d)$ • Marching Tetrahedra with L variation in the whole design space • Mesh sections normals' calculation and joining process 	Disadvantages: <ul style="list-style-type: none"> • Discrete density map values need to be equally distanced • Triple interpolation can produce surface discontinuities when working with arbitrary density maps

3.2 General design methodology and custom-built tools for graded density TPMS structures

This section compiles the previous process results, in particular the Marching Tetrahedra (MT) scripts, in an integral method for developing structures of varying thickness and/or length. The methodology was initially implemented as scripts and functions written in C# language using the RhinoCommon API inside the Grasshopper® (GH) environment of Rhinoceros® 7. After initial testing of the process, the scripts were converted to a series of GH components that can be loaded to the main user interface (UI) as a customized *BeShape* plug-in extension.

The overall modelling strategy consists in the creation of a TPMS structure with a variable density adapted to a density map obtained from Finite Element Analysis (FEA) or Topological Optimization (TO) methods. The distribution of density is used to find the required local design parameter values (local thickness and/or length) for the generation of the TPMS fundamental surface and the subsequent offset faces of the dense pattern.

This section introduces a simplified version of the design flowchart before detailing the main processes involved in the proposed methodology for the creation of graded density configurations. All processes present an in-depth explanation of their equivalent GH components. Details of the diverse classes (user-defined object constructors in C#) and component's pseudocode algorithms, as well as additional utility tools, can be consulted in Appendix A. Other components developed for the handling of Equivalent Material (EM) analysis and FEA data are detailed in section 4.2.

3.2.1 Design methodology overview

The flowchart of the proposed methodology is shown in Figure 3.21, establishing a simplified overview of the main sequence for the involved processes. The procedure starts with the definition of design specifications (i), which comprises the following entries:

- i.1 Design space (DS), which is defined as the bounding box of the solid CAD model that needs to be replaced by TPMS patterns.
- i.2 Density distribution values and positions, obtained by a FEA or TO of the CAD model.
- i.3 Target Density Map (DM) grid distance for the re-mapping of FEA or TO reference data.
- i.4 TPMS type, which defines the cellular shape to be used for the model.
- i.5 Reference voxel size and subdivision iterations to perform the DS discretization in the polygonization algorithm.
- i.6 Modelling scenario: i.e. constant density model, or graded density configuration by thickness, length or ratio (simultaneous thickness and length) variation.
- i.7 Miscellaneous design parameters conditions, depending on the graded density scenario. This entry considers length and thickness set values or limits, density range and the origin point for the surface generation.

The next step considered is the creation of the Density Map (DM) (ii), based on the reference data values, their locations inside the design space, and the target DM grid

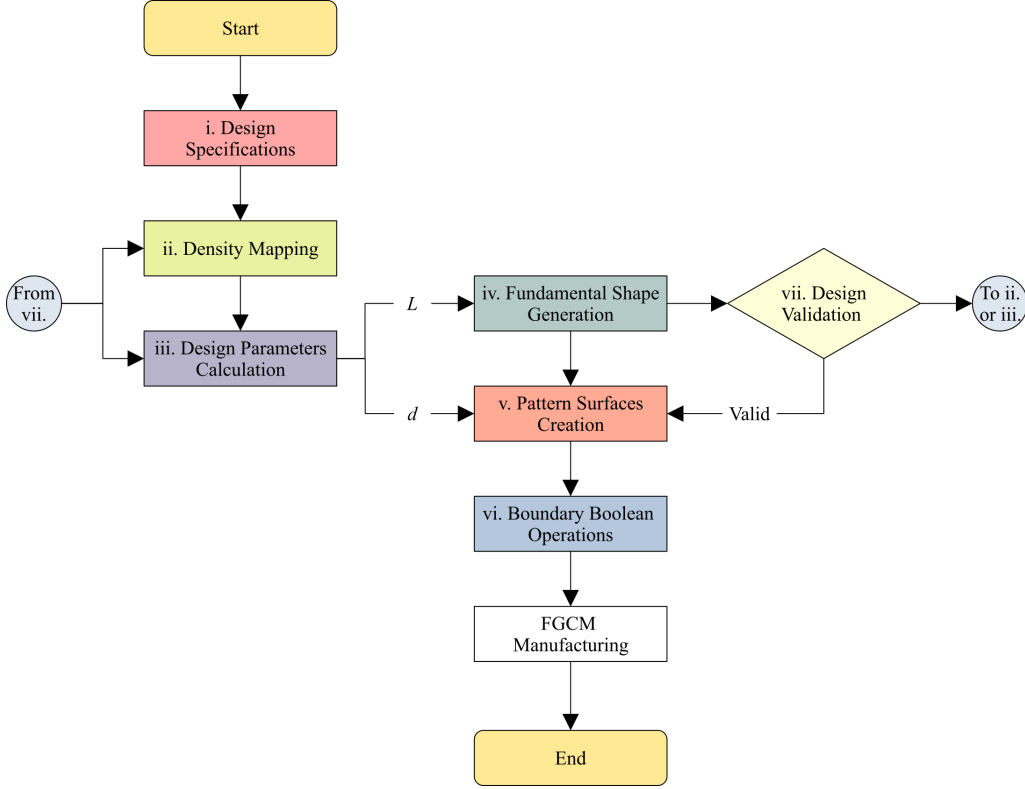


Figure 3.21: Methodology flowchart overview.

distance. For this step, additional processes for the handling of TO or FEM results are needed, further detailed in subsection 3.2.2.

With the DM definition, the design parameters are calculated depending on the modelling scenario (iii). In order to ease the generalization of the process, the thickness-to-length ratio is calculated regardless of the required variation, and used to obtain the distribution of thickness and lengths required in subsequent processes. Accordingly, the calculation process is further detailed in subsection 3.2.3.

The required length distribution (variable or constant) is used to generate the fundamental shape (iv) based on the MT methodology used in the previous implementations. This step, summarized in subsection 3.2.4, concludes with the generation of the fundamental (central) TPMS mesh.

The next step of pattern surface creation (v) considers the displacement of the fundamental shape by using the required thickness (variable or constant). This process is mainly done by an Signed Distance Field (SDF) offset process to define the inner and outer surfaces, more detailed in subsection 3.2.5. The step concludes with a mesh reconstruction by a MT algorithm.

The final dense model with the TPMS patterns is obtained by a series of boolean operations between the pattern surfaces and the design space boundaries or the final part shape. An additional process for design validation (vii) is considered for the evaluation of the generated structure by finite element methods. These validation process will be discussed in chapter 4. The extended methodology diagram is detailed in Figure 3.22. The following subsections details the processes involved for every operation, as well as their implementation as GH components.

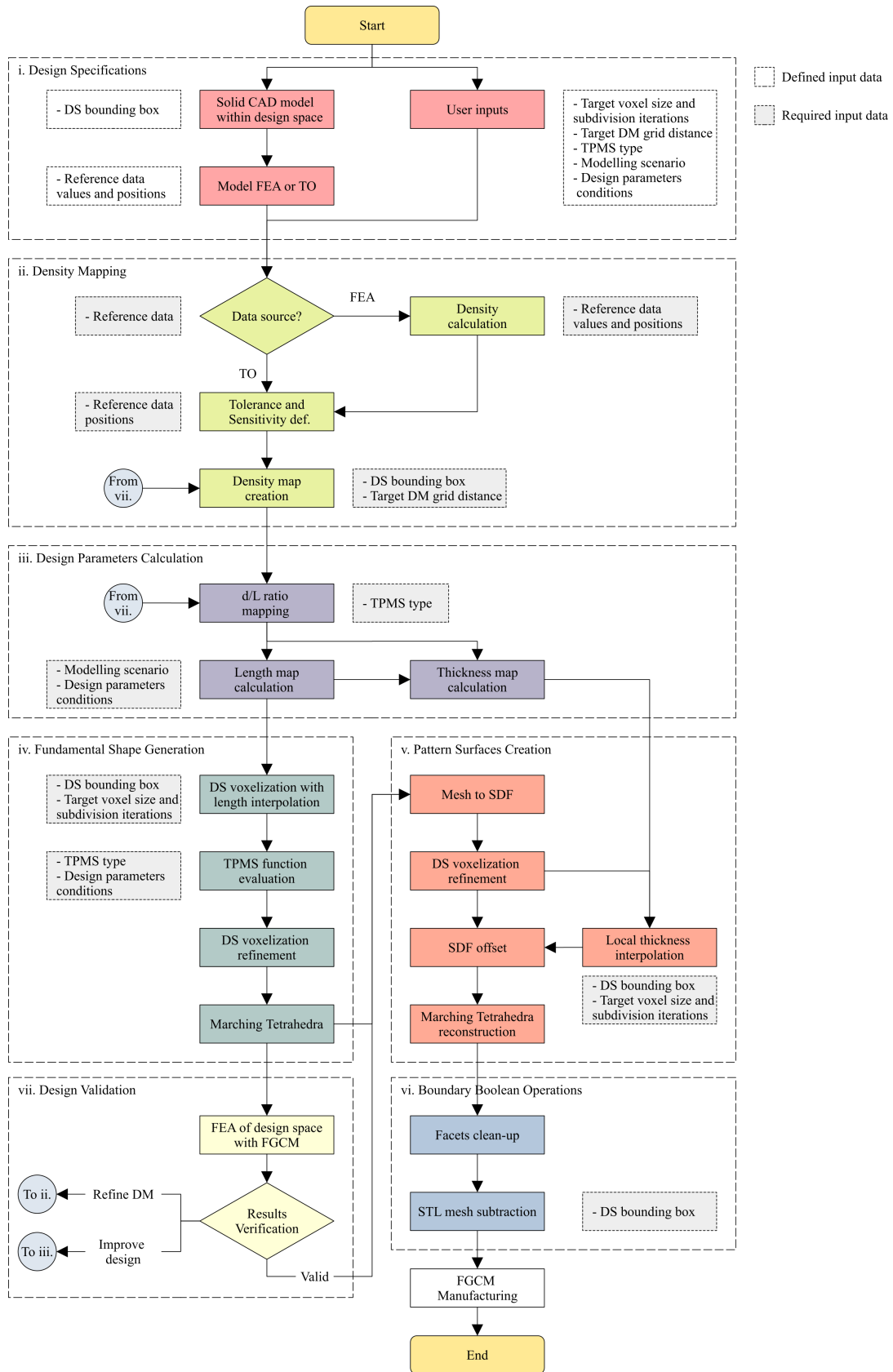


Figure 3.22: Detailed design methodology for graded density TPMS constructs.

3.2.2 Density Mapping

Process details

This stage comprises the creation of the density map (DM) to be used in the posterior calculation of design parameters. The main requisite is to have a DM represented by a regular grid, due to the discrete nature of the MT algorithm. If the reference density distribution comes from TO methods, the values and their locations are passed directly to sub-processes. However, if the density data need to be calculated from FEA results, an additional procedure is required, which will be further detailed in section 4.2.

The requirement of a uniform grid is fulfilled by performing a re-mapping of the TO or FEA-derived density distribution inside the DS. The procedure for the calculation of a local density ρ_m consist in a weighted sum operation between a group of reference density values ρ_i of r data nodes. The weight coefficients are calculated from a ratio of inverse-squared distances, as detailed in Equation 3.8 and Equation 3.9. From the equations, ω_i denotes the distance from a remapped grid point to a reference node r of the data grid. Ω is defined as the sum of inverse-squared distances from a remapped grid point to all reference nodes. The use of squared distances is selected due to the computational benefits of their calculation for distances between points in C#.

$$\rho_m = \sum_{i=1}^r \rho_i \frac{\frac{1}{\omega_i^2}}{\Omega} \quad (3.8)$$

$$\Omega = \sum_{i=1}^r \frac{1}{\omega_i^2} \quad (3.9)$$

For this process, *Tolerance* and *Sensitivity* distances are defined depending on the distance between grid points. Accordingly, *Sensitivity* represents the maximum size of the area to look for reference data points to calculate the local density value, and is set as the maximum between the remapped grid *QmapDistance* and the reference data grid point distance *GridDistance*, as defined in Equation 3.10. Both grid distances are compared as the remapping could be done by either a dense (bigger point count) density distribution or from few representative densities values.

$$sensitivity = \max(QmapDistance, GridDistance) \quad (3.10)$$

On the other hand, *Tolerance* is the maximum area from which a local density is set automatically without passing through the weighted sum procedure. It should be defined as a small value, not bigger than half the minimum between the remapped *QmapDistance* and the data grid point distance *GridDistance*, as in Equation 3.11, to limit the detection of points. If the density distribution is already uniform, this half value would permit to get only one point of reference.

$$tolerance \leq \frac{1}{2} \min(QmapDistance, GridDistance) \quad (3.11)$$

Figure 3.23 shows a graphical representations of the zones defined by the *Sensitivity* and *Tolerance* values. In most cases, the density map would be generated from a density distribution with a bigger quantity of elements, as depicted in Figure 3.23a. As an example, the density value of the point located in the centre of the grid on Figure 3.23a would be calculated by the influence of the red points inside the blue area defining the sensitivity zone, as no points are present below the tolerance limits. In contrast, the lower left example point would be set automatically from the value of the point inside the red area

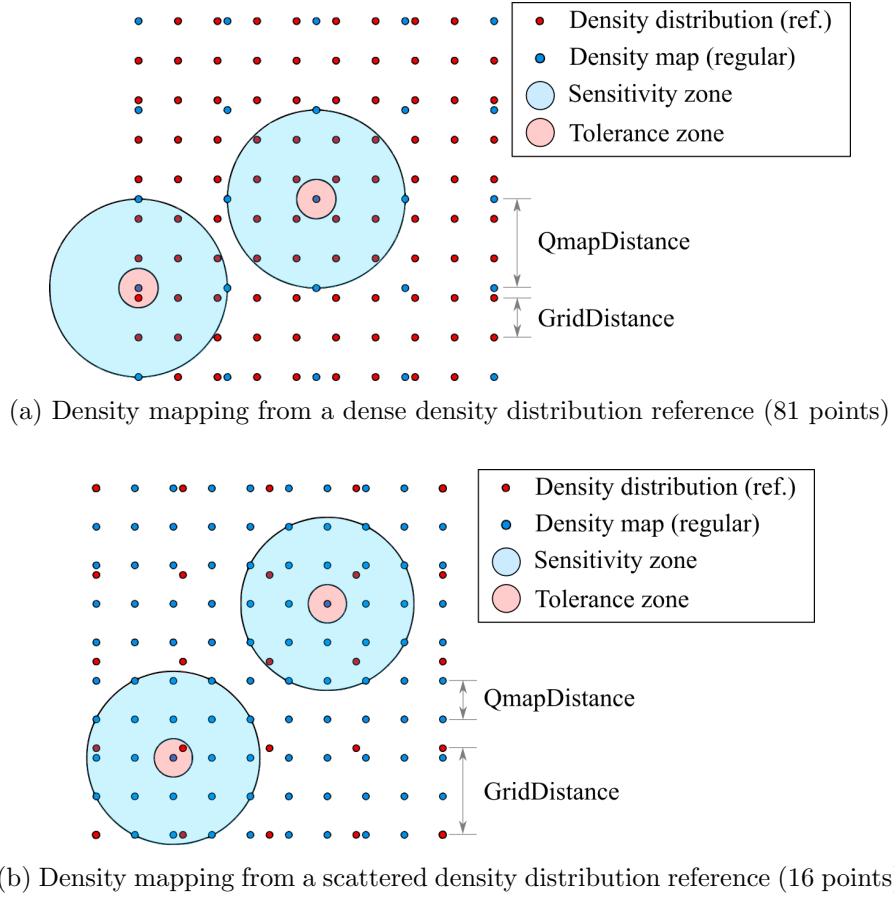


Figure 3.23: Sensitivity and tolerance zones representation.

representing the tolerance zone, without considering the neighbouring points densities. The case of a density map generation from fewer density distribution reference points is shown in Figure 3.23b. It is important to note that, in these cases, the definition of tolerance as the half minimum grid distance benefits the consideration of several reference values to find the local density.

GH component implementation

The **Density Mapping** GH component processes the tolerance and sensitivity definitions and the creation of the DM. As shown in Figure 3.24, the density node positions and values are loaded on the component's **Q_pos** and **Q_values** entries, respectively, while the target DM grid spacing is loaded in **ref_dist**. The component is activated by a boolean toggle fed to the **Run** entry.

The **approximation** entry is a selector of the method for local density calculation, which can be either "By Weights", following the process described in subsection 3.2.2, or "By Maximum" which assigns the local maximum density within the sensitivity zone. By default, the component works by applying the weighted sum method.

As the process will generate a density map inside a prismatic design space, an additional (optional) **Q_ext** input is considered to add a density value on missing spaces when working with non-prismatic reference models. If no value is assigned, **Q_ext** is set to the minimum density from **Q_values**. The last optional input, **oversize**, is a boolean used to include additional rows and columns with **Q_ext** values outside of the initial DM space. This

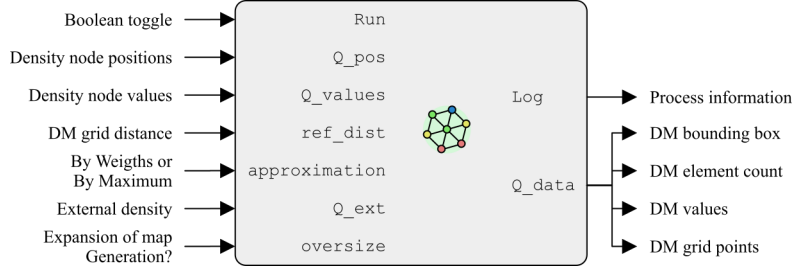


Figure 3.24: Density Mapping GH component overview.

condition is applied to have reference density value when creating a TPMS surface bigger than the DS dimension, possible required by processes of boundary boolean operations. By default, **oversize** is set to **False**.

The component outputs the DM data in **Q_data** as a collection of: a **Box** data type representing the DM bounding box, an array containing the density element's count in x , y and z coordinates, and the lists of adjusted density values and DM grid points' locations. **Q_data** information is wrapped under the **Density_Data** class for inter-component input/output (I/O). In addition, **Log** compiles information of the process, such as the sensitivity and tolerance distances, adjusted density range, approximation type and oversize condition. The pseudocode of this component can be consulted in Algorithm A.1.1.

The process starts by analysing the data grid distance from **Q_pos** on x , y and z , depending on the range and count of different values in each coordinate. This process is done by a **GridDistance** method running Equation 3.12. The x , y and z components of the reference grid positions are stored as individual *coord* lists. *count* is the number of different values found in the lists by a **Counter** method.

$$GridDistance = \frac{coord_{max} - coord_{min}}{count - 1} \quad (3.12)$$

Similarly, the grid distance on each coordinate of the required DM *QmapDistances* is found by the same **GridDistance** method, while calculating the node count by Equation 3.13 with the target DM grid distance value **ref_dist**.

$$count_{Qmap} = \frac{coord_{max} - coord_{min}}{ref_{dist}} + 1 \quad (3.13)$$

Due the possibility of having different grid distances values on x , y and z coordinates, *Sensitivity* and *Tolerance* distances are calculated using the maximum value between the *QmapDistances* and *GridDistances* results at each coordinate on Equation 3.10 and Equation 3.11.

Following, the DM bounding box (DM_{box}) is constructed based on the position coordinate range. If **oversize** is **True**, the box limits are expanded according to *QmapDistances* on each direction, in order to contain additional rows and columns of **Q_ext**.

With DM_{box} , $count_{Qmap}$ and *QmapDistances*, the regular grid of DM points is created by using a **PointCloud** method and stored as a list of points in a *Q_boxPoints* variable. For each point in *Q_boxPoints*, the component initially verifies if the point is part of the added values due to the **oversize** condition (assignment of **Q_ext**). If not, the square distance between each *Q_boxPoints* to the whole list of points in **Q_pos** is calculated. If the distance to **Q_pos** point falls outside of the sensitivity zone, the density value at **Q_pos** point is ignored. If the point is under the tolerance range, the density value is stored in a list of

"points under tolerance" for later processes. Otherwise, depending on the **approximation** type, the value is stored in either a "weight" or "maximum" values list.

After sweeping the **Q_pos** point list, if there are values in the tolerance list, the adjusted density value $Q_{adjusted}$ is set as the maximum value of the list. In the case of a Weighted approximation, the values on the "weight" list are used to calculate the adjusted density value by Equation 3.8 and Equation 3.9. For a Maximum approximation, the adjusted value is simply set to the maximum value of the "maximum" list. The component ends by returning a **Q_data** class containing the DM_{box} , $count_{Qmap}$, $Q_{adjusted}$ and $Q_{boxPoints}$.

In addition to the described processes, during the calculation of the Weighted sum, if an adjusted value is less than the minimum density value from **Q_values** (meaning that the point is far from the data on cases of modelling non-prismatic reference models), $Q_{adjusted}$ is set to the minimum density. The same is considered in the approximation by Maximum, in which, if the "maximum" list is empty (absence of reference data), the adjusted value of the node is also set to the minimum density value from **Q_values**.

3.2.3 Design Parameters Calculation

Process details

Depending on the TPMS type, the thickness-to-length ratio can be found by Equation 2.10 or Equation 2.11 for Primitive or Gyroid patterns, respectively. Each value of the density map will correspond to a local ratio value. As the ratio depends on both d and L , length values are first calculated and then used to find the corresponding thickness, as in Equation 3.14. In the case of constant length scenario, the variable thickness map is found by multiplying the length by the local ratio values. Similarly, variable length with constant thickness are found by dividing the thickness to the local ratio.

$$d = L \times ratio \quad (3.14)$$

For a simultaneous length and thickness variation, from now on denoted as a modelling by ratio variation, the length values are calculated according to the local thickness-to-length ratio; zones with bigger ratios (higher densities) are associated to smaller length values, while zones with lower ratios (low density) are set towards bigger length values. This additional process assumes a linear dependency between the ratio and the inverse of the length, as shown in Figure 3.25, by using Equation 3.15. The range of lengths values to be used needs to be selected depending on the overall part dimension. With the calculated lengths, the local thickness can be found by Equation 3.14.

$$\frac{1}{L} = \frac{1}{L_{min}} + \left(\frac{1}{L_{max}} - \frac{1}{L_{min}} \right) \left(\frac{ratio_{max} - ratio}{ratio_{max} - ratio_{min}} \right) \quad (3.15)$$

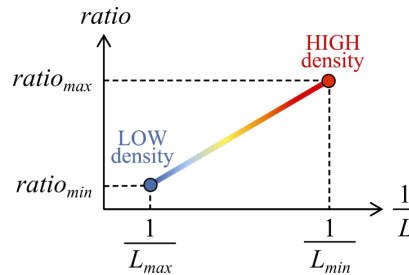


Figure 3.25: Ratio vs inverse length for simultaneous thickness and length variation.

Having defined the local (mapped) thickness and length values from the DM, posterior processes on the design methodology considers a second remapping of values by interpolation methods, depending on the DS voxel subdivision. This step is considered as the DS would normally need a bigger point cloud density for a correct surface generation.

GH component implementation

The **Design Parameter Mapping** component performs the thickness-to-ratio mapping procedure and the definition of lengths and thicknesses distributions, following the previously detailed process. The component overview is depicted in Figure 3.26. Even though **Q_data** results from the density mapping procedures are considered as an input, the component only works with the adjusted density values. Additional components for the feed of **Q_data** formed by manual density definition are detailed in section A.3.

The **TPMS_ID** input is as a selector of named values for the desired TPMS type. Currently, the process is limited to Primitive and Gyroid patterns. Similarly, **variation** has options to select the calculation process for constant design parameters, thickness variation, length variation or ratio (simultaneous thickness and length) variation. Depending on the selected variation type, the component will require different set values:

- *Constant*: procedure works by defining a set length value to **L_const**, and the component will calculate the required thickness from a single density data.
- *Thickness*: a **L_const** value is needed for the calculation of the thickness map from a density distribution.
- *Length*: the diverse length values are calculated based on a set thickness on **d_const**;
- *Ratio*: the process will calculate both length and thickness maps from a set range on lengths values fed to **L_max** and **L_min**, according to Equation 3.15

The component outputs a **modelling_conditions** data class containing the calculated length and thickness maps, the TPMS type and the selected design parameter variation. As before, a summary of the component process can be consulted on the **Log** output, which contains a reference to the modelling conditions and the range of calculated thickness and lengths.

The first operation is the creation of the thickness-to-length ratio distribution for each density value. This operation is done by a **Ratio** method as a function of the density Q and the required α , β and γ constants depending on the TPMS type by using an internal **Density_model** class storing the relative density model's factors. Once the factors have been defined, the design parameters' maps are calculated depending on the modelling condition set on **variation**, according to the previously defined process. Algorithm A.1.2 summarizes these processes.

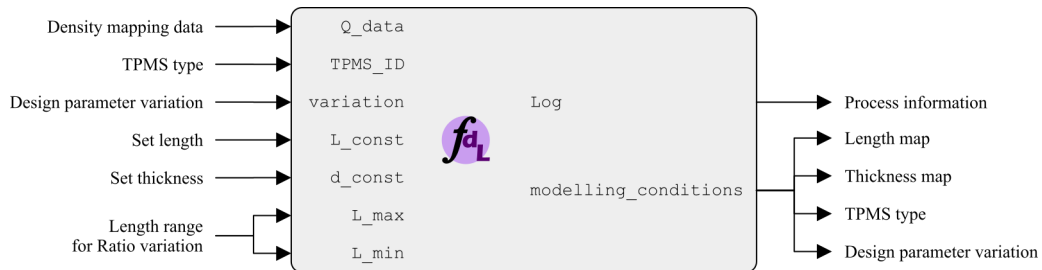


Figure 3.26: Design Parameter Mapping GH component overview.

3.2.4 Fundamental Shape Generation

Process details

Given the discrete nature of the polygonization method, the curvatures of the generated surfaces are heavily influenced by the voxel size. A good approximation for a surface considers that the line segment to represent a curved section should not span more than a circular sector of 15° [ANSYS, 2004], resulting in an approximation to radius ϵ/R error of 0.85%, according to the geometry depicted in Figure 3.27. Thus, the line segment is considered analogous to the voxel size defined by the length factor h of Equation 3.16 as a function of the radius of the curved section.

$$h = 2R_{fundamental} \sin\left(\frac{15}{2}\right) \quad (3.16)$$

Particularly, the effective radius of the circular section for the fundamental shape generation $R_{fundamental}$ depends on the pore topology of the lateral projection of the TPMS fundamental shape, as presented in Figure 3.28. Due to the TPMS geometric characteristics, these pores are not necessary circular. However, for calculation purposes, the pores are related to a circle with diameter $D = L/4$ that fits inside their topology. Therefore, the corresponding $R_{fundamental}$ is determined by Equation 3.17 for both Primitive and Gyroid patterns.

$$R_{fundamental} = \frac{1}{2} \left(\frac{L}{4} \right) \quad (3.17)$$

For the fundamental shape generation of graded density constructs, the MT algorithm generates the STL mesh from a scalar field generated from the evaluation of the TPMS function on each corner of the voxels representing the DS. As the voxel representation of the DS can be a heavy computing operation, an iterative refinement process of voxel subdivision and un-used voxel cleaning is considered.

For a general modelling case, the process works with an initial voxel size and a number of iterations to obtain the required h calculated from the minimum L of the mapped lengths. This initial voxel size is used to create a first iteration of voxels representing the DS. The location of each voxel corners is used to interpolate the required local length values which, along with the required origin for the surface generation, are used to evaluate the TPMS function by Equation 3.6 and Equation 3.7 for Primitive or Gyroid patterns, respectively.

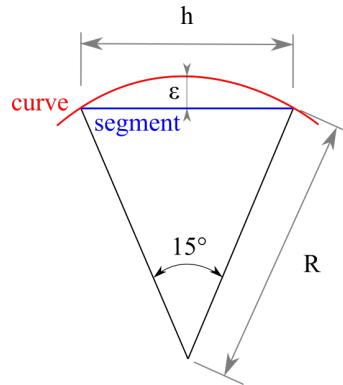


Figure 3.27: Geometry for voxel length factor definition.

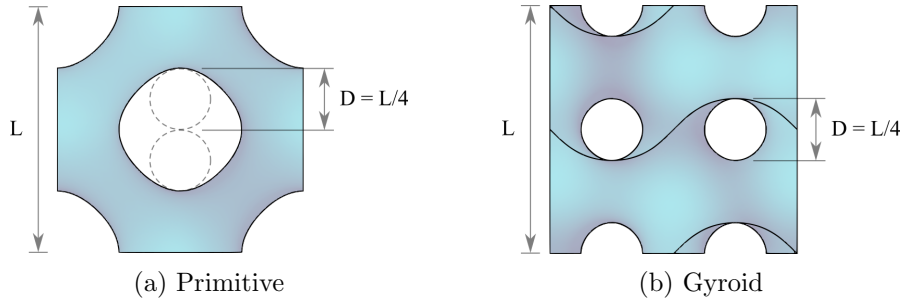


Figure 3.28: TPMS shape lateral projection.

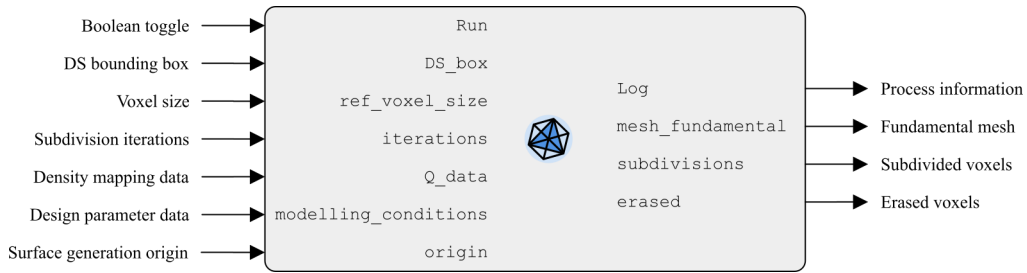


Figure 3.29: TPMS Mesh Generator GH component overview.

Then, a process of voxel refinement is considered in order to iteratively subdivide the voxels located near the fundamental shape and clean unnecessary voxels entities. The identification of effective voxels is done by analysing the sign change of their corner values. Recalling the scalar field characteristics, a sign change between points (in this case opposing corners) dictates the presence of an interface between inside and outer surface regions. Lastly, the refined voxel cloud is run through the MT algorithm in charge of the creation of the triangular facets to represent the shape. Further details of this process are discussed next.

GH component implementation

The fundamental shape generation process is performed by the **TPMS Mesh Generator** component shown in Figure 3.29. The component receives the DS bounding box on `DS_box`, an initial voxel size and number of subdivision iterations on `ref_voxel_size` and `iterations`, respectively, the results from the density mapping procedure on `Q_data`, the `modelling_conditions` defined by the parameter mapping component, and the `origin` for surface generation.

The component outputs the fundamental shape mesh generated by the adapted MT algorithm on `mesh_fundamental`, as well as general information for the generated voxel sizes (initial and refined) on the process' `Log`. The subdivided and erased voxel entities, `subdivisions` and `erased`, respectively, are output as a `Voxel` data class for process control. An additional component named `Voxel_Visualizer` was implemented to visualize these voxel data, and can be consulted in section A.3.

When `Run` is set to `False`, the component performs a set of initial preparatory operations of input verification and user feedback for the initial voxel size and calculated number of voxel subdivision iterations.

The component starts with a verification of the `ref_voxel_size`, which should be less than half the minimum value from the length map data. This maximum limit was

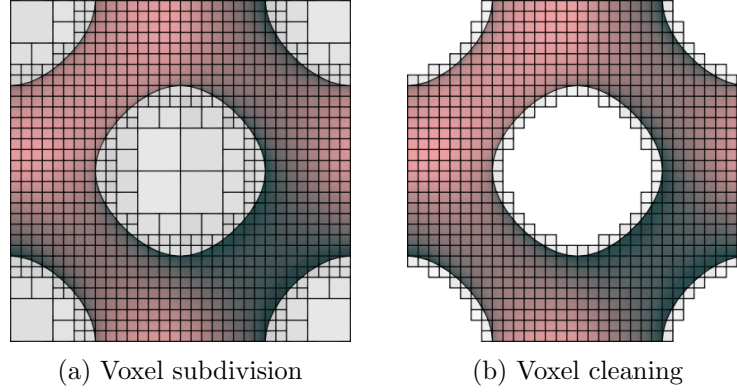


Figure 3.30: Voxel cloud processing.

defined by controlling initial voxel sizes for the generation of constant thickness unit-cells, as bigger values does not permit a correct shape generation. If `ref_voxel_size` surpasses the $size_{max}$ condition, a **RunTime Error** is generated and the process is aborted.

Once verified, the `ref_voxel_size` is used to calculate the effective initial voxel size used to populate the DS bounding box by a `Initial_voxel_size` method. This effective size is required, as the process needs to fill the DS with "whole" voxels (not fractioned). Thus, the method returns the voxel *size* as an array, and the element count on x , y and z coordinates as integers.

The last preparatory operation is a calculation of the required recursive voxel subdivision iterations needed to decrease the voxel *size* under the required h (defined by Equation 3.16 and Equation 3.17). Thus, in this scenario, voxel size is established by Equation 3.18. The results of this calculation is printed on the **Log** output for user verification, along with information of the initial voxel size and total element count.

$$size_{control} = h = \frac{\min(L_{map})}{4} \sin\left(\frac{15}{2}\right) \quad (3.18)$$

Once **Run** is set to **True**, the component starts the meshing process by running a `Voxel_cloud` method to populate the DS bounding box limits with `Voxel` data classes. `Voxel` stores information of the voxel corner points and the TPMS function evaluation results at each vertex, calculated by an internal `Evaluate` method. Thus, `Voxel_cloud` performs these calculations by using an internal `Desing` class formed by the data from `Q_data` and `modelling_conditions`.

The generated $voxel_{list}$ is then subdivided depending on the number of iterations and a threshold value by using a `Voxel_subdivision` method. In this case, the *threshold* value set to 0.01. If the multiplication of a pair of voxel corner values is less than the threshold, the voxel is considered to be sufficiently close to the TPMS shape, and thus subdivided in octants. Otherwise, the voxel is kept with the original size. This process is illustrated in Figure 3.30a.

Inside `Voxel_subdivision`, a `Voxel_cleaning` method is executed last to erase subdivided voxels that do not meet the *threshold* requirements, as depicted by Figure 3.30b. This method is also considered when `iterations` is set to 0. The subdivided list of voxels $refined_{list}$ is then used on a `Isosurfacr` method running the MT algorithm to create the fundamental mesh. A summary of the component process can be consulted in Algorithm A.1.3.

3.2.5 Pattern Surfaces Creation

Process details

In contrast to the last step for fundamental shape generation, the required voxel size for the pattern surfaces creation by SDF offset should both permit a good representation of the surface curvature, and be sufficiently small to detect the thickness of the pattern. Therefore, a corrected radius value is established by R_{SDF} (Equation 3.19), which considers the reduction of the projected diameters due to the addition of d thickness. Ultimately, the voxel size is defined as the minimum between the corrected h^* (Equation 3.20), and half the minimum thickness to be modelled.

$$R_{SDF} = \frac{1}{2} \left(\frac{L}{4} - d \right) \quad (3.19)$$

$$h^* = 2R_{SDF} \sin \left(\frac{15}{2} \right) \quad (3.20)$$

Similarly to the fundamental shape generation method, a first iteration of the DS voxel representation is obtained from an initial target voxel size. However, voxel corner's values store the distance from their location to the fundamental shape STL mesh defined in the previous design stage. This process of assigning the corresponding distance values to each voxel's corner is represented as the Mesh to SDF process in Figure 3.22.

The DS voxelization is then adjusted depending the interpolated thickness values at the voxel's corners. Thus, the offset of a SDF is found by simply adding or subtracting half the local thickness. The process concludes by running the MT algorithm with the (inner and outer) offset SDF to create the STL meshes of the pattern surfaces.

GH component implementation

The `SDF_Offset` component, shown in Figure 3.31, performs the creation of the solid TPMS pattern mesh, following the procedure of subsection 3.2.5. Similarly to the fundamental shape generation component, this tool receives the DS bounding box, a reference voxel size, number of subdivision iterations, density map and design parameters data, in addition to the shape needed to be offset on `fundamental_mesh`.

The principal outputs, `mesh_A` and `mesh_B`, are the offset meshes reconstructed by the MT algorithm. Like the previous component, process information of the subdivided and erased voxels are also reported to the user. Lastly, the refined voxel dimensions and voxel size control information is compiled on `voxel_size`.

`SDF_offset` and `TPMS_mesh_generator` have several similarities regarding the operations flow. Thus, `Voxel` data class methods were developed to accommodate both process by taking advantage of implementation's polymorphism on C#.

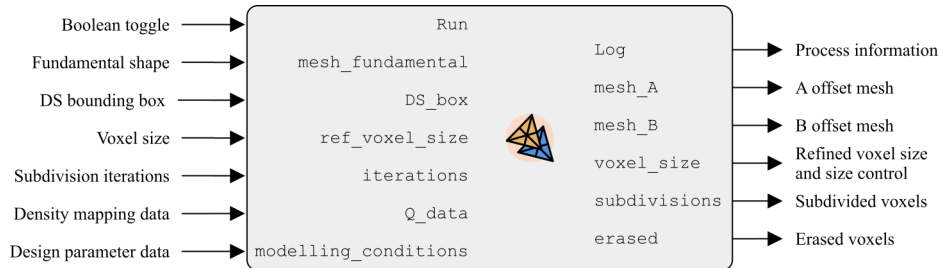


Figure 3.31: SDF Offset GH component overview.

The first difference between both processes comes at the calculation of the required h^* and number of subdivision iterations. As stated before, the effective voxel size should be sufficiently small, defined in Equation 3.21, as the minimum between h^* as a function of the radius found by Equation 3.19 and half the minimum thickness to be modelled. As before, the number of required iterations is calculated in function of recursive subdivisions needed to decrease the voxel size defined by `Initial_voxel_size` below the control value. This information is fed back to the user on the `Log`.

$$\begin{aligned} size_{control} &= \min \left(h(R_{SFD}), \frac{\min(d_{map})}{2} \right) \\ &= \min \left(\left(\frac{\min(L_{map})}{4} - \max(d_{map}) \right) \sin \left(\frac{15}{2} \right), \frac{\min(d_{map})}{2} \right) \end{aligned} \quad (3.21)$$

Once the process is activated by setting `Run` to `True`, the process runs the `Voxel_cloud` methods, with the difference that the created voxels will have the distance of each corner to the fundamental mesh, calculated by an internal `Signed_distance` method.

The voxel cloud is then refined and cleaned by the `Voxel_subdivision` and `Voxel_cleaning` methods. However, in this case, the *threshold* value is set to the maximum thickness to be modelled, thus ignoring voxels that are not part of the offset surfaces. Once refined, the voxel list is fed to a `SDF_offset` method, in which each voxel corner is adjusted depending on the required local thickness, according to the SDF property defined in Equation 3.22.

$$\forall field_{values} \text{ in } SDF_{field}, field_{offset} = field_{values} - d_{local} \quad (3.22)$$

Two offset fields are obtained, for both projections along and contrary to the mesh normals. These two fields are then separately run through the `Isosurfacers` method to obtain the `mesh_A` and `mesh_B` outputs. The summarized component pseudocode is available in Algorithm A.1.4.

3.2.6 Boundary Boolean Operations

The files generated by the process described in subsection 3.2.5 are open STL meshes representing the inner and outer surfaces of the graded TPMS pattern. To close these surfaces, boundary mesh boolean operations between the surfaces and the DS bounding box or the reference solid part are needed. These process are often case-specific, and the development of a custom GH component (as in the other processes) is not a focus of this research.

However, for the development of the solid (closed) geometries presented in the following sections of this manuscript, STL processing was performed on SpaceClaim® 2020 R2 CAD suite. The process-chain involved a combination of facets clean-up and subtraction to correct potential meshing errors before computing the intersection of regions.

3.2.7 Additional developed tools as Grasshopper components

This subsection contains a brief description of additional Grasshopper® components that were developed as an extension for the main design methodology. Accordingly, `Primitive_TPMS` and `Gyroid_TPMS` are simplified component alternatives for the design of constant thickness constructs, easing the user implementation of these type of structures. on the other hand, `Density_Finder` presents an extension for the density mapping

process, mainly to be used for the control of local densities and design parameters that can potentially aid in the definition of the required deposition or trajectory characteristics during manufacturing.

Primitive and Gyroid TPMS component

In addition to the aforementioned tools, two simplified components, named `Primitive_TPMS` and `Gyroid_TPMS` (Figure 3.32a and Figure 3.32b, respectively), were developed to easily generate TPMS assemblies with constant design parameters. These components run a combined TPMS fundamental shape and SDF offset processes, as defined by subsection 3.2.4 and subsection 3.2.5.

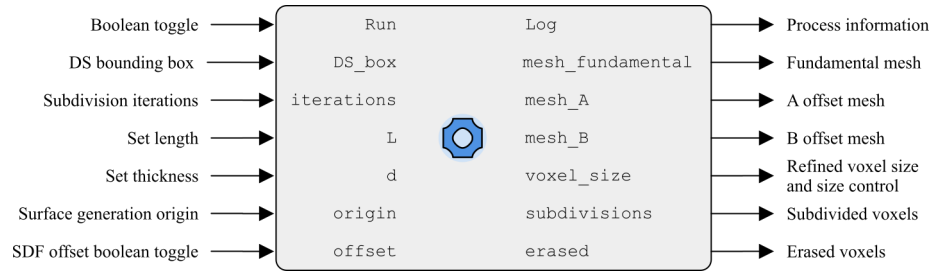
By default, the `offset` entry is set to `false`, and the component only generates the fundamental mesh when activated. If no inputs are defined, a unit-cell of $L=50\text{mm}$ and $d=2\text{mm}$ is generated from an origin point set at the centre of the origin of the global coordinate system. However, all the design parameters can be changed by the user. The simplified pseudocode of these components is detailed in Algorithm A.1.5.

Density Finder component

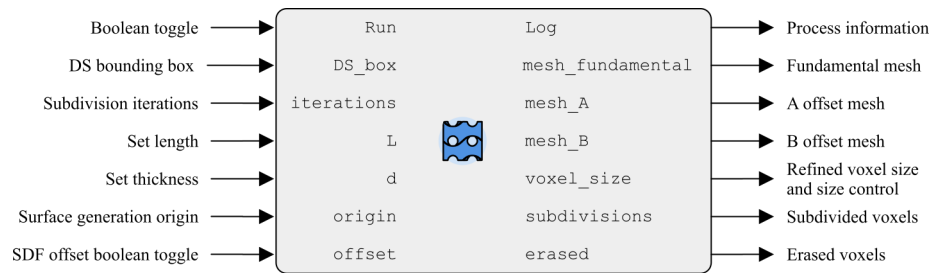
The last component to be introduced in this section is one of the main utilities components developed under the thesis framework. Accordingly, `Density_Finder` is aimed to assist the manufacturing process of graded TPMS by returning the local density in an arbitrary tool-path trajectory's position. The component, shown in Figure 3.33, receives the target trajectory point on `position` and the density mapping data `Q_data`. The variant, `Density_Finder_Plus` performs additional thickness and length calculations based on the `modelling_conditions` input.

The component outputs the local density value as a number on `Q_local` and as a `Density_Data` class on `local_Q_data`. The first output can be used in combination with an additional utility component (`Design_Parameters_Calculation`, Algorithm A.3.3) to determine the required pattern's thickness and length. The second output is aimed towards density visualization process by using `Density_Visualizer` (Algorithm A.5.1) for user verification. The Plus variation adds the functionality of `Design_Parameters_Calc` to the normal component, which can be used to adjust the machine's process parameters during manufacturing. The modified Plus variation is particularly useful in structures with simultaneously variable thickness and length. However, it can be applied under any modelling condition.

The working principle relies primarily on the utilization of `Interpolation` methods that were developed for the calculation of local thickness and lengths. Thus, depending on the input location, the local density value is interpolated by using the DM data information. It is noteworthy that the component can work with list of points, thus being able to find required values for a collection of trajectory's positions. The pseudocode of the normal component can be consulted in Algorithm A.3.1. The plus extension includes additional `Interpolation` methods to find the required local thickness and length, and is summarized in Algorithm A.3.2.



(a) Primitive TPMS GH component

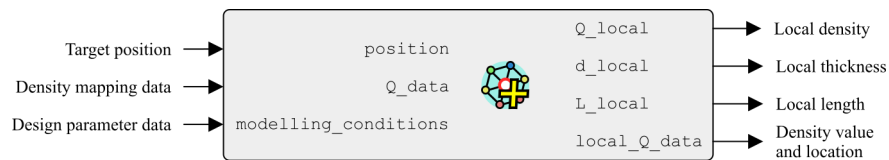


(b) Gyroid TPMS GH component

Figure 3.32: Simplified TPMS GH components overview.



(a) Density Finder



(b) Density Finder Plus

Figure 3.33: Density Finder utility GH components overview.

3.3 Modelling tests from a three-dimensional density distribution

The methodology was evaluated on a cubic design space of 100x100x100mm, considering a coordinate system located at the centre of the cube. A three-dimensional density distribution on (x, y, z) , as represented in Figure 3.34 by eight corner values between 0.15 (15%) and 0.50 (50%), is used for developing the patterns with variable design parameters. The distribution is formed by two linear density gradients in the x and y direction, for the bottom and the top faces, respectively, thus resulting in a three-dimensional distribution inside the DS.

Variable thickness tests

Variable thickness modelling scenarios were developed with a constant L of 25mm. As shown in Figure 3.35, the process is able to generate the gradual change of thickness inside the design space, while maintaining the unit-cell length. For both cases of Primitive and Gyroid patterns, the thickness variation is represented by the colour-gradient images of the central surface. These types of solutions with variable thickness are beneficial in applications where the size of unit-cell is set a-priori, such as in the development of metamaterials or regular scaffolding. For WAAM, variable thickness walls can be obtained by controlling the material deposition parameters of the weld beads.

Variable length tests

Variable length models consider a constant d of 3mm for the calculation of L values. As stated before, when applying variable length conditions, the boundaries of a unit-cell are deformed as the length varies, as evidenced by the patterns presented in Figure 3.36. Similarly to the previous examples, the length variation inside the design space is represented by the colour-gradient images of the central surface. Particularly, as Primitive pattern's unit-cells are connected by their bounding box faces, length variations in the external boundaries of the design space can present surface projections with no convergence between them. This characteristic is visible on the superior front edge of Figure 3.36a. In contrast, Gyroid patterns tend to connect the surfaces between different faces of the external boundaries of the design space. In general, length variation constructs are aimed towards AM applications where the thickness needs to be set to a constant value, such as in their implementation on uniform single-bead walls for WAAM.

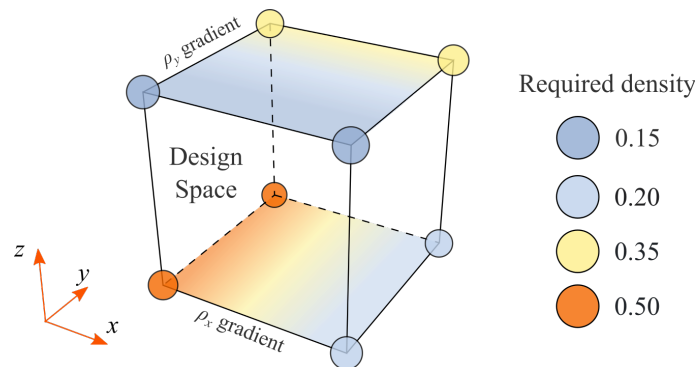


Figure 3.34: Density distribution test on (x, y, z) .

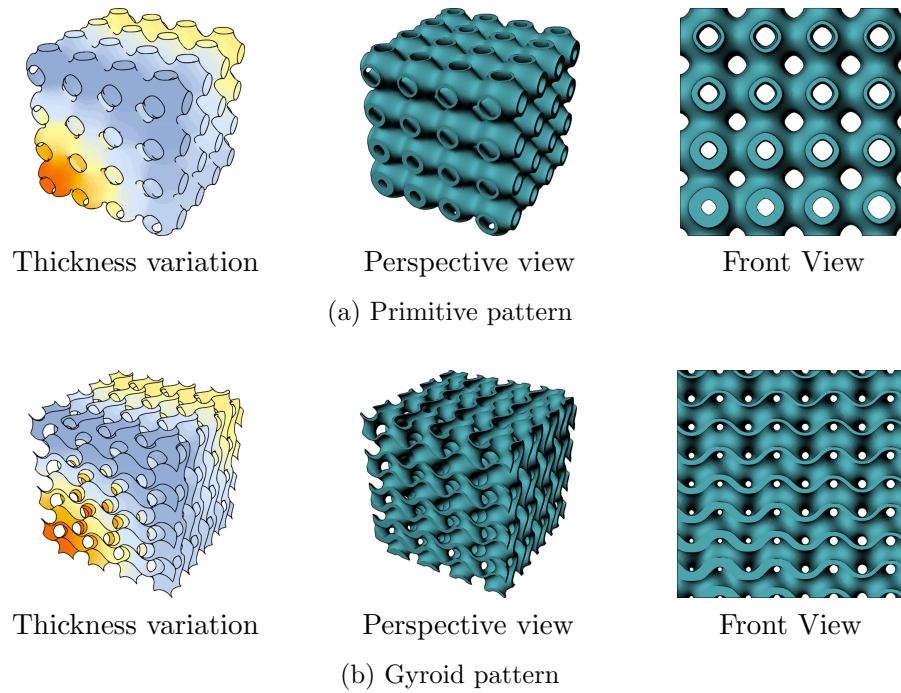


Figure 3.35: Variable thickness tests from a (x, y, z) density distribution.

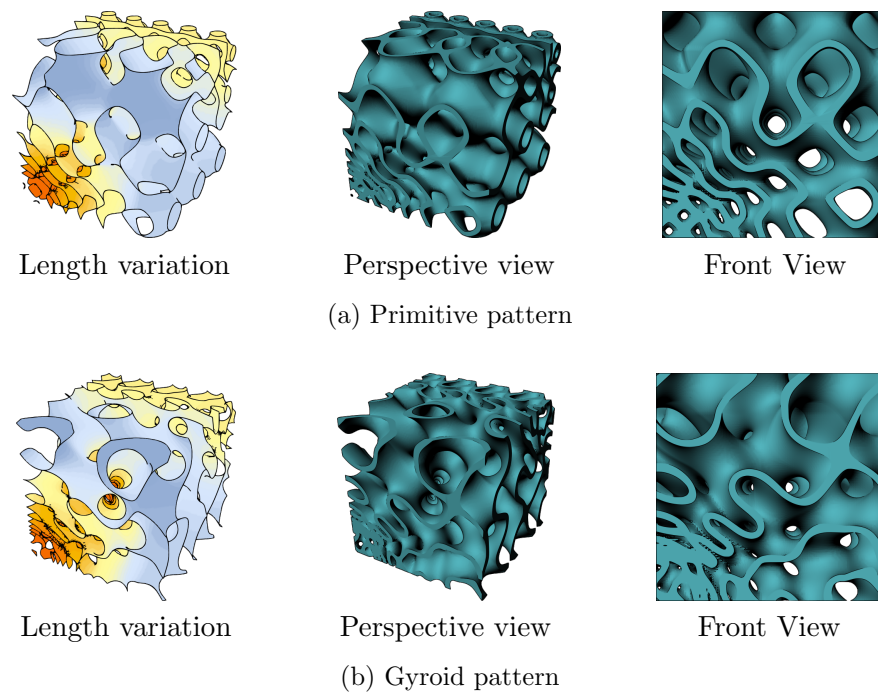


Figure 3.36: Variable length tests from a (x, y, z) density distribution.

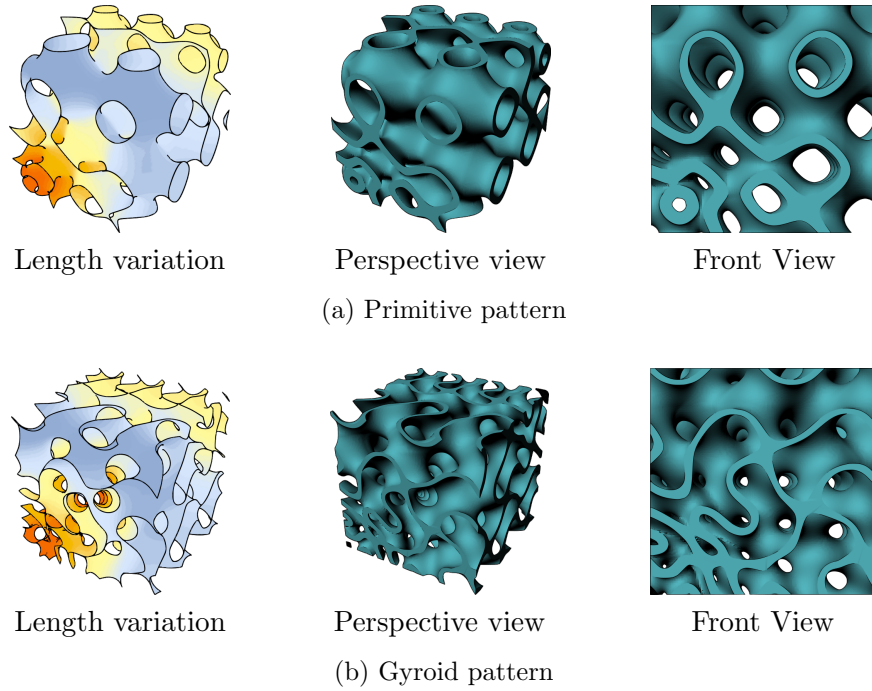


Figure 3.37: Variable thickness-to-length ratio tests from a (x, y, z) density distribution.

Table 3.3: Design parameter values range from different modelling methodologies.

TPMS	Modelling type	d [mm]	L [mm]
Primitive	Variable thickness	1.59 to 5.58	25.00
	Variable length	3.00	13.45 to 46.91
	Variable ratio	3.20 to 5.58	25.00 to 50.00
Gyroid	Variable thickness	1.22 to 4.24	25.00
	Variable length	3.00	17.69 to 61.44
	Variable ratio	2.44 to 4.24	25.00 to 50.00

Variable thickness-to-length ratio tests

For the variable ratio scenarios a length range between 25 to 50mm was used to generate the models depicted in Figure 3.37. As depicted by the top section of Figure 3.37a, the inclusion of the length limits permit to control the divergence of the surface, compared to the results in Figure 3.36a.

3.3.1 Comparison of example's design parameters

Table 3.3 summarizes the design parameters calculated in the diverse graded modelling methods from the density distribution defined in Figure 3.34. Tabulated values correspond to minimum and maximum results found at the lower and upper density limits of 0.15 and 0.50, respectively. As expected, the calculated parameter in only thickness or length variation is directly influenced by the range of density variation needed. In contrast, by defining a range of lengths in the thickness-to-length ratio variation the corresponding thickness range can be reduced from the reference values of pure thickness variation.

3.4 Graded density TPMS patterns conclusions

Even though commercial software alternatives have implemented the generation of TPMS topologies with graded density [Al-Ketan and Al-Rub, 2020], their processes are limited to linear density gradients. Furthermore, based on the available literature, a formal modelling procedure to develop TPMS models with variable density, while being able to control the patterns' thickness and unit-cell length in proportion to a three-dimensional density distribution, has not been established. Therefore, a design methodology is proposed for the development of graded density TPMS topologies, considering an independent or simultaneous variation on pattern's thickness and unit-cell's length. In particular, the development of length variation scenarios is a novel modelling procedure.

The main methodology, detailed in section 3.2, is based on a set of parameters defined by the designer, such as the selected TPMS type and modelling scenarios, among other design parameter conditions. Part of the design specifications considers the FEA or TO analysis of the DS to establish the optimized density distribution that better adjusts to a set of predefined loads. Due to the discrete nature of the employed mesh polygonization process used for the TPMS shape generation, this density distribution needs to be represented as a regular grid. As density point locations from FEA or TO procedures are not necessarily adjusted to a regular spacing, operations for density mapping (subsection 3.2.2) are defined for the regularization of these initial density distributions.

The remapped design distributions can then be related to the required local values of pattern's thickness and length, according to the procedures defined in subsection 3.2.3. The mapped values of design parameters, in particular lengths, are then used for the creation of the TPMS fundamental shape, according to a procedure based on a MT algorithm of mesh polygonization (subsection 3.2.4).

Literature studies on constant density structures have previously used a process of mesh's vertices projection along normal vectors to assign a thickness to central mesh representing the TPMS fundamental shape [Abueidda et al., 2019, Bobbert et al., 2017, Zhang et al., 2018]. However, during preliminary tests for variable thickness configurations using this method (section 3.1), it was found that this strategy can produce meshes with self-intersections and/or short facet edges, which are related to issues in the mesh Boolean operations for the creation of dense patterns. These mesh problems can be treated with additional mesh repair procedures. However, these processes usually require specialized software for mesh treatment, and a standardized procedure cannot be established due to the uncertain location of mesh issues.

Consequently, an alternative procedure for the projection of the model surfaces is proposed, consisting of a transformation of the fundamental shape to a scalar SDF, as detailed in subsection 3.2.5. Having the discrete field values of the distance to the surface, the inclusion of thickness is obtained by the sum of the desired half thickness value on each point of the field. The field is then re-meshed by a MT polygonization algorithm, thus potentially solving the offset mesh self-intersections.

All the process involved in the main design methodology were developed as a custom-built *BeShape* plug-in of Grasshopper[®] components for Rhinoceros[®] 7 CAD suite. Even though examples of graded densities have only been presented for Primitive and Gyroid TPMS, the process is able to handle any minimal surface shape by knowing their shape equation and relative density behaviour with respect to the pattern design parameters. Ultimately, the proposed general methodology should be used in combination with an assessment of the desired graded density TPMS, accounting for manufacturability restrictions of the employed AM technology.

Chapter 4

Analysis and evaluation of TPMS patterns

Introduction

This chapter is related to the design validation stages of the generated FGCM based on TPMS structures. The chapter starts with the analysis of TPMS as Equivalent or metamaterials, in order to determine the set of equations to relate the structure relative density to the mechanical properties, as detailed in section 4.1.

The application of the set of equations derived from the Equivalent Material Analysis is detailed in section 4.2, as well as the iterative validation methodology to be followed on the case study, a cantilever beam to be filled with a graded density TPMS structure derived from FEA, presented in section 4.3. Supporting information of the studied model modelling processes data are detailed in section D.2.

4.1 TPMS Equivalent Material analysis

This section explores the mechanical response of sheet-based Primitive and Gyroid patterns, following the previously established dependency of the relative density on the pattern thickness and unit-cell size. Patterns of different densities formed by a unit-cell and a structured assembly of cells instances are tested, under an Equivalent Material (EM) analysis framework to establish metamaterial properties, based on the process introduced in subsection 1.2.1. Thus, dimensionless (relative) mechanical parameters as a function of the pattern relative density are established by FEA of the structures under compressive and shear loads.

As stated before, the Gibson-Ashby models are adapted to cellular architectures assuming a macroscopic isotropic behaviour. Previous studies have determined that sheet-based Gyroid unit-cells have a structure close to isotropy [Li et al., 2019]. However, Primitive patterns may present the same Young modulus value along x , y and z axes due to their structural configuration, but the elastic behaviour of the macroscopic solid may not be isotropic (similarly to results on face centred cubic structures [Refai et al., 2020]). Based on these premises, the following sections serves as a first approach for establishing scaling laws to predict the mechanical response of the studied patterns. A more rigorous procedure for the mechanical properties determination is discussed on Appendix B.

Ultimately, the derived scaling law equations for Primitive and Gyroid patterns relative parameters can be used to relate the results of stress and deformation from FEA procedures

to a mapped density distribution for the development of Functionally Graded Cellular Materials (FGCM), as denoted by the density mapping subprocesses of Figure 3.22.

4.1.1 Finite Element modelling conditions

To establish the metamaterial properties, Finite Element analysis were conducted on shell models of a single unit-cell and an arrangement of TPMS patterns meshed by SHELL181 elements with constant thickness values using Ansys® Academic Research Mechanical, Release 2020 R2. The FE meshing was obtained by a `Mesh_to_SHELL_FE` utility component, which is detailed in section 4.2.3.

Primitive and Gyroid patterns were tested under compression and shear loads. For the unit-cell scenario, models were simulated under Periodic Boundary Conditions (PBC) for uniaxial loading and simple shear. The application of PBCs aims to relate the displacement of one face of the unit-cell to the displacements of its immediate neighbours, due to the translational symmetries existing on a cellular construct considering a simple cubic packaging [Li and Wongsto, 2004, Li, 2008]. For the following analysis, the applied PBCs are simplified in Equation 4.1 and Equation 4.2 for uniaxial displacement and shear loading, respectively, on a unit-cell of size $L_x \times L_y \times L_z$ defined in the domain $x_0 < x < x_L$, $y_0 < y < y_L$ and $z_0 < z < z_L$. From the equations, unconstrained coordinates are set as free. Traction boundary conditions are not considered, as their requirement is satisfied during the finite element process [Li and Wongsto, 2004].

PBCs of translational symmetric unit-cells for uniaxial displacement:

$$u_{x_0}\mathbf{i} = u_{x_L}\mathbf{i} \quad u_{y_0}\mathbf{j} = u_{y_L}\mathbf{j} \quad u_{z_0} - u_{z_L} = u\mathbf{k} \quad (4.1)$$

PBCs of translational symmetric unit-cells for shear loading:

$$u_{x_0} = u_{x_L} = 0\mathbf{j} + 0\mathbf{k} \quad u_{y_0} = u_{y_L} = 0\mathbf{j} \quad u_{z_0} - u_{z_L} = -u\mathbf{i} + 0\mathbf{k} \quad (4.2)$$

The pattern assembly case considers an arrangement of 64 unit-cells in a 4x4x4 distribution under mixed boundary conditions [Jia et al., 2020]. This testing element quantity for assemblies was previously deemed acceptable for mechanical response prediction, due to their good compromise between results convergence and computing times [Maskery et al., 2018a,b, Yin et al., 2020]. The employed boundary conditions are depicted in Figure 4.1 for a Primitive unit-cell and a matrix assembly of patterns. The displacements at u_{z_0} were constrained to prevent rigid body translations.

For the unit-cell scenarios, constraint equations were applied in opposite faces to guarantee the PBCs. Additional constraints were added to edge and corner vertices on Gyroid unit-cells to account for the effects of adjacent boundaries. These conditions were not considered on Primitive cases due to their topology characteristics. FE simulations considered an isotropic material with a Young modulus $E_0=200\text{GPa}$, a Shear modulus $G_0=76.92\text{GPa}$ and a Poisson's ratio $\nu_0=0.3$. A displacement u with a magnitude of 0.01mm was applied on the top surface of the patterns, according to the defined boundary conditions, to account for elastic responses only. The reaction force F_R at the applied displacement and the von-Mises stress σ were obtained from the simulation results and employed for the determination of the equivalent mechanical properties.

The Gibson-Ashby model coefficients were determined from a set of Primitive unit-cells and matrix arrangements patterns with a relative density range between 0.094 and 0.473 (9.4% to 47.3%), and Gyroid structures for a range between 0.124 and 0.624 (12.4% to 62.4%). These density ranges correspond to cells with a (constant) thickness between 2 and 10mm for a unit-cell size (length) of 50mm.

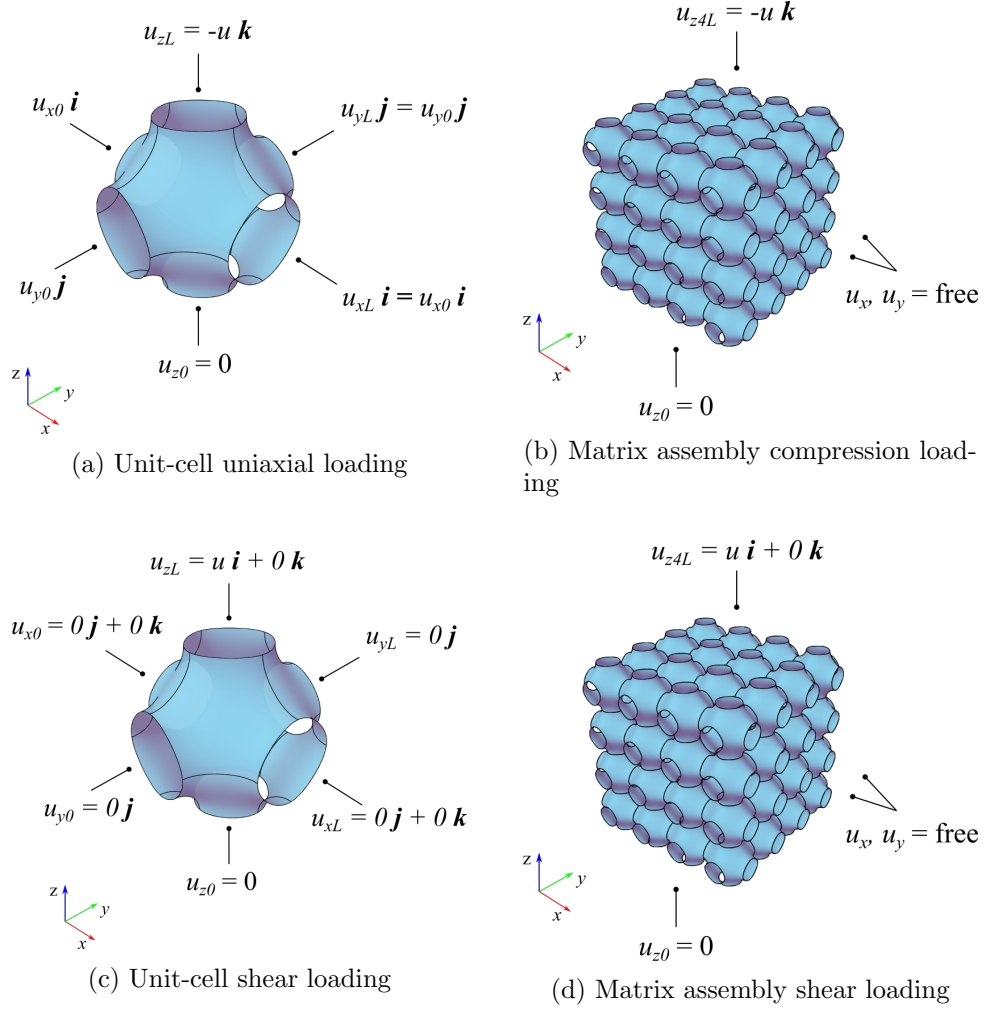


Figure 4.1: Boundary conditions for Primitive TPMS FE simulation.

Table 4.1: Gibson-Ashby model's coefficients for uniaxial compression testing scenarios.

Test conditions	ρ^* range	E^*		σ^*	
		c_1	n_1	c_3	n_3
Primitive patterns					
Unit-cell	(0.094 – 0.471)	0.478	1.190	0.487	1.135
4x4x4 assembly	(0.095 – 0.473)	0.371	1.415	0.289	1.225
Ranges from literature	(0.02 – 0.50)	(0.107 – 0.61)	(1.12 – 1.89)	(0.794 – 2.67)	(1.36 – 2.23)
Gyroid patterns					
Unit-cell	(0.124 – 0.619)	0.413	1.351	0.432	1.679
4x4x4 assembly	(0.125 – 0.624)	0.402	1.176	0.426	1.537
Ranges from literature	(0.02 – 0.49)	(0.103 – 1.14)	(1.10 – 2.23)	(0.44 – 2.74)	(1.24 – 2.10)

4.1.2 Metamaterial properties for uniaxial compression loads

The mechanical properties derived from uniaxial loads are defined by the Gibson-Ashby models for relative Young modulus E^* (Equation 1.2) and relative Strength under compression σ^* (Equation 1.4). FEA results for uniaxial compression are shown in Figure 4.2. The red curves correspond to the results from the analysis of single unit-cell and the 4x4x4 matrix assemblies under the modelling conditions defined in subsection 4.1.1. These results are contrasted with literature studies under similar conditions, as previously detailed in Table 1.5.

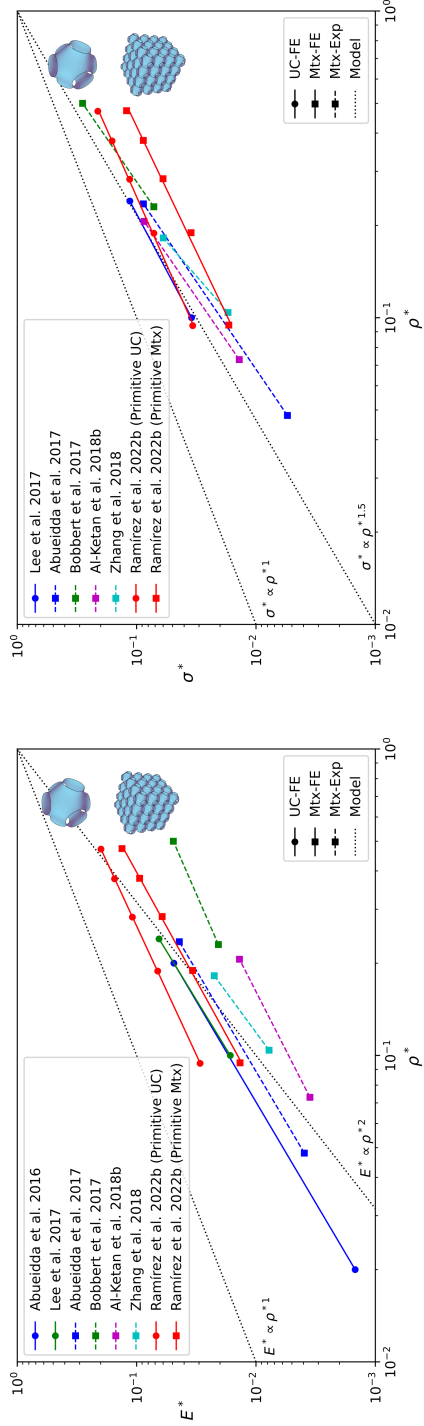
In Figure 4.2, curves from FE results are depicted as solid lines, while results from reference experimental testing are depicted by dashed lines. Results from tests on unit-cells (UC) are represented by circular markers and results from matrix arrangements (Mtx) are marked by squares. Curves for the theoretical maximum coefficients from the Gibson-Ashby model are represented by dotted lines, analogous to stretch and bending-dominated deformation mechanisms, as defined by Equation 1.6 and Equation 1.7, respectively. The power-law model's coefficients from the fitted data are summarized in Table 4.1.

It is important to note that the relative elastic modulus on unit-cells was determined from the use of PBCs, in contrast with the employment of mixed boundary conditions found in some studies [Lee et al., 2017]. The latter approach establishes the periodic condition by assigning one side of the unit-cell interface with no displacement to simulate the contact with a neighbouring cell, while considering that the opposing face has no applied stresses, in addition to the load considerations. In contrast, the employed PBCs matches the deformation reaction in opposing sides of the unit-cell, thus adding an additional degree of constraint.

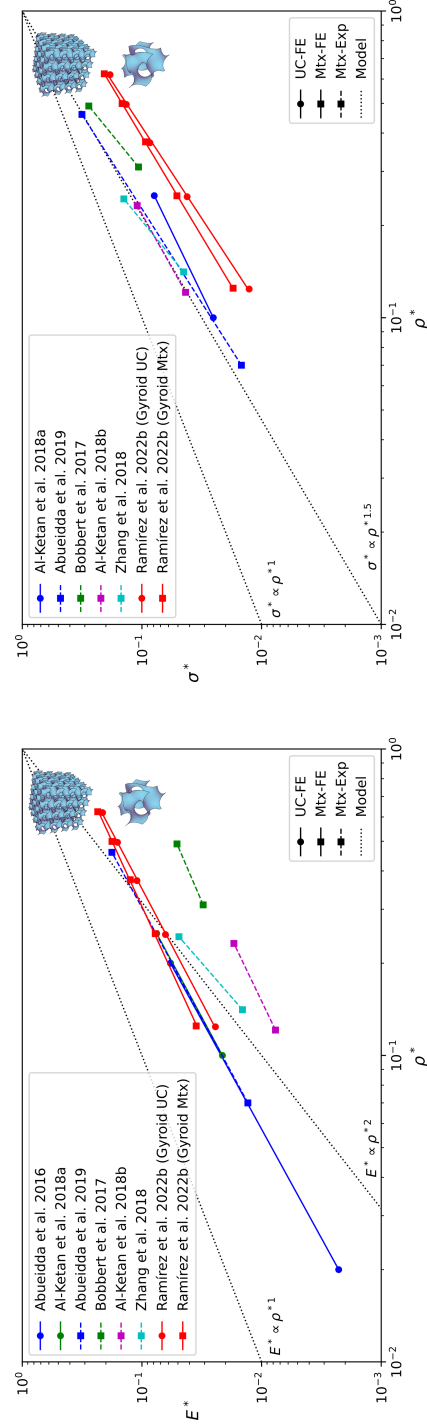
Overall results present a good agreement with the Gibson-Ashby model. As depicted in Figure 4.2a for Primitive patterns, unit-cell results for E^* showed a stretch-dominated characteristic ($n_1=1.190$), while the 4x4x4 arrangement simulation evidenced a behaviour slightly leading to a bending-dominated mechanical response ($n_1=1.415$) similar to previous experimental results on matrix assemblies. In addition, σ^* responses, shown in Figure 4.2b presents a stretch-dominated behaviour for both unit-cell ($n_3=1.135$) and the 4x4x4 assembly ($n_3=1.225$). Gyroid unit-cell and 4x4x4 matrix assembly results show a stretch-dominated deformation behaviour for the relative elastic modulus (Figure 4.2c, $n_1=1.351$ and $n_1=1.176$, respectively), while presenting a bending-dominating behaviour for relative strength in compression scenarios (Figure 4.2d, $n_3=1.679$ and $n_3=1.537$ for UC and Mtx, respectively).

The comparison between the obtained FE simulation of 4x4x4 arrangements and unit-cell results are consistent with differences observed between experimental testing on patterns' assemblies and unit-cell FE simulation of past studies. For Primitive matrix assem-

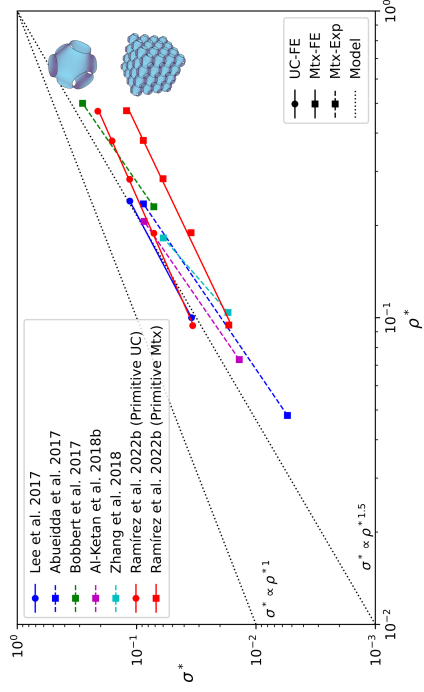
blies, the value of c tends to be lower than the results obtained for unit-cells. In contrast, a good concordance between unit-cell simulation and matrix assemblies' compression experimental results have been previously established for Gyroid patterns, and was also found in the reported FEA results. As stated before, the c coefficient accounts for the interconnectivity of the patterns. The particular shape of Gyroid TPMS can potentially explain the better correlation between unit-cell and assemblies results, as their unit-cells have a higher degree of connections with neighbour cells, and, by extension, a better interaction of constraints when applying PBCs.



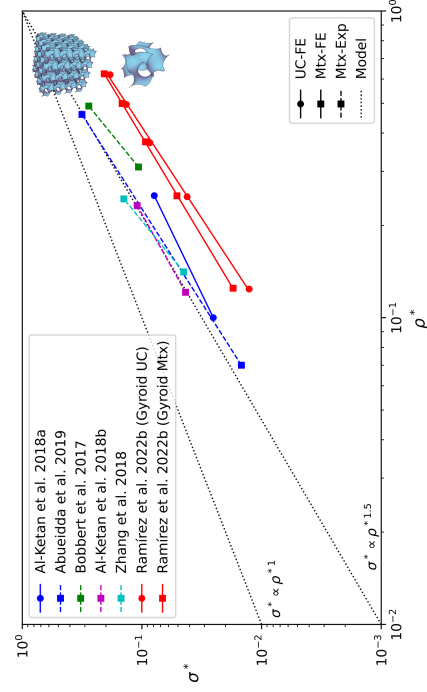
(a) Primitive: Relative Elastic modulus



(c) Gyroid: Relative Elastic modulus



(b) Primitive: Relative Strength in compression



(d) Gyroid: Relative Strength in compression

Figure 4.2: Uniaxial compression results.

Table 4.2: Gibson-Ashby model's coefficients shear testing scenarios.

Test conditions	ρ^* range	G^*		τ^*	
		c_2	n_2	c_4	n_4
Primitive patterns					
Unit-cell	(0.094 – 0.471)	0.206	1.110	0.283	1.537
4x4x4 assembly	(0.095 – 0.473)	0.120	1.223	0.133	1.530
Ranges from literature	(0.02 – 0.24)	(0.16 – 0.16)	(0.97 – 0.974)	(0.256)	(0.98)
Gyroid patterns					
Unit-cell	(0.124 – 0.619)	0.195	1.237	0.239	1.277
4x4x4 assembly	(0.125 – 0.624)	0.118	1.213	0.161	1.193
Ranges from literature	(0.02 – 0.20)	(0.305)	(1.531)	-	-

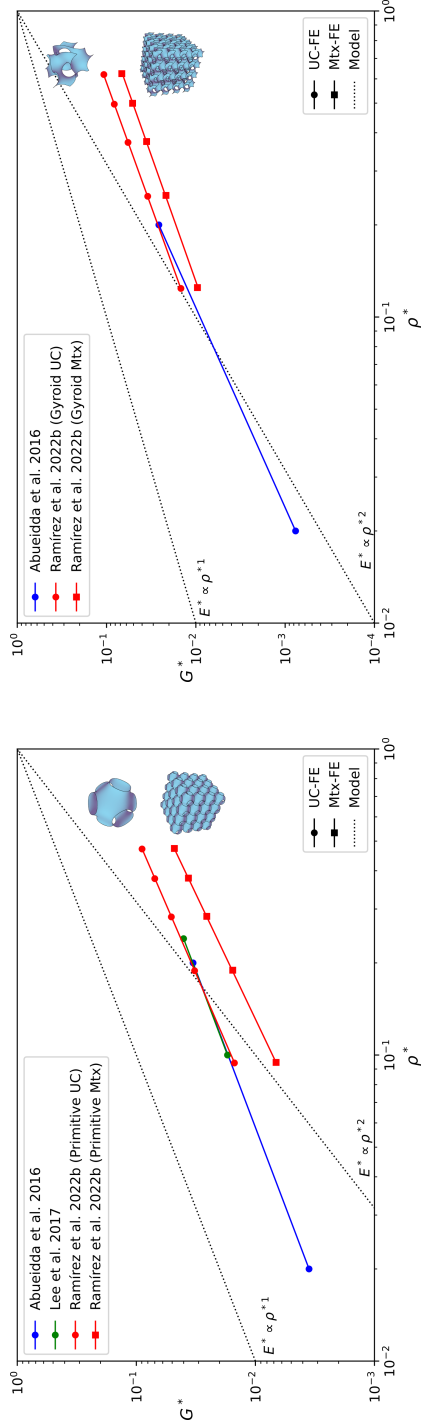
The absence of data is indicated by “-”.

4.1.3 Metamaterial properties under shear loads

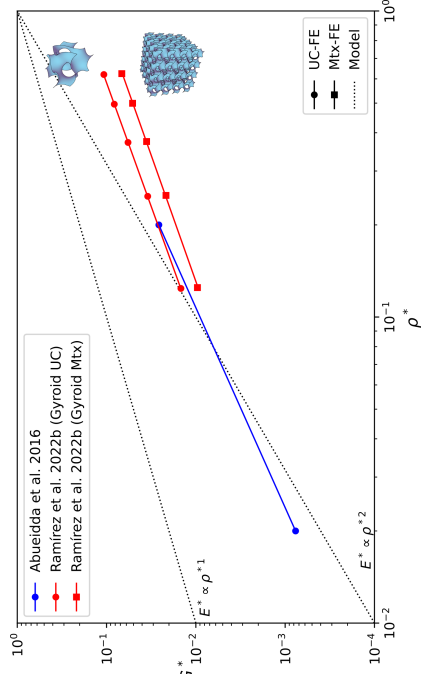
Primitive and Gyroid models were tested under shear loads by following the boundary conditions defined in Figure 4.1. FEA results are shown in Figure 4.3 following the previously established curves' representation convention. The red curves in Figure 4.3a and Figure 4.3b correspond to the results from the process described in subsection 4.1.1, and are contrasted with the available literature results, represented by the blue and green curves. In contrast, both red and blue curves on Figure 4.3c, representing the relative strength in compression response of Primitive and Gyroid patterns, respectively, correspond to new results that have not been established in the current literature. The summary for the determined model's coefficients are reported in Table 4.2.

Primitive patterns showed a stretch-dominated behaviour for relative shear modulus on both unit-cell ($n_2=1.110$) and matrix assembly ($n_2=1.223$) testing, as illustrated in Figure 4.3a. Similarly, Gyroid pattern's results (Figure 4.3b) showed stretch-dominated behaviour for unit-cells ($n_2=1.237$) and matrix ($n_2=1.213$). For relative strength under shear loads (Figure 4.3c), Primitive unit-cell and matrix ($n_4=1.537$ and $n_4=1.530$, respectively) evidenced a bending-dominated deformation behaviour, indicating that Primitive TPMS deform under a combination of stretch and bending mechanisms under shear. In contrast, Gyroid unit-cell ($n_4=1.277$) and matrix ($n_4=1.193$) results for relative strength under shear indicate a stretch-dominated behaviour.

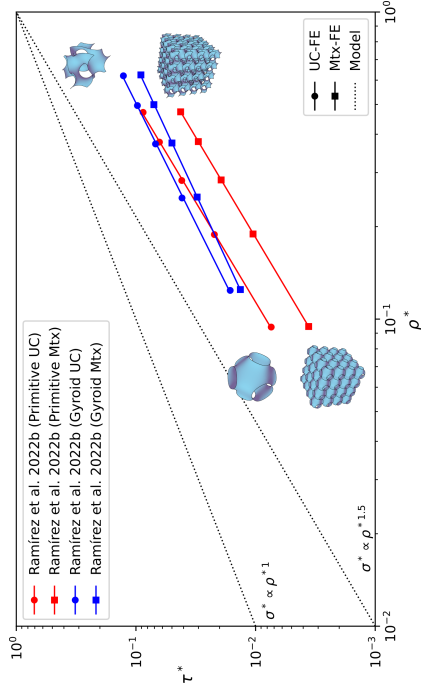
Similar to compression results, there is a difference in the c values obtained for Primitive and Gyroid patterns' unit-cells and matrix assemblies. However, there is no information available in the literature for this characteristic under shear loads to establish a comparison. For the reported results, all testing scenarios showed a decrease on c for matrix assemblies.



(a) Primitive: Relative Shear modulus



(b) Gyroid: Relative Shear modulus



(c) Relative Strength in shear

Figure 4.3: Shear load results.

4.1.4 Equivalent Material analysis conclusions

The mechanical response under compression and shear loads of Primitive and Gyroid TPMS was determined under a framework of Equivalent material. For compression scenarios, the relative elastic modulus and shear modulus of both Primitive and Gyroid pattern exhibited a stretch-dominated deformation behaviour, thus validating their employment in lightweight structural applications, where high stiffness and strength values are favoured over energy-absorption characteristics.

For Primitive patterns, unit-cell results estimate a higher resistance than the response obtained by the simulation of the matrix arrangement of patterns. In contrast, Gyroid results present a better agreement between the two simulation scenarios. These effects are consistent with previous studies on FEA of unit-cells and experimental testing of patterns arrangements under compression loads. The same effect was found for the finite element simulation of the patterns under shear loads, which has not been previously determined on the literature.

The derived equations of relative mechanical properties as a function of the relative density can be used for the developing of FGCM based on TPMS with variable density. As FGCM are related to an ordered arrangement of cellular structures, model's results for relative elastic modulus and strength in compression from matrix assemblies' simulations are considered for the determination of local densities from deformation or stress mappings.

The results obtained were published as a congress paper [Ramírez et al., 2022b]. In summary, FEA of Primitive TPMS patterns' arrangements exhibited a scaling by $0.371\rho^{*1.415}$ for E^* and a scaling by $0.289\rho^{*1.225}$ for σ^* in a density range between 0.095 and 0.473, according to the Gibson-Ashby model for mechanic properties of cellular solids. Furthermore, matrix assemblies of Gyroid patterns showed a scaling by $0.402\rho^{*1.176}$ for E^* and a scaling by $0.426\rho^{*1.537}$ for σ^* for densities between 0.125 and 0.624. In general, Gyroid TPMS on a matrix arrangement exhibit a higher stiffness than Primitive counterparts, evidenced by the results of the proportionality constant c for uniaxial compression and shear loads.

4.2 Correlation of modelling methodologies with Equivalent Material relationships

In the context of this work, the metamaterial properties defined by the EM analysis are mainly applied for the creation of a density map (DM) from FEA reference data. This density distribution is then approximated to a regular DM needed on the posterior mesh modelling operations, following the process introduced in subsection 3.2.2. As stated in subsection 1.2.1, Azman [2017] presented a method to replace a solid material by a constant-density lattice structure. However, for the determination of a density distribution from FEA, the DM needs to be formed by remapping the local density calculated from all the nodes of a FEA simulation results grid.

Even though the process detailed by Azman [2017] can calculate relative densities from the total displacement and maximum equivalent stress, the calculation of local densities is only valid for the von Mises stress results processing. The results of displacement are not directly applicable due to their accumulative nature and non-linear determination, and their integration is out of the current scope of the project.

Therefore, as established by the design methodology in Figure 3.22, the FEA of the solid CAD model will create an initial map of stress constraints, which is then related to the equation of the relative strength under compression σ^* parameters defined in section 4.1

for the calculation of the local relative densities ρ^* . This section establishes the set of custom tools developed for this purposes.

4.2.1 Finite Element Analysis data processing

This subsection details the operations of two utility components, `ANSYS_fileReader` and `Equivalent_Material_coefficients`, working as an extension to the solid CAD model FEA process on the Design Specification stages. The outputs of these components are used for the calculation of local density values from the nodes of FEA results, performed by the `Relative_Density_from_FEA` component (subsection 4.2.2).

ANSYS fileReader and Equivalent Material coefficients GH components

The `ANSYS_fileReader` (Figure 4.4) is used to get the FEA data nodes positions and values from the imported analysis results as a text file. The component receives the archive `filePath` and outputs the ordered list node locations on `positions` and their respective values on `FEA_data`. The maximum value of the collection is also reported on `max_data`. In addition, the name of the file, the maximum data value and the number of nodes is reported to the user on `Log`.

The second utility component, `Equivalent_Material_Coefficients` (Figure 4.5), outputs the c , n , and permissible design restrictions on `E_parameters` and `S_parameters`. It is important to note that, although the component outputs the parameters related to the calculation of relative young modulus (`E_parameters`), their use is currently discouraged for the determination of local densities.

The `Equivalent_Material_Coefficients` works by a user selection of the Equivalent Material model to be used, as listed below:

- Equivalent material model data, as defined by Table 4.1:
 - "primitive_M4_2022": Primitive 4x4x4 assembly model data
 - "gyroid_M4_2022": Gyroid 4x4x4 assembly model data
 - "primitive_UC_2022": Primitive unit-cell model data
 - "gyroid_UC_2022": Gyroid unit-cell model data

Other legacy model's coefficients are included for reference purposes, but their use is not recommended as their determination was not subjected to the simulation considerations presented in section 4.1. The full list of models available is detailed in section A.2. The component also performs the calculation of $\rho_{E^*}^*$ and $\rho_{\sigma^*}^*$, as defined by Equation 1.10 and Equation 1.11, for a constant density modelling scenario. These results are displayed to the user on `Log`. In addition, a TPMS type tag is output for inter-component connections. The internal operations for the `ANSYS_fileReader` and `Equivalent_Material_Coefficients` components can be consulted in Algorithm A.2.1 and Algorithm A.2.2, respectively.

4.2.2 Determination of relative density from FEA results

The `Relative_Density_from_FEA` component (Figure 4.6) is the main tool for the correlation between the Equivalent Material results and the density mapping procedures from the main design methodology. This tool works with the FEA data obtained from `ANSYS_fileReader`, and the EM model coefficients and TPMS type tag from

Equivalent_Material_Coefficients. Depending on the nature of **FEA_data**, the component calculates the relative density at each node, considering the coefficients loaded on **parameters**.

To adjust the range of calculated densities, thresholds for maximum and minimum values are loaded on **Q_max** and **Q_min**. Thus, if a calculated value is outside of this defined range, the local density adopts the threshold value. This is primarily used on the identification of areas under the lower limit (minimum density), as nodes presenting small interaction with the FEA loads will tend to have a relative density close to zero, yielding surface meshing errors. If these values are incorrectly set by the user, the relative density function limits (as detailed in Table 2.4), stored on a **Density_model** internal class, are used depending on the **TPMS_ID**.

In addition to the calculated densities, the average value is also computed and shown on **Q_average**, which can potentially be employed as the external density value input for the density mapping component (section 3.2.2). Lastly, process information and the ranges of calculated densities are grouped and output to the user on **Log**. The details of the process can be consulted in Algorithm A.2.3.

4.2.3 Evaluation of graded density constructs

As previously established in Figure 3.21, the design validation process is iterative in nature. The proposed evaluation strategy consist on analysing the graded pattern adjusted to the density distribution inside the DS by a second FEA procedure.

In the case of an unsatisfactory response of the cellular construct, a process of shape and density distribution refinement and improvement is necessary. This can be accomplished by either adjusting the density ranges used on the Density Mapping (iii) procedures, or by changing the design parameters set values on the Design Parameter Mapping (iv) processes. Once the design has been validated, the process continues with the Pattern Surfaces Creation (v) and Boundary Boolean Operations (vi) to create a solid model, or outputs the generated fundamental shape STL mesh, depending on the requirements of the designer.

FEA for the proposed validation procedure requires a combination of the fundamental shape STL mesh conversion to shell FE, and the assignation of a local thickness at each node of the shell elements. For this, two additional tools were developed to create the set of instructions for FE mesh import and variable thickness assignation as Mechanical APDL (Ansys Parametric Design Language) commands on the *Static Structural* analysis from ANSYS® Workbench, Release 2020 R2. The details of these implementations as GH components are shown next.

Developed tool for STL to finite element mesh conversion

For the finite element simulation of TPMS patterns, a customized Grasshopper® component was developed to perform the creation of the FE mesh representing the surface.

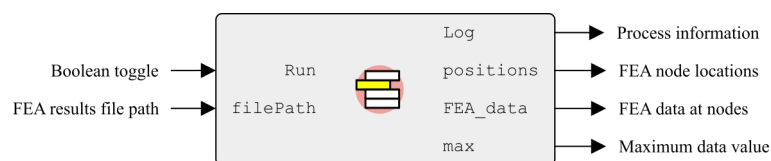


Figure 4.4: ANSYS fileReader GH component overview.

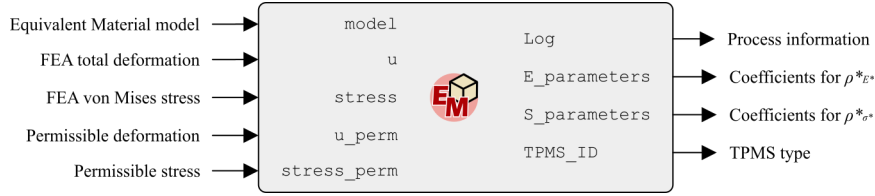


Figure 4.5: Equivalent Material coefficients GH component overview.

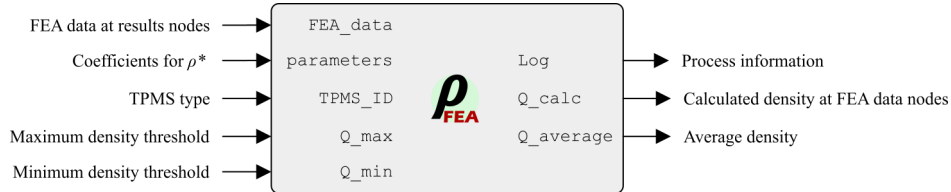


Figure 4.6: Relative Density from FEA GH component overview.

Therefore, the `Mesh_to_SHELL_FE` component, depicted in Figure 4.7, receives an arbitrary mesh on M and outputs the required node and SHELL element lists for their use in ANSYS® Mechanical APDL programming, or the required code for ANSYS® Workbench, Release 2020 R2.

As in other developed components, the process starts when `Run` is set to `True`. The input mesh nodes and faces information are collected and stored on array structures for processing. The two first outputs, `NODES` and `ELEMENTS`, produce the collection of instructions for the definition of nodes and shell finite elements, respectively, for Mechanical APDL. These outputs are generic, thus potentially being able to define any type of 4-node shell elements.

Furthermore, `WB_code` outputs the required code as a Constant Database (cdb) file to be used in Workbench (in particular Release 2020 R2). The mesh nodes and faces information are internally converted to a set of instructions defining SHELL181 FE, that can be loaded as an *External Model* to be used on *Static Structural* analysis. In addition, the component is able to autosave the Workbench code as a text file on the current GH archive directory, by using the `fileName` and `write` inputs for file naming and saving, respectively. The pseudocode detailing the internal process of this component can be consulted in Algorithm A.6.1. Even though the current component is aimed to their use on the software's 2020 release, the code outputs can be updated with a different set of header operations for their conversion to future releases.

Developed tool for assigning variable thickness to shell elements

The `Variable_thickness_ARRAY` component, shown in Figure 4.8, outputs the set of Mechanical APDL instructions to add a variable thickness value to the shell FE mesh produced by `Mesh_to_SHELL_FE`.

The component receives the fundamental shape mesh M and the density and design parameter data from previous mapping processes. When `Run` is set to `True`, the local thickness is interpolated at each vertex of the mesh by using the previous defined thickness map according to the density grid positions. The set of thicknesses is then converted to an `ARRAY` structure, which is used to hold vector data on APDL.

The complete set of instructions for loading this `ARRAY` on a *Static Structural* analysis is obtained from the `tnode` output. In addition, the optional file-save of a text file

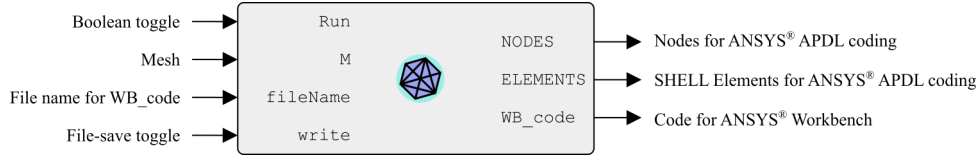


Figure 4.7: Mesh to SHELL GH component overview.



Figure 4.8: Variable Thickness ARRAY GH component overview.

containing these instructions can be done by the `file Name` and `write` entries. The details of the component processes can be consulted in Algorithm A.6.2.

Shell and solid FE simulation results comparison

To test the validity of the assignation of local thickness to shell FE meshes, a plate of 50x50mm with a thickness decrease from 5 to 3mm was modelled as both a solid file and a shell surface. As shown in Figure 4.9, the plate was tested with a load of 50N in the thinner section, with the 5mm thickness face set as fixed. Solid plate model was imported as a STEP file to ANSYS® Workbench, Release 2020 R2, while the shell surface was loaded as a Constant Database file obtained from the `Mesh_to_SHELL` GH component and the tabular thickness data from `Variable_thickness_ARRAY`.

The solid plate was meshed by SOLID186 FE, and the shell plate by SHELL181 FE. A meshing size of 1mm was used for both cases. Results for total displacement and equivalent von Mises stress are displayed in Figure 4.10 and summarized in Table 4.3. Even though shell results images (Figure 4.10c and Figure 4.10d) are displayed with a constant thickness, the thickness variation is considered during the simulation as a set of Mechanical APDL commands. The display of variable thickness shell elements is not available in the Workbench UI.

As illustrated in Figure 4.10a and Figure 4.10c, shell FE meshing present a good agreement with solid elements for total displacement results. Regarding maximum equivalent stress, shell models (Figure 4.10d) presents a difference of 2.88% compared to the solid plate results (Figure 4.10b). This can be mainly attributed to the increase of element count present on the solid FE meshing, which helps on results convergence. As shown in Figure 4.10b, the solid elements FE meshing adds additional rows of elements in the centre of the plate, which are able to predict internal stress values. Nevertheless, the approximation of results by the shell element meshing approach was deemed suitable for the evaluation of graded density TPMS structures.

Table 4.3: Plate FEA analysis results.

Case	u_{total} (mm)	σ_{eq} (MPa)	Meshing size (mm)	Elements	Nodes
Solid	2.80E-02	12.457	1.00	10200	49873
Shell	2.80E-02	12.097	1.00	2500	2601

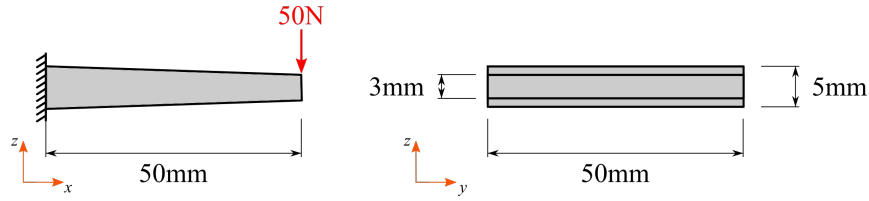
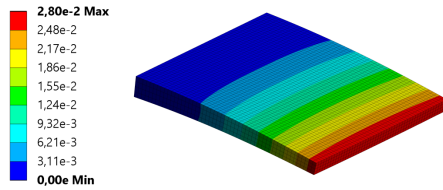
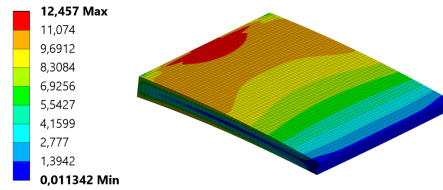


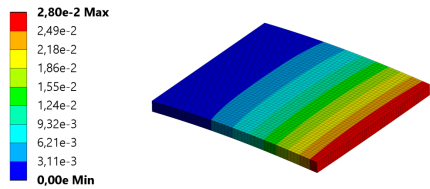
Figure 4.9: Plate dimensions and load conditions.



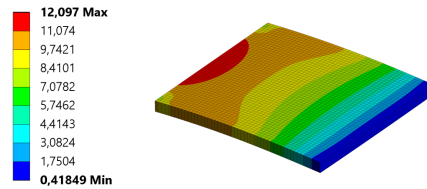
(a) Solid plate displacement results



(b) Solid plate equivalent stress results



(c) Shell plate displacement results



(d) Shell plate equivalent stress results

Figure 4.10: Uniaxial compression results.

4.3 Case study: functionally graded cantilever beam

This section contains the application of the proposed modelling methodology for the design of a cantilever beam with a variable density, represented by a functionally graded cellular construct based on the studied TPMS. Subsections are divided according to the main modelling stages. Additional support information of the modelling process, obtained from the log files of the GH components used, can be consulted in section D.2. A complementary case study illustrating the design of a C-shaped body with a graded-density Gyroid structure is detailed on Appendix C.

4.3.1 Design conditions and preliminary FEA

A cantilever beam with a length of 1500mm and a cross-sectional area of 200x300mm supporting a load of 5000N at the free-end (Figure 4.11) was used as a case study for the proposed methodology. The beam is assumed to be constructed with an isotropic material of $E_0=200\text{GPa}$ and a Poisson's ratio $\nu_0=0.3$. Permissible design conditions consider a maximum displacement of $u_{perm}=2\text{mm}$ on the free-end and a maximum stress of 250MPa with a security factor of $s_f=5$ ($\sigma_{perm}=50\text{MPa}$).

For this study, the density map was derived from a preliminary FEA of a solid model. A total displacement of $u_{max}=0.1413\text{mm}$ and a equivalent von Mises stress of $\sigma_{eq}=3.6705\text{MPa}$ under the required load were obtained by a FE simulation on Ansys[®] Academic Research Mechanical, Release 2020 R2. These results, depicted in Figure 4.12, were exported as a text file from the simulation software to be used as inputs in the posterior processes.

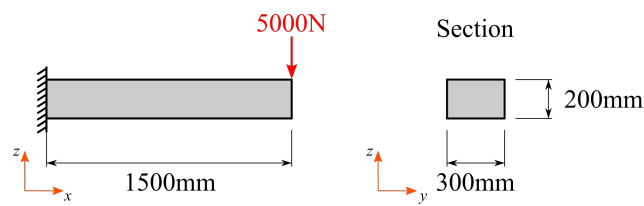
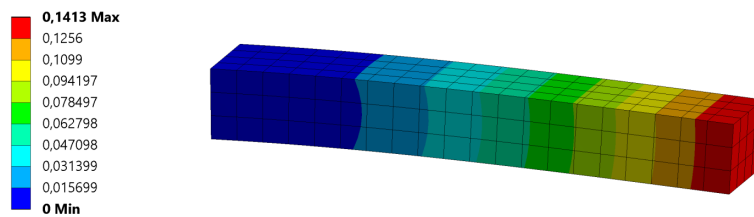
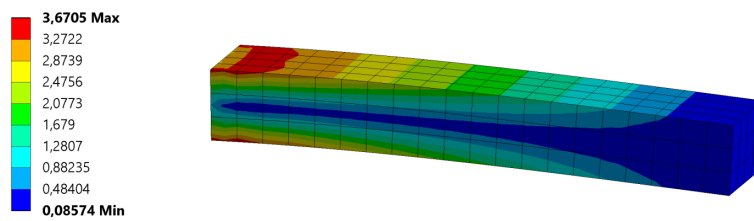


Figure 4.11: Cantilever beam dimensions and load conditions.



(a) Total displacement (mm)



(b) Equivalent stress (MPa)

Figure 4.12: Cantilever beam preliminary FEA.

4.3.2 Primitive-based cantilever

Design specifications and density mapping

The design specification process starts with the loading of the preliminary FEA of the model by using the `ANSYS_fileReader` GH component. The maximum value of the simulation results for total displacement and equivalent stress is then loaded to the `Equivalent_Material_Coefficients` component, along with the predefined permissible values. In this first calculation, the equivalent material model data is selected as `primitive_M4_2022`, corresponding to the matrix arrangement results for Primitive patterns from Table 4.1. The component performs the following calculations:

$$\rho_{E^*}^* = \left(\frac{1}{c_1} \frac{u}{u_{perm}} \right)^{\frac{1}{n_1}} = \left(\frac{1}{0.371} \frac{0.1413}{2} \right)^{\frac{1}{1.415}} = 0.310$$

$$\rho_{\sigma^*}^* = \left(\frac{1}{c_3} \frac{\sigma_{eq}}{\sigma_{perm}} \right)^{\frac{1}{n_3}} = \left(\frac{1}{0.289} \frac{3.6705}{250/5} \right)^{\frac{1}{1.225}} = 0.327$$

From this process, two reference density values are obtained: $\rho_{E^*}=0.310$ from the results of total displacement, and $\rho_{\sigma^*}=0.327$ from the equivalent stress results. Accordingly, the cantilever beam can be replaced by a constant density Primitive pattern of $\rho_{const}=0.327$, corresponding to the maximum between ρ_{E^*} and ρ_{σ^*} .

For the graded density constructs, the density map is calculated from the equivalent stress data of the preliminary FEA, and the relative strength model data obtained from the `S_parameters` output of the Equivalent Material GH component. This output contains the c_3 and n_3 coefficients to be used on the `Relative_Density_from_FEA` component running Equation 1.11. On the Primitive TPMS scenario, maximum and minimum densities of 0.50 and 0.10, respectively, were used as threshold values for the creation of the density map.

The calculated local densities from the FEA data locations is then used for the remapping of the density inside a regular grid by the `Density_Mapping` component. Accordingly, Figure 4.13 depicts a front view of the dotted representation of the density mapping process. Higher densities are represented by the bigger red dots, while the minimum density zones are depicted by the smaller blue dots. Intermediate densities are adjusted to a gradient colour and size scale. Figure 4.13a depicts a density map formed by an arrangement of 151x31x21 local density values between 0.10 and 0.325, considering a reference grid size of 10mm, used for the thickness and length variation modelling scenarios. In contrast, the variable thickness-to-length ratio model was developed from a coarser density map (31x7x5 elements between 0.10 and 0.318, Figure 4.13b) in an effort to reduce the local variability of densities that could produce excessive surface deformations. It is important to note that the maximum mapped value is slightly less than the maximum of the fed data due to the approximative nature of the process.

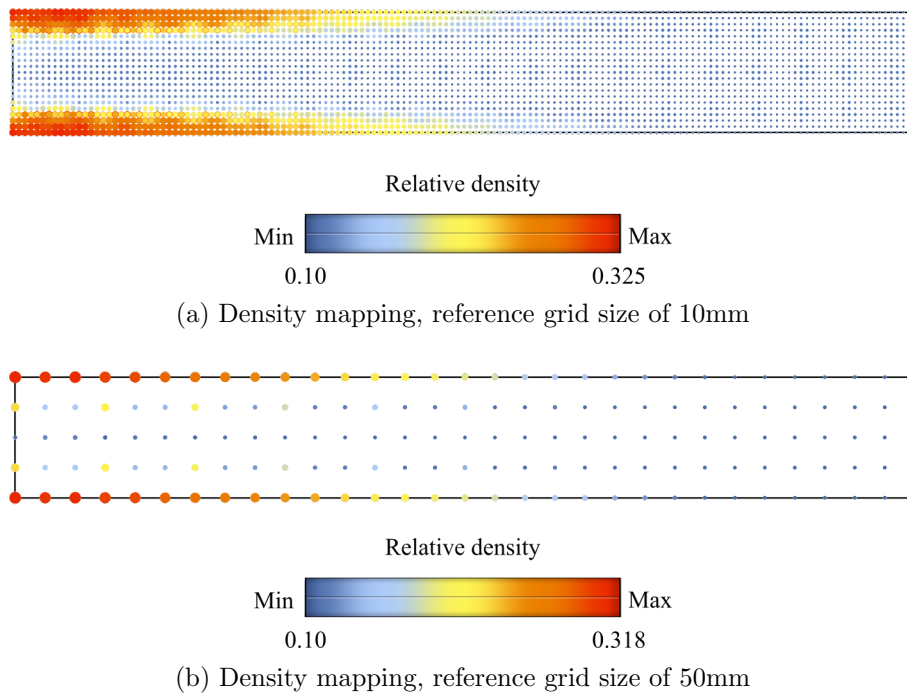


Figure 4.13: Primitive-based cantilever: Density map from preliminary FEA.

Variable thickness modelling

The graded density by variable thickness was obtained by calculating the required local thickness for a unit-cell size of $L=50\text{mm}$ by the `Densign_parameter_mapping` GH component. Accordingly, the resulting model, depicted in Figure 4.14, has a thickness range between 2.12 and 7.06mm.

The fundamental surface is obtained by setting a reference voxel size of 10mm under 3 iterative subdivisions on the `Densign_parameter_mapping`. This surface is depicted in Figure 4.14a under a gradient colour scale to represent the thickness distribution (density variation). Red zones are associated with bigger thickness values, while blue zones correspond to the minimum calculated thickness. This distribution is well adjusted to the density map (Figure 4.13) coming from the reference equivalent stress FEA data (Figure 4.12b). Due to the inclusion of the minimum density threshold (0.10) the centre and right side of the beam maintain a constant thickness value.

The model of the gradient density construct is shown in Figure 4.14b and Figure 4.14c, generated from the `SDF_Offset` GH component with a reference voxel size of 10mm and 2 voxel's subdivision iterations. Even though the GH component suggests 4 subdivision iterations, the model was generated with a smaller accuracy for demonstrative purposes. As a reminder, the current design evaluation stage does not require a closed mesh model for the simulation, just the fundamental mesh and the local mesh node's thickness.

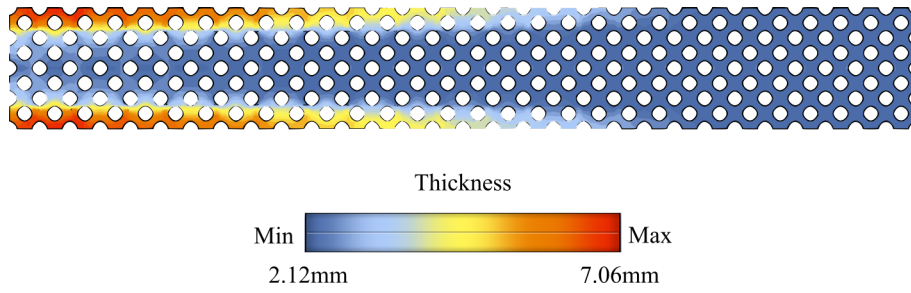
Variable length modelling

The variable length scenario was meshed for a constant thickness of $d=4\text{mm}$. The resulting fundamental mesh, shown in Figure 4.15, presents a length distribution between 28.35 and 94.26mm. This modelling case was developed only for demonstrative purposes, as the highly variance of lengths and surface discontinuities on the centre of the beam yields this model unpractical from a manufacturing point of view. The high degree of discontinuities also represents an additional challenge for the SDF offset process and final mesh treatment, reason why this case was not further evaluated.

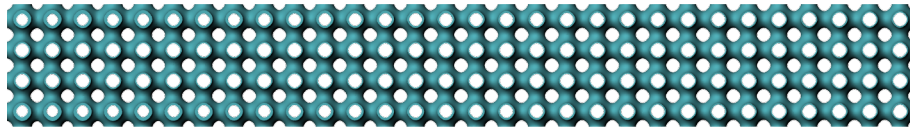
Variable thickness-to-length ratio modelling

The modelling by thickness-to-length ratio was obtained for lengths values between 40 and 50mm, thus limiting the mesh deformations found on the pure length variation scenario. This length range corresponds to thickness variations between 2.12 and 5.52mm, as obtained by the `Densign_parameter_mapping` GH component. The resulting model is shown in Figure 4.16.

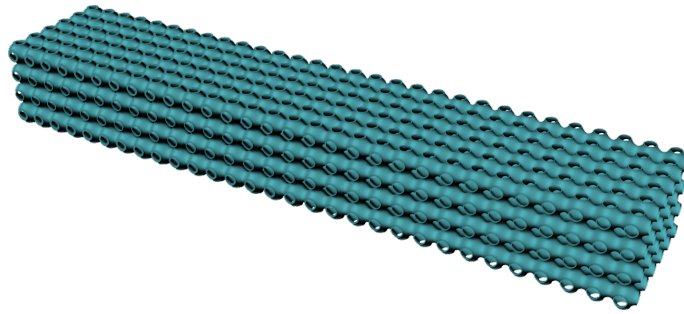
The fundamental surface, depicted in Figure 4.16a, was obtained from an initial voxel size of 8mm with 3 subdivision stages. Similarly to the thickness variation scenario, the figure depicts the thickness variation with a colour gradient, which follows the overall density map profile of Figure 4.13b. The graded density model, shown in Figure 4.14b, was generated from a voxel size of 8mm and 2 voxel's subdivision iterations.



(a) Thickness variation gradient over fundamental mesh



(b) Model front view



(c) Model perspective view

Figure 4.14: Primitive-based cantilever: Variable thickness modelling.

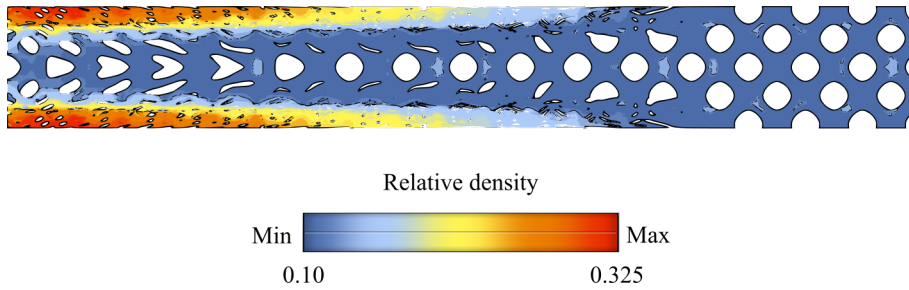
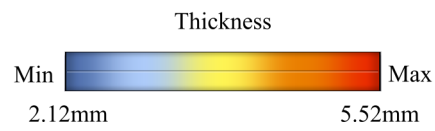
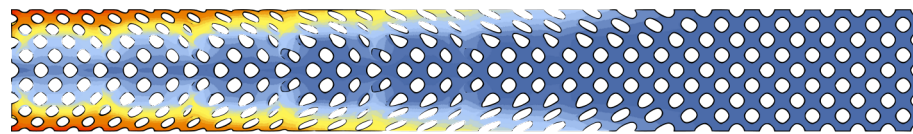
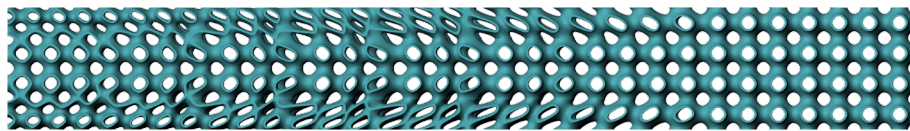


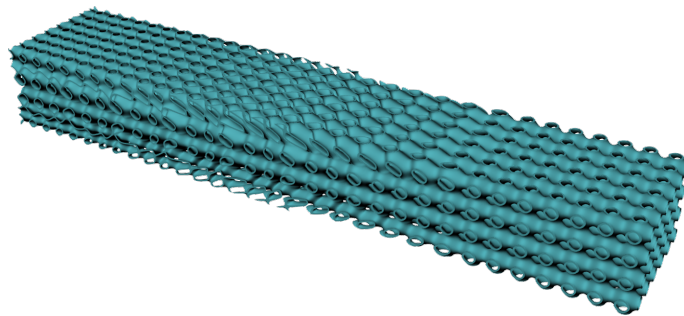
Figure 4.15: Primitive-based cantilever: Variable length fundamental mesh.



(a) Thickness variation gradient over fundamental mesh



(b) Model front view



(c) Model perspective view

Figure 4.16: Primitive-based cantilever: Variable thickness-to-length ratio modelling.

4.3.3 Gyroid-based cantilever

Design specifications and density mapping

Following a similar procedure as in the Primitive-based cantilever, the `gyroid_M4_2022` model data (matrix arrangement results for Gyroid patterns from Table 4.1) is used on the `Equivalent_Material_Coefficients` component. Accordingly, the cantilever beam can be replaced by a construct with a constant density of $\rho_{const}=0.319$, corresponding to the maximum between ρ_{E^*} and ρ_{σ^*} , calculated as follows.

$$\rho_{E^*}^* = \left(\frac{1}{c_1} \frac{u}{u_{perm}} \right)^{\frac{1}{n_1}} = \left(\frac{1}{0.402} \frac{0.1413}{2} \right)^{\frac{1}{1.176}} = 0.228$$

$$\rho_{\sigma^*}^* = \left(\frac{1}{c_3} \frac{\sigma_{eq}}{\sigma_{perm}} \right)^{\frac{1}{n_3}} = \left(\frac{1}{0.426} \frac{3.6705}{250/5} \right)^{\frac{1}{1.537}} = 0.319$$

In contrast to the Primitive-based modelling, the lower density limit of Gyroid TPMS of 0.123 will potentially improve the mechanical properties of the construct at the expense of a higher mass, due to the increase of density in the centre of the cantilever beam. Two density mapping scenarios were developed for the posterior modelling cases. Figure 4.17 depicts the dotted representation of the resulting density maps, considering a reference grid size of 10mm (Figure 4.17a) and 50mm (Figure 4.17b).

Variable thickness modelling

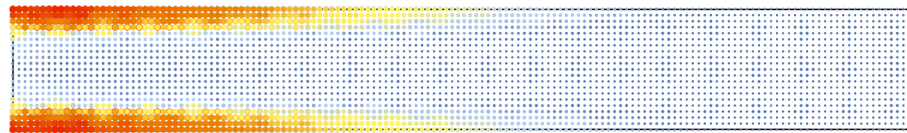
The graded density Gyroid constructs with variable thickness were obtained by setting a constant unit-cell length of $L=50\text{mm}$, corresponding to a thickness range between 2.00 and 5.24mm. Similarly to the Primitive-based scenario, the fundamental shape, shown in Figure 4.18a, was developed from a reference voxel size of 12.5mm under 3 iterative subdivision process. The surface also depicts the thickness variation of the construct by the colour gradient, which presents a good concordance with the density map shown in Figure 4.17a.

The closed model, represented in Figure 4.18b and Figure 4.14c, is obtained by setting a reference voxel size of 12.5mm and 2 subdivision iterations. Although the design conditions are not the same, given the geometric characteristics of the Gyroid patterns, the maximum thickness needed to fulfil the relative density requirements is less than on Primitive-bases models. A comparison of all the model dimensions and ranges is established in the next subsection.

Variable ratio modelling

Given the previous experience with the pure length variation scenario, this case type was omitted for the Gyroid-based modelling. Instead, the variable thickness-to-length ratio was developed with a length range between 40 and 50mm, obtaining the model shown in Figure 4.19 with thicknesses between 2.00 and 4.13mm, from the density map defined in Figure 4.17b.

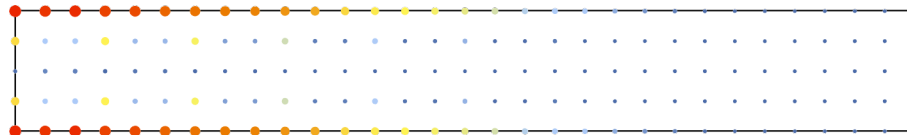
The fundamental shape (Figure 4.19a) was developed from a reference voxel size of 10mm and 3 subdivision iterations, while the closed model (Figure 4.19b and Figure 4.19c) was obtained from only 2 voxel subdivision iterations.



Relative density

Min 0.10 Max 0.317

(a) Density mapping, reference grid size of 10mm

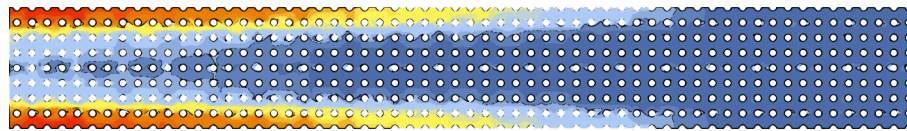


Relative density

Min 0.123 Max 0.312

(b) Density mapping, reference grid size of 50mm

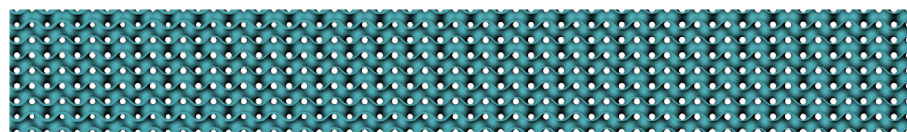
Figure 4.17: Gyroid-based cantilever: Density map from preliminary FEA.



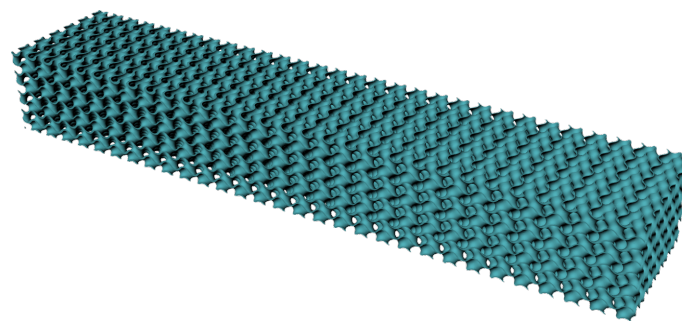
Thickness

Min 2.00mm Max 5.24mm

(a) Thickness variation gradient over fundamental mesh

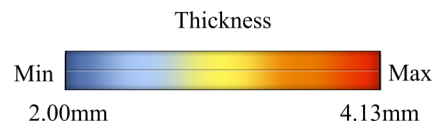
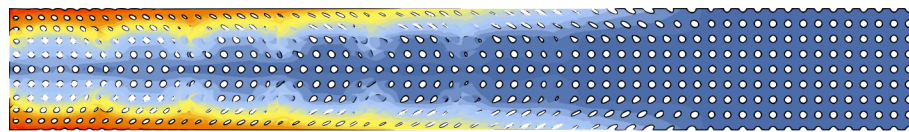


(b) Model front view

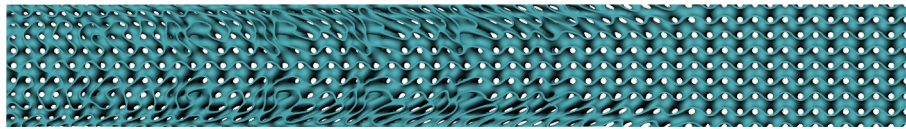


(c) Model perspective view

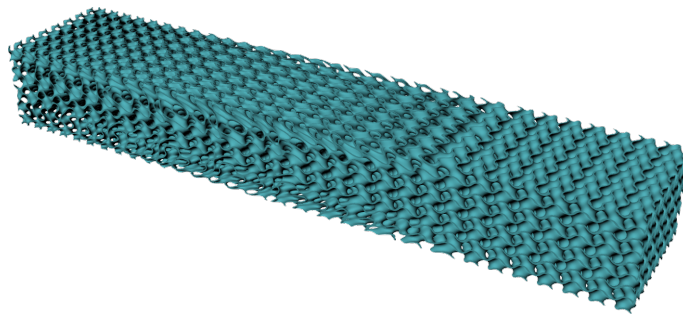
Figure 4.18: Gyroid-based cantilever: Variable thickness modelling.



(a) Thickness variation gradient over fundamental mesh



(b) Model front view



(c) Model perspective view

Figure 4.19: Gyroid-based cantilever: Variable thickness-to-length ratio modelling.

4.3.4 Modelling stage results comparison

Table 4.4 presents a summary of the modelling results for the functionally graded cantilever beam. For both Primitive and Gyroid-based models, the maximum value of the calculated density map was less than the maximum constant density, mainly due to the approximation nature of the remapping process. The biggest difference was found between the constant and the thickness-to-length ratio maximum density of Primitive-based constructs, equivalent to a discrepancy of 0.9%, due to the use of a broader grid size in the remapping process.

For both studied TPMS, the required constant density value was similar (0.327 for Primitive-based and 0.319 for Gyroid-based constructs). However, given the topological differences between patterns, the Gyroid scenario generally presents a lower thickness requirement compared to the Primitive cases. In the context of this case study, Gyroid patterns requires a thickness of 5.28mm, in contrast to the 7.11mm required for Primitive, considering the same unit-cell length in the constant density scenario. This effect is also found in the ranges of the thickness variation models. The surface thickness is a key component for the construct manufacturing by DED technologies, as it affects directly the deposition characteristics of the process. In terms of required manufacturing trajectories, Primitive patterns have less complexity.

As evidenced in Figure 4.15, the high difference of values in the length variation scenario of the Primitive-based modelling produced a surface with no practical applications. By the introduction of the thickness-to-length ratio variation, the designer is able to control the length range of the modelling, while producing a reduction of the required thicknesses range, compared to the pure thickness variation scenario. This is mainly due to the conditions detailed in subsection 3.2.3, in which the upper length limit is associated with low densities, while the lower limits is applied in the areas with a higher density requirement. As the lower length limit in the ratio variation case is lower than the constant length value set on the thickness variation case, the required thickness related to the maximum density decreases. Accordingly, this maximum thickness was reduced from 7.06mm on the thickness variation Primitive model to 5.52mm for the ratio variation case, while Gyroid-based models presented a reduction from a maximum thickness of 5.24 to 4.13mm, considering the same length variation range.

For all the models, the construct relative density was calculated by Equation 1.1 as the ratio between the TPMS-based and the solid cantilever beam volume. The volume was obtained from the mass properties of the CAD models (closed meshes). It was found that

Table 4.4: Functionally graded cantilever beam modelling summary.

TPMS	Modelling	Volume (mm ³)	ρ^*		d range (mm)	L range (mm)
			Design range	Calculated		
Primitive	Constant density	2.98E07	0.327	0.331	7.11	50.00
	Thickness variation	1.22E07	(0.10 - 0.325)	0.135	(2.12 - 7.06)	50.00
	Length variation	-	(0.10 - 0.325)	-	4.00	(28.35 - 94.26)
	Ratio variation	1.43E07	(0.10 - 0.318)	0.159	(2.12 - 5.52)	(40.00 - 50.00)
Gyroid	Constant density	2.94E07	0.319	0.326	5.28	50.00
	Thickness variation	1.42E07	(0.123 - 0.317)	0.158	(2.00 - 5.24)	50.00
	Ratio variation	1.66E07	(0.123 - 0.312)	0.184	(2.00 - 4.13)	(40.00 - 50.00)

Constant values are presented without parenthesis.

The absence of data is indicated by "-".

Calculated ρ^* obtained from Equation 1.1.

constant density scenarios presented a bigger calculated relative density than the design value. Both cases of thickness and ratio variation modelling permit to further decrease the density of the structures. Even though the control of length permits to reduce the thickness range on the ratio variation scenarios, the deformation of unit-cell's size produces an increase in the volume of the models, thus, potentially increasing the stiffness. The evaluation of the mechanical response of the variable thickness and variable thickness-to-length ratio constructs, and its comparison with the response of a constant density scenario is detailed in the next section.

4.3.5 Modelling evaluation

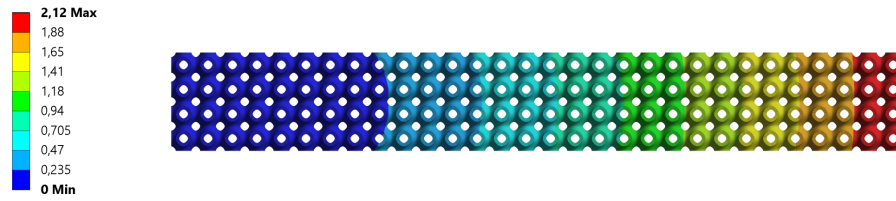
All the analysis presented in this section were run on Ansys® Academic Research Mechanical, Release 2020 R2, by the generated `WB_code` from the `Mesh_to_SHELL_FE` GH component on the diverse fundamental shape meshes. Additional steps of mesh facets' clean-up and regularization were run on SpaceClaim® Release 2020 R2 to have a better mesh distribution and, therefore, a better definition of the shell FE. The thickness distributions were added to the FE simulations by the code generated from the `Variable_thickness_ARRAY` GH component. Results from the variable thickness and variable thickness-to-length ratio are compared with the constant relative density structure.

Primitive-based models evaluation

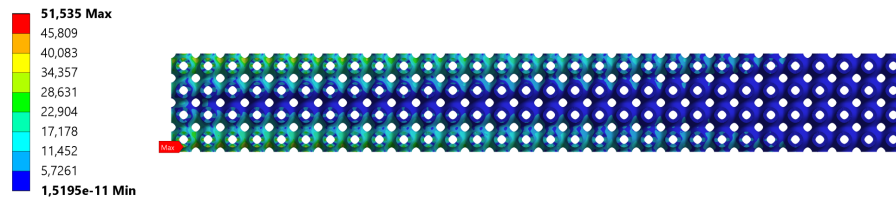
The results of total displacement and equivalent stress for the Primitive-based cantilever beam with a constant density of 0.327 are shown in Figure 4.20. The maximum displacement (Figure 4.20a) for the applied load was 2.12mm, which is slightly over the permissible set value of 2mm. In particular, this effect can be potentially attributed to the cumulative error in the relative density formula (detailed on Table 2.5). For the equivalent stress results (Figure 4.20b), even though a maximum value of 51.535MPa was obtained, an analysis of the distribution of nodal stress results showed that values over the permissible stress of 50MPa only represent the 0.00227% of the total node's count. Following a process previously adopted by Azman [2017] for the filtering of local stress concentration, a reference maximum value of $\sigma_{99.5\%}=35.688\text{MPa}$ was obtained from the 99.5% of the sorted result data, as shown by the data histogram of Figure 4.20c.

Variable thickness model's results are shown in Figure 4.21. For this case, a maximum displacement of 4.58mm was found (Figure 4.22a). The increase of free-end displacement was expected due to the reduction of the central relative density of the beam. Equivalent stress results (Figure 4.22b) had a maximum value of 81.147MPa. Following a similar process for the data processing of the constant thickness model, a filtered maximum value of $\sigma_{99.5\%}=56.908\text{MPa}$ was obtained (Figure 4.21c). For this scenario, nodal results over the permissible stress represents the 1.494% of the node's count.

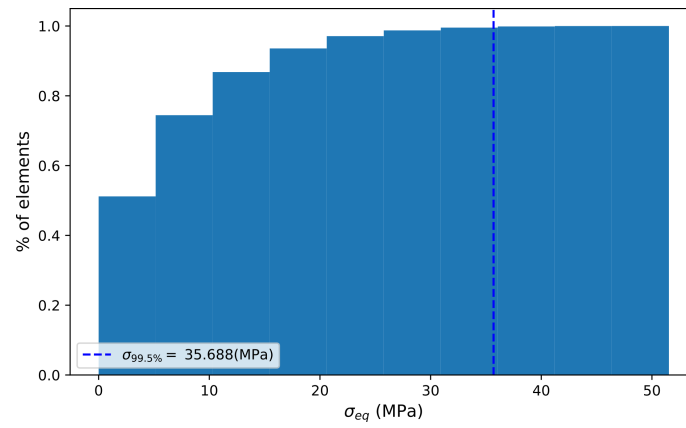
Results for the variable thickness-to-ratio scenario are shown in Figure 4.22. Total displacement results show a maximum value of 3.31mm (Figure 4.22a) corresponding to a reduction from the pure thickness variation scenario. Equivalent stress results (Figure 4.22b) show a maximum value of 1477.4MPa located near the centre of the beam in the areas with minimum stress influence. Upon further inspection, this local maximum was attributed to mesh import inconsistencies. Accordingly, Figure 4.22c presents the histogram of values and the filtered stress value of $\sigma_{99.5\%}=53.11\text{MPa}$. Results over the permissible stress are found only on the 0.678% of nodes.



(a) Total displacement (mm)

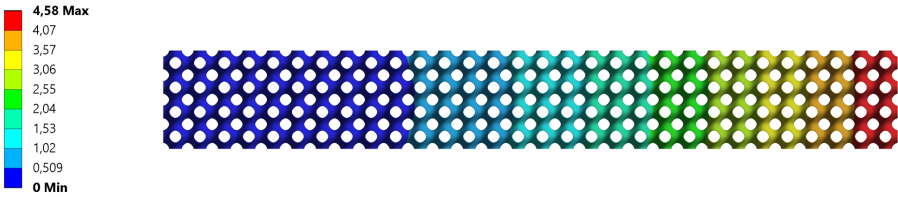


(b) Equivalent stress (MPa)

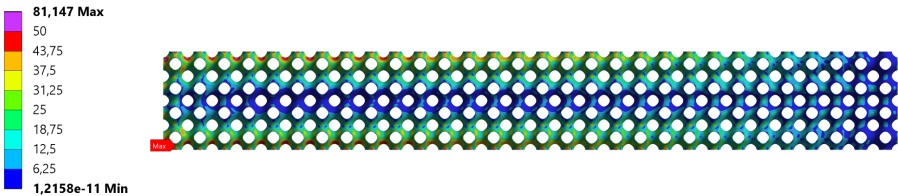


(c) Histogram of equivalent stress data

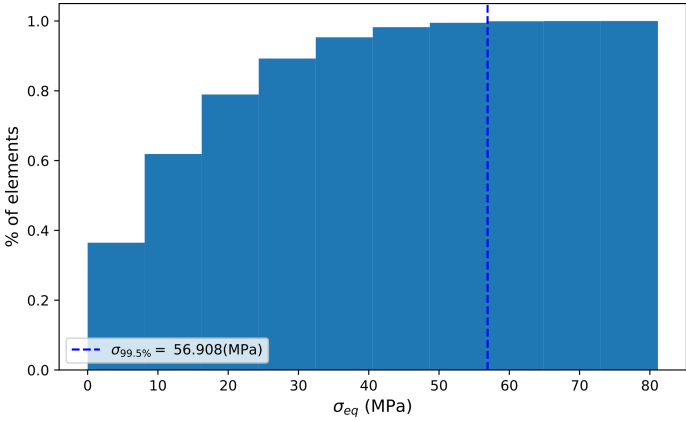
Figure 4.20: Primitive-based cantilever: Constant density evaluation.



(a) Total displacement (mm)

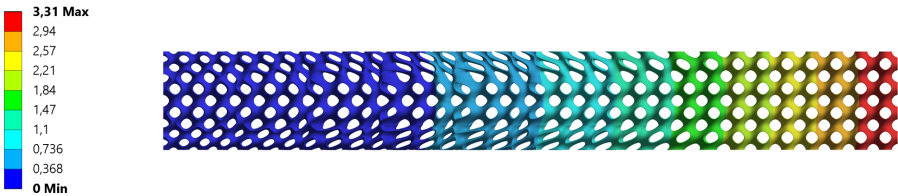


(b) Equivalent stress (MPa)

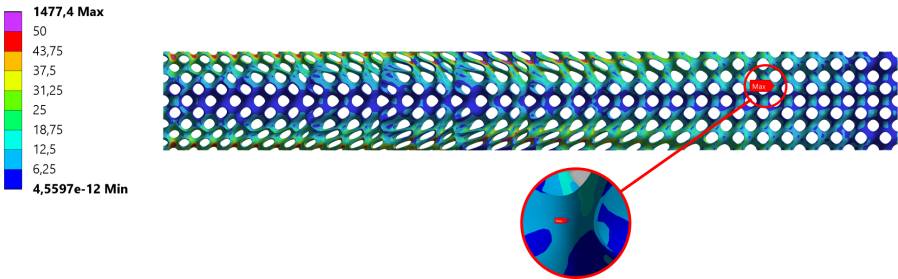


(c) Histogram of equivalent stress data

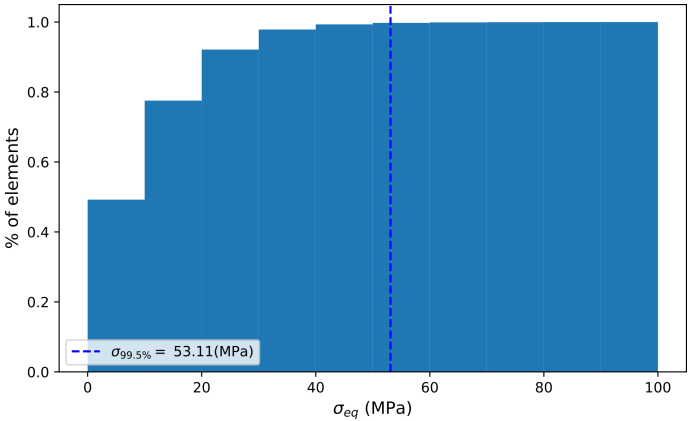
Figure 4.21: Primitive-based cantilever: Variable thickness evaluation.



(a) Total displacement (mm)



(b) Equivalent stress (MPa)



(c) Histogram of equivalent stress data

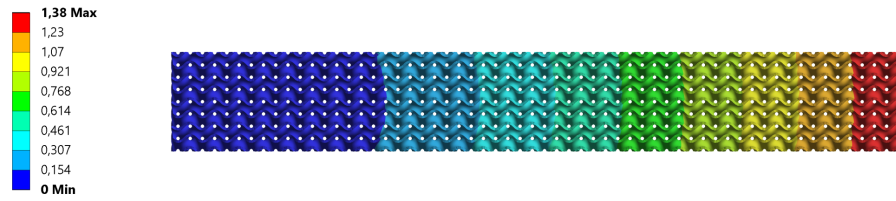
Figure 4.22: Primitive-based cantilever: Variable thickness-to-length ratio evaluation.

Gyroid-based models evaluation

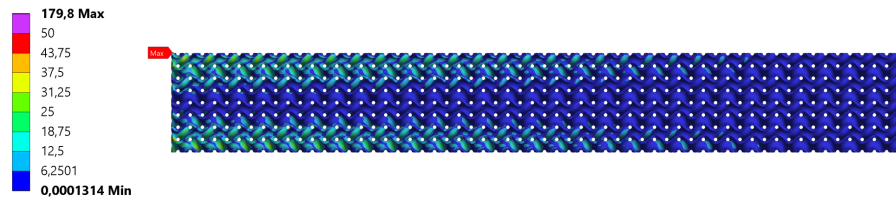
The constant density Gyroid-based construct evaluation results are detailed in Figure 4.23. For this scenario, a total displacement on the free-end of 1.38mm was obtained (Figure 4.23a), which is less than the permissible displacement. A maximum stress value of 179.8MPa was found near the edge of the fixed faces, as shown in Figure 4.23b. However, values over permissible stress were found in the 0.00021% of nodes. Figure 4.23c was used to determine the filtered stress value of $\sigma_{99.5\%}=24.91\text{MPa}$. For a correct visualization, the histogram only shows values below 50MPa, due to the high dispersion of results.

In contrast, the variable thickness scenario showed a maximum displacement of 2.3mm, as depicted in Figure 4.24a. Equivalent stress results (Figure 4.24b) showed a maximum of 249.59MPa. Values that are over the permissible stress represents the 0.00302% of the total node count. The filtered stress from the stress histogram (Figure 4.24c) was determined as $\sigma_{99.5\%}=34.864\text{MPa}$.

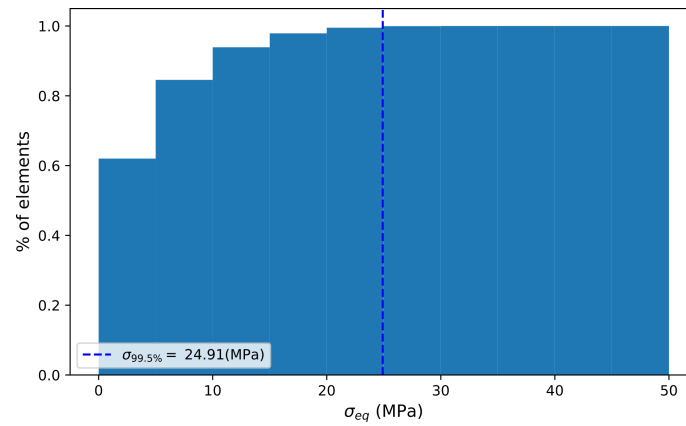
Lastly, the results for variable thickness-to-length ratio on the Gyroid-based model are shown in Figure 4.25. For this case, the maximum displacement presents a decrease to 2.17mm (Figure 4.25a) and a filtered equivalent stress of $\sigma_{99.5\%}=38.34\text{MPa}$. Is important to note that this model presented the higher variability of stress results (Figure 4.25b) mainly attributed to FE mesh importing errors of the highly complex surface. Nevertheless, nodal results over the permissible stress were only found in the 0.134% of nodes.



(a) Total displacement (mm)

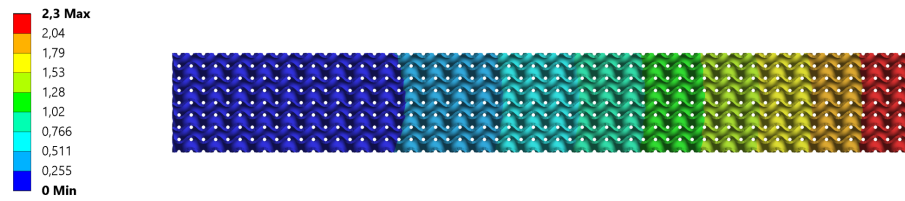


(b) Equivalent stress (MPa)

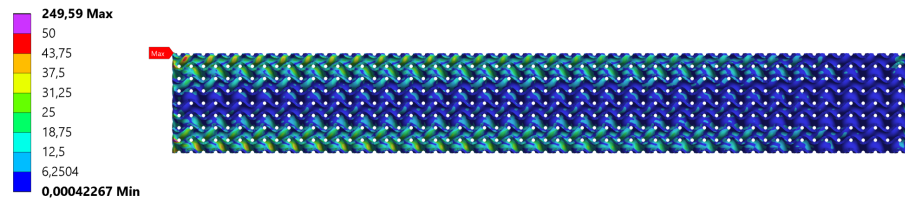


(c) Histogram of equivalent stress data

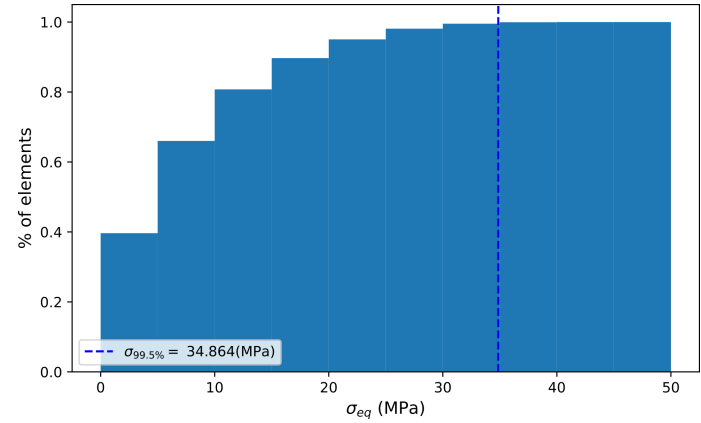
Figure 4.23: Gyroid-based cantilever: Constant density evaluation.



(a) Total displacement (mm)

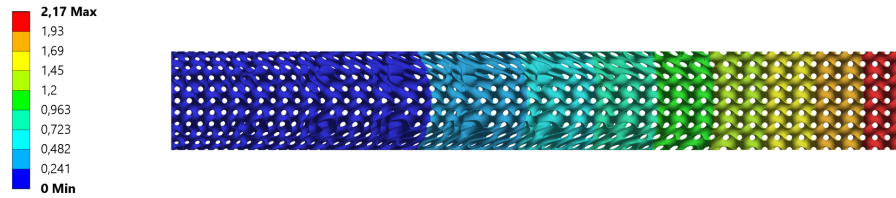


(b) Equivalent stress (MPa)

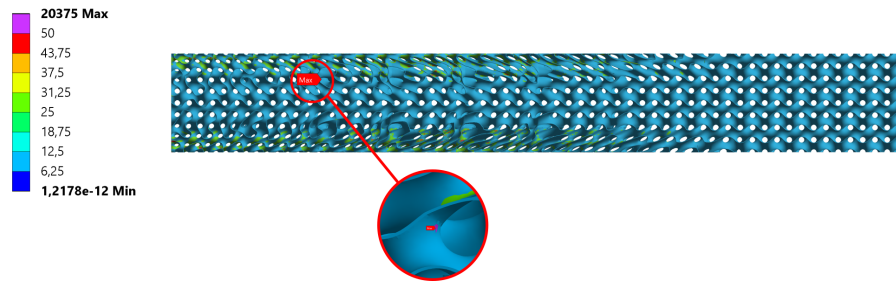


(c) Histogram of equivalent stress data

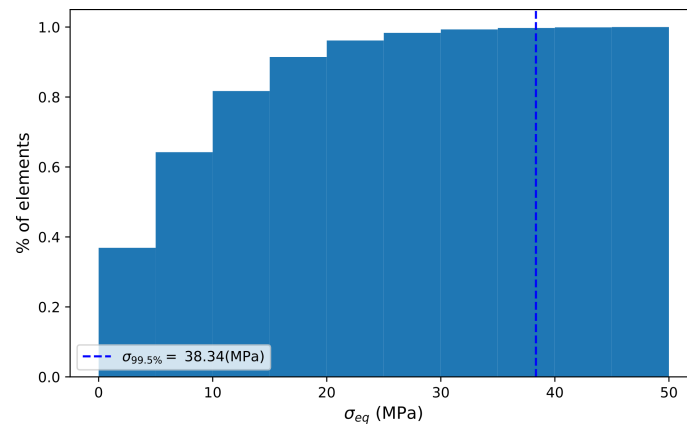
Figure 4.24: Gyroid-based cantilever: Variable thickness evaluation.



(a) Total displacement (mm)



(b) Equivalent stress (MPa)



(c) Histogram of equivalent stress data

Figure 4.25: Gyroid-based cantilever: Variable thickness-to-length ratio evaluation.

Results' comparison and model's redesign

The evaluation results are summarized in Table 4.5. Even though the constant density models had an overall better mechanical response, considering the permissible set values, the variable density cases can be subjected to a refinement process of the design parameters and/or density map to better distribute the loads, while further reducing the overall construct volume.

As evidenced by the results, Gyroid-based models tend to have a higher stiffness compared with the Primitive cases. This effect is potentially related to geometric characteristics, as Gyroid patterns have a higher degree of connection between the faces of neighbouring unit cells. In relation to the of thickness variation and thickness-to-length variation, the increase in the lower density limit of Gyroid-based models (0.123), in comparison with the Primitive-based scenarios (0.10), has also a strong relation to the reduction of the free-end displacement due to the increase of the overall stiffness of the structure. This is further verified by the model's redesign results.

For both Primitive and Gyroid-based models, there is a reduction on the free-end displacement for thickness-to-length ratio variation in comparison with the thickness variation scenario. This was previously identified in the modelling stages, as the ratio variation constructs presented a higher calculated density (volume ratio with respect to the solid cantilever beam). Ultimately, results confirm that variable ratio constructs can further increase the stiffness of the resulting structure by the introduction of the unit-cell's deformation.

To illustrate the iterative construct refinement process, the variable thickness-to-rate models were redesigned by considering a lower density limit of 0.20 for both Primitive and Gyroid-based constructs. As shown in Figure 4.26a, the redesigned Primitive model presented a thickness distribution from 4.29 to 5.52mm; while the Gyroid construct (Figure 4.26b) had a thickness range between 3.27 and 4.13mm. This corroborates that Gyroid patterns tend to be thinner than Primitive scenarios for similar density ranges.

The redesigned models were evaluated by FEA, following the procedure described in previous sections. The result of these analysis is also presented in Table 4.5. As the centre of the density map is now adjusted to a bigger density condition, the resulting models have an increase in the overall stiffness. This is evidenced by the reduction on total displacement results. For the Primitive-based redesign, the displacement of the free end reduced from 3.31mm in the first variable ratio design to 2.61mm, as shown in Figure 4.27a. Gyroid-based counterpart presented a total displacement of 1.66mm (Figure 4.28a), in contrast with the 2.17mm displacement from the initial variable ratio design.

Table 4.5: Functionally graded cantilever beam evaluation results summary.

Modelling	ρ^*	u_{total} (mm)	σ_{eq} (MPa)		Nodes	
			$\sigma_{eq\ max}$	$\sigma_{99.5\%}$	Count	% over σ_{perm}
Permissible values		2.00	50.00			
Primitive-based						
Constant density	0.327	2.12	51.535	35.688	4.36E06	0.00227
Thickness variation	(0.10 - 0.325)	4.58	81.147	56.908	4.36E06	1.494
Ratio variation	(0.10 - 0.318)	3.31	1477.4	53.11	4.81E06	0.678
Ratio variation redesign	(0.20 - 0.318)	2.61	2835.5	41.804	4.55E06	0.161
Gyroid-based						
Constant density	0.319	1.38	179.8	24.91	5.69E06	0.00021
Thickness variation	(0.123 - 0.317)	2.30	249.59	34.864	5.69E06	0.00302
Ratio variation	(0.123 - 0.312)	2.17	20375	38.34	6.40E06	0.134
Ratio variation redesign	(0.20 - 0.312)	1.66	10500	30.074	6.02E06	0.0168

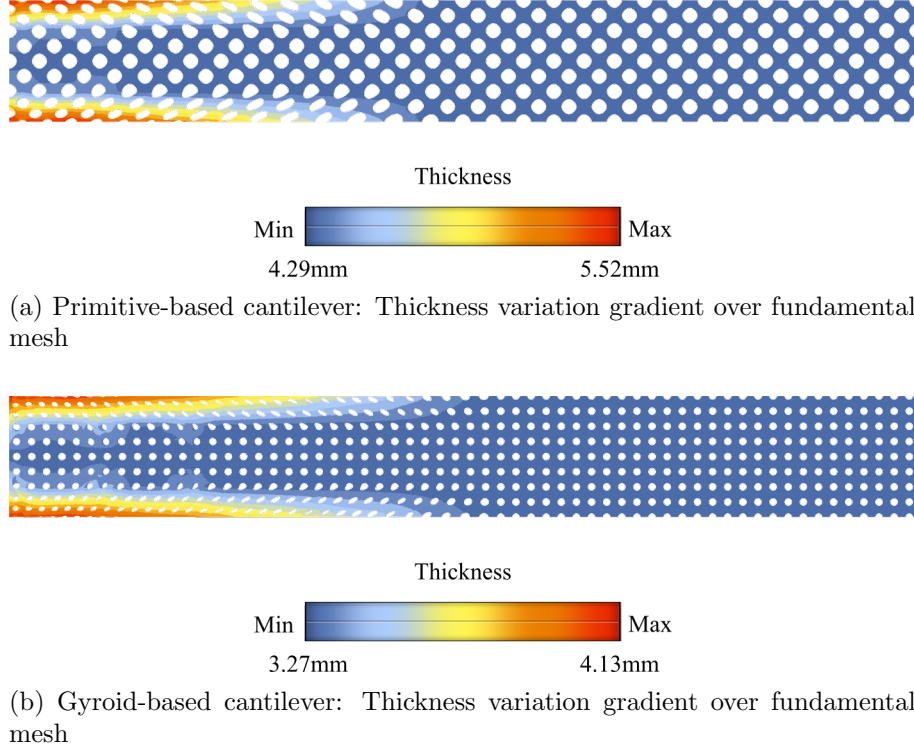
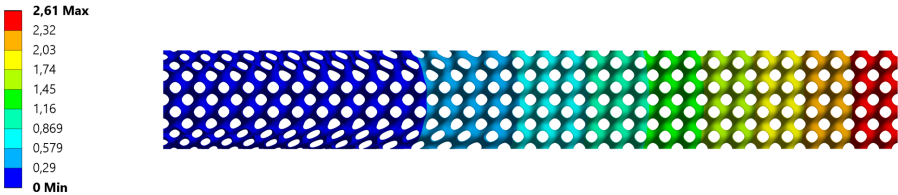


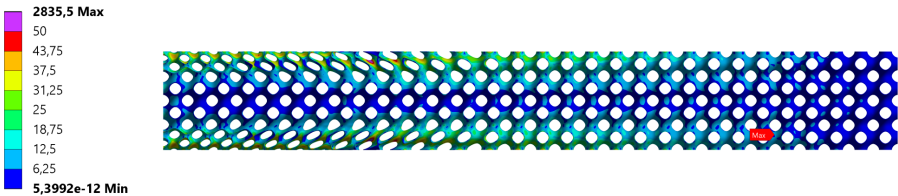
Figure 4.26: Variable thickness-to-length ratio redesign.

In general, equivalent stress results presented a good agreement with the permissible set values, regardless of high local maximum stress. This was verified by two approaches: the filtering of the maximum stress value at the 99.5% of the sorted stress data, and by establishing the percentage of nodes that showed a value over σ_{perm} . For the filtering analysis, both constant density constructs of Primitive and Gyroid patterns showed a value lower than the permissible condition. This result was expected, as the analysed structures are similar in principle to the constant thickness constructs used for the determination of the Equivalent Material properties. It was found that the filtered results in all other design scenarios was higher than the constant density case.

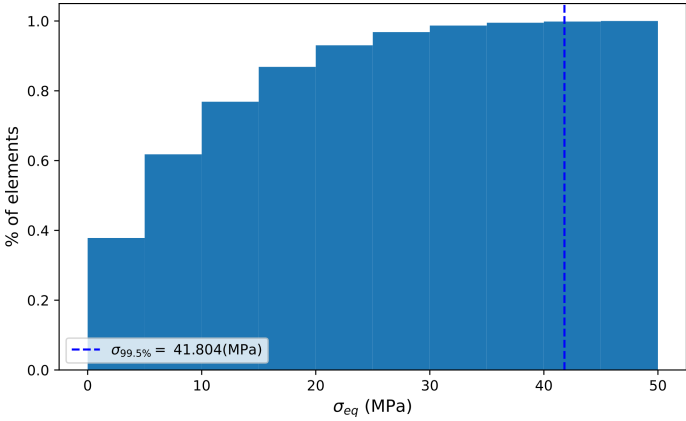
For the majority of the models, the percentage of nodes that showed values over σ_{perm} are relatively low with the exception of the Primitive-based model with thickness variation, in which the 1.494% of nodes presented values outside of the permissible stress. In particular, this analysis permitted to assess the validity of the results found for the various thickness-to-length ratio models, which all presented high local values in areas with low stress influences. These high results were attributed to mesh import errors, as depicted in Figure 4.22b and Figure 4.25b. However, for ratio variation scenarios, FE nodal results outside of permissible stress limits were present in a maximum of 0.678% of the total node count.



(a) Total displacement (mm)

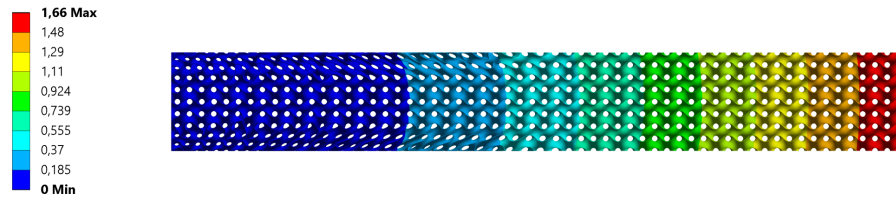


(b) Equivalent stress (MPa)

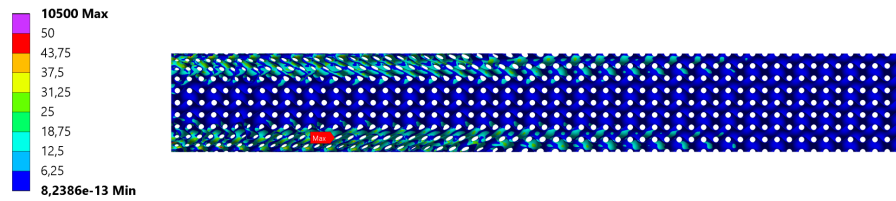


(c) Histogram of equivalent stress data

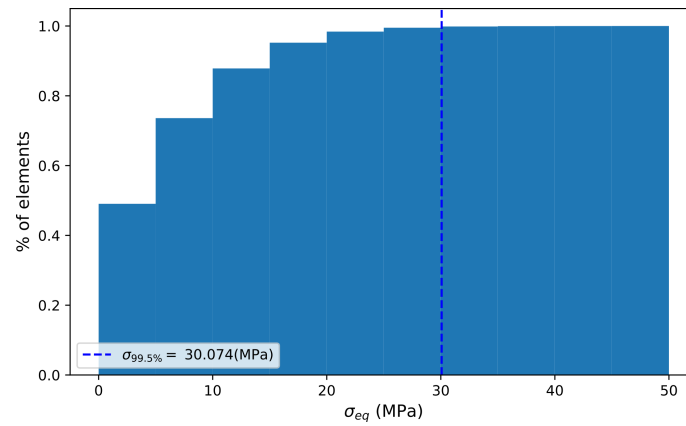
Figure 4.27: Primitive-based cantilever: Redesign evaluation.



(a) Total displacement (mm)



(b) Equivalent stress (MPa)



(c) Histogram of equivalent stress data

Figure 4.28: Gyroid-based cantilever: Redesign evaluation.

4.4 Analysis and evaluation of TPMS patterns conclusions

This chapter detailed the process for obtaining the metamaterial properties of Primitive and Gyroid TPMS under an Equivalent Material analysis framework, and their application to develop a cantilever beam with an internal structure of variable density.

The Equivalent Material analysis in section 4.1 established the relative mechanical properties of Primitive and Gyroid patterns under compression (Table 4.1) and shear (Table 4.2) loads, as a function of the relative density. These properties were determined by a FEA of the studied TPMS unit-cells and a matrix arrangement of 4x4x4 cells. The simulation of matrix assemblies was not found on the consulted literature for TPMS mechanical properties. In addition, the presented results fills the gap on the determination of relative strength under shear loads.

Metamaterial properties related to compression loads (relative Young modulus E^* and relative strength σ^*) are the key aspects to relate the equivalent stress results from a preliminary FEA of a solid model to the required local densities of a graded density construct. In particular, the modelled properties from the simulation of a 4x4x4 matrix arrangement of Primitive and Gyroid unit-cells was used to develop a cantilever beam with an internal structure of variable density.

Even though the models used for the determination of local densities cannot be directly applied for the prediction of the macroscopic mechanical behaviour, the design validation stages of the proposed methodology perform a final FEA of the functionally graded construct, evaluating the response of the whole heterogeneous structure and comparing those results with the permissible design conditions.

Based on the diverse models obtained for a Primitive and Gyroid-based cantilever beam, it was found that the introduction of a simultaneous variation on thickness and length of the unit-cells produced an overall better distribution of loads, as the controlled surface deformations produce structure with more stiffness compared with the thickness variation scenarios. Length variation scenarios showed no practical application due to the lack of control in the deformation of unit-cell boundaries.

Chapter 5

General conclusions and future work

5.1 Concluding remarks

Previous chapters presents a collection of methods and tools for the design of lightweight TPMS-based parts to be manufactured by AM processes. The conclusions of this work are detailed below, according to the research strategy scope.

Modelling of generic pattern models

As established in chapter 1, Triply Periodic Minimal Surfaces (TPMS) have been considered as a promising alternative to lattice unit-cells for the development of cellular constructs. Their unique surface characteristics give them the possibility to create structures with better mechanical properties. From the family of TPMS, special attention was given to Primitive and Gyroid patterns in view of their potential manufacturability advantages over other topologies, as determined by the initial research project evaluation.

TPMS model's can be obtained by either a variation of the level-set C of the implicit surface equation, or by assigning a thickness to a central (fundamental) surface. Previous efforts in the literature have studied the effects of a C variation on the relative density of Gyroid patterns, and the work detailed in subsection 2.1.1 expanded this relationships to Primitive TPMS. However, level-set variation modelling can introduce an uncontrolled deviation in the thickness of patterns with constant density, as shown in Figure 2.3. This lack of control in the models' properties is considered disadvantageous due to the complexity of correlating the relative density to traditional design parameters of lattice structures, i.e. features' thicknesses and unit-cell length.

Ultimately, the modelling of TPMS structures was accomplished by a triangular mesh polygonization of a Signed Distance Field (SDF) representing the surface, based on a Marching Tetrahedra (MT) algorithm. This custom-built implementation allowed the parametrization of the model generation by relating the surface generation to the pattern thickness d and unit-cell length L . The effects of these design parameters are discussed in the next section.

Definition of parameters for density variation

The relation between the patterns' density and their design parameters is an important step towards the creation of Functionally Graded Cellular Materials (FGCM). Being mathematically defined surfaces, modelling of the fundamental shape of TPMS patterns is

heavily influenced by the effects of the selected values on their design variables. Chapter 2 presented how the relative density of the studied TPMS responds to a variation of d and L . There is no information in the available literature regarding the combined effect of these parameters, thus, this study fills these gaps in geometric modelling analysis.

Accordingly, a relative density ρ^* equation was proposed as a function of the patterns' thickness-to-length ratio $\frac{d}{L}$, as established in Equation 2.9. It was found that this identity had a maximum approximation error of 1.02% for Primitive and 0.65% for Gyroid patterns. Equation 2.9 maxima shows that the factor β' is analogous to the maximum relative density and the factor α' to the maximum length-to-thickness $\frac{L}{d}$ ratio that can be modelled. The equation is not mathematically defined for values outside these limits.

From the analysis of the relative density equations, it was found that the equation is valid for a relative density range from 0.095 to 0.711 for Primitive (Equation 2.10) and from 0.123 to 0.688 for Gyroid (Equation 2.11), as summarized in Table 2.4. These equations can be further improved by the inclusion of manufacturing constraints for the redefinition of α' and/or β' factors by a Gradient Optimization approach.

Development of gradient density structures

The key objective for the development of FGCM is the adaptation of TPMS patterns to a three-dimensional density map related to the solid material's load scenario. Even though commercial software alternatives have implemented the generation of TPMS constructs with graded density, their processes are limited to linear gradients. Consequently, chapter 3 proposes a formal modelling procedure for TPMS-based graded density constructs, while being able to control the patterns' thickness and unit-cell length in proportion to a three-dimensional density distribution. The process is defined for constructs of variable thickness, length and simultaneous thickness and length variation.

The proposed methodology, shown in Figure 3.22 and detailed in section 3.2, is divided in six stages. A set of designer inputs such as design parameter variation, TPMS type, design space boundaries, among other preliminary operations are defined in the design specification stage (i). This information is then used to create the density map (ii) to be used for the calculation of local design parameters (iii). The mapped parameters are then used for the generation of the fundamental TPMS shape (iv) and the creation of the offset pattern surfaces (v). To define a closed mesh, this offset surfaces are then run through a series of mesh cleaning and boolean operations (vi). Additional process for design validation (vii) are also considered and further detailed in chapter 4. All the process involved in the main design methodology were developed as a set of tools in a custom-built *BeShape* plug-in containing Grasshopper[®] components for Rhinoceros[®] 7 CAD suite.

For the density mapping operations, the developed operations are able to handle reference density maps from topological optimization (TO) or calculate the required local densities from the results of preliminary finite element analysis (FEA) of the solid model. As these reference density grids are not necessarily adjusted to a regular grid, the process also performs a remapping of the reference data to have an orderly distribution of values, which is required for the subsequent polygonization algorithm.

Furthermore, given the discrete nature of the MT algorithm used for fundamental mesh creation and SDF offset of the pattern surfaces, a process of voxel subdivision is applied for the optimization of the calculation process. In this context, the polygonization algorithm is first calculated with a coarse voxel distribution, which is then cleaned and subdivided depending on the location of the voxel with respect to the surface. As an example, this process was able to generate the Gyroid pattern with variable thickness-to-length ratio

used in the cantilever beam study with 3E06 voxels, from an initial distribution of 1E05 entities, erasing 3.6E06 unused voxels from the subdivision processes.

Even though the methodology was only applied for Primitive and Gyroid TPMS, the process is able to handle any minimal surface shape by knowing their shape equation and relative density behaviour with respect to the pattern design parameters. Ultimately, the proposed general methodology should be used in combination with an assessment of the desired graded density TPMS, accounting for manufacturability restrictions of the employed AM technology.

Evaluation of graded models

A cantilever beam loaded at the free-end was used as a case study for the evaluation of constructs generated by the proposed methodology. For this, chapter 4 details the process to obtain the metamaterial properties of Primitive and Gyroid patterns under an Equivalent Material framework. The obtained relative mechanical property models for compression (Table 4.1) and shear (Table 4.2) loads as a function of the relative density fills the gaps found in the literature for the Finite Element (FE) simulation on TPMS matrix arrangements and the definition of relative strength for shear scenarios. In addition, a process is proposed to calculate the required local density from preliminary FEA results of the solid material based on metamaterial properties related to compression loads (relative Young modulus E^* and relative strength σ^*), as an alternative to a density mapping from TO procedures.

The evaluation of the variable density constructs is performed by a custom-built tool (`Mesh_to_SHELL_FE`) to convert the fundamental surface STL mesh to a FE mesh as a Constant Database file able to be imported to ANSYS® Workbench, Release 2020 R2. This mesh data import must be combined with the code supplied by a second tool (`Variable_thickness_ARRAY`) which assigns the local thickness to the nodes as a set of Mechanical APDL (Ansys Parametric Design Language) instructions.

The FEA results for equivalent stress of the cantilever beam were used for the definition of the required density map and the posterior modelling operations. Primitive and Gyroid-based constructs with thickness and thickness-to-length ratio variation were developed and tested under the same loading conditions as the solid cantilever model, and compared to a structure with constant density TPMS. In general, Gyroid-based constructs tends to have a higher resistance due to the topological properties of the surface, for lower thickness values. Even though constant density scenarios are naturally stronger than the design parameter variation counterparts (for both TPMS patterns), they present a higher volume which can be critical in lightweight applications.

The two tested variation scenarios showed a decrease in the overall relative density. In particular, the simultaneous variation on pattern thickness and length is able to increase the stiffness of the construct, compared with thickness variation scenarios, at the expense of an increase of the construct volume. Furthermore, the resistance in both cases can be further improved by modifying the set design parameters and/or density map. Length variation scenarios showed no practical application due to the lack of control in the deformation of unit-cell boundaries.

5.2 Work perspectives

Manufacturing of functionally graded TPMS constructs

This research presented the creation of TPMS structures with a variation of their relative density in a strict design focus. Even though the BeShape project framework considers the manufacturing aspects of the application of TPMS for lightweight constructs, the fabrication of this type of cellular structures by WAAM is still on early stages.

Academic partners of the project were able to develop a slicing methodology to generate the deposition trajectories to be followed, which was applied for the manufacturing of a Primitive unit-cell with constant bead thickness. However, there is still ground to be covered for the manufacturing of Gyroid patterns, especially for an in-depth study of the rate of change on surface normal vectors, and, consequently, on the inclination of the robot arm for deposition.

Regarding graded density constructs, it was identified that variable thickness TPMS patterns can be generated by the control of deposition velocity during WAAM procedures. Even though some of the developed tools (e.g. the `Density_Finder_Plus` GH component) can be used to extract the local density, thickness and length values from an arbitrary point in a trajectory, a method has not been defined to relate actual manufacturing conditions to the design parameters of TPMS.

Improvement of relative density models and metamaterial properties data

As previously stated in chapter 2, the relative density equations can be improved by the inclusion of manufacturing limitations of TPMS structures. In this sense, the α' and β' coefficients related to the minimum manufacturable length-to-thickness ratio $\frac{L}{d}$ and maximum pattern density, respectively, can be improved by knowing the fabrication limitations of TPMS. With the knowledge for one of the parameters, the second one, and the exponential parameter γ' , can be approximated by using a Gradient Optimization algorithm to reduce the approximation errors of the proposed relative density equations. Is important to note that, these type of analysis can be made to any AM technology, potentially creating a library of coefficients as a function of the manufacturing process.

The TPMS metamaterial properties presented in this work were derived from FE simulation data of TPMS unit-cells and matrix arrangements of cells. These relative mechanical properties can be obtained from experimental testing of manufactured constructs. Thus, the diverse models can be contrasted with these results, potentially defining a new set of equations matching real part behaviour.

Revision of data process-chain

The current implementation of modelling, mesh cleaning and finite element evaluation of graded density constructs involves a series of different CAD and FEA tools. Current process-chain establishes the modelling stages on the Grasshopper® environment of Rhinoceros® 7, STL mesh cleaning on SpaceClaim® 2020 R2, and models evaluation on Ansys® Academic Research Mechanical, Release 2020 R2.

There is a possible lose in files' quality due to the successive imports, specially on the import process for the evaluation stages evidenced in subsection 4.3.5. As noted in the results, imported meshes for the variable thickness-to-length models had a tendency to present meshing errors, even though the meshes were correctly verified beforehand. These particular issues could be potentially corrected by updating the implementations to current versions of the simulation software or to work with other program alternatives.

Calculation of effective elastic properties

As previously stated on chapter 4, the Gibson-Ashby models are limited to the characterization of cellular materials with an isotropic macroscopic behaviour, and the utilization of the scaling laws for the determination of local densities from FEA data can present errors. This was partially addressed by the introduction of a final FEA analysis evaluation of the graded density construct. However, a more rigorous analysis is needed for the improvement of the current procedures.

Accordingly, the use of numerical homogenization methods can be used for the determination of effective elastic properties based on the strain energy of periodic media. Even though these processes were not part of the initial focus of the study, an example of their application for a Primitive unit-cell can be consulted on Appendix B.

Optimization of GH components

Even though the creation of the *BeShape* plug-in for Grasshopper® was a step forward to the improvement and ease of implementation of the proposed methodology, there is still room for optimization in the generated code. For instance, some generic data classes (such as voxel clouds between the fundamental shape generation and SDF offset components) can be used as additional inputs for boosting internal processes.

In addition, alternatives to the Marching Tetrahedra algorithm, such as a double Marching Cubes algorithm for polygonization, can also be developed for the improvement of the quality of the generated STL meshes. There is also room for improvement in the development of tools for STL mesh to parametric surface conversion.

Bibliography

- Diab W. Abueidda, Rashid K. Abu Al-Rub, Ahmed S. Dalaq, Dong-Wook Lee, Kamran A. Khan, and Iwona Jasiuk. Effective conductivities and elastic moduli of novel foams with triply periodic minimal surfaces. *Mechanics of Materials*, 95:102–115, April 2016. ISSN 0167-6636. doi: 10.1016/j.mechmat.2016.01.004. URL <https://www.sciencedirect.com/science/article/pii/S0167663616000053>.
- Diab W. Abueidda, Mete Bakir, Rashid K. Abu Al-Rub, Jörgen S. Bergström, Nahil A. Sobh, and Iwona Jasiuk. Mechanical properties of 3D printed polymeric cellular materials with triply periodic minimal surface architectures. *Materials & Design*, 122: 255–267, May 2017. ISSN 0264-1275. doi: 10.1016/j.matdes.2017.03.018. URL <http://www.sciencedirect.com/science/article/pii/S0264127517302575>.
- Diab W. Abueidda, Mohamed Elhebeary, Cheng-Shen (Andrew) Shiang, Siyuan Pang, Rashid K. Abu Al-Rub, and Iwona M. Jasiuk. Mechanical properties of 3D printed polymeric Gyroid cellular structures: Experimental and finite element study. *Materials & Design*, 165:107597, March 2019. ISSN 0264-1275. doi: 10.1016/j.matdes.2019.107597. URL <http://www.sciencedirect.com/science/article/pii/S0264127519300176>.
- M. Afshar, A. Pourkamali Anaraki, H. Montazerian, and J. Kadkhodapour. Additive manufacturing and mechanical characterization of graded porosity scaffolds designed based on triply periodic minimal surface architectures. *Journal of the Mechanical Behavior of Biomedical Materials*, 62:481–494, September 2016. ISSN 1751-6161. doi: 10.1016/j.jmbbm.2016.05.027. URL <http://www.sciencedirect.com/science/article/pii/S1751616116301552>.
- M. Afshar, A. Pourkamali Anaraki, and H. Montazerian. Compressive characteristics of radially graded porosity scaffolds architected with minimal surfaces. *Materials Science and Engineering: C*, 92:254–267, November 2018. ISSN 0928-4931. doi: 10.1016/j.msec.2018.06.051. URL <http://www.sciencedirect.com/science/article/pii/S0928493117339048>.
- S. M. Ahmadi, G. Campoli, S. Amin Yavari, B. Sajadi, R. Wauthle, J. Schrooten, H. Weinans, and A. A. Zadpoor. Mechanical behavior of regular open-cell porous biomaterials made of diamond lattice unit cells. *Journal of the Mechanical Behavior of Biomedical Materials*, 34:106–115, June 2014. ISSN 1751-6161. doi: 10.1016/j.jmbbm.2014.02.003. URL <https://www.sciencedirect.com/science/article/pii/S1751616114000356>.
- Oraib Al-Ketan and Rashid K. Abu Al-Rub. MSLattice: A free software for generating uniform and graded lattices based on triply periodic minimal surfaces. *Material Design & Processing Communications*, n/a(n/a):e205, 2020. ISSN 2577-6576. doi: 10.1002/mdp2.

205. URL <http://onlinelibrary.wiley.com/doi/abs/10.1002/mdp2.205>. eprint: <https://onlinelibrary.wiley.com/doi/pdf/10.1002/mdp2.205>.
- Oraib Al-Ketan, Rachid Rezgui, Reza Rowshan, Huifeng Du, Nicholas X. Fang, and Rashid K. Abu Al-Rub. Microarchitected Stretching-Dominated Mechanical Metamaterials with Minimal Surface Topologies. *Advanced Engineering Materials*, 20(9):1800029, 2018a. ISSN 1527-2648. doi: 10.1002/adem.201800029. URL <http://onlinelibrary.wiley.com/doi/abs/10.1002/adem.201800029>. eprint: <https://onlinelibrary.wiley.com/doi/pdf/10.1002/adem.201800029>.
- Oraib Al-Ketan, Reza Rowshan, and Rashid K. Abu Al-Rub. Topology-mechanical property relationship of 3D printed strut, skeletal, and sheet based periodic metallic cellular materials. *Additive Manufacturing*, 19:167–183, January 2018b. ISSN 2214-8604. doi: 10.1016/j.addma.2017.12.006. URL <http://www.sciencedirect.com/science/article/pii/S2214860417303767>.
- Dheyaa S. J. Al-Saedi, S. H. Masood, Muhammad Faizan-Ur-Rab, Amer Alomarah, and P. Ponnusamy. Mechanical properties and energy absorption capability of functionally graded F2BCC lattice fabricated by SLM. *Materials & Design*, 144:32–44, April 2018. ISSN 0264-1275. doi: 10.1016/j.matdes.2018.01.059. URL <https://www.sciencedirect.com/science/article/pii/S026412751830073X>.
- Pedro Almeida and S. Williams. Innovative process model of Ti–6Al–4V additive layer manufacturing using cold metal transfer (CMT). pages 25–36, January 2010.
- Rita Ambu and Anna Eva Morabito. Porous Scaffold Design Based on Minimal Surfaces: Development and Assessment of Variable Architectures. *Symmetry*, 10(9):361, September 2018. doi: 10.3390/sym10090361. URL <https://www.mdpi.com/2073-8994/10/9/361>. Number: 9 Publisher: Multidisciplinary Digital Publishing Institute.
- Rita Ambu and Anna Eva Morabito. Modeling, Assessment, and Design of Porous Cells Based on Schwartz Primitive Surface for Bone Scaffolds, June 2019. URL <https://www.hindawi.com/journals/tswj/2019/7060847/>. ISSN: 2356-6140 Library Catalog: www.hindawi.com Pages: e7060847 Publisher: Hindawi Volume: 2019.
- S. Amin Yavari, S. M. Ahmadi, R. Wauthle, B. Pouran, J. Schrooten, H. Weinans, and A. A. Zadpoor. Relationship between unit cell type and porosity and the fatigue behavior of selective laser melted meta-biomaterials. *Journal of the Mechanical Behavior of Biomedical Materials*, 43:91–100, March 2015. ISSN 1751-6161. doi: 10.1016/j.jmbbm.2014.12.015. URL <https://www.sciencedirect.com/science/article/pii/S1751616114003944>.
- M. Ansari, E. Jabari, and E. Toyserkani. Opportunities and challenges in additive manufacturing of functionally graded metallic materials via powder-fed laser directed energy deposition: A review. *Journal of Materials Processing Technology*, 294:117117, August 2021. ISSN 0924-0136. doi: 10.1016/j.jmatprotec.2021.117117. URL <https://www.sciencedirect.com/science/article/pii/S0924013621000777>.
- Inc. ANSYS. Ansys® Element Reference Manual, Release 10.0, [Chapter 4. Element Library, SHELL63], ANSYS, Inc., 2004.
- M. F. Ashby. The properties of foams and lattices. *Philosophical Transactions of the Royal Society A: Mathematical, Physical and Engineering Sciences*, 364(1838):15–30,

- January 2006. doi: 10.1098/rsta.2005.1678. URL <https://royalsocietypublishing.org/doi/full/10.1098/rsta.2005.1678>.
- M. F. Ashby and R. F. Mehl Medalist. The mechanical properties of cellular solids. *Metallurgical Transactions A*, 14(9):1755–1769, September 1983. ISSN 1543-1940. doi: 10.1007/BF02645546. URL <https://doi.org/10.1007/BF02645546>.
- Abdul Hadi Azman. *Method for integration of lattice structures in design for additive manufacturing*. PhD thesis, Université Grenoble Alpes, February 2017. URL <https://tel.archives-ouvertes.fr/tel-01688758>.
- J. Banhart and H.-W. Seeliger. Aluminium Foam Sandwich Panels: Manufacture, Metallurgy and Applications. *Advanced Engineering Materials*, 10(9):793–802, 2008. ISSN 1527-2648. doi: 10.1002/adem.200800091. URL <http://onlinelibrary.wiley.com/doi/abs/10.1002/adem.200800091>. eprint: <https://onlinelibrary.wiley.com/doi/pdf/10.1002/adem.200800091>.
- Bernd Baufeld, Omer Van der Biest, and Rosemary Gault. Additive manufacturing of Ti-6Al-4V components by shaped metal deposition: Microstructure and mechanical properties. *Materials & Design*, 31:S106–S111, June 2010. ISSN 0261-3069. doi: 10.1016/j.matdes.2009.11.032. URL <http://www.sciencedirect.com/science/article/pii/S0261306909006529>.
- F. S. L. Bobbert, K. Lietaert, A. A. Eftekhari, B. Pouran, S. M. Ahmadi, H. Weinans, and A. A. Zadpoor. Additively manufactured metallic porous biomaterials based on minimal surfaces: A unique combination of topological, mechanical, and mass transport properties. *Acta Biomaterialia*, 53:572–584, April 2017. ISSN 1742-7061. doi: 10.1016/j.actbio.2017.02.024. URL <http://www.sciencedirect.com/science/article/pii/S1742706117301290>.
- Colin Bonatti and Dirk Mohr. Mechanical performance of additively-manufactured anisotropic and isotropic smooth shell-lattice materials: Simulations & experiments. *Journal of the Mechanics and Physics of Solids*, 122:1–26, January 2019a. ISSN 0022-5096. doi: 10.1016/j.jmps.2018.08.022. URL <http://www.sciencedirect.com/science/article/pii/S0022509617309614>.
- Colin Bonatti and Dirk Mohr. Smooth-shell metamaterials of cubic symmetry: Anisotropic elasticity, yield strength and specific energy absorption. *Acta Materialia*, 164:301–321, February 2019b. ISSN 1359-6454. doi: 10.1016/j.actamat.2018.10.034. URL <http://www.sciencedirect.com/science/article/pii/S1359645418308346>.
- Paul Bourke. Polygonising a scalar field, 1994. URL [http://lemur.cmp.uea.ac.uk/Research/ivis/backup/PhD/RonaniViSSstuff\(Website\)/Polygonisingascalarfield.pdf](http://lemur.cmp.uea.ac.uk/Research/ivis/backup/PhD/RonaniViSSstuff(Website)/Polygonisingascalarfield.pdf).
- Paul Bourke. Polygonising a scalar field using tetrahedrons, 1997. URL <http://paulbourke.net/geometry/polygonise/>.
- D Brackett, I Ashcroft, and R Hague. Topology Optimization for Additive Manufacturing. *Proceedings of the 2011 International Solid Freeform Fabrication Symposium*, page 15, 2011.

- Manfredo P. do Carmo. *Differential Geometry of Curves and Surfaces: Revised and Updated Second Edition*. Courier Dover Publications, December 2016. ISBN 978-0-486-81797-2. Google-Books-ID: gg2xDQAAQBAJ.
- E. Catmull and J. Clark. Recursively generated B-spline surfaces on arbitrary topological meshes. *Computer-Aided Design*, 10(6):350–355, November 1978. ISSN 0010-4485. doi: 10.1016/0010-4485(78)90110-0. URL <https://www.sciencedirect.com/science/article/pii/0010448578901100>.
- Sing Ying Choy, Chen-Nan Sun, Kah Fai Leong, and Jun Wei. Compressive properties of functionally graded lattice structures manufactured by selective laser melting. *Materials & Design*, 131:112–120, October 2017. ISSN 0264-1275. doi: 10.1016/j.matdes.2017.06.006. URL <https://www.sciencedirect.com/science/article/pii/S0264127517305890>.
- C. R. Cunningham, J. M. Flynn, A. Shokrani, V. Dhokia, and S. T. Newman. Invited review article: Strategies and processes for high quality wire arc additive manufacturing. *Additive Manufacturing*, 22:672–686, August 2018. ISSN 2214-8604. doi: 10.1016/j.addma.2018.06.020. URL <http://www.sciencedirect.com/science/article/pii/S2214860418303920>.
- Adrita Dass and Atieh Moridi. State of the Art in Directed Energy Deposition: From Additive Manufacturing to Materials Design. *Coatings*, 9(7):418, July 2019. ISSN 2079-6412. doi: 10.3390/coatings9070418. URL <https://www.mdpi.com/2079-6412/9/7/418>. Number: 7 Publisher: Multidisciplinary Digital Publishing Institute.
- Laurent Delrieu. C# isosurface - Grasshopper Developer, June 2020. URL <https://discourse.mcneel.com/t/c-isosurface/103491/2>. Library Catalog: discourse.mcneel.com.
- K. S. Derekar. A review of wire arc additive manufacturing and advances in wire arc additive manufacturing of aluminium. *Materials Science and Technology*, 34(8):895–916, May 2018. ISSN 0267-0836. doi: 10.1080/02670836.2018.1455012. URL <https://doi.org/10.1080/02670836.2018.1455012>.
- V. S. Deshpande, M. F. Ashby, and N. A. Fleck. Foam topology: bending versus stretching dominated architectures. *Acta Materialia*, 49(6):1035–1040, April 2001a. ISSN 1359-6454. doi: 10.1016/S1359-6454(00)00379-7. URL <http://www.sciencedirect.com/science/article/pii/S1359645400003797>.
- V. S. Deshpande, N. A. Fleck, and M. F. Ashby. Effective properties of the octet-truss lattice material. *Journal of the Mechanics and Physics of Solids*, 49(8):1747–1769, August 2001b. ISSN 0022-5096. doi: 10.1016/S0022-5096(01)00010-2. URL <https://www.sciencedirect.com/science/article/pii/S0022509601000102>.
- Donghong Ding, Zengxi Pan, Dominic Cuiuri, and Huijun Li. Wire-feed additive manufacturing of metal components: technologies, developments and future interests. *The International Journal of Advanced Manufacturing Technology*, 81(1):465–481, October 2015. ISSN 1433-3015. doi: 10.1007/s00170-015-7077-3. URL <https://doi.org/10.1007/s00170-015-7077-3>.
- Donghong Ding, Zengxi Pan, Dominic Cuiuri, Huijun Li, Nathan Larkin, and Stephen van Duin. Automatic multi-direction slicing algorithms for wire based additive manufacturing. *Robotics and Computer-Integrated Manufacturing*, 37:139–150, February 2016.

- ISSN 0736-5845. doi: 10.1016/j.rcim.2015.09.002. URL <http://www.sciencedirect.com/science/article/pii/S0736584515000873>.
- Akio Doi and Akio Koide. An Efficient Method of Triangulating Equi-Valued Surfaces by Using Tetrahedral Cells. *IEICE TRANSACTIONS on Information and Systems*, E74-D (1):214–224, January 1991. ISSN , 0916-8532. URL https://search.ieice.org/bin/summary.php?id=e74-d_1_214&category=D&year=1991&lang=E&abst=. Publisher: The Institute of Electronics, Information and Communication Engineers.
- A. G. Evans, J. W. Hutchinson, N. A. Fleck, M. F. Ashby, and H. N. G. Wadley. The topological design of multifunctional cellular metals. *Progress in Materials Science*, 46 (3):309–327, January 2001. ISSN 0079-6425. doi: 10.1016/S0079-6425(00)00016-5. URL <http://www.sciencedirect.com/science/article/pii/S0079642500000165>.
- Jiawei Feng, Jianzhong Fu, Zhiwei Lin, Ce Shang, and Xiaomiao Niu. Layered in-fill area generation from triply periodic minimal surfaces for additive manufacturing. *Computer-Aided Design*, 107:50–63, February 2019. ISSN 0010-4485. doi: 10.1016/j.cad.2018.09.005. URL <http://www.sciencedirect.com/science/article/pii/S0010448517302592>.
- William E. Frazier. Metal Additive Manufacturing: A Review. *Journal of Materials Engineering and Performance*, 23(6):1917–1928, June 2014. ISSN 1544-1024. doi: 10.1007/s11665-014-0958-z. URL <https://doi.org/10.1007/s11665-014-0958-z>.
- Wei Gao, Yunbo Zhang, Devarajan Ramanujan, Karthik Ramani, Yong Chen, Christopher B. Williams, Charlie C. L. Wang, Yung C. Shin, Song Zhang, and Pablo D. Zavattieri. The status, challenges, and future of additive manufacturing in engineering. *Computer-Aided Design*, 69:65–89, December 2015. ISSN 0010-4485. doi: 10.1016/j.cad.2015.04.001. URL <http://www.sciencedirect.com/science/article/pii/S0010448515000469>.
- Lorna J. Gibson and Michael F. Ashby. *Cellular Solids: Structure and Properties*. Cambridge Solid State Science Series. Cambridge University Press, Cambridge, 2 edition, 1997. ISBN 978-0-521-49911-8. doi: 10.1017/CBO9781139878326. URL <https://www.cambridge.org/core/books/cellular-solids/BC25789552BAA8E3CAD5E1D105612AB5>.
- Annamaria Gisario, Michele Kazarian, Filomeno Martina, and Mehrshad Mehrpouya. Metal additive manufacturing in the commercial aviation industry: A review. *Journal of Manufacturing Systems*, 53:124–149, October 2019. ISSN 0278-6125. doi: 10.1016/j.jmsy.2019.08.005. URL <http://www.sciencedirect.com/science/article/pii/S0278612519300731>.
- R. Gümrük and R. A. W. Mines. Compressive behaviour of stainless steel micro-lattice structures. *International Journal of Mechanical Sciences*, 68:125–139, March 2013. ISSN 0020-7403. doi: 10.1016/j.ijmecsci.2013.01.006. URL <https://www.sciencedirect.com/science/article/pii/S0020740313000118>.
- Seung Chul Han, Jeong Woo Lee, and Kiju Kang. A New Type of Low Density Material: Shellular. *Advanced Materials*, 27(37):5506–5511, 2015. ISSN 1521-4095. doi: 10.1002/adma.201501546. URL <http://onlinelibrary.wiley.com/doi/abs/10.1002/adma.201501546>. eprint: <https://onlinelibrary.wiley.com/doi/pdf/10.1002/adma.201501546>.

- J.-Y. Hascoët, V. Querard, and M. Rauch. Interests of 5 axis toolpaths generation for Wire Arc Additive Manufacturing of aluminum alloys. *Journal of Machine Engineering*, Vol. 17, No. 3, 2017. ISSN 1895-7595. URL <http://yadda.icm.edu.pl/yadda/element/bwmeta1.element.baztech-7e3203dd-6426-4b82-bbd2-257b322df0ea>.
- R. Hedayati, A. M. Leeflang, and A. A. Zadpoor. Additively manufactured metallic pentamode meta-materials. *Applied Physics Letters*, 110(9):091905, February 2017. ISSN 0003-6951. doi: 10.1063/1.4977561. URL <http://aip.scitation.org/doi/10.1063/1.4977561>. Publisher: American Institute of Physics.
- R. Hedayati, S. M. Ahmadi, K. Lietaert, B. Pouran, Y. Li, H. Weinans, C. D. Rans, and A. A. Zadpoor. Isolated and modulated effects of topology and material type on the mechanical properties of additively manufactured porous biomaterials. *Journal of the Mechanical Behavior of Biomedical Materials*, 79:254–263, March 2018. ISSN 1751-6161. doi: 10.1016/j.jmbbm.2017.12.029. URL <https://www.sciencedirect.com/science/article/pii/S1751616117305738>.
- ISO/ASTM. ISO/ASTM 52900:2021 Additive manufacturing — General principles — Fundamentals and vocabulary, 2021. URL <https://www.iso.org/cms/render/live/en/sites/isoorg/contents/data/standard/07/45/74514.html>.
- Heran Jia, Hongshuai Lei, Panding Wang, Jinxin Meng, Chuanlei Li, Hao Zhou, Xiaoyu Zhang, and Daining Fang. An experimental and numerical investigation of compressive response of designed Schwarz Primitive triply periodic minimal surface with non-uniform shell thickness. *Extreme Mechanics Letters*, 37:100671, May 2020. ISSN 2352-4316. doi: 10.1016/j.eml.2020.100671. URL <http://www.sciencedirect.com/science/article/pii/S2352431620300468>.
- Alistair Jones, Martin Leary, Stuart Bateman, and Mark Easton. TPMS Designer: A tool for generating and analyzing triply periodic minimal surfaces. *Software Impacts*, 10:100167, November 2021. ISSN 2665-9638. doi: 10.1016/j.simpa.2021.100167. URL <https://www.sciencedirect.com/science/article/pii/S2665963821000713>.
- Dongseok Kang, Sanghu Park, Yong Son, Simo Yeon, Sang Hoon Kim, and Ilyong Kim. Multi-lattice inner structures for high-strength and light-weight in metal selective laser melting process. *Materials & Design*, 175:107786, August 2019. ISSN 0264-1275. doi: 10.1016/j.matdes.2019.107786. URL <https://www.sciencedirect.com/science/article/pii/S0264127519302230>.
- Hermann Karcher, Konrad Polthier, Jacek Klinowski, and Alan Lindsay Mackay. Construction of triply periodic minimal surfaces. *Philosophical Transactions of the Royal Society of London. Series A: Mathematical, Physical and Engineering Sciences*, 354 (1715):2077–2104, September 1996. doi: 10.1098/rsta.1996.0093. URL <https://royalsocietypublishing.org/doi/abs/10.1098/rsta.1996.0093>. Publisher: Royal Society.
- Martin Leary, Maciej Mazur, Joe Elambasseril, Matthew McMillan, Thomas Chirent, Yingying Sun, Ma Qian, Mark Easton, and Milan Brandt. Selective laser melting (SLM) of AlSi12Mg lattice structures. *Materials & Design*, 98:344–357, May 2016. ISSN 0264-1275. doi: 10.1016/j.matdes.2016.02.127. URL <https://www.sciencedirect.com/science/article/pii/S0264127516302726>.

- Dong-Wook Lee, Kamran A. Khan, and Rashid K. Abu Al-Rub. Stiffness and yield strength of architected foams based on the Schwarz Primitive triply periodic minimal surface. *International Journal of Plasticity*, 95:1–20, August 2017. ISSN 0749-6419. doi: 10.1016/j.ijplas.2017.03.005. URL <http://www.sciencedirect.com/science/article/pii/S0749641916302388>.
- Hongshuai Lei, Chuanlei Li, Jinxin Meng, Hao Zhou, Yabo Liu, Xiaoyu Zhang, Pand-ing Wang, and Daining Fang. Evaluation of compressive properties of SLM-fabricated multi-layer lattice structures by experimental test and micro-CT-based finite element analysis. *Materials & Design*, 169:107685, May 2019. ISSN 0264-1275. doi: 10.1016/j.matdes.2019.107685. URL <https://www.sciencedirect.com/science/article/pii/S0264127519301224>.
- Nikita Letov and Yaoyao Fiona Zhao. A geometric modelling framework to support the design of heterogeneous lattice structures with non-linearly varying geometry. *Journal of Computational Design and Engineering*, 9(5):1565–1584, October 2022. ISSN 2288-5048. doi: 10.1093/jcde/qwac076. URL <https://doi.org/10.1093/jcde/qwac076>.
- Dawei Li, Ning Dai, Xiaotong Jiang, and Xiaosheng Chen. Interior structural optimization based on the density-variable shape modeling of 3D printed objects. *The International Journal of Advanced Manufacturing Technology*, 83(9):1627–1635, April 2016. ISSN 1433-3015. doi: 10.1007/s00170-015-7704-z. URL <https://doi.org/10.1007/s00170-015-7704-z>.
- Dawei Li, Wenhe Liao, Ning Dai, Guoying Dong, Yunlong Tang, and Yi Min Xie. Optimal design and modeling of gyroid-based functionally graded cellular structures for additive manufacturing. *Computer-Aided Design*, 104:87–99, November 2018. ISSN 0010-4485. doi: 10.1016/j.cad.2018.06.003. URL <http://www.sciencedirect.com/science/article/pii/S0010448518300381>.
- Dawei Li, Wenhe Liao, Ning Dai, and Yi Min Xie. Comparison of Mechanical Properties and Energy Absorption of Sheet-Based and Strut-Based Gyroid Cellular Structures with Graded Densities. *Materials*, 12(13):2183, January 2019. doi: 10.3390/ma12132183. URL <https://www.mdpi.com/1996-1944/12/13/2183>.
- Shuguang Li. Boundary conditions for unit cells from periodic microstructures and their implications. *Composites Science and Technology*, 68(9):1962–1974, July 2008. ISSN 0266-3538. doi: 10.1016/j.compscitech.2007.03.035. URL <https://www.sciencedirect.com/science/article/pii/S0266353807001534>.
- Shuguang Li and Anchana Wongsto. Unit cells for micromechanical analyses of particle-reinforced composites. *Mechanics of Materials*, 36(7):543–572, July 2004. ISSN 0167-6636. doi: 10.1016/S0167-6636(03)00062-0. URL <https://www.sciencedirect.com/science/article/pii/S0167663603000620>.
- Sakkadech Limmahakhun, Adekunle Oloyede, Kriskrai Sitthiseripratip, Yin Xiao, and Cheng Yan. Stiffness and strength tailoring of cobalt chromium graded cellular structures for stress-shielding reduction. *Materials & Design*, 114:633–641, January 2017. ISSN 0264-1275. doi: 10.1016/j.matdes.2016.11.090. URL <https://www.sciencedirect.com/science/article/pii/S0264127516314915>.
- William E. Lorensen and Harvey E. Cline. Marching cubes: A high resolution 3D surface construction algorithm. *ACM SIGGRAPH Computer Graphics*, 21(4):163–169, August

1987. ISSN 0097-8930. doi: 10.1145/37402.37422. URL <https://doi.org/10.1145/37402.37422>.
- Alan L. Mackay. Periodic minimal surfaces. *Physica B+C*, 131(1-3):300–305, August 1985. ISSN 0378-4363. doi: 10.1016/0378-4363(85)90163-9. URL <http://www.sciencedirect.com/science/article/pii/0378436385901639>. Publisher: North-Holland.
- Tobias Maconachie, Martin Leary, Bill Lozanovski, Xuezhe Zhang, Ma Qian, Omar Faruque, and Milan Brandt. SLM lattice structures: Properties, performance, applications and challenges. *Materials & Design*, 183:108137, December 2019. ISSN 0264-1275. doi: 10.1016/j.matdes.2019.108137. URL <https://www.sciencedirect.com/science/article/pii/S0264127519305751>.
- S. Manokruang, F. Vignat, M. Museau, and M. Linousin. Model of weld beads geometry produced on surface temperatures by Wire and Arc Additive Manufacturing (WAAM). *IOP Conference Series: Materials Science and Engineering*, 1063(1):012008, February 2021a. ISSN 1757-899X. doi: 10.1088/1757-899X/1063/1/012008. URL <https://doi.org/10.1088/1757-899x/1063/1/012008>. Publisher: IOP Publishing.
- Supasit Manokruang, Frederic Vignat, Matthieu Museau, and Maxime Limousin. Process Parameters Effect on Weld Beads Geometry Deposited by Wire and Arc Additive Manufacturing (WAAM). In Lionel Roucoules, Manuel Paredes, Benoit Eynard, Paz Morer Camo, and Caterina Rizzi, editors, *Advances on Mechanics, Design Engineering and Manufacturing III*, Lecture Notes in Mechanical Engineering, pages 9–14, Cham, 2021b. Springer International Publishing. ISBN 978-3-030-70566-4. doi: 10.1007/978-3-030-70566-4_3.
- F. Martina, J. Mehnen, S. W. Williams, P. Colegrove, and F. Wang. Investigation of the benefits of plasma deposition for the additive layer manufacture of Ti-6Al-4V. *Journal of Materials Processing Technology*, 212(6):1377–1386, June 2012. ISSN 0924-0136. doi: 10.1016/j.jmatprotec.2012.02.002. URL <http://www.sciencedirect.com/science/article/pii/S0924013612000532>.
- I. Maskery, N. T. Aboulkhair, A. O. Aremu, C. J. Tuck, I. A. Ashcroft, R. D. Wildman, and R. J. M. Hague. A mechanical property evaluation of graded density Al-Si10-Mg lattice structures manufactured by selective laser melting. *Materials Science and Engineering: A*, 670:264–274, July 2016. ISSN 0921-5093. doi: 10.1016/j.msea.2016.06.013. URL <http://www.sciencedirect.com/science/article/pii/S092150931630658X>.
- I. Maskery, N. T. Aboulkhair, A. O. Aremu, C. J. Tuck, and I. A. Ashcroft. Compressive failure modes and energy absorption in additively manufactured double gyroid lattices. *Additive Manufacturing*, 16:24–29, August 2017a. ISSN 2214-8604. doi: 10.1016/j.addma.2017.04.003. URL <https://www.sciencedirect.com/science/article/pii/S2214860417301203>.
- I. Maskery, A. O. Aremu, L. Parry, R. D. Wildman, C. J. Tuck, and I. A. Ashcroft. Effective design and simulation of surface-based lattice structures featuring volume fraction and cell type grading. *Materials & Design*, 155:220–232, October 2018a. ISSN 0264-1275. doi: 10.1016/j.matdes.2018.05.058. URL <http://www.sciencedirect.com/science/article/pii/S026412751830443X>.

- I. Maskery, L. Sturm, A. O. Aremu, A. Panesar, C. B. Williams, C. J. Tuck, R. D. Wildman, I. A. Ashcroft, and R. J. M. Hague. Insights into the mechanical properties of several triply periodic minimal surface lattice structures made by polymer additive manufacturing. *Polymer*, 152:62–71, September 2018b. ISSN 0032-3861. doi: 10.1016/j.polymer.2017.11.049. URL <http://www.sciencedirect.com/science/article/pii/S0032386117311175>.
- Ian Maskery, Alexandra Hussey, Ajit Panesar, Adedeji Aremu, Christopher Tuck, Ian Ashcroft, and Richard Hague. An investigation into reinforced and functionally graded lattice structures. *Journal of Cellular Plastics*, 53(2):151–165, March 2017b. ISSN 0021-955X. doi: 10.1177/0021955X16639035. URL <https://doi.org/10.1177/0021955X16639035>.
- Maciej Mazur, Martin Leary, Shoujin Sun, Martin Vcelka, Darpan Shidid, and Milan Brandt. Deformation and failure behaviour of Ti-6Al-4V lattice structures manufactured by selective laser melting (SLM). *The International Journal of Advanced Manufacturing Technology*, 84(5):1391–1411, May 2016. ISSN 1433-3015. doi: 10.1007/s00170-015-7655-4. URL <https://doi.org/10.1007/s00170-015-7655-4>.
- S. McKown, Y. Shen, W. K. Brookes, C. J. Sutcliffe, W. J. Cantwell, G. S. Langdon, G. N. Nurick, and M. D. Theobald. The quasi-static and blast loading response of lattice structures. *International Journal of Impact Engineering*, 35(8):795–810, August 2008. ISSN 0734-743X. doi: 10.1016/j.ijimpeng.2007.10.005. URL <https://www.sciencedirect.com/science/article/pii/S0734743X07001376>.
- Ferry P. W. Melchels, Katia Bertoldi, Ruggero Gabbrielli, Aldrik H. Velders, Jan Feijen, and Dirk W. Grijpma. Mathematically defined tissue engineering scaffold architectures prepared by stereolithography. *Biomaterials*, 31(27):6909–6916, September 2010. ISSN 0142-9612. doi: 10.1016/j.biomaterials.2010.05.068. URL <http://www.sciencedirect.com/science/article/pii/S0142961210007210>.
- Walter Mickel, Gerd E. Schröder-Turk, and Klaus Mecke. Tensorial Minkowski functionals of triply periodic minimal surfaces. *Interface Focus*, 2(5):623–633, October 2012. doi: 10.1098/rsfs.2012.0007. URL <http://royalsocietypublishing.org/doi/10.1098/rsfs.2012.0007>. Publisher: Royal Society.
- Edvard Rudolf Neovius. *Bestimmung zweier spezieller periodischer Minimalflächen*. Akad. Abhandlungen, Helsingfors. Frenckell, 1883.
- Tuan D. Ngo, Alireza Kashani, Gabriele Imbalzano, Kate T.Q. Nguyen, and David Hui. Additive manufacturing (3D printing): A review of materials, methods, applications and challenges. *Composites Part B: Engineering*, 143:172–196, June 2018. ISSN 13598368. doi: 10.1016/j.compositesb.2018.02.012. URL <https://linkinghub.elsevier.com/retrieve/pii/S1359836817342944>.
- L. Nguyen, J. Buhl, and M. Bambach. Decomposition algorithm for tool path planning for wire-arc additive manufacturing. *Journal of Machine Engineering*, Vol. 18, No. 1, 2018. URL <http://yadda.icm.edu.pl/baztech/element/bwmeta1.element.baztech-9a36a1e7-0433-4505-9797-c496dd7b9ad6>.
- Ajit Panesar, Meisam Abdi, Duncan Hickman, and Ian Ashcroft. Strategies for functionally graded lattice structures derived using topology optimisation for Additive Manufacturing. *Additive Manufacturing*, 19:81–94, January 2018. ISSN 2214-8604.

- doi: 10.1016/j.addma.2017.11.008. URL <https://www.sciencedirect.com/science/article/pii/S221486041730115X>.
- C. G. Pickin, S. W. Williams, and M. Lunt. Characterisation of the cold metal transfer (CMT) process and its application for low dilution cladding. *Journal of Materials Processing Technology*, 211(3):496–502, March 2011. ISSN 0924-0136. doi: 10.1016/j.jmatprotec.2010.11.005. URL <http://www.sciencedirect.com/science/article/pii/S0924013610003456>.
- Daniel Piker. Isosurfaces / Signed Distance Fields - Grasshopper, February 2021. URL <https://discourse.mcneel.com/t/isosurfaces-signed-distance-fields/118745>. Library Catalog: discourse.mcneel.com.
- A. Radman, X. Huang, and Y. M. Xie. Topology optimization of functionally graded cellular materials. *Journal of Materials Science*, 48(4):1503–1510, February 2013. ISSN 1573-4803. doi: 10.1007/s10853-012-6905-1. URL <https://doi.org/10.1007/s10853-012-6905-1>.
- Srinivasan Rajagopalan and Richard A. Robb. Schwarz meets Schwann: Design and fabrication of biomorphic and durataxic tissue engineering scaffolds. *Medical Image Analysis*, 10(5):693–712, October 2006. ISSN 1361-8415. doi: 10.1016/j.media.2006.06.001. URL <https://www.sciencedirect.com/science/article/pii/S1361841506000405>.
- E. A. Ramírez, Nicolas Beraud, Franck Pourroy, François Villeneuve, and Matthieu Museau. Influence des paramètres de conception sur la densité relative de cellules à base de surfaces minimales triplement périodiques (TPMS) pour la fabrication additive. In *17e Colloque National S-mart*, en visioconférence, France, March 2021a. URL <https://hal.archives-ouvertes.fr/hal-03290639>.
- E. A. Ramírez, N. Béraud, F. Pourroy, F. Villeneuve, and M. Museau. Design parameters effects on relative density of triply periodic minimal surfaces for additive manufacturing. *Procedia CIRP*, 100:13–18, January 2021b. ISSN 2212-8271. doi: 10.1016/j.procir.2021.05.002. URL <https://www.sciencedirect.com/science/article/pii/S2212827121004601>.
- Emilio A. Ramírez, Nicolas Beraud, Franck Pourroy, François Villeneuve, and Matthieu Museau. A design methodology for graded density triply periodic minimal surfaces. *Proceedings of the International Joint Conference on Mechanics, Design Engineering and Advanced Manufacturing (JCM 2022)*, 2022a.
- Emilio A. Ramírez, Nicolas Beraud, Franck Pourroy, François Villeneuve, and Matthieu Museau. Equivalent Material analysis of Triply Periodic Minimal Surfaces. *Proceedings of the 25ème Congrès Français de Mécanique (CFM 2022)*, 2022b.
- Khalil Refai, Marco Montemurro, Charles Brugger, and Nicolas Saintier. Determination of the effective elastic properties of titanium lattice structures. *Mechanics of Advanced Materials and Structures*, 27(23):1966–1982, December 2020. ISSN 1537-6494. doi: 10.1080/15376494.2018.1536816. URL <https://doi.org/10.1080/15376494.2018.1536816>. Publisher: Taylor & Francis eprint: <https://doi.org/10.1080/15376494.2018.1536816>.
- A. Reuss. Berechnung der Fließgrenze von Mischkristallen auf Grund der Plastizitätsbedingung für Einkristalle. *ZAMM - Journal of Applied Mathematics and Mechanics / Zeitschrift für Angewandte Mathematik und Mechanik*, 9

- (1):49–58, 1929. ISSN 1521-4001. doi: 10.1002/zamm.19290090104. URL <http://onlinelibrary.wiley.com/doi/abs/10.1002/zamm.19290090104>. eprint: <https://onlinelibrary.wiley.com/doi/pdf/10.1002/zamm.19290090104>.
- P. Robert, M. Museau, and H. Paris. Effect of Temperature on the Quality of Welding Beads Deposited with CMT Technology. In *2018 IEEE International Conference on Industrial Engineering and Engineering Management (IEEM)*, pages 680–684, December 2018. doi: 10.1109/IEEM.2018.8607636. ISSN: 2157-362X.
- Pascal Robert, Matthieu Museau, Henri Paris, Alexis van Wesemael, and Xavier Gostiaux. Recouvrement acier par technologie CMT : Réalisation et propriétés mécaniques. In *16ème Colloque National S.mart*, Les Karellis, France, April 2019. URL <https://hal.archives-ouvertes.fr/hal-03192506>.
- Pascal Robert, Nicolas Beraud, Matthieu Museau, and Henri Paris. A guide to select strain sensors to be embedded in smart metal parts built by WAAM. In *Conférence Manufacturing 21*, Angers (Virtuel), France, June 2021. URL <https://hal.archives-ouvertes.fr/hal-03350560>.
- Tiago A. Rodrigues, V. Duarte, R. M. Miranda, Telmo G. Santos, and J. P. Oliveira. Current Status and Perspectives on Wire and Arc Additive Manufacturing (WAAM). *Materials*, 12(7):1121, January 2019. doi: 10.3390/ma12071121. URL <https://www.mdpi.com/1996-1944/12/7/1121>.
- Jianzhong Ruan, Todd E. Sparks, Ajay Panackal, F. W. Liou, Kunayut Eiamsa-ard, Kevin Slattery, Hsin-Nan Chou, and Mary Kinsella. Automated Slicing for a Multiaxis Metal Deposition System. *Journal of Manufacturing Science and Engineering*, 129(2):303–310, April 2007. ISSN 1087-1357. doi: 10.1115/1.2673492. URL <https://asmedigitalcollection-asme-org.gaelnomade-1.grenet.fr/manufacturingscience/article/129/2/303/471943/Automated-Slicing-for-a-Multiaxis-Metal-Deposition>.
- E. Sallica-Leva, A. L. Jardini, and J. B. Fogagnolo. Microstructure and mechanical behavior of porous Ti–6Al–4V parts obtained by selective laser melting. *Journal of the Mechanical Behavior of Biomedical Materials*, 26:98–108, October 2013. ISSN 1751-6161. doi: 10.1016/j.jmbbm.2013.05.011. URL <https://www.sciencedirect.com/science/article/pii/S1751616113001768>.
- Gianpaolo Savio, Roberto Meneghello, and Gianmaria Concheri. Design of variable thickness triply periodic surfaces for additive manufacturing. *Progress in Additive Manufacturing*, 4(3):281–290, September 2019. ISSN 2363-9520. doi: 10.1007/s40964-019-00073-x. URL <https://doi.org/10.1007/s40964-019-00073-x>.
- Maik Rudolf Johann Scherer. Gyroid and Gyroid-Like Surfaces. In Maik Rudolf Johann Scherer, editor, *Double-Gyroid-Structured Functional Materials: Synthesis and Applications*, Springer Theses, pages 7–19. Springer International Publishing, Heidelberg, 2013. ISBN 978-3-319-00354-2. doi: 10.1007/978-3-319-00354-2_2. URL https://doi.org/10.1007/978-3-319-00354-2_2.
- Alan Hugh Schoen. *Infinite Periodic Minimal Surfaces Without Self-intersections*. National Aeronautics and Space Administration, 1970. Google-Books-ID: LxOb.NIMLtMC.

- Hermann Amandus Schwarz. *Gesammelte mathematische Abhandlungen*. American Mathematical Soc., 1972. ISBN 978-0-8284-0260-6. Google-Books-ID: cKWBJBcM_18C.
- Deepak Sharma and Somashekhar S. Hiremath. Additively manufactured mechanical metamaterials based on triply periodic minimal surfaces: Performance, challenges, and application. *Mechanics of Advanced Materials and Structures*, 0(0):1–31, August 2021. ISSN 1537-6494. doi: 10.1080/15376494.2021.1948151. URL <https://doi.org/10.1080/15376494.2021.1948151>. Publisher: Taylor & Francis .eprint: <https://doi.org/10.1080/15376494.2021.1948151>.
- M. Smith, Z. Guan, and W. J. Cantwell. Finite element modelling of the compressive response of lattice structures manufactured using the selective laser melting technique. *International Journal of Mechanical Sciences*, 67:28–41, February 2013. ISSN 0020-7403. doi: 10.1016/j.ijmecsci.2012.12.004. URL <https://www.sciencedirect.com/science/article/pii/S0020740312002639>.
- Thomas Tancogne-Dejean, Marianna Diamantopoulou, Maysam B. Gorji, Colin Bonatti, and Dirk Mohr. 3D Plate-Lattices: An Emerging Class of Low-Density Metamaterial Exhibiting Optimal Isotropic Stiffness. *Advanced Materials*, 30(45):1803334, 2018. ISSN 1521-4095. doi: 10.1002/adma.201803334. URL <http://onlinelibrary.wiley.com/doi/abs/10.1002/adma.201803334>. .eprint: <https://onlinelibrary.wiley.com/doi/pdf/10.1002/adma.201803334>.
- Evangelos Tyflopoulos, Flem David Tollnes, Martin Steinert, and Anna Olsen. State of the art of generative design and topology optimization and potential research needs, 2018. URL <https://www.designsociety.org/publication/40924/State+of+the+art+of+generative+design+and+topology+optimization+and+potential+research+needs>.
- Pinar Urhal, Andrew Weightman, Carl Diver, and Paulo Bartolo. Robot assisted additive manufacturing: A review. *Robotics and Computer-Integrated Manufacturing*, 59:335–345, October 2019. ISSN 0736-5845. doi: 10.1016/j.rcim.2019.05.005. URL <http://www.sciencedirect.com/science/article/pii/S0736584518303636>.
- Benjamin Vayre, Frédéric Vignat, and François Villeneuve. Metallic additive manufacturing: state-of-the-art review and prospects. *Mechanics & Industry*, 13(2): 89–96, 2012. ISSN 2257-7777, 2257-7750. doi: 10.1051/meca/2012003. URL <http://www.cambridge.org/core/journals/mechanics-and-industry/article/metallic-additive-manufacturing-stateoftheart-review-and-prospects/C18A48653A671D0375A49506829C5A33>.
- W. Voigt. Ueber die Beziehung zwischen den beiden Elasticitätsconstanten isotroper Körper. *Annalen der Physik*, 274(12):573–587, 1889. ISSN 1521-3889. doi: 10.1002/andp.18892741206. URL <http://onlinelibrary.wiley.com/doi/abs/10.1002/andp.18892741206>. .eprint: <https://onlinelibrary.wiley.com/doi/pdf/10.1002/andp.18892741206>.
- H. G. von Schnering and R. Nesper. Nodal surfaces of Fourier series: Fundamental invariants of structured matter. *Zeitschrift für Physik B Condensed Matter*, 83(3): 407–412, October 1991. ISSN 1431-584X. doi: 10.1007/BF01313411. URL <https://doi.org/10.1007/BF01313411>.

- S. W. Williams, F. Martina, A. C. Addison, J. Ding, G. Pardal, and P. Colegrove. Wire + Arc Additive Manufacturing. *Materials Science and Technology*, 32(7):641–647, May 2016. ISSN 0267-0836. doi: 10.1179/1743284715Y.0000000073. URL <https://doi.org/10.1179/1743284715Y.0000000073>.
- Meinhard Wohlgemuth, Nataliya Yufa, James Hoffman, and Edwin L. Thomas. Triply Periodic Bicontinuous Cubic Microdomain Morphologies by Symmetries. *Macromolecules*, 34(17):6083–6089, August 2001. ISSN 0024-9297. doi: 10.1021/ma0019499. URL <https://doi.org/10.1021/ma0019499>. Publisher: American Chemical Society.
- Frederik Wulle, Daniel Coupek, Florian Schäffner, Alexander Verl, Felix Oberhofer, and Thomas Maier. Workpiece and Machine Design in Additive Manufacturing for Multi-Axis Fused Deposition Modeling. *Procedia CIRP*, 60:229–234, January 2017. ISSN 2212-8271. doi: 10.1016/j.procir.2017.01.046. URL <http://www.sciencedirect.com/science/article/pii/S2212827117300471>.
- Zefeng Xiao, Yongqiang Yang, Ran Xiao, Yuchao Bai, Changhui Song, and Di Wang. Evaluation of topology-optimized lattice structures manufactured via selective laser melting. *Materials & Design*, 143:27–37, April 2018. ISSN 0264-1275. doi: 10.1016/j.matdes.2018.01.023. URL <https://www.sciencedirect.com/science/article/pii/S0264127518300303>.
- Shanqing Xu, Jianhu Shen, Shiwei Zhou, Xiaodong Huang, and Yi Min Xie. Design of lattice structures with controlled anisotropy. *Materials & Design*, 93:443–447, March 2016. ISSN 0264-1275. doi: 10.1016/j.matdes.2016.01.007. URL <http://www.sciencedirect.com/science/article/pii/S0264127516300120>.
- A. Yakovlev, E. Trunova, D. Grevey, M. Pilloz, and I. Smurov. Laser-assisted direct manufacturing of functionally graded 3D objects. *Surface and Coatings Technology*, 190(1):15–24, January 2005. ISSN 0257-8972. doi: 10.1016/j.surfcoat.2004.07.070. URL <http://www.sciencedirect.com/science/article/pii/S0257897204005936>.
- Chunze Yan, Liang Hao, Ahmed Hussein, Simon Lawrence Bubb, Philippe Young, and David Raymont. Evaluation of light-weight AlSi10Mg periodic cellular lattice structures fabricated via direct metal laser sintering. *Journal of Materials Processing Technology*, 214(4):856–864, April 2014a. ISSN 0924-0136. doi: 10.1016/j.jmatprotec.2013.12.004. URL <https://www.sciencedirect.com/science/article/pii/S0924013613003804>.
- Chunze Yan, Liang Hao, Ahmed Hussein, Philippe Young, and David Raymont. Advanced lightweight 316L stainless steel cellular lattice structures fabricated via selective laser melting. *Materials & Design*, 55:533–541, March 2014b. ISSN 0261-3069. doi: 10.1016/j.matdes.2013.10.027. URL <https://www.sciencedirect.com/science/article/pii/S0261306913009540>.
- Lei Yang, Raya Mertens, Massimiliano Ferrucci, Chunze Yan, Yusheng Shi, and Shoufeng Yang. Continuous graded Gyroid cellular structures fabricated by selective laser melting: Design, manufacturing and mechanical properties. *Materials & Design*, 162:394–404, January 2019. ISSN 0264-1275. doi: 10.1016/j.matdes.2018.12.007. URL <http://www.sciencedirect.com/science/article/pii/S0264127518308785>.
- Nan Yang, Zhi Quan, Dawei Zhang, and Yanling Tian. Multi-morphology transition hybridization CAD design of minimal surface porous structures for use in tissue engineering. *Computer-Aided Design*, 56:11–21, November 2014. ISSN 0010-4485. doi:

- 10.1016/j.cad.2014.06.006. URL <http://www.sciencedirect.com/science/article/pii/S0010448514001249>.
- Nan Yang, Shoujun Wang, Lilan Gao, Yutao Men, and Chunqiu Zhang. Building implicit-surface-based composite porous architectures. *Composite Structures*, 173:35–43, August 2017. ISSN 0263-8223. doi: 10.1016/j.compstruct.2017.04.004. URL <http://www.sciencedirect.com/science/article/pii/S0263822316305931>.
- Hanfeng Yin, Zhipeng Liu, Jinle Dai, Guilin Wen, and Chao Zhang. Crushing behavior and optimization of sheet-based 3D periodic cellular structures. *Composites Part B: Engineering*, 182:107565, February 2020. ISSN 1359-8368. doi: 10.1016/j.compositesb.2019.107565. URL <https://www.sciencedirect.com/science/article/pii/S1359836819322978>.
- Dong J. Yoo. Porous scaffold design using the distance field and triply periodic minimal surface models. *Biomaterials*, 32(31):7741–7754, November 2011. ISSN 0142-9612. doi: 10.1016/j.biomaterials.2011.07.019. URL <http://www.sciencedirect.com/science/article/pii/S0142961211007903>.
- Li Yuan, Songlin Ding, and Cuie Wen. Additive manufacturing technology for porous metal implant applications and triple minimal surface structures: A review. *Bioactive Materials*, 4:56–70, December 2019. ISSN 2452-199X. doi: 10.1016/j.bioactmat.2018.12.003. URL <http://www.sciencedirect.com/science/article/pii/S2452199X18300768>.
- Lei Zhang, Stefanie Feih, Stephen Daynes, Shuai Chang, Michael Yu Wang, Jun Wei, and Wen Feng Lu. Energy absorption characteristics of metallic triply periodic minimal surface sheet structures under compressive loading. *Additive Manufacturing*, 23:505–515, October 2018. ISSN 2214-8604. doi: 10.1016/j.addma.2018.08.007. URL <http://www.sciencedirect.com/science/article/pii/S2214860418304688>.
- Miao Zhao, Fei Liu, Guang Fu, David Z. Zhang, Tao Zhang, and Hailun Zhou. Improved Mechanical Properties and Energy Absorption of BCC Lattice Structures with Triply Periodic Minimal Surfaces Fabricated by SLM. *Materials*, 11(12):2411, December 2018. doi: 10.3390/ma11122411. URL <https://www.mdpi.com/1996-1944/11/12/2411>.
- Miao Zhao, David Z. Zhang, Fei Liu, Zhonghua Li, Zhibo Ma, and Zhihao Ren. Mechanical and energy absorption characteristics of additively manufactured functionally graded sheet lattice structures with minimal surfaces. *International Journal of Mechanical Sciences*, 167:105262, February 2020. ISSN 0020-7403. doi: 10.1016/j.ijmecsci.2019.105262. URL <https://www.sciencedirect.com/science/article/pii/S002074031933437X>.
- Feng Zhu, Guoxing Lu, Dong Ruan, and Zhihua Wang. Plastic Deformation, Failure and Energy Absorption of Sandwich Structures with Metallic Cellular Cores. *International Journal of Protective Structures*, 1(4):507–541, December 2010. ISSN 2041-4196. doi: 10.1260/2041-4196.1.4.507. URL <https://doi.org/10.1260/2041-4196.1.4.507>. Publisher: SAGE Publications.
- Robert W. Zimmerman. Hashin-Shtrikman bounds on the poisson ratio of a composite material. *Mechanics Research Communications*, 19(6):563–569, November 1992. ISSN 0093-6413. doi: 10.1016/0093-6413(92)90085-O. URL <https://www.sciencedirect.com/science/article/pii/0093641392900850>.

Appendices

Appendix A

BeShape plug-in for Grasshopper

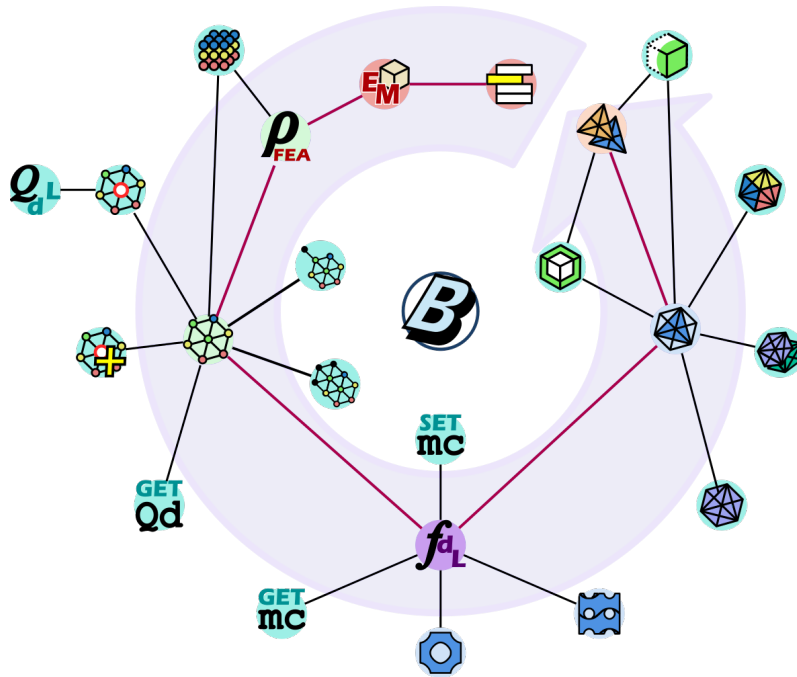

























Figure A.1: BeShape GH plug-in components family.

Introduction

The components detailed in the following section are grouped in Table A.1. All the components were developed using the RhinoCommon API inside the Grasshopper[®] environment of Rhinoceros[®] 7, and were compiled as a custom *BeShape* plug-in for the creation and modification of Primitive and Gyroid TPMS (Figure A.1). The implementations' source codes are not included in this document.

Table A.1: Developed Grasshopper components.

Category	Process	GH Component	Algorithm
TPMS Modelling	Design Specifications	 ANSYS fileReader	A.2.1
		 Equivalent Material Coefficients	A.2.2
	Density Mapping	 Density Mapping	A.1.1
		 Relative Density from FEA	A.2.3
	Design Parameter Mapping	 Design Parameters Mapping	A.1.2
	Fundamental Shape Generation	 Gyroid TPMS	A.1.5
		 Primitive TPMS	A.1.5
		 TPMS Mesh Generator	A.1.3
	Pattern Surface Creation	 SDF Offset	A.1.4
	Utility Components	Main Process utilities	 Density Finder
 Density Finder Plus			A.3.2
 Design Parameters Calculation			A.3.3
 DS Box Expand			A.3.4
Process Data		 Get modelling_conditions	A.4.4
		 Get Qdata	A.4.1
		 Q to Qdata	A.4.2
		 Q Distribution to Qdata	A.4.3
		 Set modelling_conditions	A.4.5
		Visualization	 Density Visualizer
 Mesh Color by DM			A.5.2
 Voxel Visualizer			A.5.3
FE Creation		 Mesh to SHELL	A.6.1
		 Variable Thickness ARRAY	A.6.2

A.1 Main methodology components for Graded density pattern assemblies' design

This section compiles the pseudocodes of the main process components, and fast TPMS pattern generators.

A.1.1 Density Mapping

Algorithm A.1.1 summarizes the Density Mapping process detailed in section 3.2.2.

Algorithm A.1.1 Density Mapping GH component

```

1: Load user inputs
2: if Run then
3:    $coord_{lists} \leftarrow$  Lists of node positions
4:    $datagridDistances \leftarrow \text{GridDistance}(coord_{lists}, \text{Counter}(coord_{lists}))$ 
5:    $count_{Qmap} \leftarrow \text{Counter}(coord_{lists}, ref_{dist})$ 
6:    $QmapDistances \leftarrow \text{GridDistance}(coord_{lists}, count_{Qmap})$ 
7:    $MaxGridDistance \leftarrow \max(datagridDistances)$ 
8:    $MaxQmapDistance \leftarrow \max(QmapDistances)$ 
9:    $sensitivity \leftarrow \max(QmapDistance, GridDistance)$ 
10:   $tolerance \leftarrow \min(MaxGridDistance, MaxQmapDistance)/2$ 
11:   $DM_{box} \leftarrow \text{Box}(coord_{lists}, \text{oversize})$ 
12:   $Q_{boxPoints} \leftarrow \text{PointCloud}(DM_{box}, coord_{lists}, QmapDistances)$ 
13:  for all points in  $Q_{boxPoints}$  do
14:    if Boundary point  $\wedge$  oversize then
15:       $Q_{adjusted} \text{ Add}(Q_{ext})$ 
16:    else
17:      for all input nodes position do
18:         $distance \leftarrow \text{DistanceToSquared}(Q_{pos}, Q_{boxPoints})$ 
19:        if distance < sensitivity then
20:          if distance < tolerance then
21:             $Q_{tolerance} \text{ Add}(Q_{pos})$ 
22:          else if approximation == By Weights then
23:             $Q_{weight} \text{ Add}(Q_{pos})$ 
24:          else if approximation == By Maximum then
25:             $Q_{maximum} \text{ Add}(Q_{pos})$ 
26:          end if
27:        end if
28:      end for
29:      if values on tolerance list then
30:         $Q_{adjusted} \text{ Add}(\max(Q_{tolerance}))$ 
31:      else if approximation == By Weights then
32:         $Q_{adjusted} \text{ Add weighted sum of } Q_{weight}$ 
33:      else if approximation == By Maximum then
34:         $Q_{adjusted} \text{ Add}(\max(Q_{maximum}))$ 
35:      end if
36:    end if
37:  end for
38: end if
39:  $Q\_data \leftarrow DM_{box}, count_{Qmap}, Q_{adjusted}, Q_{boxPoints}$ 
40: return  $Q\_data$ 

```

A.1.2 Design Parameter Mapping

Algorithm A.1.2 summarizes the Design Parameter Mapping process detailed in section 3.2.3.

Algorithm A.1.2 Design Parameter Mapping GH component

```

1: Load inputs
2:  $\alpha, \beta, \gamma \leftarrow \text{density\_model}(\text{TPMS\_ID})$ 
3: for all  $Q$  value do
4:    $ratio \leftarrow \text{Ratio}(\alpha, \beta, \gamma, Q)$ 
5: end for
6: if Constant modelling then
7:    $L_{map} \leftarrow L\_const$ 
8:    $d_{map} \leftarrow L\_const \times ratio_{const}$ 
9: else if Thickness modelling then
10:   $L_{map} \leftarrow L\_const$ 
11:  for all  $ratio$  do
12:     $d_{map} \text{ Add}(L\_const \times ratio)$ 
13:  end for
14: else if Length modelling then
15:  for all  $ratio$  do
16:     $L_{map} \text{ Add}(d\_const / ratio)$ 
17:  end for
18:   $d_{map} \leftarrow d\_const$ 
19: else if Ratio modelling then
20:   $rmax, rmin \leftarrow \max(ratio), \min(ratio)$ 
21:   $L_{map} \leftarrow L(L\_max, L\_min, rmax, rmin)$ 
22:  for all  $L$  do
23:     $d_{map} \text{ Add}(L \times ratio)$ 
24:  end for
25: end if
26:  $\text{modelling\_conditions} \leftarrow L_{map}, d_{map}, \text{TPMS\_ID}, \text{variation}$ 
27: return  $\text{modelling\_conditions}$ 

```

A.1.3 TPMS Mesh Generator

Algorithm A.1.3 summarizes the TPMS mesh generator process detailed in section 3.2.4.

Algorithm A.1.3 TPMS Mesh Generator GH component

```

1: Load inputs
2:  $\text{Design} \leftarrow \text{Q\_data}, \text{modelling\_conditions}$ 
3:  $\text{size}_{\max} \leftarrow \max(L_{\text{map}})/2$ 
4: if voxel size >  $\text{size}_{\max}$  then
5:   return RunTime Error
6: end if
7:  $\text{size}, nx, ny, nz \leftarrow \text{Initial\_voxel\_size}(\text{DS\_box}, \text{ref\_voxel\_size})$ 
8:  $h \leftarrow \text{factor}(\min(L_{\text{map}}))$ 
9:  $\text{size}_{\text{control}} \leftarrow h$ 
10: Log Add SubdivisionIterations( $\text{size}_{\text{control}}, \text{size}$ )
11: if Run then
12:    $\text{voxel}_{\text{list}} \leftarrow \text{Voxel\_cloud}(\text{DS\_box}, \text{Design}, \text{size}, nx, ny, nz)$ 
13:    $\text{threshold} \leftarrow 0$ 
14:    $\text{refined}_{\text{list}} \leftarrow \text{Voxel\_subdivision}(\text{voxel}_{\text{list}}, \text{iterations}, \text{threshold})$ 
15:    $\text{refined}_{\text{list}}, \text{erased}_{\text{list}} \leftarrow \text{Voxel\_cleaning}(\text{voxel}_{\text{list}}, \text{threshold})$ 
16:    $\text{mesh\_fundamental} \leftarrow \text{Isosurfacers}(\text{refined}_{\text{list}})$ 
17:    $\text{subdivisions} \leftarrow \text{refined}_{\text{list}}$ 
18:    $\text{erased} \leftarrow \text{erased}_{\text{list}}$ 
19:   return mesh_fundamental, subdivisions, erased
20: end if
21: return Log

```

A.1.4 SDF Offset

Algorithm A.1.4 summarizes the SDF Offset process detailed in section 3.2.5.

Algorithm A.1.4 SDF Offset GH component

```

1: Load inputs
2:  $\text{Design} \leftarrow \text{Q\_data, modelling\_conditions}$ 
3:  $\text{size}_{\max} \leftarrow \max(L_{\text{map}})/2$ 
4: if voxel size >  $\text{size}_{\max}$  then
5:   return RunTime Error
6: end if
7:  $\text{size}, nx, ny, nz \leftarrow \text{Initial\_voxel\_size}(\text{DS\_box}, \text{ref\_voxel\_size})$ 
8:  $h \leftarrow \text{factor}(\min(L_{\text{map}}), \max(d_{\text{map}}))$ 
9:  $\text{size}_{\text{control}} \leftarrow \min(h, \min(d_{\text{map}})/2)$ 
10: Log Add SubdivisionIterations( $\text{size}_{\text{control}}, \text{size}$ )
11: if Run then
12:    $\text{voxel}_{\text{list}} \leftarrow \text{Voxel\_cloud}(\text{DS\_box}, \text{Design}, \text{size}, nx, ny, nz)$ 
13:    $\text{threshold} \leftarrow \max(L_{\text{map}})$ 
14:    $\text{refined}_{\text{list}} \leftarrow \text{Voxel\_subdivision}(\text{voxel}_{\text{list}}, \text{iterations}, \text{threshold})$ 
15:    $\text{refined}_{\text{list}}, \text{erased}_{\text{list}} \leftarrow \text{Voxel\_cleaning}(\text{voxel}_{\text{list}}, \text{threshold})$ 
16:    $SDF_A, SDF_B \leftarrow \text{SDF\_offset}$ 
17:    $\text{mesh}_A \leftarrow \text{Isosurfacers}(SDF_A)$ 
18:    $\text{mesh}_B \leftarrow \text{Isosurfacers}(SDF_B)$ 
19:    $\text{voxel\_size} \leftarrow \text{size}, \text{size}_{\text{control}}$ 
20:    $\text{subdivisions} \leftarrow \text{refined}_{\text{list}}$ 
21:    $\text{erased} \leftarrow \text{erased}_{\text{list}}$ 
22:   return mesh_A, mesh_B, voxel_size, subdivisions, erased
23: end if
24: return Log

```

A.1.5 Simplified TPMS

Algorithm A.1.5 summarizes the process of the Primitive TPMS and Gyroid TPMS components, discussed in section 3.2.7.

Algorithm A.1.5 Primitive and Gyroid TPMS GH components

```

1: Load inputs
2:  $\text{Design} \leftarrow \text{Q\_data, modelling\_conditions}$ 
3:  $\text{size}_{\max} \leftarrow \max(L_{\text{map}})/2$ 
4: if voxel size >  $\text{size}_{\max}$  then
5:   return RunTime Error
6: end if
7:  $\text{size, nx, ny, nz} \leftarrow \text{Initial\_voxel\_size}(\text{DS\_box, ref\_voxel\_size})$ 
8:  $h \leftarrow \text{factor}(\min(L_{\text{map}}))$ 
9:  $\text{size}_{\text{control}} \leftarrow h$ 
10: Log Add SubdivisionIterations( $\text{size}_{\text{control}}, \text{size}$ )
11: if Run then
12:    $\text{voxel}_{\text{list}} \leftarrow \text{Voxel\_cloud}(\text{DS\_box, Design, size, nx, ny, nz})$ 
13:    $\text{threshold} \leftarrow 0$ 
14:    $\text{refined}_{\text{list}} \leftarrow \text{Voxel\_subdivision}(\text{voxel}_{\text{list}}, \text{iterations, threshold})$ 
15:    $\text{refined}_{\text{list}}, \text{erased}_{\text{list}} \leftarrow \text{Voxel\_cleaning}(\text{voxel}_{\text{list}}, \text{threshold})$ 
16:    $\text{mesh\_fundamental} \leftarrow \text{Isosurfacer}(\text{refined}_{\text{list}})$ 
17:   if offset then
18:      $h \leftarrow \text{factor}(\min(L_{\text{map}}), \min(d_{\text{map}}))$ 
19:      $\text{size}_{\text{control}} \leftarrow \min(h, \min(d_{\text{map}})/2)$ 
20:     Log Add SubdivisionIterations( $\text{size}_{\text{control}}, \text{size}$ )
21:      $\text{voxel}_{\text{list}} \leftarrow \text{Voxel\_cloud}(\text{DS\_box, Design, size, nx, ny, nz})$ 
22:      $\text{threshold} \leftarrow \max(L_{\text{map}})$ 
23:      $\text{refined}_{\text{list}} \leftarrow \text{Voxel\_subdivision}(\text{voxel}_{\text{list}}, \text{iterations, threshold})$ 
24:      $\text{refined}_{\text{list}}, \text{erased}_{\text{list}} \leftarrow \text{Voxel\_cleaning}(\text{voxel}_{\text{list}}, \text{threshold})$ 
25:      $SDF_A, SDF_B \leftarrow \text{SDF\_offset}$ 
26:      $\text{mesh\_A} \leftarrow \text{Isosurfacer}(SDF_A)$ 
27:      $\text{mesh\_B} \leftarrow \text{Isosurfacer}(SDF_B)$ 
28:   end if
29:    $\text{voxel\_size} \leftarrow \text{size, size}_{\text{control}}$ 
30:    $\text{subdivisions} \leftarrow \text{refined}_{\text{list}}$ 
31:    $\text{erased} \leftarrow \text{erased}_{\text{list}}$ 
32:   return mesh_fundamental, mesh_A, mesh_B, voxel_size, subdivisions, erased
33: end if
34: return Log

```

A.2 Components for Equivalent Material analysis

A.2.1 ANSYS fileReader

Algorithm A.2.1 summarizes process to read an exported results file from ANSYS[®], as detailed in section 4.2.1. The process works by an internal **FEAdata** class that stores the positions and values extracted from the input results text file.

Algorithm A.2.1 ANSYS fileReader GH component

```

1: Load inputs
2: if Run then
3:   dataLines  $\leftarrow$  ReadAllLines(filePath)
4:   for all dataLines do
5:     FEAdata  $\leftarrow$  dataLines
6:   end for
7:   positions  $\leftarrow$  FEAdata.positions
8:   FEA_data  $\leftarrow$  FEAdata.values
9:   max  $\leftarrow$  max(FEAdata.values)
10:  Log  $\leftarrow$  max, dataLines.Count
11: end if
12: return positions, FEA_data, max, Log

```

A.2.2 Equivalent Material Coefficients

As introduced in section 4.2.1, the full list of available models contained in the `Equivalent_Material_Coefficients` component. The models' reference data is stored on an internal `EM_model` class. Algorithm A.2.2 summarizes the component's internal processes

- Equivalent material model data, as defined by Table 4.1:
 - "primitive_M4_2022": Primitive 4x4x4 assembly model data
 - "gyroid_M4_2022": Gyroid 4x4x4 assembly model data
 - "primitive_UC_2022": Primitive unit-cell model data
 - "gyroid_UC_2022": Gyroid unit-cell model data
- Legacy model data, not included in this document:
 - "primitive_UC_old": Primitive unit-cell model data, solid TPMS model, constrained boundaries
 - "primitive_M4_old": Primitive 4x4x4 assembly model data, solid TPMS model, constrained boundaries
 - "gyroid_M4_old": Gyroid 4x4x4 assembly model data, solid TPMS model, constrained boundaries
- Legacy data from a BeShape project intern' analysis, not included in this document:
 - "primitive_oussama": Primitive unit-cell model data, solid TPMS model, free boundaries
 - "gyroid_oussama": Gyroid unit-cell model data, solid TPMS model, free boundaries
 - "primitive_oussama_V2": Primitive unit-cell model data, solid TPMS model, constrained boundaries
 - "gyroid_oussama_V2": Gyroid unit-cell model data, solid TPMS model, constrained boundaries

Algorithm A.2.2 Equivalent Material Coefficients GH component

```

1: Load inputs
2:  $model\_ref \leftarrow EM\_model$ 
3:  $c_1, n_1, c_3, n_3 \leftarrow model\_ref(model)$ 
4:  $\rho_E \leftarrow RelDensity(u, u\_perm, c_1, n_1)$ 
5:  $\rho_S \leftarrow RelDensity(stress, stress\_perm, c_3, n_3)$ 
6: if  $\rho_E > \rho_S$  then
7:   Log  $\leftarrow$  "Predominant effects of deformation"
8:   Log  $\leftarrow$  "Use E_Model.coefficients data"
9: else if  $\rho_S > \rho_E$  then
10:  Log  $\leftarrow$  "Predominant effects of stress"
11:  Log  $\leftarrow$  "Use S_Model.coefficients data"
12: end if
13: E_parameters  $\leftarrow c_1, n_1, u\_perm$ 
14: S_parameters  $\leftarrow c_3, n_3, stress\_perm$ 
15: TPMS_ID gets EM_model.ID
16: return E_parameters, S_parameters, TPMS_ID, Log

```

A.2.3 Relative Density from FEA

Algorithm A.2.3 summarizes process to calculated the relative density from FEA data nodes, as detailed in subsection 4.2.2.

Algorithm A.2.3 Relative Density from FEA GH component

```

1: Load inputs
2:  $Q_{max} \leftarrow Q_{max}$ 
3:  $Q_{min} \leftarrow Q_{min}$ 
4: if  $Q_{max} > \text{upper limit}$  then
5:    $Q_{max} \leftarrow \text{Density\_model}(\text{TPMS\_ID}).\text{GetLimits}(\text{maximum})$ 
6: end if
7: if  $Q_{min} < \text{lower limit}$  then
8:    $Q_{min} \leftarrow \text{Density\_model}(\text{TPMS\_ID}).\text{GetLimits}(\text{minimum})$ 
9: end if
10:  $c, n, \text{param\_perm}, \text{data\_type} \leftarrow \text{parameters}$ 
11: for all FEA nodes do
12:   if ( then  $\text{data\_type} = \text{deformation}$  )
13:      $\text{data} \leftarrow \text{ABS}(\text{FEA\_data} - \text{max}(\text{FEA\_data}))$ 
14:   else
15:      $\text{data} \leftarrow \text{FEA\_data}$ 
16:   end if
17:    $Q \leftarrow \text{RelDensity}(\text{data}, \text{param\_perm}, c, n)$ 
18:   if ( then  $Q > Q_{max}$  )
19:      $Q \leftarrow Q_{max}$ 
20:   else if  $Q < Q_{min}$  then
21:      $Q \leftarrow Q_{min}$ 
22:   end if
23:    $\text{rel\_density} \text{ Add}(Q)$ 
24: end for
25:  $Q\_calc \leftarrow \text{rel\_density}$ 
26:  $Q\_average \leftarrow \text{Average}(\text{rel\_density})$ 
27:  $\text{Log} \leftarrow \text{TPMS\_ID}, Q\_average, Q\_calc$ 
28: return  $Q\_calc, Q\_average, \text{Log}$ 

```

A.3 Main process utility components

This section compiles pseudocodes of utility process components.

A.3.1 Density Finder

Algorithm A.3.1 summarizes the Density Finder process detailed in section 3.2.7. The Plus variation is shown in Algorithm A.3.2.

Algorithm A.3.1 Density Finder utility GH component

```

1: Load inputs
2: for all positions do
3:    $density \leftarrow \text{Interpolation}(position, Q\_data)$ 
4:    $Q_{grid} \leftarrow position$ 
5: end for
6:  $Q\_local \leftarrow density$ 
7:  $local\_Q\_data \leftarrow \text{Density\_data}(density, Q_{grid})$ 
8: return  $Q\_local, local\_Q\_data$ 

```

Algorithm A.3.2 Density Finder Plus utility GH component

```

1: Load inputs
2: for all positions do
3:    $density \leftarrow \text{Interpolation}(position, Q\_data)$ 
4:    $thickness \leftarrow \text{Interpolation}(position, d_{map})$ 
5:    $length \leftarrow \text{Interpolation}(position, L_{map})$ 
6:    $Q_{grid} \leftarrow position$ 
7: end for
8:  $Q\_local \leftarrow density$ 
9:  $d\_local \leftarrow thickness$ 
10:  $L\_local \leftarrow length$ 
11:  $local\_Q\_data \leftarrow \text{Density\_data}(density, Q_{grid})$ 
12: return  $Q\_local, d\_local, L\_local, local\_Q\_data$ 

```

A.3.2 Design Parameter Calculation

The `Design_Parameter_Calculation` component, shown in Figure A.2, calculates the density Q , thickness d or length L depending on the component inputs. If a value is set for the density input, the parameter needs either a thickness or length to find the corresponding missing parameter. Else, the density is calculated when defining a thickness and length. The process is summarized on the pseudocode from Algorithm A.3.3.



Figure A.2: Design Parameter Calculation utility GH component overview.

Algorithm A.3.3 Design Parameter Calculation utility GH component

```

1: Load inputs
2:  $\alpha, \beta, \gamma \leftarrow \text{density\_model}(\text{TPMS\_ID})$ 
3: if  $Q \neq 0$  then
4:    $ratio \leftarrow \text{Ratio}(\alpha, \beta, \gamma, Q)$ 
5:   if  $d \neq 0$  then
6:      $L = d / ratio$ 
7:   else if  $L \neq 0$  then
8:      $d = L \times ratio$ 
9:   end if
10: else
11:   if  $d \neq 0 \wedge L \neq 0$  then
12:      $Q \leftarrow \text{RelDensity}(\alpha, \beta, \gamma, d, L)$ 
13:   end if
14: end if
15: return  $Q, d, L$ 

```

A.3.3 DS Box Expand

DS_Box_Expand component performs an adjustment of the DS bounding box dimensions, depending on the **oversize** condition. This component, shown in Figure A.3, is to be used before the Fundamental Shape Generation components, when applying an **oversize** to the density mapping. Log outputs information of the internal process, which is summarized in Algorithm A.3.4.

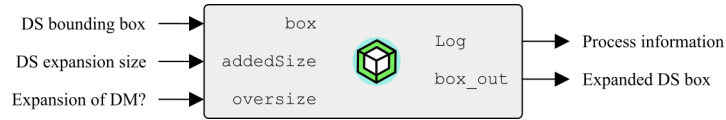


Figure A.3: DS Box Expand utility GH component overview.

Algorithm A.3.4 DS Box Expand utility GH component

```

1: Load inputs
2: if oversize then
3:   box_out  $\leftarrow$  Box(box, addedSize)
4:   Log  $\leftarrow$  Box expand message
5: else
6:   box_out  $\leftarrow$  Box
7:   Log  $\leftarrow$  Original Box dimension message
8: end if
9: return Log, box_out

```

A.4 Process data components

To ease the connections between components, two abstract classes, **Q_data** and **Modelling_conditions**, are used to group a series of variables from the outputs of the **Density_Mapping** and **Design_Parameter_Mapping** components, respectively. Even though these classes ease the I/O of data, they can be a black box for the user, thus the following components present methods for reading/setting data from/to these internal classes.

A.4.1 Get and Set Qdata

The **Get_Qdata** component (Figure A.4) reads the info stored on a **Q_data** class. The component reads the class properties' values and outputs them in the corresponding fields, as detailed in Algorithm A.4.1. As a reminder, **Q_data** is formed by an arrange of (n_x, n_y, n_z) (**DM_size**) relative density values **Q** in an ordered grid **Q_grid**, contained inside a **DM_box** bounding box.

Two options are available for setting a **Q_data** class, by a single density value to be contained in a bounding box or by establishing a ordered distribution of densities. The first option is run by the **Q_to_Qdata** component depicted in Figure A.5. Accordingly, the tool receives as inputs the desired (constant) relative density **Q** value to be distributed inside a bounding box **Q_box**. Algorithm A.4.2 details the pseudocode of this component.

The second setting option, **Q_Distribution_to_Qdata** (Figure A.6), receives the relative density values and positions, **Q_values** and **Q_pos**, respectively, and the number of elements representing their distribution on each coordinate (**nx**, **ny** and **nz**). The bounding box of these values is processed internally. Algorithm A.6 presents further details of the internal processes.

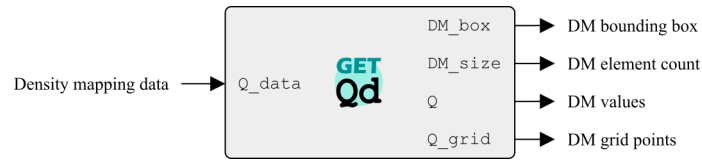


Figure A.4: Get Qdata GH component overview.



Figure A.5: Q to Qdata GH component overview.

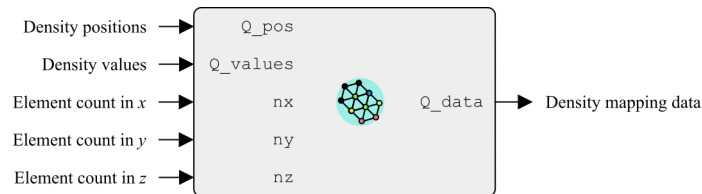


Figure A.6: Q Distribution to Qdata GH component overview.

Algorithm A.4.1 Get Qdata GH component

```

1: Load inputs
2: DM_box  $\leftarrow$  Q_data.DM_box
3: DM_size  $\leftarrow$  Q_data.DM_size
4: Q  $\leftarrow$  Q_data.Q
5: Q_grid  $\leftarrow$  Q_data.Q_grid
6: return DM_box, DM_size, Q, Q_grid

```

Algorithm A.4.2 Q to Qdata GH component

```

1: Load inputs
2: DM_box  $\leftarrow$  Q_box
3: DM_size  $\leftarrow$  (nx, ny, nz)
4: Q  $\leftarrow$  Q_values
5: Q_grid  $\leftarrow$  Q_positions
6: Q_data  $\leftarrow$  DM_box, DM_size, Q, Q_grid
7: return Q_data

```

Algorithm A.4.3 Q Distribution to Qdata GH component

```

1: Load inputs
2: DM_box  $\leftarrow$  Bounding box of Q_values
3: DM_size  $\leftarrow$  Q_data.DM_size
4: Q  $\leftarrow$  Q_data.Q
5: Q_grid  $\leftarrow$  Q_data.Q_grid
6: Q_data  $\leftarrow$  DM_box, DM_size, Q, Q_grid
7: return Q_data

```

A.4.2 Get and Set Modelling conditions

Reading of the `Modelling_conditions` data class contents is done by the `Get_modelling_conditions` component (Figure A.7, Algorithm A.4.4) and the customized creation of this class can be done by the `set_modelling_conditions` (Figure A.8, Algorithm A.4.5) component. The data class contains a collection of the thickness distribution `d_map`, the length mapping `L_map`, the TPMS type tag `TPMS_ID` and the required type of modelling `variation`.



Figure A.7: Get modelling_conditions GH component overview.



Figure A.8: Set modelling_conditions GH component overview.

Algorithm A.4.4 Get modelling_conditions GH component

- 1: Load inputs
 - 2: `d_map` \leftarrow `modelling_conditions.d_map`
 - 3: `L_map` \leftarrow `modelling_conditions.L_map`
 - 4: `TPMS_ID` \leftarrow `modelling_conditions.TPMS_ID`
 - 5: `variation` \leftarrow `modelling_conditions.variation`
 - 6: **return** `d_map`, `L_map`, `TPMS_ID`, `variation`
-

Algorithm A.4.5 Set modelling_conditions GH component

- 1: Load inputs
 - 2: `modelling_conditions` \leftarrow `d_map`, `L_map`, `TPMS_ID`, `variation`
 - 3: **return** `modelling_conditions`
-

A.5 Utility components for visualization

This section contains a set of tools for data visualization, mainly applied for process control purposes.

A.5.1 Density Visualizer

The `Density_visualizer` component (Figure A.9) performs the conversion of a density mapping data `Q_data` to a collection of point locations `P`, colours `C` and sizes `size` to be used in combination with the `Dot Display` GH tool for visualizing a collection of data as coloured points.

The assignation of colours depending on the density value works with a `Gradient` class storing the colour preset. The gradient is defined between the maximum and minimum values from the map, therefore, each density can be related to a different colour value. Similarly, the maximum dot size is related to the maximum density value Q_{max} , decaying until a third of this value for the minimum density Q_{min} . Accordingly, the sizing of the dots dot_size is accomplished by Equation A.1 as a function of a local density Q . The pseudocode of the process is shown on Algorithm A.5.1.

$$dotSize = \frac{max_size - \frac{max_size}{3}}{Q_{max} - Q_{min}} (Q - Q_{min}) + \frac{max_size}{3} \quad (A.1)$$

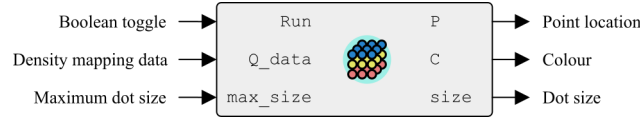


Figure A.9: Density visualizer GH component overview.

Algorithm A.5.1 Density visualizer GH component

```

1: Load inputs
2:  $Q_{max} \leftarrow \max(Q\_data.Q)$ 
3:  $Q_{min} \leftarrow \min(Q\_data.Q)$ 
4:  $gradient \leftarrow \text{Gradient}(Q_{max}, Q_{min})$ 
5: for all density values do
6:    $color \leftarrow \text{colour at } gradient(Q\_data.Q)$ 
7:    $size \leftarrow dotSize(Q\_data.Q, max\_size)$ 
8: end for
9:  $P \leftarrow Q\_data.Q\_grid$ 
10:  $C \leftarrow color$ 
11:  $size \leftarrow size$ 
12: return  $P, C, size$ 

```

A.5.2 Mesh Color by Density Map

The `Mesh_Color_by_Density_Map` (Figure A.10) performs the colouring of a STL mesh depending on the local density. The process first interpolates the density at each vertex of `mesh` from the density map defined `Q_data`. Similarly to the `Density_visualizer` component, each density is associated to a different colour from a `Gradient` between Q_{max} and Q_{min} . Each colour is then assigned to the mesh and returned on `colored_mesh` for their visualization. Algorithm A.5.2 details the pseudocode of this component. Examples of its application can be seen on the colour-gradient images of the fundamental shapes in section 3.3.

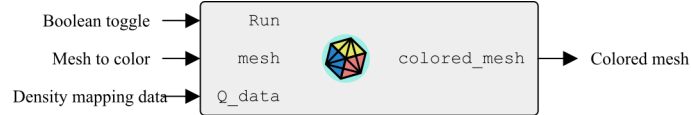


Figure A.10: Mesh Color by Density Map GH component overview.

Algorithm A.5.2 Mesh Color by Density Map GH component

- 1: Load inputs
 - 2: $Q \leftarrow \text{Interpolation}(\text{mesh.Vertices}, Q_data)$
 - 3: $Q_{max} \leftarrow \max(Q)$
 - 4: $Q_{min} \leftarrow \min(Q)$
 - 5: $gradient \leftarrow \text{Gradient}(Q_{max}, Q_{min})$
 - 6: **for all** density values **do**
 - 7: `colored_mesh` \leftarrow `mesh.VertexColors.Add(colour at $gradient(Q)$)`
 - 8: **end for**
 - 9: **return** `VertexColors`
-

A.5.3 Voxel Visualizer

The subdivided (refined) and erased voxels list obtained from the Fundamental Shape Generation and Patterns Surface Creation processes components (section 3.2.4 and section 3.2.5, respectively) produces abstract voxel classes storing the corner locations and the scalar field value, among other design information, associated with them. For their visualization and control, the **Voxel_visualizer** component (Figure A.11) creates a set of Box entities to represent a **voxel_list**. Applications of this component can be seen on the voxel cloud processing images shown in section 3.3. Algorithm A.5.3 presents the details of the internal component operations.



Figure A.11: Voxel Visualizer GH component overview.

Algorithm A.5.3 Voxel Visualizer GH component

```

1: Load inputs
2: for all voxels do
3:    $xSize \leftarrow \text{Interval}(\text{voxel.X.min}, \text{voxel.X.max})$ 
4:    $ySize \leftarrow \text{Interval}(\text{voxel.Y.min}, \text{voxel.Y.max})$ 
5:    $zSize \leftarrow \text{Interval}(\text{voxel.Z.min}, \text{voxel.Z.max})$ 
6:    $boxes \text{ Add}(\text{Box}(xSize, ySize, zSize))$ 
7: end for
8:  $\text{voxelBox} \leftarrow boxes$ 
9: return voxelBox

```

A.6 Finite Element processing components

A.6.1 Mesh to SHELL FE

Algorithm A.6.1 summarizes the STL to finite element mesh conversion process detailed in section 4.2.3.

Algorithm A.6.1 Mesh to SHELL FE GH component

```

1: Load inputs
2: if Run then
3:    $p \leftarrow \text{M.Vertices}$ 
4:    $f \leftarrow \text{M.Faces}$ 
5:   for all  $p$  do
6:      $N \text{ Add}(p \text{ on APDL format})$ 
7:   end for
8:   for all  $f$  do
9:      $E \text{ Add}(f \text{ on APDL format})$ 
10:  end for
11:   $full\_code \text{ Add}(\text{Workbench header instructions})$ 
12:   $full\_code \text{ Add}(\text{NBLOCK}(p))$ 
13:   $full\_code \text{ Add}(\text{EBLOCK}(f))$ 
14:   $\text{NODES} \leftarrow N$ 
15:   $\text{ELEMENTS} \leftarrow E$ 
16:   $\text{WB\_code} \leftarrow full\_code$ 
17:  if write then
18:     $\text{WB\_code}$  saved as fileName.txt in the current GH directory
19:  end if
20: end if
21: return  $\text{NODES}$ ,  $\text{ELEMENTS}$ ,  $\text{WB\_code}$ 

```

A.6.2 Variable Thickness ARRAY

Algorithm A.6.2 summarizes the codification of local thickness as a set of Mechanical APDL instructions, as detailed in section 4.2.3.

Algorithm A.6.2 Variable Thickness ARRAY GH component

```

1: Load inputs
2: if Run then
3:   for all Vertices do
4:      $d \leftarrow \text{Interpolation}(\text{vertex}, d\_map, Q\_data)$ 
5:      $local\_thickness \text{ Add}(d)$ 
6:   end for
7:    $tnode \leftarrow \text{ARRAY}(local\_thickness)$ 
8:   if write then
9:      $tnode$  saved as fileName.txt in the current GH directory
10:  end if
11: end if
12: return  $tnode$ 

```

Appendix B

Determination of effective elastic properties

As stated in subsection 1.2.1, the employed Gibson-Ashby models are adapted to cellular architectures assuming an isotropic macroscopic behaviour. Previous studies have determined that sheet-based Gyroid unit-cells have a structure close to isotropy [Li et al., 2019]. However, Primitive patterns may present the same Young modulus value along x , y and z axes due to their structural configuration, but the elastic behaviour of the macroscopic solid may not be isotropic.

A proposed approach by Refai et al. [2020] establishes that the mechanical behaviour between different scales can be predicted by a numerical homogenization technique based on the strain energy of periodic media, assuming that the unit-cell of the cellular configuration and the homogeneous solid have the same total strain energy (same deformation rate).

The process consists in evaluating the stiffness matrix \mathbf{C} of the cellular structure by applying an average strain field ε_{ij}^0 , considering six independent applications of an uniaxial strain field $\bar{\varepsilon}_\beta^0$, as shown in Equation B.1, for each of the strain tensor components. The columns of the stiffness matrix are determined by Equation B.2.

$$\bar{\varepsilon}_\beta^0 \neq 0 \text{ and } \bar{\varepsilon}_\gamma^0 = 0 \quad \gamma = 1, \dots, 6 ; \gamma \neq \beta \quad (\text{B.1})$$

$$C_{\alpha\beta} = \frac{\bar{\sigma}_\alpha}{\bar{\varepsilon}_\beta^0} \quad (\text{B.2})$$

The set of PBCs applied are summarized below, considering a unit-cell of size $2a_1 \times 2a_2 \times 2a_3$ defined in the domain $-a_i < x_i < a_i$, for $i = 1, 2, 3$.

Constraint equations on unit-cell faces:

$$\begin{aligned} u_i(a_1, x_2, x_3) - u_i(-a_1, x_2, x_3) &= 2a_1\varepsilon_{i1}^0 \\ u_i(x_1, a_2, x_3) - u_i(x_1, -a_2, x_3) &= 2a_2\varepsilon_{i2}^0 \\ u_i(x_1, x_2, a_3) - u_i(x_1, x_2, -a_3) &= 2a_3\varepsilon_{i3}^0 \end{aligned} \quad (\text{B.3})$$

Constraint equations on unit-cell edges:

$$\begin{aligned}
u_i(a_1, a_2, x_3) - u_i(-a_1, -a_2, x_3) - 2a_1\varepsilon_{i1}^0 - 2a_2\varepsilon_{i2}^0 &= 0 \\
u_i(a_1, -a_2, x_3) - u_i(-a_1, a_2, x_3) - 2a_1\varepsilon_{i1}^0 + 2a_2\varepsilon_{i2}^0 &= 0 \\
u_i(a_1, x_2, a_3) - u_i(-a_1, x_2, -a_3) - 2a_1\varepsilon_{i1}^0 - 2a_3\varepsilon_{i3}^0 &= 0 \\
u_i(a_1, x_2, -a_3) - u_i(-a_1, x_2, a_3) - 2a_1\varepsilon_{i1}^0 + 2a_3\varepsilon_{i3}^0 &= 0 \\
u_i(x_1, a_2, a_3) - u_i(x_1, -a_2, -a_3) - 2a_2\varepsilon_{i2}^0 - 2a_3\varepsilon_{i3}^0 &= 0 \\
u_i(x_1, a_2, -a_3) - u_i(x_1, -a_2, a_3) - 2a_2\varepsilon_{i2}^0 + 2a_3\varepsilon_{i3}^0 &= 0
\end{aligned} \tag{B.4}$$

Constraint equations on unit-cell corners:

$$\begin{aligned}
u_i(a_1, a_2, a_3) - u_i(-a_1, -a_2, -a_3) - 2a_1\varepsilon_{i1}^0 - 2a_2\varepsilon_{i2}^0 - 2a_3\varepsilon_{i3}^0 &= 0 \\
u_i(a_1, a_2, -a_3) - u_i(-a_1, -a_2, a_3) - 2a_1\varepsilon_{i1}^0 - 2a_2\varepsilon_{i2}^0 + 2a_3\varepsilon_{i3}^0 &= 0 \\
u_i(-a_1, a_2, a_3) - u_i(a_1, -a_2, -a_3) + 2a_1\varepsilon_{i1}^0 - 2a_2\varepsilon_{i2}^0 - 2a_3\varepsilon_{i3}^0 &= 0 \\
u_i(a_1, -a_2, a_3) - u_i(-a_1, a_2, -a_3) - 2a_1\varepsilon_{i1}^0 + 2a_2\varepsilon_{i2}^0 - 2a_3\varepsilon_{i3}^0 &= 0
\end{aligned} \tag{B.5}$$

Ultimately, the equivalent homogeneous anisotropic continuum properties can be calculated from the components of the compliance matrix $\mathbf{S} = \mathbf{C}^{-1}$.

To illustrate the procedure described above, a Primitive unit-cell of $L=50\text{mm}$ and $d=2\text{mm}$ ($\rho^* = 0.094$) is considered for analysis. The material for this topology is assumed to be elastic, with a Young modulus of 3.96GPa and a Poisson's ratio of $\nu=0.4$. The FE mesh was modelled by using 4-node tetrahedral solid elements (SOLID285) with four degrees of freedoms per node (three translations and one hydrostatic pressure), suitable for general materials from irregular CAD meshes. The finite element calculation was performed by a script in ANSYS[®] Mechanical APDL.

Accordingly, the effective elastic properties for the Primitive pattern are summarized in Table B.1. The studied topology shows a cubic symmetry behaviour at the macroscopic scale. In order to validate the results from the homogenization procedure, the values need to fall under appropriate bounds, which are discussed next.

The first verification is established by the Reuss-Voigt bounds [Voigt, 1889, Reuss, 1929], derived from linear elasticity analysis. The bounds can be determined by a law of mixtures, considering the volume fractions of the solid phase f_2 (TPMS architecture) and void f_1 , and their corresponding elastic properties. Thus, the upper C_{UB}^{RV} and lower C_{LB}^{RV} bounds can be determined by Equation B.6 and Equation B.7, respectively. From the equations, C_{gen} correspond to the elastic property (i.e. E, G, ν).

$$C_{UB}^{RV} = f_2 C_{gen} + f_1 C_{void} \tag{B.6}$$

$$C_{UB}^{RV} = \frac{f_2}{C_{gen}} + \frac{f_1}{C_{void}} \tag{B.7}$$

Following, the Hashin-Shtrikman bounds, detailed on [Zimmerman, 1992], are derived under the assumption that the material is homogeneous on a scale larger than any inhomogeneity and continuous displacements between adjacent phases [Refai et al., 2020]. Considering the two predefined phases, Equation B.8 and Equation B.9 establish the upper and lower bounds for the effective bulk K and shear G moduli, respectively. The bounds for Young modulus E and Poisson's ratio ν are detailed in Equation B.10 and Equation B.11, respectively.

Table B.1: Effective elastic properties results: Primitive UC $\rho^* = 0.094$.

Elastic property	E_1 E_2 E_3 (MPa)	G_{12} G_{23} G_{13} (MPa)	ν_{12} ν_{23} ν_{13}
Value	74.41 74.47 74.14	65.25 64.93 64.99	0.411 0.408 0.410

Table B.2: Elastic properties bounds.

Bounds	Reuss-Voigt	Hashin-Shtrikman
E (MPa)	(0.000 - 372.240)	(0.000 - 197.174)
G (MPa)	(0.000 - 132.943)	(0.000 - 77.077)
ν	(-1.000 - 0.500)	(-1.000 - 0.500)

$$K_{LB}^{HS} \leq K \leq K_{UB}^{HS} \quad (B.8)$$

$$K_{UB}^{HS} = K_2 + \frac{(K_1 - K_2)(3K_2 + 4G_2)f_1}{(3K_2 + 4G_2) + 3(K_1 - K_2)f_2}$$

$$K_{LB}^{HS} = K_1 + \frac{(K_2 - K_1)(3K_1 + 4G_1)f_2}{(3K_1 + 4G_1) + 3(K_2 - K_1)f_1}$$

$$G_{LB}^{HS} \leq G \leq G_{UB}^{HS} \quad (B.9)$$

$$G_{UB}^{HS} = G_2 + \frac{5G_2(G_1 - G_2)(3K_2 + 4G_2)f_1}{5G_2(3K_2 + 4G_2) + 6(G_1 - G_2)(K_2 + 2G_2)f_2}$$

$$G_{LB}^{HS} = G_1 + \frac{5G_1(G_2 - G_1)(3K_1 + 4G_1)f_2}{5G_1(3K_1 + 4G_1) + 6(G_2 - G_1)(K_1 + 2G_1)f_1}$$

$$\frac{K_{LB}^{HS} G_{LB}^{HS}}{3K_{LB}^{HS} + G_{LB}^{HS}} \leq E \leq \frac{K_{UB}^{HS} G_{UB}^{HS}}{3K_{UB}^{HS} + G_{UB}^{HS}} \quad (B.10)$$

$$\frac{3K_{LB}^{HS} - 2G_{UB}^{HS}}{6K_{LB}^{HS} + 2G_{UB}^{HS}} \leq \nu \leq \frac{3K_{UB}^{HS} - 2G_{LB}^{HS}}{6K_{UB}^{HS} + 2G_{LB}^{HS}} \quad (B.11)$$

The calculated bounds are summarized on Table B.2. The elastic properties of the void phase were set to a small value (1E-04) to avoid indeterminate results. The effective elastic properties fall under the respective bounds, thus validating their determination. In addition, Table B.3 summarizes the relative values of the Young and Shear moduli and their bounds, found by dividing them by the solid material E , to establish a comparison with the previous results found by the Gibson-Ashby models in section 4.1.

Even though the previous relative data also falls under the respective bounds, it has been determined that Gibson-Ashby models can only predict the mechanical properties of a cellular material up to relative densities of 20% [Refai et al., 2020]. Thus, further analysis of Primitive and Gyroid topologies with different relative densities are needed for establishing their characterization by the procedure detailed in this appendix. Nevertheless, regardless of the model used for the determination of local densities, the design validation stages of the proposed methodology perform a final FEA of the functionally graded construct, evaluating the response of the whole heterogeneous structure and comparing those results with the permissible design conditions.

Table B.3: Relative elastic properties.

	E	G
Effective (average)	0.0188	0.0164
Gibson-Ashby UC	0.0294	0.0150
Gibson-Ashby Matrix	0.0136	0.0067
Reuss-Voigt bounds	(0.000 - 0.0940)	(0.000 - 0.0335)
Hashin-Shtrikman bounds	(0.000 - 0.0497)	(0.000 - 0.0194)

Appendix C

C-shaped body case study

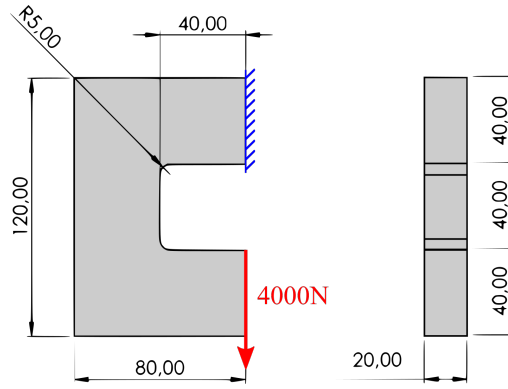


Figure C.1: C-shaped body: Dimensions and load conditions.

This complementary case study is illustrated for the design of a Gyroid-based FGCM with simultaneous thickness and length variation adapted to a C-shaped body, shown in Figure C.1, considering a material with a density of 4429Kg/m³, a Young modulus of 114GPa, a Poisson's ratio of 0.33, and a load of 4000N applied at the free end. Permissible design conditions establish a maximum displacement of 2mm at the free end and a maximum stress of 1100MPa with a safety factor of 2. All the calculations and images for the graded model were obtained from the use of the customized GH components of the *BeShape* plug-in.

The preliminary FEA for the applied load in the solid body is shown on Figure C.2. Accordingly, a constant relative density of $\rho_E^* = 0.281$ is obtained from the total displacement results, while a value of $\rho_\sigma^* = 0.592$ is obtained from the equivalent stress by applying the scaling laws for Gyroid matrix arrangements from section 4.1. As the effects of stress are predominant for the calculation of constant relative density values, the equivalent stress data is used for the calculation of local density values.

The density mapping procedure is illustrated on Figure C.3. According to the design methodology, the preliminary data from the FEA of the part (Figure C.2b) is used to calculate the local density values (Figure C.3a), which are then adjusted to a regular grid size of 8mm, shown in Figure C.3b. It is noteworthy that the density ranges from the FEA distribution and the regular grid are not the same. The lower limit is increased from a relative density of 0.095 to 0.300 by the inclusion of a minimum density threshold in the remapping process. In the other hand, the higher density limit is reduced from 0.592 (calculated maximum) to 0.476 (approximated maximum). The suitability of these ranges

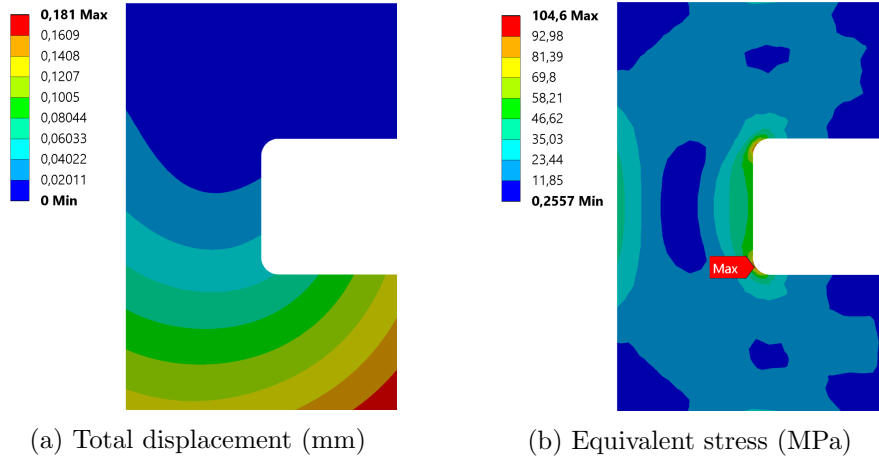


Figure C.2: C-shaped body: Preliminary FEA.

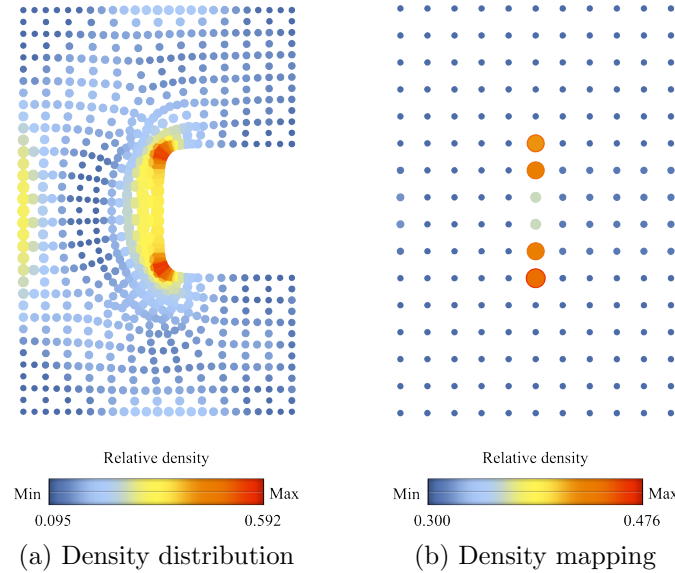


Figure C.3: C-shaped body: Density mapping from FEA.

is validated on the design evaluation stages.

Based on the mapped density values, the local design parameters are calculated for a simultaneous thickness and length variation. The graded model, shown on Figure C.4, has presents a thickness between 0.50 and 0.64mm, for unit-cells sizes between 4.00 and 5.00mm. As detailed in subsection 3.2.3, higher density zones are associated with smaller unit-cell sizes with bigger thicknesses, while lower density zones contain bigger unit-cells with smaller local thickness. Figure C.4a presents a colour gradient according to the density map. The graded model (Figure C.4b) represents the 32% of the original C-shaped body mass. The mass body information can be consulted in Table C.1.

With the information of local thickness values and the location of the mesh vertices of the fundamental mesh, the design is evaluated following the considerations detailed on subsection 4.2.3. The FEA results for total displacement and equivalent stress are depicted in Figure C.5. In addition, Table C.1 summarizes the evaluation results and presents a comparison with the FEA of a constant density modelling scenario. Similarly to the cantilever case study, the use of a graded density configuration reduces the overall

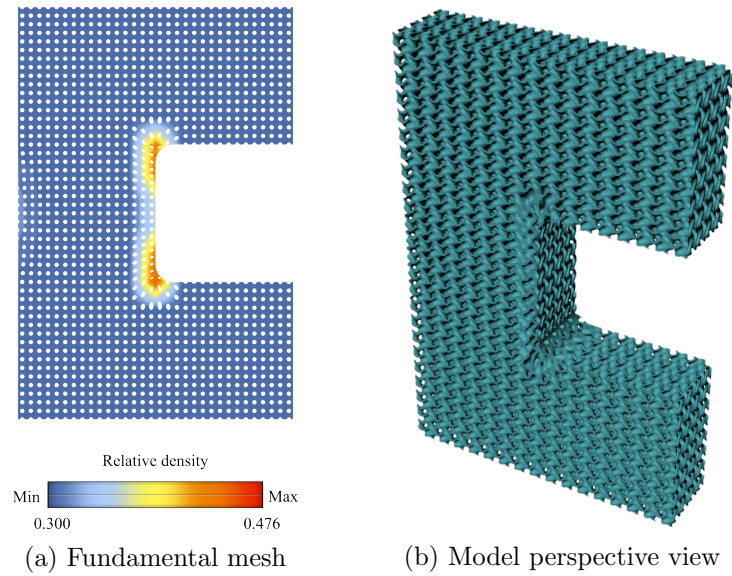


Figure C.4: C-shaped body: Modelling.

Table C.1: Functionally graded C-shaped body evaluation results.

Modelling	ρ^*	Mass (g)	u_{total} (mm)	σ_{eq} (MPa)		Nodes	
				$\sigma_{eq \ max}$	$\sigma_{99.5\%}$	Count	% over σ_{perm}
Solid body	1.000	709.63					
Permissible design values			2.00	550.00			
Gyroid-based							
Constant density	0.592	421.15	0.82	55560	189.19	5.31E06	0.0103
Ratio variation	(0.300 - 0.476)	231.23	1.81	20375	400.90	4.01E06	0.1437

stiffness of the structure, evidenced by the increase of the displacement at the free end.

The maximum stress value of the graded design was found in a different location from the expected stress concentration, according to the preliminary stress distribution, and was attributed to local defects on the imported mesh. Following the same procedure of the cantilever case study, an analysis of the equivalent stress results histogram yields that stress values over the permissible condition are found on less than 0.143% of the data. Ultimately, both, the representative stress of $\sigma_{99.5\%}=400.90\text{MPa}$ and the total displacement at the free end on the variable ratio design, falls under the predefined permissible conditions.

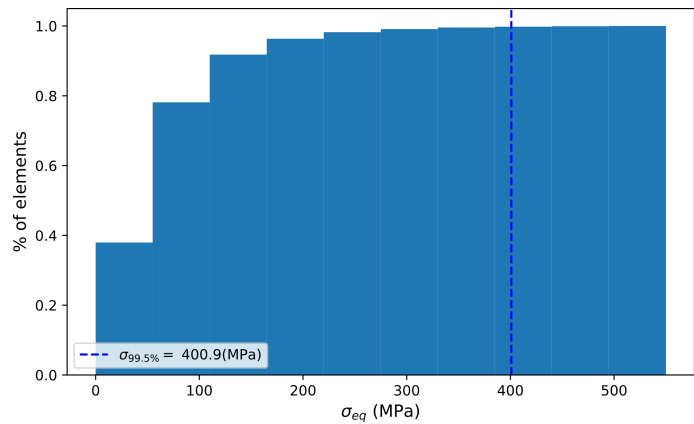
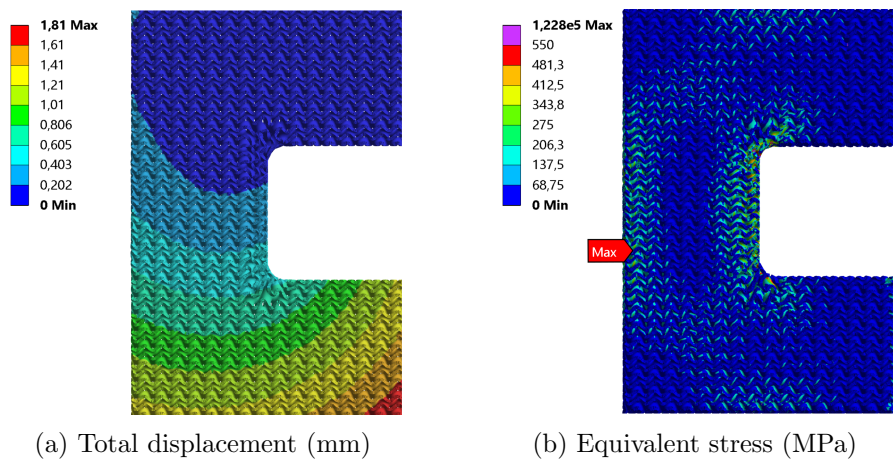


Figure C.5: C-shaped body: Variable thickness-to-length ratio evaluation.

Appendix D

Support information

D.1 Algorithm for relative density equation factors' optimization

Algorithm D.1.1 details the pseudocode followed for the factor optimization to obtain a reduction of the Residual Sum of Squares in the proposed relative density equations of section 2.2.

Algorithm D.1.1 Gradient Descent for α, β, γ optimization

```
1:  $RD \leftarrow$  Rhinoceros CAD data
2: Construct  $RSS(\alpha, \beta, \gamma)$ 
3:  $\theta_0 \leftarrow \alpha_0, \beta_0, \gamma_0$ 
4:  $\theta_k \leftarrow \theta_0$ 
5: while  $\eta_{k+1} - \eta_k < \text{precision}$  do
6:    $\theta_{k+1} \leftarrow \theta_k - \eta_k \nabla RSS(\theta_k)$ 
7:    $\eta_{k+1}$  adjustment
8:   if  $RSS(\theta_{k+1}) < RSS(\theta_k)$  then
9:      $\theta_k \leftarrow \theta_{k+1}$ 
10:  end if
11: end while
12: return  $\theta_{k+1}$ 
```

D.2 Cantilever Beam case study

The following subsections details the Log outputs corresponding to feedback information for the user from the diverse GH components involved in the design of a functionally graded cantilever beam.

Design specifications

Preliminary FEA test was run through a relatively coarse FE mesh (1471 nodes), given the simplicity of the cantilever geometry. Below are the details of the Log outputs from the `ANSYS_fileReader` component, while loading total deformation and equivalent stress results. This data is used for both modelling scenarios: graded density construct with Primitive and Gyroid TPMS.

```
ANSYS_fileReader
File : total_deformation.txt
Nodes : 1471
Max value : 0.1413
```

```
ANSYS_fileReader
File : eq_stress.txt
Nodes : 1471
Max value : 3.6705
```

Modelling using Primitive TPMS

The Log output for the `Equivalent_Material_Coefficients` component when loading the maximum displacement and equivalent stress values from the preliminary FEA is shown below, detailing the calculated relative density for the constant density scenario ($\rho_S = 0.327$).

```
Eq_Material_coefficients
Used model: primitive_M4_2022
rho_E = 0.31
rho_S = 0.327
=> Predominant effects of stress
=> Use S_Model_coefficients data
```

Density Mapping

The density mapping is done by two steps, first the calculation of the densities from the FEA data, and then the remapping procedure in a regular grid. Below are the Log details of the `Relative_Density_from_FEA` and `Density_Mapping` GH components.

```
FEA_Relative_Density_Calculator
TPMS ID 0 : Primitive
Density limit : 0.711
Q_calc = 0.100 to 0.327
Q_average = 0.145
```

Density mapping from a reference grid size of 10mm:

```

Density_Mapping
Approximation by : Weights
Tolerance(mm) : 5.00
Sensitivity(mm) : 37.50
Q = 0.100 to 0.325
Density grid of 151x31x21 elements
Grid oversize = False

```

Density mapping from a reference grid size of 50mm:

```

Density_Mapping
Approximation by : Weights
Tolerance(mm) : 18.75
Sensitivity(mm) : 50.00
Q = 0.100 to 0.318
Density grid of 31x7x5 elements
Grid oversize = False

```

Variable thickness modelling

The design parameter mapping process log is detailed below for the variable thickness Primitive scenario.

```

Densign_parameter_mapping
TPMS ID 0 : Primitive
Modelling variation : Thickness
d[mm] = 2.12 to 7.06
L[mm] = 50.00 to 50.00

```

The fundamental mesh generation of the variable thickness scenario was obtained from a reference voxel size of 10mm with 3 voxel subdivision iterations. Is worth noticing that the voxel cleaning process was able to erase 5.54E06 elements that are not necessary for the MT algorithm. The log of this process is detailed bellow.

```

TPMS_Mesh_Generator
Initial voxel
- Count : 90000
- Size(x,y,z) : (10.00,10.00,10.00)

Control size : 1.63
Calculated subdivision iterations : 3
Calculated voxel size(x,y,z) : (1.25,1.25,1.25)

Refined voxel after 3 iteration(s)
- Count : 5774400
- Size(x,y,z) : (1.25,1.25,1.25)

5544720 erased voxel(s)

```

Lastly, the SDF offset process Log is shown below. As this process was developed just for demonstrative purposes of the closed meshes, the voxel subdivision was decreased to 2 iterations. Similarly, the process was able to erase 3.69E06 voxels with no information for the required meshing process.

```

SDF_offset
Initial voxel
- Count : 107008
- Size(x,y,z) : (10.00,10.00,10.00)

Control size : 1.06
Calculated subdivision iterations : 4
Calculated voxel size(x,y,z) : (0.63,0.63,0.63)

Refined voxel after 2 iteration(s)
- Count : 2129865
- Size(x,y,z) : (2.50,2.50,2.50)

3690767 erased voxel(s)

```

Variable length modelling

For the variable length modelling, the design parameter mapping process Log is detailed below.

```

Densign_parameter_mapping
TPMS ID 0 : Primitive
Modelling variation : Length
d[mm] = 4.00 to 4.00
L[mm] = 28.35 to 94.26

```

In this case, the fundamental mesh was generated from a reference voxel size of 12.5mm with 3 subdivision iterations. The process Log is detailed below.

```

TPMS_Mesh_Generator
Initial voxel
- Count : 46080
- Size(x,y,z) : (12.50,12.50,12.50)

Control size : 0.92
Calculated subdivision iterations : 4
Calculated voxel size(x,y,z) : (0.78,0.78,0.78)

Refined voxel after 3 iteration(s)
- Count : 4052331
- Size(x,y,z) : (1.56,1.56,1.56)

3346444 erased voxel(s)

```

Variable thickness-to-length ratio modelling

The variable ratio scenario design parameter mapping Log is detailed below.

```

Densign_parameter_mapping
TPMS ID 0 : Primitive
Modelling variation : Ratio
d[mm] = 2.12 to 5.52
L[mm] = 40.00 to 50.00

```

A reference voxel size of 8mm with 3 subdivision iterations was used to generate the fundamental mesh. This process Log is detailed next.

```

TPMS_Mesh_Generator
Initial voxel
- Count : 172975
- Size(x,y,z) : (8.02,8.11,8.00)

Control size : 1.31
Calculated subdivision iterations : 3
Calculated voxel size(x,y,z) : (1.00,1.01,1.00)

Refined voxel after 3 iteration(s)
- Count : 9850607
- Size(x,y,z) : (1.00,1.01,1.00)

8493472 erased voxel(s)

```

The SDF offset was developed with 2 iterative voxel subdivisions, just for demonstrative purposes. The process Log is detailed below.

```

SDF_offset
Initial voxel
- Count : 205200
- Size(x,y,z) : (8.00,8.00,8.15)

Control size : 1.06
Calculated subdivision iterations : 3
Calculated voxel size(x,y,z) : (1.00,1.00,1.02)

Refined voxel after 2 iteration(s)
- Count : 4186157
- Size(x,y,z) : (2.00,2.00,2.04)

7437856 erased voxel(s)

```

Constant density modelling

Lastly, the constant density scenario used the same fundamental shape as in the thickness variation scenario. Similarly, the SDF offset process was obtained from 2 voxel subdivision iterations, as detailed by the process Log below.

```

SDF_offset
Initial voxel
- Count : 107008
- Size(x,y,z) : (10.00,10.00,10.00)

Control size : 1.17
Calculated subdivision iterations : 4
Calculated voxel size(x,y,z) : (0.63,0.63,0.63)

Refined voxel after 2 iteration(s)
- Count : 3344832
- Size(x,y,z) : (2.50,2.50,2.50)

2475800 erased voxel(s)

```

Modelling using Gyroid TPMS

The Log output for the coefficients determination is shown below, detailing the calculated relative density for the constant density scenario ($\rho_S = 0.319$).

```
Eq_Material_coefficients
Used model: gyroid_M4_2022
rho_E = 0.228
rho_S = 0.319
=> Predominant effects of stress
=> Use S_Model_coefficients data
```

Density Mapping

Similarly to the Primitive scenario, the density mapping is done by the remapping of the densities calculated from the FEA data. Below are the Log details of the relative density calculation from FEA and density mapping processes.

```
FEA_Relative_Density_Calculator
TPMS ID 1 : Gyroid
Density limit : 0.688
Q_calc = 0.123 to 0.319
Q_average = 0.164
```

Density mapping from a reference grid size of 10mm:

```
Density_Mapping
Approximation by : Weights
Tolerance(mm) : 5.00
Sensitivity(mm) : 37.50
Q = 0.123 to 0.317
Density grid of 151x31x21 elements
Grid oversize = False
```

Density mapping from a reference grid size of 50mm:

```
Density_Mapping
Approximation by : Weights
Tolerance(mm) : 18.75
Sensitivity(mm) : 50.00
Q = 0.123 to 0.312
Density grid of 31x7x5 elements
Grid oversize = False
```

Variable thickness modelling

The variable thickness scenario design parameter mapping Log is detailed below.

```
Densign_parameter_mapping
TPMS ID 1 : Gyroid
Modelling variation : Thickness
d[mm] = 2.00 to 5.24
L[mm] = 50.00 to 50.00
```

The fundamental shape was obtained by using a voxel size of 12.5mm and 3 voxel subdivision iterations, as detailed by the process Log shown next.

```

Initial voxel
- Count : 46080
- Size(x,y,z) : (12.50,12.50,12.50)

Control size : 1.63
Calculated subdivision iterations : 3
Calculated voxel size(x,y,z) : (1.56,1.56,1.56)

Refined voxel after 3 iteration(s)
- Count : 4230720
- Size(x,y,z) : (1.56,1.56,1.56)

4443840 erased voxel(s)

```

The SDF offset process was obtained from 2 voxel subdivision iterations. The process Log is shown below.

```

SDF_offset
Initial voxel
- Count : 51425
- Size(x,y,z) : (12.56,12.80,12.94)

Control size : 1
Calculated subdivision iterations : 4
Calculated voxel size(x,y,z) : (0.79,0.80,0.81)

Refined voxel after 2 iteration(s)
- Count : 1506527
- Size(x,y,z) : (3.14,3.20,3.24)

1755525 erased voxel(s)

```

Variable thickness-to-length ratio modelling

The design parameter mapping process Log for the variable ratio construct is shown below.

```

Densign_parameter_mapping
TPMS ID 1 : Gyroid
Modelling variation : Ratio
d[mm] = 2.00 to 4.13
L[mm] = 40.00 to 50.00

```

With these results, the fundamental shape was obtained from a voxel size of 10mm under 3 subdivision iterations, as detailed by the process Log below.

```

TPMS_Mesh_Generator
Initial voxel
- Count : 90000
- Size(x,y,z) : (10.00,10.00,10.00)

Control size : 1.31
Calculated subdivision iterations : 3
Calculated voxel size(x,y,z) : (1.25,1.25,1.25)

Refined voxel after 3 iteration(s)

```

```
- Count : 7453787
- Size(x,y,z) : (1.25,1.25,1.25)
```

```
7039364 erased voxel(s)
```

The SDF process Log is shown next. This step considered 2 voxel subdivision iterations.

```
SDF_offset
Initial voxel
- Count : 107008
- Size(x,y,z) : (10.00,10.00,10.00)

Control size : 1
Calculated subdivision iterations : 4
Calculated voxel size(x,y,z) : (0.63,0.63,0.63)
```

```
Refined voxel after 2 iteration(s)
- Count : 3004008
- Size(x,y,z) : (2.50,2.50,2.50)
```

```
3632845 erased voxel(s)
```

Constant density modelling

As before, the fundamental mesh of the constant density case is the same as in the variable thickness scenario. The SDF offset process Log is shown below, for 2 voxel subdivision iterations.

```
SDF_offset
Initial voxel
- Count : 51425
- Size(x,y,z) : (12.56,12.80,12.94)

Control size : 1.29
Calculated subdivision iterations : 4
Calculated voxel size(x,y,z) : (0.79,0.80,0.81)
```

```
Refined voxel after 2 iteration(s)
- Count : 1991414
- Size(x,y,z) : (3.14,3.20,3.24)
```

```
1274194 erased voxel(s)
```

Redesign of variable thickness-to-length constructs

The collection of logs from the redesign of Primitive-based constructs with variable ratio is detailed below.

```
Density_Mapping
Approximation by : Weights
Tolerance(mm) : 18.75
Sensitivity(mm) : 50.00
Q = 0.200 to 0.318
Density grid of 31x7x5 elements
Grid oversize = False
```



```

Densign_parameter_mapping
TPMS ID 0 : Primitive
Modelling variation : Ratio
d[mm] = 4.29 to 5.52
L[mm] = 40.00 to 50.00

TPMS_Mesh_Generator
Initial voxel
- Count : 172975
- Size(x,y,z) : (8.02,8.11,8.00)

Control size : 1.31
Calculated subdivision iterations : 3
Calculated voxel size(x,y,z) : (1.00,1.01,1.00)

Refined voxel after 3 iteration(s)
- Count : 9614524
- Size(x,y,z) : (1.00,1.01,1.00)

8111014 erased voxel(s)

```

Similarly, below are the compiled Log outputs for the Gyroid-based redesign.

```

Density_Mapping
Approximation by : Weights
Tolerance(mm) : 18.75
Sensitivity(mm) : 50.00
Q = 0.200 to 0.312
Density grid of 31x7x5 elements
Grid oversize = False

Densign_parameter_mapping
TPMS ID 1 : Gyroid
Modelling variation : Ratio
d[mm] = 3.27 to 4.13
L[mm] = 40.00 to 50.00

TPMS_Mesh_Generator
Initial voxel
- Count : 90000
- Size(x,y,z) : (10.00,10.00,10.00)

Control size : 1.31
Calculated subdivision iterations : 3
Calculated voxel size(x,y,z) : (1.25,1.25,1.25)

Refined voxel after 3 iteration(s)
- Count : 7318560
- Size(x,y,z) : (1.25,1.25,1.25)

6604448 erased voxel(s)

```

D.3 C-shaped body case study

The collection of Log outputs from the diverse GH components used for the C-shaped body case study are gathered below.

```

ANSYS_fileReader
File : Cshape_deformation.txt
Nodes : 3893
Max value : 0.18099

ANSYS_fileReader
File : Cshape_stress.txt
Nodes : 3893
Max value : 104.57

Eq_Material_coefficients
Used model: gyroid_M4_2022
rho_E = 0.281
rho_S = 0.592
=> Predominant effects of stress
=> Use S_Model_coefficients data

FEA_Relative_Density_Calculator
TPMS ID 1 : Gyroid
Density limits : 0.123 to 0.688
Q_calc = 0.300 to 0.592
Q_average = 0.311

Density_Mapping
Approximation by : Weights
Tolerance(mm) : 1.67
Sensitivity(mm) : 8.00
Q = 0.300 to 0.476
Density grid of 11x4x16 elements
Grid oversize = False

Densign_parameter_mapping
TPMS ID 1 : Gyroid
Modelling variation : Ratio
d[mm] = 0.50 to 0.64
L[mm] = 4.00 to 5.00

TPMS_Mesh_Generator
Initial voxel
- Count : 351000
- Size(x,y,z) : (1.00,1.00,1.00)

Control size : 0.13
Calculated subdivision iterations : 3
Calculated voxel size(x,y,z) : (0.13,0.13,0.13)

Refined voxels after 2 iteration(s)
- Count : 5850562
- Size(x,y,z) : (0.25,0.25,0.25)

5754037 erased voxel(s)

```


Appendix E

Résumé étendu

Introduction

La fabrication additive arc-fil (*Wire and Arc Additive Manufacturing* : WAAM), qui fait partie des technologies de dépôt de matière sous énergie concentrée (*Direct Energy Deposition* : DED) est une technologie récente de fabrication qui utilise un arc électrique comme source de chaleur pour fusionner un fil métallique. Ainsi, des pièces tridimensionnelles sont construites en empilant des cordons de soudure de tout type de matériau soudable. Ces procédés se sont révélés très prometteurs pour les applications industrielles, notamment en raison de leur vitesse de fabrication plus élevée que ceux des technologies à lit de poudre métallique, de la possibilité de créer des pièces de grande taille car le volume de la chambre n'est pas limité et du rendement élevé des matériaux [Gisario et al., 2019]. La faculté de produire des pièces allégées reste cependant peu exploitée aujourd'hui dans le contexte WAAM.

Le projet BeShape, financé par l'Agence Nationale de la Recherche (ANR), aborde la conception de pièces légères fabriquées par apport de fil et arc électrique en proposant de voir les structures produites comme un assemblage de motifs. L'objectif principal du projet est de proposer une démarche de conception permettant d'obtenir des pièces légères par assemblage de motifs prédéfinis fabricables par WAAM, afin de profiter des libertés offertes par ces procédés tout en respectant les contraintes de fabricabilité et les exigences formulées par le concepteur. Le projet BeShape est coordonné par le laboratoire G-SCOP (Sciences pour la conception, l'Optimisation et la Production) de l'Université Grenoble Alpes, en partenariat avec le laboratoire COSMER (Conception de Systèmes Mécaniques et Robotiques) de l'Université de Toulon et les partenaires industriels DPRI, PRODWAYS et SAFRAN AE. Plus précisément, ce manuscrit présente les travaux sur la conception et l'évaluation mécanique des structures, effectués au laboratoire G-SCOP, tandis que l'analyse des contraintes de fabrication et la génération des parcours d'outils sont au centre des préoccupations du laboratoire COSMER.

Ce manuscrit détaille la création des surfaces, l'adaptation de la conception à une carte de densité préétablie et l'évaluation de ces constructions en utilisant des surfaces minimales triplement périodiques (*Triply Periodic Minimal Surfaces* : TPMS) comme motifs de construction pour des matériaux cellulaires à gradient fonctionnel (*Functionally Graded Cellular Materials* : FGCM), en raison de l'identification préalable de conditions de fabrication favorables effectuée par le laboratoire COSMER et d'une revue de la littérature sur l'application et la caractérisation de ces structures.

La question de recherche à examiner est la suivante :

Comment concevoir des pièces légères basées sur des motifs TPMS pouvant être fabriquées par des procédés de type dépôt de matière sous énergie concentrée (DED) ?

Les sections suivantes présentent un résumé étendu en français du manuscrit, en soulignant les principales contributions de chaque section. De plus, des publications rédigées par l’auteur ont été acceptées pour : une introduction formelle d’une méthodologie de conception. [Ramírez et al., 2022a], la définition de la réponse mécanique en fonction de la densité relative de la structure [Ramírez et al., 2022b] et les équations établissant la densité relative en fonction des paramètres de conception [Ramírez et al., 2021b,a].

E.1 Etat de l’art

Dans le chapitre 1, à partir d’une revue de littérature sur la fabrication additive métallique (*Additive Manufacturing* : AM) et l’adéquation des motifs TPMS, ce manuscrit vise à combler les lacunes actuelles sur les méthodes et les outils pour la modélisation des structures TPMS à gradient de densité.

Fabrication additive métallique

Dans le cadre du projet BeShape, la recherche de cette thèse est orientée vers la conception de motifs paramétriques complexes à fabriquer par fabrication additive arc/fil (WAAM). Par conséquent, une comparaison des différentes technologies de fabrication additive métallique est d’abord proposée pour mettre en évidence les avantages et les limites des technologies fil par rapport aux technologies lit de poudre ou projection de poudre.

Parmi les différentes catégories de processus AM, l’apport de matières métalliques est généralement traité par des technologies de fusion sur lit de poudre (*Powder Bed Fusion* : PBF) ou de dépôt de matière sous énergie concentrée (DED). Ainsi, ISO/ASTM [2021] définit le PBF comme un ”procédé dans lequel l’énergie thermique fusionne sélectivement des régions d’un lit de poudre” et le DED comme un ”procédé dans lequel une énergie thermique focalisée est utilisée pour fusionner des matériaux en les faisant fondre au moment où ils sont déposés”, tout en établissant que la source d’énergie peut être un laser, un faisceau d’électrons ou un arc de plasma, entre autres.

Une autre catégorisation a été présentée antérieurement par Frazier [2014], classifiant l’AM métallique en fonction de l’apport de matière : systèmes à lit de poudre, à projection de poudre et à apport par fil. À partir des définitions de ISO/ASTM [2021], les deux dernières méthodes d’apport de matière sont considérées comme des procédés DED [Dass and Moridi, 2019]. Le Tableau 1.1 (section 1.1) résume quelques avantages et inconvénients de ces apports, ainsi que les technologies développées, pour établir un comparatif entre les systèmes avec apports de matière par poudre et par fil.

Ensuite, un état de l’art sur les matériaux cellulaires est présenté avec un focus particulier sur les surfaces minimales triplement périodiques (TPMS), étant donné l’intérêt de ces structures dans le contexte du projet Beshape.

Usage des TPMS au sein des matériaux cellulaires

Les matériaux cellulaires, caractérisés par un réseau connecté de cellules unitaires, peuvent être configurés pour créer des structures robustes avec un changement significatif de

leur comportement comparé à celui de leur matériau constitutif [Maconachie et al., 2019]. Il a été montré que les conséquences de la topologie de ces constructions cellulaires sont plus importantes que le matériau constitutif. Des matériaux cellulaires à gradient fonctionnel (FGCM) peuvent être obtenus en changeant leur propriété progressivement dans l'espace, soit par une modification de la composition ou de la microstructure du matériau en mélangeant des matières premières différentes au cours de la fabrication [Ansari et al., 2021], soit par une distribution optimisée de la densité relative des cellules unitaire dans l'espace de conception [Yang et al., 2019].

En particulier, les FGCM à densité variable présentent une plus grande efficacité du matériau [Maskery et al., 2017b] et de meilleures capacités d'absorption d'énergie [Choy et al., 2017, Li et al., 2019] que leurs homologues uniformes. La conception de ce type de structure est généralement liée à l'application d'une carte de densité issue d'une démarche d'optimisation topologique (TO) [Li et al., 2018].

Les travaux antérieurs sur les FGCM se concentrent principalement sur les cellules unitaires à base de poutres (*strut-based*) [Al-Saedi et al., 2018], mais ces géométries impliquent des difficultés de fabrication et présentent des concentrations de contraintes importantes à la liaison des poutres. Pour surmonter ces problèmes, l'utilisation de FGCM basés sur des TPMS est un sujet de recherche d'actualité du fait de leur capacité à créer des matériaux avec des composantes continues et interconnectées [Abueidda et al., 2019].

Une surface minimale triplement périodique est caractérisée par une courbure moyenne nulle en tout point, ce qui minimise localement l'aire, et s'étend périodiquement dans trois directions indépendantes sans auto-intersections. La mise en œuvre de TPMS pour remplir des produits est intéressante car leurs propriétés topologiques permettent un support entre les couches présentant des avantages de fabrication par rapport aux treillis basés sur des poutres [Yan et al., 2014b].

Résumé des manques de la littérature

L'utilisation de cellules unitaires TPMS est une alternative attrayante pour le développement de structures cellulaires légères en raison de leurs avantages significatifs par rapport aux structures traditionnelles en treillis en ce qui concerne la fabricabilité, le comportement mécanique et leur capacité d'autoportance entre les couches déposées en raison de leurs caractéristiques de surface. Bien que la fabrication de modèles métalliques TPMS ait été largement testée par des procédés PBF, leur fabrication par des technologies WAAM reste un domaine de recherche inexploré. Dans le contexte du projet BeShape, l'application des TPMS sur les technologies WAAM est basée sur des recherches sur la conception mécanique et l'évaluation de motifs adaptés à une carte de densité donnée, ainsi que sur l'analyse des contraintes de fabrication et la génération de parcours d'outils. En conséquence, le travail présenté dans les chapitres suivants se concentrera sur la conception de TPMS, en particulier les motifs primitifs et gyroïdes, en raison de leurs avantages potentiels en termes de fabricabilité par rapport à d'autres structures de surface minimales, comme déterminé par l'évaluation initiale du projet.

La modélisation de la forme fondamentale des structures TPMS est fortement influencée par les effets des valeurs sélectionnées pour leurs variables de conception, à savoir le paramètre level-set C sur les constructions *skeletal-based*, ou l'épaisseur d et la longueur L des cellules unitaires sur les *sheet-based* topologies. Bien que des travaux antérieurs aient étudié les effets de C sur la densité relative des cellules unitaires (uniquement pour les modèles Gyroïdes [Li et al., 2019]), l'influence d'autres paramètres de conception n'a pas encore été étudiée. Par conséquent, le chapitre 2 présentera les effets de d et L sur les TPMS Primitifs et Gyroïdes, ainsi que les effets de C sur les motifs primitifs, ce qui n'a

pas été envisagé auparavant dans la littérature. L'analyse des effets des paramètres de conception a pour but de déterminer comment la densité relative des motifs réagit à leur variation.

La relation entre la densité des motifs et leurs paramètres de conception est une étape importante vers la création de FGCM. Même si des approches précédentes dans la littérature ont développé des FGCM à densité variable à partir d'une carte de densité obtenue par TO [Li et al., 2018, Panesar et al., 2018], une procédure de modélisation formelle n'a pas été établie. Par conséquent, une proposition de méthodologie pour la conception de FGCM basée sur des TPMS à densité variable est présentée dans le chapitre 3.

Enfin, même si des évaluations antérieures des avantages de ces constructions à gradient de densité par rapport aux scénarios à densité constante ont été présentées dans la littérature, elles utilisent généralement des distributions de densité linéaires [Maconachie et al., 2019]. Ainsi, l'un des objectifs de cette thèse est d'analyser des FGCM élaborés à partir d'une carte de densité tridimensionnelle. En particulier, un processus permettant de corrélérer les résultats d'analyse par éléments finis d'un matériau plein à une distribution de densité spécifique sera introduit, comme alternative à une cartographie de densité à partir de procédures TO. Ces processus sont présentés dans le chapitre 4.

E.2 Effets des paramètres de conception des TPMS sur leur densité relative

Le chapitre 2 détaille la construction mathématique des TPMS et les paramètres qui influencent leur forme, ainsi que la détermination d'une équation de densité relative en fonction des paramètres de conception du motif.

Modélisation des structures TPMS

En tant que surfaces définies mathématiquement, les TPMS sont généralement définies par des équations implicites. Dans le contexte de cette étude, l'équation E.1 et l'équation E.2 détaillent les fonctions pour les motifs Primitif et Gyroïde, respectivement. Le facteur de dilatation $\lambda = 2\pi/L$, définit la périodicité du motif en fonction de la longueur L d'une cellule unitaire cubique. Les deux topologies TPMS étudiées sont représentées sur la Figure E.1.

$$f_P(x, y, z) = \cos(\lambda_x x) + \cos(\lambda_y y) + \cos(\lambda_z z) \quad (\text{E.1})$$

$$f_G(x, y, z) = \cos(\lambda_x x) \sin(\lambda_y y) + \cos(\lambda_y y) \sin(\lambda_z z) + \cos(\lambda_z z) \sin(\lambda_x x) \quad (\text{E.2})$$

Pour la représentation des surfaces, la modélisation des TPMS utilise classiquement l'algorithme *Marching Cubes* (MC), qui est une procédure efficace pour extraire des iso-surfaces dans des espaces de données 3D [Feng et al., 2019]. L'algorithme génère la surface par une approche de voxelisation en évaluant la fonction implicite $\phi(x, y, z)$ présentée dans l'équation E.3. Chaque voxel est défini comme contenant ou comme étant en dehors de la surface. Les résultats sont utilisés pour créer une facette triangulaire qui dépend des valeurs des sommets de chaque voxel. Pour plus d'information sur cette procédure on peut se référer à Lorensen and Cline [1987]. Pour une valeur du level-set C égale à 0, la surface générée divise la boîte englobante cubique en deux secteurs égaux. Cette surface représente la surface fondamentale du TPMS.

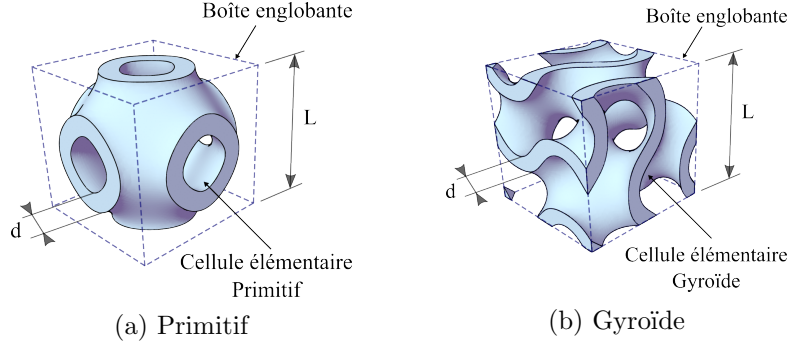


Figure E.1: Topologies à épaisseur constante pour les structures TPMS.

$$\phi(x, y, z) = f_{P,G}(x, y, z) - C \quad (\text{E.3})$$

Des outils de conception ont été développés pour générer des structures volumiques en faisant varier la valeur du level-set C [Jones et al., 2021, Al-Ketan and Al-Rub, 2020], en utilisant la relation entre C et la densité relative pour des modèles coques [Li et al., 2018, 2019, Zhao et al., 2018]. Cependant les structures à densité uniforme engendrés par ce type de modélisation ne présentent pas une épaisseur constante.

Comme l'objectif de ce travail est de relier la densité relative des motifs à leur épaisseur et à la longueur de la cellule unitaire, une approche de modélisation par décalage de surface a été proposée pour garantir une épaisseur contrôlable. Afin de créer un modèle volumique du TPMS, la surface fondamentale est utilisée comme surface centrale à partir de laquelle les limites intérieures et extérieures de la structure sont obtenues. Pour cela, chaque sommet est déplacé de part et d'autre de la moitié de l'épaisseur locale souhaitée d du motif le long des vecteurs normaux de la surface.

Détermination de la fonction de densité relative

Afin d'établir la densité relative en fonction des paramètres de conception, plusieurs ensembles de structures Primitif et Gyroïde ont été générés, avec différentes longueurs et épaisseurs. Pour chaque modèle, le densité relative RD issue du modèle CAO maillé a été calculée comme le rapport entre le volume de la structure et celui d'une boîte cubique englobante, comme montré dans l'équation E.4.

$$RD = \frac{\text{volume de la structure}}{\text{volume de la boîte englobante}} \quad (\text{E.4})$$

L'équation de densité relative ρ^* proposée suppose que les surfaces intérieure et extérieure des modèles volumiques, obtenues par décalage de la surface fondamentale du TPMS, peuvent être assimilées à une sphère unitaire. Cette approche de modélisation est envisageable du fait de la formulation mathématique du TPMS. Les équations de surface pour le TPMS sont dérivées des formules de Weierstrass, qui sont un ensemble d'intégrales elliptiques [von Schnering and Nesper, 1991] et leur paramétrage peut être considéré comme l'inverse de la carte de Gauss des zones de surface dans une sphère unitaire [Mickel et al., 2012]. En conséquence, la densité relative peut être déterminée par l'équation E.5 en fonction du rapport épaisseur/longueur, où les coefficients α' , β' et γ' sont considérés comme des constantes dont la valeurs dépend du type de TPMS.

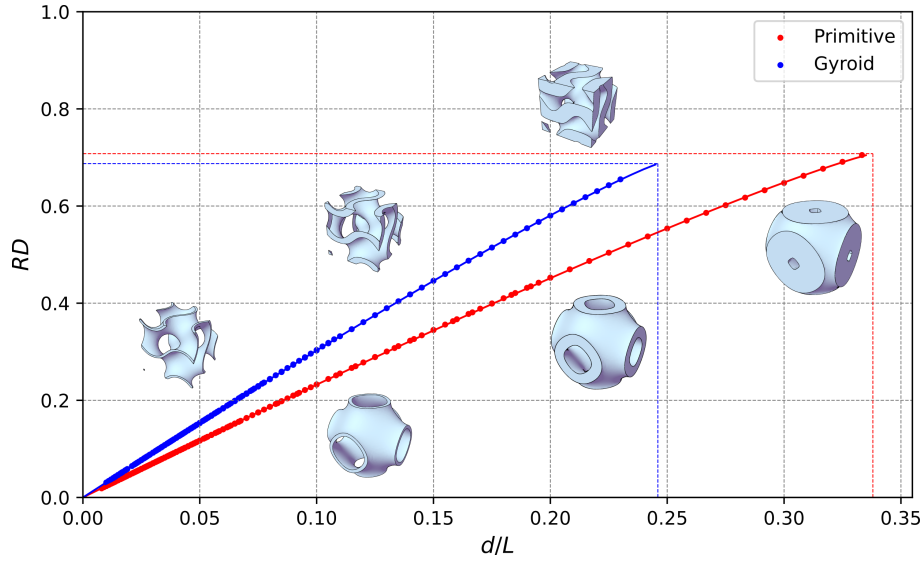


Figure E.2: Densité relative RD fonction du rapport des paramètres de conception $\frac{d}{L}$ pour les structures Primitif et Gyroïde.

$$\rho^* \left(\frac{d}{L} \right) = \beta' - \beta' \left(1 - \alpha' \frac{d}{L} \right)^{\gamma'} \quad (\text{E.5})$$

Afin de déterminer les paramètres de cette équation, les données RD ont été reportées sur un graphique en fonction du rapport épaisseur/longueur $\frac{d}{L}$, comme le montre la Figure E.2. Pour déterminer les coefficients, une régression non linéaire et une procédure d'optimisation par descente de gradient ont été utilisées à partir des données RD précédentes. Les équations obtenues pour les modèles Primitif et Gyroïde sont détaillées dans Equation 2.10 et Equation 2.11, respectivement (sous-section 2.2.2).

Une analyse plus approfondie des maxima de l'équation E.5 montre que le coefficient β' est analogue à la densité relative maximale, et le coefficient α' au rapport longueur/épaisseur $\frac{L}{d}$ maximal pouvant être modélisé. L'équation n'est pas définie pour les valeurs situées en dehors de ces limites.

E.3 Méthodologie de conception des structures TPMS à gradient de densité

La méthodologie de conception et son implémentation pour la création de TPMS à densité variable est détaillée dans le chapitre 3. La création de TPMS d'épaisseur et/ou de longueur variable par la méthodologie proposée est basée sur un algorithme de polygonisation *Marching Tetrahedra* (MT), à la place du MC, pour la création de la surface du motif. Plusieurs outils pour la construction des structures ont été développés, qui sont détaillés dans les annexes.

Même si certains logiciels commerciaux permettent de générer des structures TPMS à densité graduelle [Al-Ketan and Al-Rub, 2020], les possibilités sont limitées aux gradients linéaires. De plus, sur la base de la littérature disponible, il n'existe pas de procédure de modélisation formelle pour développer des structures TPMS avec une densité variable, tout en étant capable de contrôler l'épaisseur des motifs et la longueur des cellules unitaires en fonction d'une carte de densité tridimensionnelle.

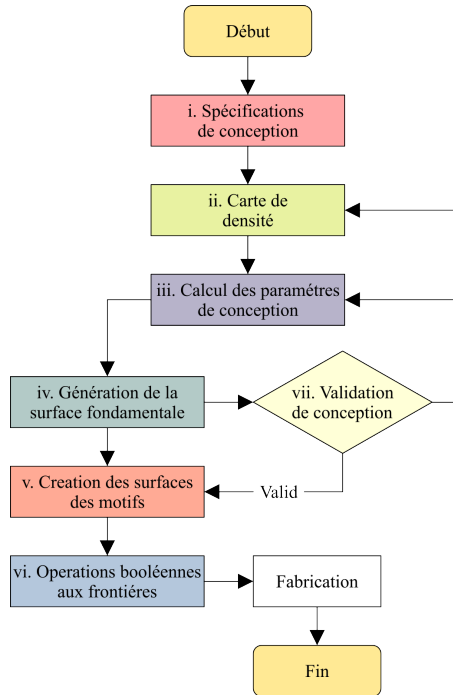


Figure E.3: Méthodologie de conception pour les structures TPMS à gradient fonctionnel.

En outre, la littérature sur les structures à densité constante utilise un processus de projection des sommets des maillages le long des vecteurs normaux pour attribuer une épaisseur à un maillage central représentant la forme fondamentale du TPMS [Abueidda et al., 2019, Zhang et al., 2018]. Cependant, cette stratégie peut produire des maillages avec des auto-intersections et/ou des bords de facettes courts, qui proviennent de problèmes dans les opérations booléennes pour la création de motifs denses. Ces problèmes de maillage doivent être traités par des procédures supplémentaires de réparation de maillage. Cependant, ces procédés nécessitent un logiciel spécialisé dans le traitement des maillages, et une procédure standardisée ne peut être établie en raison de la localisation incertaine de ces problèmes.

Par conséquent, une méthodologie de conception est proposée pour la conception de TPMS à densité graduelle, en considérant une variation indépendante ou simultanée de l'épaisseur du motif et de la longueur de la cellule unitaire. En particulier, une nouvelle procédure de modélisation pour des scénarios de variation de longueur est proposée. Une procédure alternative pour créer les épaisseurs des modèles est introduite, consistant en une transformation de la forme fondamentale en un champ de distances signées (*Signed Distance Field* : SDF), qui résout les problèmes d'auto-intersections des maillages.

La méthodologie proposée pour les structures TPMS à gradient fonctionnel est représentée sur la Figure E.3. Elle comprend : (i) la définition des spécifications de conception, (ii) la création d'une carte de densité, (iii) le calcul des paramètres de conception, (iv) la génération de la surface fondamentale, (v) la création des surfaces de la structure, (vi) la génération finale du STL et (vii) les opérations de validation de la conception. Les sections ci-dessous détaillent le processus de chaque étape principale.

Spécifications de conception

La procédure de conception commence par la définition des données d'entrée et certaines opérations préliminaires, dont :

- i.1 Le domaine de conception (*Design Space* : DS), défini comme le volume enveloppe qui doit être rempli par la structure TPMS..
- i.2 La distribution de densité en valeur et position, obtenue par calcul élément fini (FEA) ou TO à partir du modèle CAO..
- i.3 Le pas souhaité de la carte de densité pour le re-mapping des données de références FEA ou TO.
- i.4 La sélection du type de TPMS, définissant la forme de la cellule utilisée pour le modèle.
- i.5 La taille de référence du voxel et les itérations de subdivision à effectuer pour discrétiser le domaine de conception avec l'algorithme de polygonisation.
- i.6 Le scénario de variation de densité : c.-à-d. un modèle à densité constante ou à densité variable par l'épaisseur, la longueur ou la variation simultanée de longueur et d'épaisseur.
- i.7 Différents paramètres de conception, fonction du scénario de variation de densité, comme la valeur de longueur et d'épaisseur ou leurs limites, la plage de densité et le point de départ de la génération de la surface.

Carte de densité

La carte de densité (*Density Map* : DM) est créée à partir des données de référence, de leur emplacement dans le DS et du pas souhaité de la DM. En raison de la nature discrète de l'algorithme de polygonisation pour la génération du maillage STL, la condition principale est d'avoir une DM représentée par une grille régulière.

Si la distribution de densité de référence est obtenue à partir de TO, les valeurs et leurs emplacements sont transmis directement aux sous-processus de re-mapping. Pour les valeurs de référence provenant de données FEA sous forme de contraintes de Von Mises, les densités locales doivent être calculées par l'application des modèles de Gibson-Ashby reliant la densité relative aux propriétés mécaniques relatives. La définition de ces modèles est détaillée au Chapitre 4.

L'exigence d'une grille uniforme est satisfaite en effectuant un re-mapping, au sein du DS, de la distribution de densité issue de TO ou de FEA. La procédure de calcul d'une densité ρ_m^* sur la grille uniforme consiste en une somme pondérée de r nœuds de densité de référence ρ_i^* . Les coefficients de pondération sont calculés comme l'inverse des distances au carré.

Calcul des paramètres de conception

Après la détermination de la DM, les paramètres de conception sont calculés en fonction du scénario de variation de densité et du type de TPMS. Le ratio épaisseur/longueur (d/L) est déterminé en fonction de la densité relative. Afin d'avoir un processus générique, ce ratio est calculé indépendamment du scénario de variation de densité spécifié. Il est utilisé pour obtenir la distribution spécifique de l'épaisseur et des longueurs dans les étapes ultérieures.

Comme le ratio dépend à la fois de l'épaisseur d et de la longueur L de la cellule unitaire, les valeurs de longueur sont d'abord calculées, puis utilisées pour trouver l'épaisseur correspondante. Dans le cas d'un scénario à longueur constante, la carte des épaisseurs est déterminée en multipliant la longueur par les valeurs locales du ratio. De même, une longueur variable avec une épaisseur constante est obtenue en divisant l'épaisseur par la valeur locale du ratio. Pour un scénario de variation simultanée de la longueur et de l'épaisseur, les valeurs de longueur sont calculées en fonction du ratio local. Ainsi, les zones présentant un ratio élevé (densité plus forte) sont associées à des valeurs de longueur faibles, tandis que les zones présentant un ratio faible (faible densité) sont associées à des valeurs de longueur importantes.

Après la définition de la carte des épaisseurs et longueurs à partir de la DM, les étapes suivantes de la méthodologie effectuent un deuxième mapping par interpolation, en fonction de la taille des voxels du DS. Cette étape est nécessaire car en général une génération correcte de la surface du TPMS nécessite une grande densité de points.

Génération de la surface fondamentale

En utilisant un algorithme de *Marching Tetrahedra* (MT), une polygonisation en maillage STL de la forme de base des constructions à densité variable est générée suivant la distribution de longueur requise (variable ou constante). Étant donné la nature discrète de la méthode de polygonisation, les courbures des surfaces générées sont fortement influencées par la taille des voxels. Une bonne approximation d'une surface nécessite qu'un segment de droite représentant une section de courbe ne s'étende pas sur un secteur circulaire de plus de 15° [ANSYS, 2004].

L'algorithme MT génère le maillage STL à partir de l'évaluation de la fonction TPMS sur chaque coin des voxels représentant le DS. Comme la voxélisation du DS peut être une opération informatiquement lourde, un processus de raffinement itératif par subdivision des voxels et de nettoyage des voxels inutilisés est mis en place.

Création des surfaces des motifs

L'étape suivante de la création de la surface du motif consiste à déplacer la forme fondamentale en utilisant l'épaisseur requise (variable ou constante). Ce processus est principalement réalisé par un processus de décalage par SDF pour définir les surfaces intérieures et extérieures et une reconstruction du maillage par un algorithme MT.

Contrairement à la dernière étape de génération de formes fondamentales, la taille de voxel requise pour la création de surfaces de motifs par décalage SDF doit à la fois permettre une bonne représentation de la courbure de la surface, et être suffisamment petite pour détecter l'épaisseur du motif.

Opérations booléennes aux frontières

Les fichiers générés par les processus précédents sont des maillages STL ouverts représentant les surfaces intérieures et extérieures du motif TPMS à gradient. Le modèle fermé final avec les motifs TPMS est obtenu par une série d'opérations booléennes sur le maillage entre les surfaces du motif et les frontières de l'espace de conception ou la forme finale de la pièce.

Ces étapes sont souvent spécifiques à chaque cas et le développement d'un outil de conception personnalisé (comme pour les autres processus) n'était pas au centre de ces recherches. Cependant, pour le développement des constructions volumique (fermées)

présentées dans les sections suivantes, le traitement STL a été effectué sur la suite de CAO SpaceClaim® 2020 R2. La chaîne de traitement comprenait une combinaison de nettoyage et de soustraction des facettes pour corriger les erreurs potentielles de maillage avant de calculer l'intersection des régions.

Validation de conception

Un processus itératif supplémentaire de validation de la conception est envisagé pour l'évaluation de la structure générée par des méthodes éléments finis. L'analyse par éléments finis nécessite la conversion du maillage STL de la forme fondamentale en éléments finis de type coque ainsi que l'attribution d'une épaisseur locale à chaque nœud des éléments coques. Pour cela, deux outils supplémentaires ont été développés pour créer l'ensemble des instructions pour l'importation du maillage éléments finis et l'assignation d'une épaisseur variable en tant que commandes APDL pour une analyse grâce au module d'analyse statique des structures du logiciel ANSYS® Workbench, Release 2020 R2.

Dans le cas d'une réponse insatisfaisante de la structure cellulaire (contrainte excessive ou déformation en dehors des conditions de travail), un processus de raffinement et d'amélioration de la forme et de la distribution de la densité est nécessaire. Cela peut se faire soit en ajustant les plages de densité utilisées dans les procédures de mapping de la densité, soit en modifiant les valeurs des paramètres de conception dans les processus de calcul des paramètres de conception. Une fois la conception validée, le processus se poursuit avec la création des surfaces de motifs et les opérations booléennes aux frontières pour créer un modèle solide, en fonction des exigences du concepteur.

E.4 Analyse et évaluation des structures TPMS

Le chapitre 4 se concentre sur les étapes de validation des TPMS issus du processus de conception proposé. Une étude de cas avec différentes stratégies de variation de la densité est utilisée pour évaluer la faisabilité de la méthodologie, tout en comparant les résultats à une configuration pièce pleine. De plus, ce chapitre contient l'étude de la réponse mécanique des TPMS en fonction de leur densité. Ces réponses mécaniques sont utilisées dans la méthodologie de conception pour générer des structures avec des variations de densité en fonction des résultats de simulation par la méthode des éléments finis.

L'application de la méthodologie est proposée pour la conception et l'évaluation d'une poutre en porte-à-faux sollicitée mécaniquement. L'objectif est de créer une construction cellulaire à gradient fonctionnel, basée sur les types de TPMS étudiés, qui présente une réponse mécanique homogène. Des informations complémentaires sur le processus de modélisation, à partir des log files des outils de conception développés, peuvent être consultées dans la section D.2 des annexes.

La méthode de conception et évaluation proposée est illustrée au travers d'une étude de cas : la conception d'une pièce en C remplie par FGCM de type Gyroïdes, offrant simultanément des variations de longueur et d'épaisseur. La Figure E.4 rassemble des images successives du processus de conception. Telle que présentée sur la Figure E.4b, la carte de densité a été obtenue à partir d'une grille de pas égal à 8mm, et présente un intervalle de densité relative compris entre 0,30 et 0,476 à partir des résultats d'une analyse FEA préliminaire (Figure E.4a). Même si cette carte de densité réduit le nombre de points par rapport aux résultats FEA de référence, la surface fondamentale de la Figure E.4c est bien en accord avec les densités locales représentées par les différentes couleurs.

Le modèle géométrique final de la Figure E.4 présente une distribution de cellules

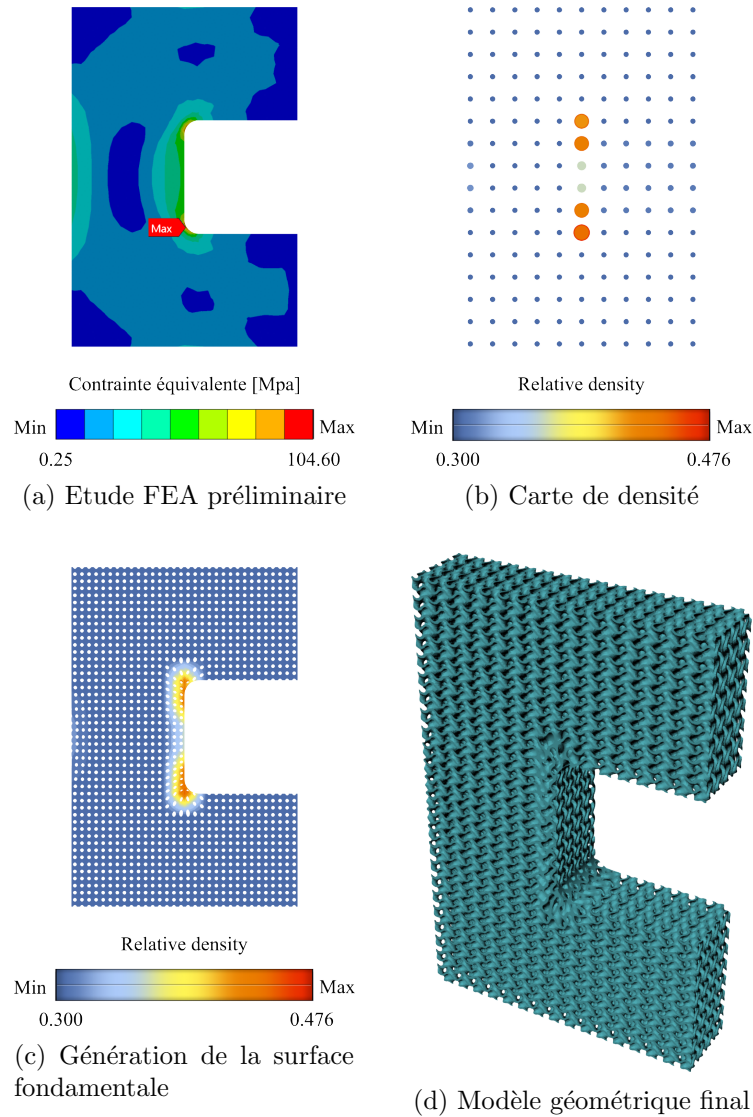


Figure E.4: Illustration des étapes de la méthode proposée.

unitaires d'une épaisseur comprise entre 0,50 et 0,64mm, et de longueurs comprises entre 4 et 5mm. Il correspond à une masse totale de 230g, ce qui représente 32% de la masse du volume plein. L'évaluation du modèle proposé et le processus de conception sont détaillés dans l'annexe C. Le déplacement total maximum obtenu s'élève à 1,81mm au niveau de l'extrémité chargée, ce qui reste bien dans les limites fixées.

E.5 Conclusions et perspectives

Finalement, le chapitre 5 présente les conclusions générales et les perspectives résultat de cette étude sur les structures TPMS adaptables.

Conclusions

Les surfaces minimales triplement périodiques (TPMS) ont été considérées comme une alternative prometteuse aux cellules en treillis pour le développement de constructions

cellulaires de grandes dimensions produites en WAAM. Leurs caractéristiques spécifiques donnent la possibilité de créer des structures avec de meilleures propriétés mécaniques. La modélisation des structures TPMS Primitif et Gyroïde a été réalisée par une polygonisation en mailles triangulaires d'un champ de distances signées (SDF) représentant la surface, à partir d'un algorithme de Marching Tetrahedra (MT). Cette implémentation personnalisée a permis de paramétrer la génération du modèle en fonction de l'épaisseur du motif d et de la longueur de la cellule unitaire L .

La relation entre la densité relative des structures et leurs paramètres de conception est une étape importante vers la création de matériaux cellulaires à gradient fonctionnel (FGCM). En conséquence, une équation de densité relative ρ^* a été proposée en fonction du rapport épaisseur/longueur des motifs $\frac{d}{L}$, comme établi dans l'équation E.5. Ces équations peuvent être encore améliorées par l'inclusion de contraintes de fabrication pour la redéfinition des facteurs α' et/ou β' par une approche d'optimisation par gradient.

L'objectif clé du développement des FGCM est l'adaptation des motifs TPMS à une carte de densité tridimensionnelle liée au scénario de charge du matériau solide. Même si la méthodologie n'a été appliquée qu'aux TPMS Primitif et Gyroïde, le processus proposé est capable de traiter n'importe quelle forme de surface minimale en connaissant leur équation de forme et leur comportement de densité relative par rapport aux paramètres de conception du motif. Au final, la méthodologie proposée devrait être couplée à une évaluation du TPMS à densité graduelle souhaitée en fonction des contraintes de fabrication de la technologie AM utilisée.

L'évaluation des constructions à densité variable est effectuée à l'aide d'un outil développé (`Mesh_to_SHELL_FE`) pour convertir le maillage STL de la surface fondamentale en un maillage FE sous la forme d'un fichier de base de données pouvant être importé dans ANSYS® Workbench, version 2020 R2. Il est constaté que la variation simultanée de l'épaisseur et de la longueur du motif est capable d'augmenter la rigidité de la structure, par rapport aux scénarios de simple variation de l'épaisseur, au prix d'une augmentation du volume de la structure. En outre, la résistance dans les deux cas peut être encore améliorée en modifiant les paramètres de conception fixés et/ou la carte de densité. Les scénarios à base uniquement de variation de longueur n'ont pas montré d'application pratique en raison en particulier du manque de contrôle des déformations aux frontières des cellules.

Perspectives

Même si la thèse est fortement influencée par l'application WAAM du projet BeShape, les contributions sont suffisamment génériques pour être appliquées à différentes technologies AM. En effet, les contraintes de fabrication liées au WAAM ne sont pas au centre de cette étude. Les partenaires académiques du projet ont pu développer une méthodologie de découpage en tranches pour générer les trajectoires de fabrication à suivre par le bras du robot. Cette méthode a été appliquée pour la fabrication d'une cellule unitaire primitive avec une épaisseur de cordon constante. Il reste encore du chemin à parcourir pour la fabrication de motifs Gyroïdes.

En ce qui concerne les constructions à densité graduelle, il a été identifié que des motifs TPMS d'épaisseur variable peuvent être générés par le contrôle de la vitesse de dépôt pendant les procédures WAAM. Même si certains des outils développés (par exemple le composant `GH Density_Finder_Plus`) peuvent être utilisés pour extraire les valeurs de densité, d'épaisseur et de longueur locales d'un point arbitraire d'une trajectoire, aucune méthode n'a été définie pour relier les conditions de fabrication réelles aux paramètres de conception des TPMS.

Comme indiqué précédemment dans le chapitre 2, les équations de densité relative peuvent être améliorées par l'inclusion des limites de fabrication des structures TPMS. En ce sens, les coefficients α' et β' liés au rapport longueur/épaisseur minimum manufacturable $\frac{L}{d}$ et à la densité maximale du motif, respectivement, peuvent être améliorés en connaissant les limites de fabrication des TPMS. Avec la connaissance d'un des paramètres, le second, et le paramètre exponentiel γ' , peuvent être approximés par l'algorithme d'optimisation du gradient pour réduire les erreurs d'approximation des équations de densité relative proposées. Il est important de noter que ce type d'analyse peut être effectué pour n'importe quelle technologie AM, créant potentiellement une bibliothèque de coefficients en fonction du processus de fabrication.